UNIVERSITÀ DI PARMA

UNIVERSITÀ DEGLI STUDI DI PARMA

DOTTORATO DI RICERCA IN

FISICA

CICLO XXXVI

Molecular Spins for Quantum Information:

new platforms for error correction, simulation and initialization

Coordinatore:
Chiar.ma Prof.ssa Raffaella Burioni

Tutore:
Chiar.mo Prof. Paolo Santini

Co-Tutore:
Chiar.mo Prof. Alessandro Chiesa

Dottorando: Mario Chizzini

Anni Accademici 2020/2021 - 2022/2023

UNIVERSITÀ DI PARMA

UNIVERSITY OF PARMA

DOCTOR OF PHILOSOPHY IN

PHYSICS

CYCLE XXXVI

Molecular Spins for Quantum Information:

new platforms for error correction, simulation and initialization

Coordinator:
Prof. Raffaella Burioni

Supervisor:
Prof. Paolo Santini

Co-supervisor:
Prof. Alessandro Chiesa

PhD student: Mario Chizzini

Accademic years 2020/2021 - 2022/2023

To my parents.

Internal illustrations:

When necessary, Copyright Permissions for internal illustrations are reported inside the document. Details are reported in Copyright Permissions section at the end of the document.

Design:

This document was typeset by the Author using LaTeX markup language on TeXstudio editor.

MIUR subjects:

FIS/03

Contents

List of Figures

List of Tables

Notations

List of abbreviations:

AFM	Auxiliary Fermion Method
BK	Braviy Kitaev (mapping)
COBYLA	Constrained Optimization BY Linear Approximations
CISS	Chiral Induced Spin Selectivity
CNOT	Control NOT (gate)
DMI	Dzyaloshinskii-Moriya Interaction
DP	De Polarizing (errors)
EPR	Electron Paramagnetic Resonance
ET	Electron Transfer
GHZ	Greenberger-Horne-Zeilinger (state)
HEA	Hardware Efficient Ansatz
HHA	Hardware Heuristic Ansatz
Id	Identity (gate)
JW	Jordan Wigner (mapping)
MNM	Molecular Nanomagnet
NISQ	Noisy Intermediate Scale Quantum (device)
N.N.	Nnearest Neighbours
N.N.N.	Next Nnearest Neighbours
PaS	Phase and Scale
PE	Photon Excitation
PMA	Physically Motivated Ansatz
PR	Planar Rotation (decomposition)
QC	Quantum Computer
QEC	Quantum Eerror Correction

QEM	Quantum Eerror Mitigation
QFT	Quantum Fourier Transform
QHR	Quantum Householder Reflections (decomposition)
QIP	Quantum Information Processing
Q_M	Quantum Merit
QPE	Quantum Phase Estimation
QPT	Quantum Process Tomography
QST	Quantum State Tomography
RO	Read Out (errors)
RP	Radical Pair
SH	Spin Hamiltonian
SIM	Single Ion Magnets
SIS	Superconductor Insulator Superconductor
SPSA	Simultaneous Perturbation Stochastic Approximation
TR	Thermal Relaxation (errors)
TR-EPR	Time Resolve Electron Paramagnetic Resonance
UCC	Unitary Coupled Cluster
V_Q	Quantum Volume
VQE	Variational Quantum Eigensolver
ZFS	Zero Field Splitting

Abstract

Quantum information processing has emerged as a forefront area of research, holding the promise to address classical intractable problems. There are several areas in which quantum computers are expected to bring a disruptive contribution and one among all is the simulation of quantum systems. In the last decades, several quantum computing architectures have been proposed and experimentally tested: among the most developed are superconducting qubits, trapped ions, and photonic systems. However, despite the significant technological advancement, the path towards the realization of a scalable and fault-tolerant quantum computer remains full of challenges. This scenario underscores the need to explore alternative possibilities and an intriguing one are Molecular Nanomagnets (MNMs).

Discovered in the early 90s, these systems combine classical macroscopic magnet behaviour with quantum properties making them excellent candidates for quantum architectures. Leveraging on the spin degrees of freedom inherent in these systems, they can show at low energy a well resolved energy spectrum addressable by electromagnetic pulses. These systems have naturally long coherence times that reach in some cases up to times on the order of milliseconds allowing a coherent control and manipulation. Furthermore, MNMs can be chemical engineered allowing for a precise tuning of their properties and thus a great flexibility for different applications.

This thesis collects the results of the research conducted by my group and me over the past three years. The thematic common at all works is the use of MNMs for the quantum architectures. Within this broad field, research can be divided into two primary strands: exploring the potential of a qudit-based computation and designing molecules that are intrinsically protected against decoherence. Regarding the former, a qudit approach can simplify quantum circuits by reducing the number of objects to be controlled and thus the number of two-body gates.

This approach has been investigated both for quantum simulation and for quantum error correction applications. Regarding the latter, through the modelling of decoherence and the analysis of the mechanisms that generate it, it has been possible to identify a general property that systems must have in order to be intrinsically protected against decoherence. As in precedence, this property can be useful for both quantum computation and error correction. Besides these main topics, we have also worked on the design of time-resolved EPR experiments aimed at detecting chiral induced spin selectivity (CISS). Although this phenomenon is not fully understood, it is interesting for several applications, including quantum technologies. In particular, it could be exploited for the initialization and readout of MNMs. Finally, we have worked with state-of-art quantum computers, exploring the variational quantum eigensolver algorithm. We have investigated physically motivated ansatz, i.e., ansatz tailored to respect the properties of the target system such as conserved quantities or symmetries, showing that this approach can significantly extend the capabilities of this algorithm. As a study case, we look at small spin models.
The work is structured as follows: the first two chapters (1 and 2) serve as an introduction to standard qubit-based quantum information processing and MNM for quantum computation, respectively. These chapters provide a comprehensive overview of the subject and introduce key concepts that form the basis of subsequent studies. Chapters 3 and 4 present the main results related to quantum error correction applications, while chapters 5 and 6 focus on quantum computation and simulation. Chapter 7 discusses the analysis relative to CISS experiments while chapter 8 presents the studies relatives to variational quantum eigensolver algorithm.

CHAPTER 1

Introduction to Quantum Information Theory

Quantum Information Processing (QIP) emerged in the early 1980s and has since captured the interest of the scientific community, making it one of the hottest topics today [1–4]. This field stems from the intersection of classical information theory and quantum mechanics.

The first application for which quantum computers have been ideated is the simulation of quantum systems. As well as support for scientific investigations, classical computation has long served as a research method. However, as classical architectures continued to exhibit significant growth in capabilities, it was already clear that certain problems, such as the simulation of large quantum systems, would remain unsolvable by classical means [5]. The computational cost, measured in terms of both memory and processing time, grows exponentially as the size of the system increases, making the classical approach impractical [6, 7]. A new class of computer was needed to simulate physics, and quantum computers (QCs) are the answer. QCs introduce a paradigm shift by using intrinsically quantum elements, from which they inherit the peculiar physical properties of quantum mechanics. By basing their computation on the same logic as the systems they want to simulate, QCs are able to simulate them efficiently, with an exponential advantage over their classical counterpart. Many other interesting applications where QCs show an advantage have been discovered. These cover various fields such as cryptography, secure telecommunications, search and optimisation problems. These possibilities open the doors to a new and exciting era of computing.

This chapter aims to provide a comprehensive introduction to quantum information theory, laying the theoretical groundwork for subsequent parts of this work. In the beginning are described the basic yet fundamental concept of the quantum bit (qubit), which is the building block for quantum computers. Then quantum gates, the logical operations used to manipulate qubits, are introduced. By composing these operations a generic quantum algorithm is formed. This

work presents principally quantum simulation: its fundamental steps and possible applications are introduced. Next, the challenges posed by imperfect devices are addressed and the different forms of noise that arise during computation are examined [8]. To handle errors effectively, a formalism based on Kraus operators is developed. Some error mitigation techniques are first presented, and then quantum error correction is introduced. These procedures are the fundamental tools to achieve a fault-tolerant computation. Lastly, a computation based on multi-valued units (qudit) is introduced.

1.1 Quantum Information Processing

A quantum computer is a machine that performs calculations based on the principles of quantum mechanics. Its quantum nature grants it a distinctive logic of operation, resulting in exceptional properties. The fundamental unit for storing and processing quantum information is known as a quantum bit or qubit [9, 10]. The qubit, like its classical counterpart, the bit, is a theoretical construct that allows the representation of a two-dimensional subspace, defined by two orthogonal states, independent of the underlying physical system. This assumption is based on the simple but fundamental consideration that all two-dimensional subspaces are informationally equivalent [11]. These two states, denoted as $|0\rangle$ and $|1\rangle$ in Dirac notation, define the so-called computational basis (or Z-basis). However, unlike the classical units, a qubit can be prepared in a superposition state encompassing a combination of the two basis states. The geometric representation of the state of a qubit is as follows:

$$|\Psi\rangle = \cos\theta\,|0\rangle + e^{i\varphi}\sin\theta\,|1\rangle\,. \tag{1.1}$$

where θ and φ are real parameters. The first angle defines the probability amplitude of being in either of the basis states, while the second one determines the relative phase. If one wants to give a physical interpretation to these parameters, linking them to properties of quantum mechanics, one can say that the angle θ is associated with the concept of quantum superposition, while φ encapsulates the wave-function nature of a quantum state, underlying interference phenomena. The Bloch sphere gives an intuitive visual representation of a qubit (refer to Fig. 1.1). Each point on the sphere's surface corresponds to a possible quantum state, uniquely determined, up to a global phase, by the two aforementioned angles. The states of the computational base are usually placed on the north and south poles of the sphere, i.e. along the z-axis from which derives the denomination as z-basis. It should be noted that any pair of points on opposite sides of the sphere forms a possible basis. The pair of states along the other principal

Cartesian axes are generally referred to as the x-basis and the y-basis. Data access

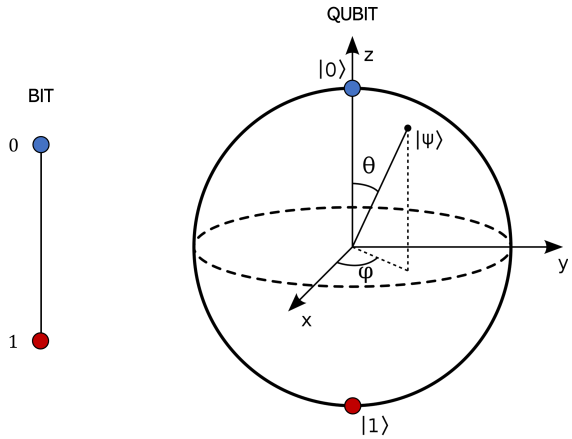

Figure 1.1: Visual representation of a classical (left) and quantum (right) bits .

marks another significant difference between quantum and classical computers. Whereas a classical computation can be stopped, partial results examined, and the process resumed without affecting the final output, any access to a quantum state inevitably perturbs the wave function.
The information that a single qubit can handle compared to a classical bit is considerable. But the real advantage comes as the spatial dimension increases. Now, let's consider the state defined by two distinct qubits. The product basis $|\Psi_1\rangle \otimes |\Psi_2\rangle$ is formed by four orthogonal states $|00\rangle, |01\rangle, |10\rangle, |11\rangle$ and the most general wave-function can be geometrically represented as:

$$|\Psi\rangle = \alpha\,|00\rangle + \beta\,|01\rangle\,\gamma\,|10\rangle + \delta\,|11\rangle \tag{1.2}$$

where α, β, γ, and δ are complex parameters which satisfy the normalization constraint $|\alpha|^2 + |\beta|^2 + |\gamma|^2 + |\delta|^2 = 1$. Generalising it for n qubit systems, the Hilbert space it represents is composed of 2^n states. For a moderately large number of qubits $n \gtrsim 50$, this volume of data becomes intractable for any classical computer [6]. The exponential growth of the information that a register of qubits can hold, together with the ability to operate on all states simultaneously, are the origin of the exponential advantage of quantum devices. Last, but not least, the final aspect which distinguish quantum and classical states is the quantum correlation or entanglement. This phenomenon, theoretically discussed by the Bell inequalities and experimentally demonstrated for the first time in the 1980s, is one of the most intriguing aspects of quantum mechanics [12–15]. In this respect, Jonh Preskill compares a quantum system to a book [6]: "With a 'classical'

book, every time you read a page, you learn a certain amount of total information. After reading all the pages, you know the system perfectly. This is not possible with the 'quantum' book. If you want to read it, you cannot do it page by page, but you have to make collective observations of many pages at once." This form of non classical correlation, together with the delicate nature of the wave function are the foundation of secure quantum communication [16]. This phenomenon cannot be enclosed in a simple definition. However, can be argued that the state of a set of qubits is entangled if the state of a single qubit cannot be represented independently of the state of the others.
The concurrency $\mathcal{C}$ introduced by Wootters in [17] is a metric to quantify the amount of entanglement. $\mathcal{C}$ ranges from 0 to 1, where a value of 0 indicates a state that is not entangled, while a value of 1 represents a maximally entangled state. In the case of two-qubit in a mixed state ρ, $\mathcal{C}$ is defined starting from the Hermitian operator R:

$$R = \sqrt{\sqrt{\rho}\tilde{\rho}\sqrt{\rho}} \tag{1.3}$$

where $\tilde{\rho} = (\sigma_y \otimes \sigma_y)\rho^*(\sigma_y \otimes \sigma_y)$. Calculating R eigenvalues λ_1, λ_2, λ_3, λ_4 (in descending order), the concurrence is given by:

$$\mathcal{C} = \max(0, \lambda_1 - \lambda_2 - \lambda_3 - \lambda_4) \ . \tag{1.4}$$

Under certain conditions, this definition can be extended to any dimensional space.

1.1.1 DiVincenzo's Criteria

In principle, any quantum system that contains two quantum states can be utilized to implement a physical qubit [18]. Examples include the orientation of a spin-half particle, the two orthogonal polarization states of a photon, or a pair of electronic energy levels in an atom, ion, or quantum dot. The theoretical physicist David P. DiVincenzo has identified five (plus two) criteria as guidelines for evaluating and identifying potential physical systems that can be used to build a functional quantum computer [19]. Here, these criteria are briefly summarized:

1) *A scalable physical system with well-characterized qubits.* The physical system should be scalable, meaning it can be expanded to encode multiple qubits. Additionally, the qubits in the system should be well-characterized, meaning their properties and behavior are well-understood.

2) *The ability to initialize the state of the qubits to a simple fiducial state, such as* $|00\ldots0\rangle$. The system should allow the qubits to be prepared in a known and well-defined fiducial state, typically the ground state.

3) *Long relevant decoherence times, much longer than the gate-operation time.* The system should have long decoherence times, meaning the quantum states of the qubits remain stable and coherent for a sufficiently long time compared to the time required to perform gate operations.

4) *A "universal" set of quantum gates.* A universal set of quantum gates refers to a specific set of basic quantum operations that can be combined to implement any quantum computation. The system should be capable of implementing this universal set of gates to perform arbitrary quantum operations.

5) *A qubit-specific measurement capability.* The system should have the ability to measure the states of individual qubits without disturbing the states of other qubits. This measurement capability is essential for extracting information from the qubits during computation.

Over the years, several architectures have been identified and developed [20]. However, despite the remarkable technological improvements [21–23], no technology today fully satisfies all the requirements. The main limitations lie in the implementation of gates and the relatively short decoherence times, which are still insufficient to implement arbitrarily long circuits.
The most advanced IBM hardware available today (early 2024), like the Torino device, according to data provided by the company exhibits single-qubit gate errors on the order of 10^{-4} and two-qubit gate errors on the order of 10^{-3}, while the average decoherence times are around 150 μs.
In addition to the aforementioned five conditions, two more requirements are necessary in quantum communication:

6) *The ability to interconvert stationary and flying qubits.* In quantum communication, it is necessary to convert stationary qubits, which are used for quantum computing operations, into flying qubits, such as photons, that can be transmitted. This conversion allows for the transmission of quantum information over long distances using existing optical communication infrastructure. The ability to efficiently and reliably convert between these two types of qubits is crucial for quantum communication protocols.

7) *The ability to faithfully transmit flying qubits between specified locations.* To enable quantum communication, it is essential to transmit flying qubits between designated locations while preserving the coherence of the quantum information they carry. This requirement ensures that the quantum information remains intact and can be faithfully recovered at the receiving location.

1.2 Quantum Gates

The evolution of a quantum system from one state to another can be represented by a unitary transformation which is a global operation on the system. However, it is not always practical to implement an evolution that affects the whole system, so it is convenient to rewrite it in terms of local operations. Most architectures are often limited in their direct implementation to single and two-qubit gates. Therefore, it becomes necessary to define a universal set of operations that can decompose any desired unitary transformation into a sequence of these basic gates [24]. Typically, a universal gate set consists of two single-qubit gates that enable rotations around non-parallel axes of the Bloch sphere, along with a two-qubit gate that creates entanglement between qubits. This set of gates permits the capability to implement any quantum algorithm. The gate set characterizes a quantum platform because it significantly impacts the performance of the decomposition strategies. A broader set of available gates can greatly enhance the efficiency of decomposing, leading to improved performance and computational capabilities.
In this section, the principal operations used in quantum computing are described. Starting with the most general operations, the gates that are relevant to the logical meaning their transformations represents are then highlighted.

1.2.1 Single-qubit gates

Single-qubit gates in quantum computing are operations that manipulate the state of a single qubit. The most general form of a single-qubit gate is a unitary rotation of the $SU(2)$ group [25]. It can be represented by the matrix:

$$U(\theta,\phi,\lambda) = \begin{pmatrix} \cos\theta/2 & -e^{i\lambda}\sin\theta/2 \\ e^{i\phi}\sin\theta/2 & e^{i(\phi+\lambda)}\cos\theta/2 \end{pmatrix}, \tag{1.5}$$

where θ, ϕ, and λ are independent real parameters. This general rotation allows for the transformation of any point on the Bloch sphere to any other point.
From this general form, specific single-qubit gates around the main axes can be defined, up to a global phase, by choosing appropriate parameters. These gates are:

$$\begin{aligned} U(0,0,\lambda) &\propto R_z(\lambda) = \exp\left(-i\frac{\lambda}{2}\sigma_z\right), \\ U(\theta,-\pi/2,\pi/2) &\propto R_x(\theta) = \exp\left(-i\frac{\theta}{2}\sigma_x\right), \\ U(\theta,0,0) &\propto R_y(\theta) = \exp\left(-i\frac{\theta}{2}\sigma_y\right), \end{aligned} \tag{1.6}$$

where R_x, R_y, and R_z are rotations around the x, y, and z axes, respectively, and σ_x, σ_y, and σ_z are the corresponding Pauli matrices.
Any unitary single-qubit operator W can be decomposed into a sequence of rotations around two non-parallel axes, n and m, as follows:

$$W = e^{i\alpha} R_n(\beta) R_m(\gamma) R_n(\delta) \qquad n, m \in \{x, y, z\}, \tag{1.7}$$

with suitable choices of the parameters α, β, γ, and δ [26]. This decomposition allows us to implement any general rotation on a quantum device by performing rotations around two axes. Therefore, to implement arbitrary single-qubit rotations, it is sufficient to have the capability to perform rotations around two non-parallel axes.
Within the realm of single-qubit gates, certain rotations stand out due to the intuitive logic they represent. Two such gates are the Hadamard gate (H) and the NOT gate (X).

$$\begin{aligned} H = U(\pi/2, 0, \pi) &= \frac{1}{\sqrt{2}} \begin{pmatrix} 1 & 1 \\ 1 & -1 \end{pmatrix} \\ X = U(\pi, 0, \pi) &= \begin{pmatrix} 0 & 1 \\ 1 & 0 \end{pmatrix} \end{aligned} \tag{1.8}$$

These gates, shown in Eq. 1.8, possess distinct functionalities and play significant roles in quantum computations. The Hadamard gate operates by exchanging the superposition state $\frac{|0\rangle+|1\rangle}{\sqrt{2}}$ (or $\frac{|0\rangle-|1\rangle}{\sqrt{2}}$) with the non-superposition state $|0\rangle$ (or $|1\rangle$). It essentially enables a qubit to transition between a balanced combination of both states and a definite state. In other words, this gate allows for switching from the computational basis to the X-basis and vice versa. In fact, two subsequent applications correspond to the identity $HH = I$. Furthermore, this operation can also be seen as a quantum Fourier transform on a two-dimensional system.
The NOT gate, often referred to as the Pauli-X gate, swaps the two orthogonal states of the computational basis: $|0\rangle$ and $|1\rangle$. It performs a logical negation, flipping the qubit from one state to its orthogonal counterpart. It is important to remark that, despite its name, the NOT gate does not transform any general state $|\psi\rangle$ into its exact orthogonal state $|\psi\rangle_\perp$.

1.2.2 Two-qubit gates

Two-qubits gates are operations that manipulate the states of two qubits simultaneously. The canonical gate $\mathrm{Can}(t_x, t_y, t_z) = \exp\left(-i(t_x\sigma_x \otimes \sigma_x + t_y\sigma_y \otimes \sigma_y + t_z\sigma_z \otimes \sigma_z)\right)$ defines the most general two-qubit gate form which any other can be derived. Its

matrix representation reads as:

$$\mathrm{Can}(t_x,t_y,t_z)=\begin{pmatrix} e^{-it_z}\cos(t_x-t_y) & 0 & 0 & -ie^{-it_z}\sin(t_x-t_y) \\ 0 & \cos(t_x+t_y) & i\sin(t_x+t_y) & 0 \\ 0 & i\sin(t_x+t_y) & \cos(t_x+t_y) & 0 \\ ie^{it_z}\cos(t_x-t_y) & 0 & 0 & e^{it_z}\cos(t_x-t_y) \end{pmatrix} \tag{1.9}$$

This operation, combined by single-qubit gates acting before and after, generates all other two-qubit gates [27]. Furthermore this operation has a strong physical meaning because it represents an exchange interaction [25].
Among all the possible operations, the class of controlled rotations can be identified. The logic of these gates and their matrix representations are similar. Controlled operations typically exhibit a hierarchy among qubits, where the state of one, known as the target, is altered based on the state of another, known as the control. Importantly, the state of the control qubit remains unchanged throughout this process.
In the most general form, the controlled operation is a $U2$ rotation and its matrix representation reads as:

$$CU=\begin{pmatrix} 1 & 0 & 0 & 0 \\ 0 & 1 & 0 & 0 \\ 0 & 0 & e^{i\gamma}\cos\left(\frac{\theta}{2}\right) & -e^{i(\gamma+\lambda)}\sin\left(\frac{\theta}{2}\right) \\ 0 & 0 & e^{i(\gamma+\phi)}\sin\left(\frac{\theta}{2}\right) & e^{i(\gamma+\phi+\lambda)}\cos\left(\frac{\theta}{2}\right) \end{pmatrix}. \tag{1.10}$$

It can be shown that all this class is locally equivalent to $\mathrm{Can}(t_x,t_y=0,t_z=0)$ and therefore it can be rewritten in terms of it and a few single body operations [27].
The most famous controlled gate is probability the control-NOT or CNOT gate. The control qubit determines whether or not to apply an X gate to the target qubit. The CNOT gate is particularly valuable as it generates entanglement and is frequently employed as part of universal gate sets. The matrix representation of the CNOT gate is as follows:

$$\mathrm{CNOT}=\begin{pmatrix} 1 & 0 & 0 & 0 \\ 0 & 1 & 0 & 0 \\ 0 & 0 & 0 & 1 \\ 0 & 0 & 1 & 0 \end{pmatrix} \tag{1.11}$$

Another commonly used two-body gate is the controlled-phase gate (C_φ), which is represented by the following matrix:

$$C_\varphi = \begin{pmatrix} 1 & 0 & 0 & 0 \\ 0 & 1 & 0 & 0 \\ 0 & 0 & 1 & 0 \\ 0 & 0 & 0 & e^{-i\varphi} \end{pmatrix} \tag{1.12}$$

where φ is a real parameter. The controlled-phase gate applies a phase factor of $e^{-i\varphi}$ only to the state $|11\rangle$ while leaving the other basis states unchanged. Also this operation creates entanglement between the qubits, making it useful in gate sets.
In the specific case $\varphi = \pi$, it is common to refer to this gate as the C_z gate. It is worth noting that the CNOT gate and the C_z shift gate are closely related to each other. They can be transformed into one another using two Hadamard gates. This similarity allows for the interchangeability of the CNOT and the C_z in quantum computations, depending on convenience and the specific requirements of the algorithm or circuit being implemented.
Another widely used two-qubit gate is the SWAP gate 1.13, which exchange the states of the two qubits. For instance, it transforms $|01\rangle$ into $|10\rangle$ mean while states $|00\rangle$ and $|11\rangle$ are not touch. The SWAP gate does not generate entanglement and thus cannot be used as part of a universal set. Often this operation cannot be implemented directly, but it can be achieved by using three successive CNOT gates, where the middle one exchanges the target and control qubits with respect to the other two gates. The matrix representation of the SWAP gate is given by:

$$SWAP = \begin{pmatrix} 1 & 0 & 0 & 0 \\ 0 & 0 & 1 & 0 \\ 0 & 1 & 0 & 0 \\ 0 & 0 & 0 & 1 \end{pmatrix} \tag{1.13}$$

Since most quantum architectures do not allow direct operations between all pairs of qubits, this gate is often needed during computation to connect logical qubits that are not physically connected.

to move the information stored into qubits among hardware physical units. Indeed, most of quantum architectures do not allow direct operations between all pairs of qubits and therefore requiring to .

The XY gate is defined as follows:

$$XY(\theta) = \text{Can}(\theta/2, \theta/2, 0) = \begin{pmatrix} 1 & 0 & 0 & 0 \\ 0 & \cos(\theta) & -i\sin(\theta) & 0 \\ 0 & -i\sin(\theta) & \cos(\theta) & 0 \\ 0 & 0 & 0 & 1 \end{pmatrix} \tag{1.14}$$

This operation is a particular case of the canonical gate ($t_z = 0$, $t_x = t_y = \theta/2$) and it represents the evolution $e^{-i\frac{\theta}{2}(\sigma_x \otimes \sigma_x + \sigma_y \otimes \sigma_y)}$ note as XX+YY interaction. Its action is to partially exchange the states $|01\rangle$ and $|10\rangle$ while simultaneously adding a phase of $-i$. For $\theta = \frac{\pi}{2}$, it is commonly referred to as the iSWAP gate. The XY gate can be rewritten in terms of two generalized CPhase gates and a few single qudit gates [28]. Apart form an overall phase, the $ZZ = e^{-i(\sigma_z \otimes \sigma_z)\tau}$ evolution operator is decomposed in terms of C_φ as follows:

$ZZ(\theta) \; =$ 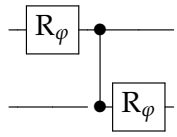

(1.15)

where the central gate control phase gate has angle $\varphi = \tau$ and $\mathrm{R}_\varphi = e^{i\varphi/2} R_z(\varphi)$. Form this, any other spin-spin evolution operator can be obtained as:

$$e^{-i(s_\alpha \otimes s_\beta)\tau} = [u_\alpha \otimes u_\beta] ZZ [u_\alpha \otimes u_\beta]^\dagger \tag{1.16}$$

where $\alpha, \beta = \{x, y, z\}$, $u_x = R_y(\pi/2)$, $u_y = R_x(3\pi/2)$, and $u_z = I$.

1.3 Quantum Circuits and Algorithms

In classical information theory, any computational process can be represented as a circuit of logic gates operating on bits. Similarly, in quantum information theory, algorithms are described as a sequence of unitary operations that define a quantum circuit. Quantum circuits are composed of a register of qubits, that defines the computational space, a sequence of operations, that defines the quantum algorithm and a classical communication channel or classical register, which is used to read the measurement operations.

A quantum circuit generally begins with the initialization of the quantum register in a fiduciary state, commonly denoted as $|000\ldots0\rangle$. Then, the sequence of gates is implemented. In the end, a measurement procedure is employed to extract a classical information about the state of the qubits. This information is transmitted by means of the classical register.

The dimensions of a circuit, in terms of the number of qubits and the number

of sequentially executed gates, are commonly referred to as the "width" and "depth" of the circuit, respectively. When discussing the size of circuits, the terms "wide" and "depth" are used to describe circuits with a large number of qubits or gates, indicating that they require significant computational resources. Conversely, the terms "narrow" and "shallow" are used to describe circuits with a small number of qubits or gates, indicating their relatively smaller size or computational requirements. Quantum circuits are graphical representation as a musical score where qubits are the horizontal lines and gates take the place of notes. An example of such a circuit, generated using the Qiskit library [29], is shown in Fig. 1.2: The circuit is composed by three qubits represented by the first three

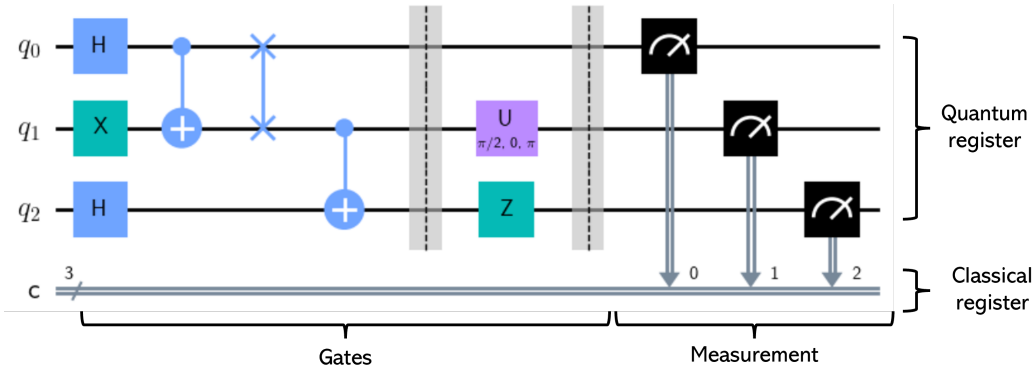

Figure 1.2: Example of a circuit generated using the Qiskit library by IBM [29].

parallel horizontal lines, along with a classical communication channel depicted by the last double-parallel line. To correctly interpret the diagram, we read the sequence of operations from left to right. Initially, the qubits are initialized in the $|0\rangle$ state. Each operation is represented by a symbol, such as H for the Hadamard gate and X for the NOT gate. Multi-qubit gates are indicated by a vertical line connecting the qubits upon which they act. In the case of the CNOT gate, the control qubit is denoted by a dot, while the target qubit is represented by a cross. At the end of the circuit, measurements are applied to the qubits, and the measurement outcomes are transmitted through the classical channel.

1.3.1 Quantum Fourier Transform

The Quantum Fourier Transform (QFT) is the quantum analogue of the discrete Fourier transform [30]. It enables the mapping of the amplitudes of a quantum state into the frequency basis or Fourier basis. The QFT exhibits an exponential advantage compared to its classical counterpart. For a space of dimension $N = 2^n$ where n is the number of qubits, it requires only $O\left(n^2\right)$ gates, as opposed to the

classical case which requires $O(n2^n)$ gates. The QFT is a fundamental component of many quantum algorithms, most notably Shor's factorization algorithm and quantum phase estimation [31, 32]. Unfortunately, QFT does not speed up the computation of classical data and hence is only useful in classical applications as sound analysis.
Defining an orthonormal basis $|0\rangle, \ldots, |N-1\rangle$ of dimension N, the action of the QFT transformation is given by:

$$|j\rangle \rightarrow \frac{1}{\sqrt{N}} \sum_{k=0}^{N-1} e^{i2\pi jk/N} |k\rangle \quad . \tag{1.17}$$

Since the QFT is a linear transformation, the action on a general state $\sum_{j=0}^{N-1} x_j |j\rangle$ is defined as the sum of the linear transformations on the basis states $|j\rangle$. Alternatively, the QFT can be represented as a unitary matrix:

$$F_N = \frac{1}{\sqrt{N}} \begin{pmatrix} 1 & 1 & 1 & \ldots & 1 \\ 1 & w & w^2 & \ldots & w^{N-1} \\ 1 & w^2 & w^4 & \ldots & w^{2(N-1)} \\ \vdots & \vdots & \vdots & & \vdots \\ 1 & w^{N-1} & w^{2(N-1)} & \ldots & w^{(N-1)(N-1)} \end{pmatrix}$$

where $w = e^{\frac{i2\pi}{N}}$. In the case of a single qubit ($n = 1$) it corresponds to the Hadamard gate, $F_2 = H$.
Figure 1.3 shows the circuit representation of the QFT. The circuit has a modular structure and involves only Hadamard and controlled-rotations around the z-axis. On the right side of the circuit is depicted the final state of each qubit. The

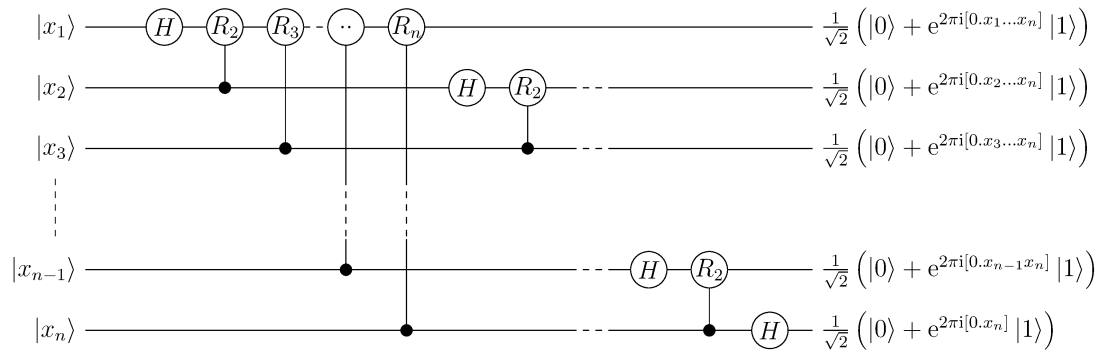

Figure 1.3: Quantum Fourier Transform circuit: H indicates the standard Hadamard gates while R_i are z rotations of angle w^i. This picture has been reproduced from [33] under the license CC BY-SA 4.0.

whole system wave-function is given by the tensor product of all terms and is compactly written as the $QFT(|x\rangle) = \frac{1}{\sqrt{N}} \bigotimes_{j=1}^{N} \left(|0\rangle + w_N^{x2^{n-j}} |1\rangle \right)$.

1.3.2 Digital versus Analog Quantum Simulators

One of the first applications where quantum computers are expected to have a disruptive impact is the simulation of entangled quantum systems [6]. Imagine having a quantum system described by the Hamiltonian $\mathcal{H}$ which, at the initial time $t = 0$, is in the state $|\Psi(0)\rangle$. The state at a generic time τ is defined as:

$$|\Psi(t)\rangle = e^{-i\mathcal{H}\tau} |\Psi(0)\rangle \tag{1.18}$$

where we consider $\hbar = 1$. Explicitly calculating the evolution operator $U = e^{-i\mathcal{H}\tau}$ and solving the linear system are not trivial tasks for classical computers. Indeed, the exponential growth of the operator size with the dimension of the underlying quantum mechanical system leads to an exponential growth of the required resources both in terms of time and memory. Consequently, classical computers can only handle relatively small sized problems. The strong interest of the scientific community in this field is outlined by the wide range of approximation techniques that have been developed over the years. However, these methods, which come at the cost of limited precision or validity of the results, have only the power to mitigate the underlying problem.
Thanks to their intrinsic properties, quantum computers are the natural platform for solving such tasks [25]. The resources needed for quantum simulation grow only polynomially with system size. While non-trivial applications like Grover or Shor algorithms require at least thousands of qubits, even a small architecture of a few tens of qubits could simulate problems that are already intractable on classical computers [34].
When looking at quantum simulations, it is important to distinguish between two categories of devices and approaches [35]:

- **Analog Simulators**: the simulation is carried out on a device that mimics the evolution of the target system. The relationship between the target and simulator systems is established at the hardware level, requiring dedicated devices to address specific problems. The simulator is generally controlled only through global addressing. This approach holds great promise for near-future applications, as even in the presence of noise, qualitative features of interesting models can be achieved. However, analog simulators would not work as a basis for general computation because they do not satisfy DiVincenzo's criteria. These machines can be built using advanced architectures such as trapped ions and superconducting circuits [36].

- **Digital Simulators**: the target system is described in the mathematical formalism of quantum mechanics, and it is represented on the hardware through a mapping of the system algebra into the hardware algebra. Local manipulation methods are employed to control the evolution. Their action is formally described by unitary transformations, which, as we have seen, are called gates in the terminology of quantum computing. Digital simulators can address general problems, making them universal devices. In long-term applications these architectures could benefit from Quantum Error Correction.

In this work, digital simulators are considered. A quantum simulation can be split up into three main steps: modelling, mapping, and gate decomposition. In the first step, the modelling, the investigated physical system has to be defined in terms of a mathematical formulation. We are free to choose the set of variables and operators which appear more appropriate. The important thing is that these capture all the dynamical information of the system.
Now we can proceed to the second step, which consists in mapping the of mathematical description of the model into the hardware algebra, i.e. the qubit algebra. For example, with respect to the problem of simulating fermionic systems, the most famous mapping is the Jordan-Wigner, which is presented in detail in Chapter 6.Assuming we have successfully addressed this mapping challenge, we can then move on to the final step.
In this last step, our goal is to decompose the time evolution operator into gates and construct the corresponding quantum circuit. However, we need to keep in mind Lloyd's Theorem [37]. Conceptually, this theorem states that a quantum computer can efficiently simulate a quantum system if the interactions between its subsystems can be described locally. Luckily, this restriction is not limiting in many practical cases, as most of the models we use to describe nature are based on this assumption. Hence, we assume that the Hamiltonian $\mathcal{H}$ we considered before, can be rewritten as a sum of local terms:

$$\mathcal{H} = \sum_l \mathcal{H}_l \quad . \tag{1.19}$$

In the case that all pairs of terms commute $[\mathcal{H}_l, \mathcal{H}_{l'}] = 0$ for $\forall\ l, l'$

$$e^{-i\mathcal{H}\tau} = \prod_l e^{-i\mathcal{H}_l\tau} \quad . \tag{1.20}$$

However, in general not all pairs of terms commute and the previous equation does not hold. The Lie-Trotter formula comes to our aid [10]. This allows the

disjunction of the evolution operators of the different parts of the Hamiltonian

$$e^{-i\mathcal{H}\tau} = \left(\prod_l e^{-i\mathcal{H}_l\tau/n}\right)^n + O\left(\frac{\tau^2}{n}\right) \quad . \tag{1.21}$$

The global evolution of the systems at time τ can be approximated by a sequence of n shorter evolutions of time τ/n commonly called Trotter steps. By increasing the number of Trotter steps, it is possible to reduce the digital error, i.e. the approximation error introduced by the formula, to any desired level of precision. However, achieving a higher level of accuracy also results in deeper and more complex circuits. Alternative strategies, such as higher-degree formulas like the "Suzuki-Trotter" [38] and "Post-Suzuki" methods [39, 40], have been proposed to address these challenges.

It is important to note that the error provided by formula 1.21 is an upper bound for the committed error. However, this bound often tends to overestimate the real error. Having an accurate estimation is crucial for efficient resource utilization. In reference [41], it has been demonstrated that the bound can be limited to $O\left(\frac{\tau^2}{n}\sum_{\gamma_1,\gamma_2}||[H_{\gamma_1},H_{\gamma_2}]||\right)$ where $||A||$ is the spectral norm of the operator A.

Now, let's focus on gate decomposition. By utilizing a universal gate set, we can decompose any operator into a series of elementary gates (as discussed in Chapter X for some standard cases). Each operator is then expressed as a sequence of single and two-qubit gates. These chains of operations form the main core of the quantum circuit. To complete the circuit, we need to incorporate the initial state preparation at the beginning and a set of measurements at the end. The state initialization allows us to reconstruct the state $|\Psi(0)\rangle$ starting from the confident state $|00\ldots0\rangle$. The measurement procedure, formally $\langle\Psi(t)|A|\Psi(t)\rangle$ terminates the circuit providing access to observable quantity A on the final state. Not always these are trivial tasks. In particular, highly correlated quantum states or observable are not always easy to prepare or measure.

The one presented is a general and schematic picture of a quantum simulation procedure. Specific methods and techniques are often required for practical implementation of particular cases. Furthermore, we want to remark that this approach could be applied to any problem which can be mathematically formulated in a Hamiltonian-like form.

1.3.3 State and Process Tomography

Quantum State Tomography (QST) is a procedure that permits to fully characterize the state of a register of qubits. It is used to reconstruct the density matrix after the execution of an algorithm. The procedure requires to repeatedly reconstruct and measure the state of the qubits on a Hilbert-space basis of the register.

Therefore, for the procedure to be effective, it is essential that the state can be consistently recreated multiple times. This procedure is described below, starting from the particular case of a single qubit, and then generalised for n qubits.
In the case of a single qubit, a viable basis is given by the four matrices $I/\sqrt{2}, X/\sqrt{2}, Y/\sqrt{2}$, and $Z/\sqrt{2}$. The density matrix ρ can be rewritten as :

$$\rho = \frac{tr(I\rho)I + tr(X\rho)X + tr(Y\rho)Y + tr(Z\rho)Z}{2} \tag{1.22}$$

where the trace procedure $tr(A\rho)$ corresponds to measuring the expectation value of the observable A on the state ρ, $tr(A\rho) \equiv \langle A|\rho|A\rangle$.
Similarly, in the case of an n-qubit state, it can be defined as follows

$$\rho = \sum_{\vec{v}} \frac{tr(\sigma_{v_1} \otimes \sigma_{v_2} \otimes \cdots \otimes \sigma_{v_n}\rho)\sigma_{v_1} \otimes \sigma_{v_2} \otimes \cdots \otimes \sigma_{v_n}}{2^n} \tag{1.23}$$

where the sum is over $\vec{v}$ which v_i entries are chosen from the above defined set. This procedure necessitates d^2 statistical measure where d is the size of the Hilbert space. Since the computational space d grows exponentially with the number of qubits $d = 2^n$, state tomography is a valuable tool for characterizing small quantum systems while its applicability to large ones is not practically feasible. In fact, rather than fully characterising the final state, in quantum computation it is more common to measure specific observables of interest.
From QST, it is possible to define another technique, known as Quantum Process Tomography (QPT), which enables the characterization of the evolution of small quantum systems and expressing it as a linear map. This procedure is useful, for example, to characterise experimental implementations of gates operating in the presence of systematic noise or other implementation imperfections [10, 42]. QPT basically consists of performing the QST on a basis of system states. This basis can be composed of d^2 pure states $\{|\Psi_1^0\rangle, |\Psi_2^0\rangle, ..., |\Psi_{d^2}^0\rangle\}$, where d is the Hilbert space dimension, such that $\{|\Psi_1^0\rangle\langle\Psi_1^0|, |\Psi_2^0\rangle\langle\Psi_2^0|, ..., |\Psi_{d^2}^0\rangle\langle\Psi_{d^2}^0|\}$ forms a basis set for the matrix space. Starting from each eigenstate and letting the system evolve under the action of the target process, state tomography is performed on each evolved state. Knowing the action of the process on all eigenstates, the action on a general state $|\Psi\rangle$ is determined by linear extension.
Using the super-operator formalism, very convenient in this context, the linear map $\mathcal{L}$ that represent the process evolution is obtained by solving the linear system:

$$\widetilde{|\Psi_i^\tau\rangle} = \mathcal{L}\widetilde{|\Psi_i^0\rangle} \tag{1.24}$$

where $\widetilde{|\Psi_i^\tau\rangle}$ and $\widetilde{|\Psi_i^0\rangle}$ are super-operators formed by horizontally stacking the vectorized density matrices. $\mathcal{L}$ is in a $d^2 \times d^2$ matrix. Figure 1.4 shows the his-

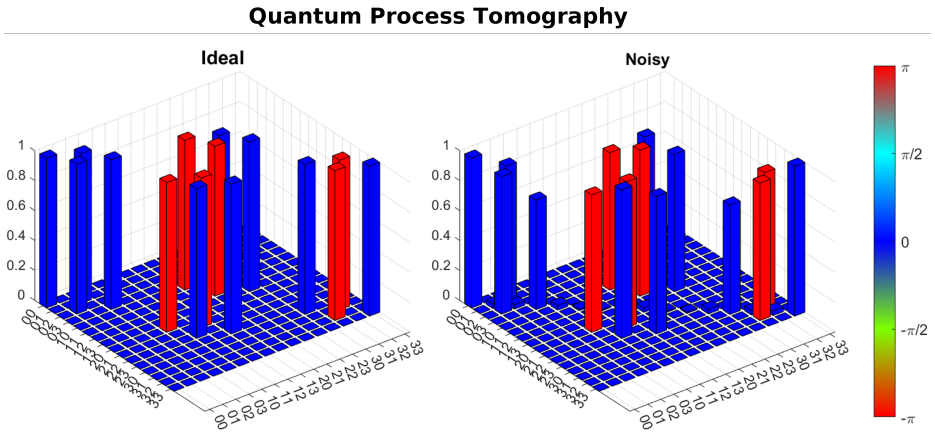

Figure 1.4: Bar plot of the liner map of a simple single qudit $d = 4$ operation where $1 - 2$ levels are swapped. On the left side an ideal implementation is considered, while on the right side the incoherent dynamics generated by pure dephasing $T_2 = 50$ ns is taken into account.

togram representation of the linear map of a single qudit gate $d = 4$ where states 1-2 are exchanged for an ideal (left) and noisy (right) implementation. The labels represent the different entries of a density matrix where 00, 11, 22 and 33 are the diagonal elements while all others represent the coherence. The colour of the bars indicates the phases. Reading the linear map, it is possible to interpret the effect of the gate; for example, it is easy to see that 11 goes into 22 and vice versa. The noisy case takes into account the effect of pure dephasing with $T_2 = 50$ ns for an implementation time of about 6 ns. Compared to the ideal case, as expected, there is a clear suppression of the coherences, as can be seen for instance from the (03,03) entry.

1.4 Noise Modeling

As noted in 1.1.1, no current architecture fully satisfies all the DiVincenzo criteria, and one of the major limitations is noise. In this section, the different types of noise are analysed, identifying their sources and effects. This analysis allows for a better understanding of the problem and therefore a better understanding of how to deal with it. These studies are in fact the base for the construction of QEC theory.
The analysis starts by dividing the different sources of errors into two main categories, based on their origin:

- **Coherent errors**: These errors arise due to a partial or incorrect knowledge

of the system dynamics. They can be viewed as inaccuracies in the implementation of quantum gates. Coherent errors are often systematic in nature. Through careful characterization, these errors can be corrected or mitigated to some extent.

- **Incoherent errors**: This category encompasses errors that result from the interaction between the quantum system and its surrounding environment. These errors are typically stochastic and arise due to various factors such as thermal fluctuations, electromagnetic interference, and other forms of noise. Incoherent errors can lead to the loss of quantum coherence and the degradation of quantum information.

The typical example of a coherent error is the incorrect implementation of a single qubit rotation. If the system dynamics is not perfectly known, a rotation of an incorrect angle or, otherwise not along the correct axis could erroneously be implemented. These errors tend to be systematic and therefore they can be mitigated by better characterising the system. In contrast, incoherent errors, which arise from the interactions of the qubits with the environment, are stochastic in nature and consequently more complex to correct. Both coherent and incoherent errors pose significant challenges in quantum information processing. Many efforts are made to develop mitigation and correction strategies to minimize the impact of error and improve the reliability of quantum computers.
In the following paragraphs, a formalism to describe the effect of errors is established and then the different error channels are introduced.

1.4.1 Operator-sum representation

Operator-sum representation, or Kraus representation after its discoverer, is a powerful formalism to describe the effect of errors on quantum systems. This formalism is able to capture the effects on the target system resulting from the interaction with a secondary system, generally the environment, in terms of operators that act only on the subspace of the principal system. In other words, these operators capture the effects of the interactions without having to work on the product space of the two systems. This is generally very useful for simulating the dynamics between qubits and the environment.
Let's define the initial state of the principal quantum systems ρ and the initial state of the environment $\rho_{env} = |e_o\rangle\langle e_o|$ where, without loss of generality, it is assumed to be a pure state. Supposing that after a certain time the system and the environment are no more in interaction, the evolved state of the system ρ' is

obtained as:

$$\rho' = Tr_{env}\left[U(\rho \otimes \rho_{env})U^\dagger\right] , \tag{1.25}$$

where U is a unitary operator which describes the interaction. This equation can be rewritten expliciting the trace operation as $\sum_k \langle e_k|e_k\rangle$:

$$\begin{aligned} \rho' &= \sum_k \langle e_k| \left[U(\rho \otimes |e_0\rangle\langle e_0|)U^\dagger\right] |e_k\rangle \\ &= \sum_k \mathcal{E}_k \rho \mathcal{E}_k^\dagger \\ &= \mathcal{E}(\rho) , \end{aligned} \tag{1.26}$$

where $|e_k\rangle$ is a basis for the states of ρ_{env} and $\mathcal{E}_k = \langle e_k|U|e_0\rangle$ are the so called Kraus operators that act on the subspace of the principal systems. In general, the inequality $\sum_k \mathcal{E}_k^\dagger \mathcal{E}_k \leq I$ holds and means that the trace is not preserved. If the relation $\sum_k \mathcal{E}_k^\dagger \mathcal{E}_k = I$ is satisfied, the operators are said to be trace-preservers.
In the following sections, this formalism is used to define the effect of noise on quantum states. In this context, Kraus operators are also called noise or error operators.

1.4.2 Noise Channels

In this section, the principal noise channels that describe errors affecting qubits are presented [10]. Having a model that captures, albeit under certain approximations, the main features of these phenomena is essential for understanding them.

Classical Bit Flip

Before introducing the different channels for quantum noise, it is helpful to build some intuition by considering the classical case. In a classical device what can happen is that a bit initially in state 0 (or 1) can flip with a certain probability $1 - p$ to state 1 (or 0), respectively. This concept can be graphically represented as depicted in Figure 1.5.
Formalizing the above expression in mathematical language, a transition matrix can be defined as follows:

$$\begin{bmatrix} q_0^{fin} \\ q_1^{fin} \end{bmatrix} = \begin{bmatrix} p & 1-p \\ 1-p & p \end{bmatrix} \begin{bmatrix} q_0^{in} \\ q_1^{in} \end{bmatrix}$$

Here, $q^{in/fin}$ are the probabilities before and after the error occurs. Now, extending this concept to qubits is straightforward.

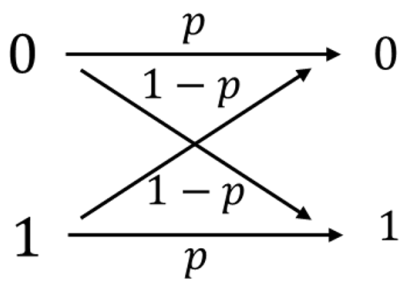

Figure 1.5: Visualization of the effect of different error channels with $p = 0.7$ on the Bloch sphere.

Bit Flip

The first quantum channel to be considered is the analog of the bit-flip error in the classical case. The action of this channel is to flip a qubit initially in state $|0\rangle$ (or $|1\rangle$) to state $|1\rangle$ (or $|0\rangle$) with a certain probability of $1 - p$. This error is represented by the following operators:

$$\mathcal{E}_0 = \sqrt{p}I = \sqrt{p}\begin{pmatrix} 1 & 0 \\ 0 & 1 \end{pmatrix} \tag{1.27}$$

$$\mathcal{E}_1 = \sqrt{1-p}\sigma_x = \sqrt{1-p}\begin{pmatrix} 0 & 1 \\ 1 & 0 \end{pmatrix} \tag{1.28}$$

Thus, the effect on a generic state ρ can be mathematically formalized as follows:

$$\rho' = p\ \mathcal{E}_0\rho\mathcal{E}_0^\dagger + (1-p)\ \mathcal{E}_1\rho\mathcal{E}_1^\dagger \tag{1.29}$$

The effect of the bit-flip error on a qubit's state can be visualized as a contraction of the $\hat{y} - \hat{z}$ plane on the Bloch sphere, as depicted in Figure 1.6.

Phase Flip

The second channel presented is the phase-flip channel. This error lacks a classical counterpart. Its action is to add a phase of -1 to state $|1\rangle$ with a certain probability $1 - p$. The error operators are defined as follows:

$$\mathcal{E}_0 = \sqrt{p}I = \sqrt{p}\begin{pmatrix} 1 & 0 \\ 0 & 1 \end{pmatrix} \tag{1.30}$$

$$\mathcal{E}_1 = \sqrt{1-p}\sigma_z = \sqrt{1-p}\begin{pmatrix} 1 & 0 \\ 0 & -1 \end{pmatrix} \tag{1.31}$$

The action of the phase-flip error on a qubit can be visualized as a contraction of the $\hat{x} - \hat{y}$ plane on the Bloch sphere, as illustrated in Figure 1.6. As shown in section 1.2.1, by means of two rotations along two non-parallel axes, any generic rotation can be reconstructed. Similarly, all the error channels presented later can be obtained by a combination of these first two errors. In order to define QEC schemes capable of achieving fault tolerance, it will therefore be necessary to design codes capable of correcting both forms of error simultaneously.

Bit-Phase Flip

Combining the above two channels, a third one named the bit-phase flip is defined. This error is described by the following operators:

$$\mathcal{E}_0 = \sqrt{p}I = \sqrt{p}\begin{pmatrix} 1 & 0 \\ 0 & 1 \end{pmatrix} \tag{1.32}$$

$$\mathcal{E}_1 = \sqrt{1-p}\sigma_y = \sqrt{1-p}\begin{pmatrix} 0 & -i \\ i & 0 \end{pmatrix} \tag{1.33}$$

The effect on the Bloch sphere is a contraction of the $\hat{z} - \hat{x}$ plane, as depicted in Figure 1.6.

Depolarizing

The depolarizing channel is defined as a uniform action of the three errors: bit flip, phase flip, and bit-phase flip. Its effect is expressed by the following equation:

$$\mathcal{E}(\rho) = p\,\rho + \frac{1-p}{3}(\sigma_x\rho\sigma_x + \sigma_y\rho\sigma_y + \sigma_z\rho\sigma_z) \ . \tag{1.34}$$

The depolarizing channel's geometric interpretation is a uniform contraction of the Bloch sphere in all directions (see Figure 1.6).

Amplitude Damping

Another notable noise channel is the amplitude damping channel that describes energy dissipation and therefore is linked to the T_1 relaxation time. This error is described by the following operators:

$$\mathcal{E}_0 = \begin{pmatrix} 1 & 0 \\ 0 & \sqrt{1-p} \end{pmatrix} \tag{1.35}$$

$$\mathcal{E}_1 = \begin{pmatrix} 0 & \sqrt{p} \\ 0 & 0 \end{pmatrix} \quad . \tag{1.36}$$

The probability p is typically associated with T_1 using a relation like $p = e^{-t/T_1}$ where t is time. In the Bloch sphere's graphical representation, this channel's effect is observed as a contraction of the sphere along with a shift of its centre towards the $|0\rangle$ pole.

Phase Damping

Related to the relaxation time T_2 is the phase-damping channel. The error operators are:

$$\mathcal{E}_0 = \begin{pmatrix} 1 & 0 \\ 0 & \sqrt{1-p} \end{pmatrix} \tag{1.37}$$

$$\mathcal{E}_1 = \begin{pmatrix} 0 & 0 \\ 0 & \sqrt{p} \end{pmatrix} \quad . \tag{1.38}$$

where $\sqrt{1-p} = e^{-t/(2T_2)}$. By manipulating the operators, phase damping can be expressed in terms of phase flip operators with a normalization factor. Thus, the action on the Bloch sphere remains the same.

Measurement

Measurement errors represent the last channel considered. In ideal measurements, the measurement operation is determined by the projection operators $\hat{P}_0 = |0\rangle\langle 0|$ and $\hat{P}_1 = |1\rangle\langle 1|$, projecting the system into one of its eigenstates. However, real measurements introduce errors. The effective physical source underlying the process can differ depending on the hardware. For example, in superconducting qubits the main sources are thermal excitation and T_1 decay, whereas in ion traps the uncertainty arises from the technical challenge of detecting the dark states of the ions and collisions[43]. The action of a real measurement process can be described by generalized projection operators $\bar{P}_0$ and $\bar{P}_1$:

$$\bar{P}_0 = (1 - P_{p0m1}) |0\rangle \langle 0| + P_{p0m1} |1\rangle \langle 1| \tag{1.39}$$

$$\bar{P}_1 = (1 - P_{p1m0}) |1\rangle \langle 1| + P_{p1m0} |0\rangle \langle 0| \quad . \tag{1.40}$$

Here, these operators consider the probabilities of preparing the system in state $|0\rangle$ or $|1\rangle$ and measuring $|0\rangle$ or $|1\rangle$, respectively. Estimating readout errors is typically accomplished experimentally by initializing qubits in either the $|0\rangle$ or $|1\rangle$ state and measuring them immediately afterward. Any deviations from the ideal behaviour are attributed to readout errors.
Understanding and characterizing these noise channels are crucial for assessing and mitigating errors in quantum systems. This understanding forms an essential part of the study of quantum error correction and fault-tolerant quantum computing.

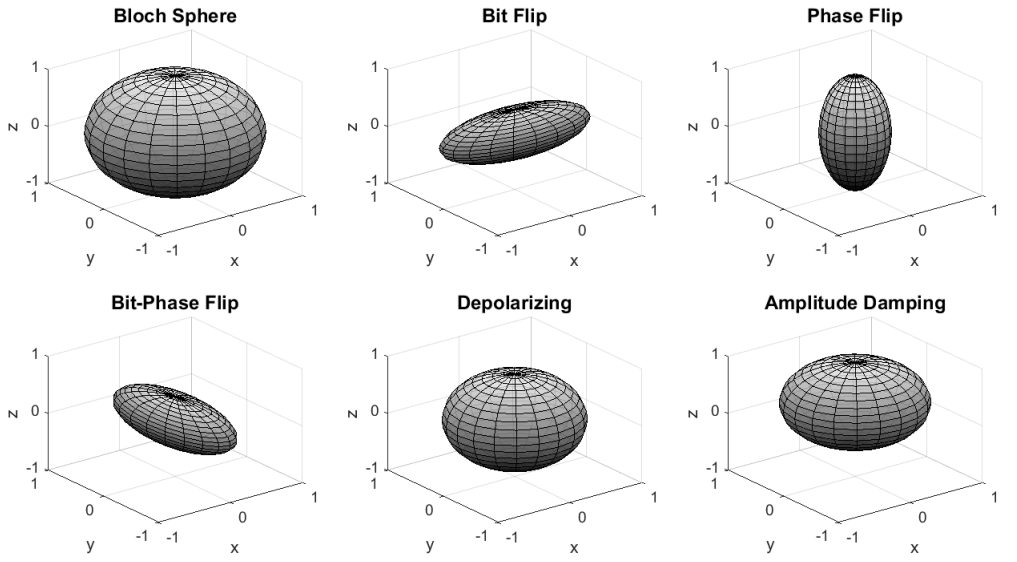

Figure 1.6: Visualization of the effect of different error channels on the Bloch sphere with $p = 0.7$.

1.5 Performance Metrics and Distance Measure

Although technological advancement is leading to significant improvements in hardware capabilities, near-term and next-near future devices will have to coexist with noise. Furthermore, in this early stage, these architectures will not benefit from quantum error correction (QEC) techniques. The performance of an

architecture in the presence of noise requires proper consideration. The metrics used for classical computers are not suitable for this purpose. In order to evaluate and compare the performance of different devices, it is therefore necessary to establish metrics specific to quantum devices. In this section, two metrics are presented: one to assess the "quality" of a single qubit in the implementation of operations and one to assess the performance of architectures.
The last part of this section also introduces two proximity measures, the trace distance and fidelity, which are used to estimate the proximity of two quantum states. These measures are commonly used to evaluate the precision of the implementation of a single operation or a whole circuit.

1.5.1 Figure of Merit

The fulfilment of the third DiVincenzo criterion is contingent upon the decoherence time of the qubits significantly exceeding the duration of gate implementations. This statement implies that quantum information processing requires not only robust qubits with prolonged decoherence times but also efficient gate operations. Fulfilling these conditions is also often in conflict for technical reasons. Striking an optimal balance between these two temporal aspects is paramount, as a prolonged coherence time is advantageous only if it can coexist with reasonably short gate operation time.
In order to rigorously quantify how well an architecture satisfies the above statement, and to enable comparisons between different technologies, the figure of merit used, denoted Q_M, is calculated as the ratio of the system coherence time to the gate operation time. This quantity encapsulates the essence of the above statement in a single positive value that is easy to calculate and compare.

1.5.2 Quantum Volume

Inside the complex picture of noisy devices, it is not obvious how to estimate the effective computational power of an architecture. Traditional metrics, such as the number of operations per unit of time, do not capture the significant aspects. Merely considering the number of qubits or the speed of gate execution does not provide a comprehensive understanding of the hardware's true functionality. To address this, in 2019 IBM proposed a novel metric called "quantum volume" (Q_V) as a standardized unit of measurement for NISQ devices with a limited number of qubits (typically up to 50 qubits) [44]. Quantum volume is designed to capture the capabilities of the hardware in a single real number, facilitating easy comparisons among different devices.

The evaluation of the quantum volume is based on the execution of random modular circuits, i.e. circuits with a block structure within which randomly defined gates are applied. These circuits are characterized by two parameters: the width m, i.e. the number of qubits (taken always as even), and the depth d, i.e. the number of blocks. The evolution operator of the whole circuit, denoted as U, is obtained as the product of m step evolution $U = U^1 U^2 \dots U^m$. The operators U^t, where t goes from 1 to m, consist of $m/2$ two-qubit interactions between pairs of qubits randomly chosen. The circuit can be optimized through a transpiling process. Taking into account the device topology, gate set, noise characterization and even additionally qubits if available the circuit is rewritten in an optimal way to reduce errors. In the end, also error mitigation techniques can be applied. The fidelity of the simulation is evaluated comparing them to the exact solution. If the results surpass an acceptance threshold, the quantum volume (Q_V) can be explicitly calculated using the formula:

$$\log_2 Q_V = \underset{m}{\operatorname{argmax}} \min(m, d(m)) \ . \tag{1.41}$$

In summary, the Quantum Volume (Q_V) is a metric that defines the largest square circuit, with the same depth and width, that can be implemented on a quantum device without the noise significantly corrupting the results. Quantum Volume is a comprehensive measure of a quantum device's capabilities. It takes into account several factors, including the number of physical qubits, qubit connectivity, gate set performance, decoherence time, software and compiler performance, and parallelization capabilities [45, 46]. As the time of writing this work, Quantuum currently holds the record for the highest achieved quantum volume, reaching a value of 2^{19} [47]. This accomplishment marks the first instance of a five-digit quantum volume achieved by a company. However, other companies such as IBM, Honeywell, Google, and Rigetti have also announced ambitious development projects with the goal of increasing the quantum volume to the order of hundreds of thousands or even millions within the next five years. This rapid advancement reflects the continuous progress and growing potential of NISQ devices, opening up new frontiers in the field of quantum computing.

1.5.3 Proximity Measurement

When dealing with two quantum states, it is often useful to quantify their proximity or similarity. Such measures help evaluate the precision of algorithm implementations or assess the effects of noise.
Similar to classical information, the first measure that can be introduced is the

trace distance D. Given two density matrices ρ and σ, it is defined as the trace norm of the difference of the two density matrices:

$$D(\rho,\sigma) = \frac{1}{2}\text{tr}|\rho - \sigma|. \tag{1.42}$$

For two commuting matrices, i.e. matrices diagonal in the same basis, this measure corresponds to the classical trace distance. The trace distance assumes values between 0 and 1 and approaches zero as the states ρ and σ become increasingly similar.
Another commonly used quantity is the fidelity $\mathcal{F}$:

$$\mathcal{F}(\rho,\sigma) = \text{tr}|\sqrt{\rho^{1/2}\sigma\rho^{1/2}}|. \tag{1.43}$$

The fidelity ranges between zero and one, where zero represents orthogonal states and one represents identical states. In the case of two commuting density matrices, also the fidelity reduces to the classical definition. Furthermore, it can be shown that the fidelity is invariant under unitary transformations and symmetric with respect to inputs. Often, it is more convenient to look at the inverse of fidelity, i.e. the committed error or infidelity, defined as $\mathcal{E} = 1 - \mathcal{F}^2$. Indeed, assuming low error rates, $\mathcal{E}$ has a clearer representation especially on the logarithmic scale.
Trace distance and fidelity are closely related, and it can be demonstrated that holds the following inequality :

$$1 - \mathcal{F}(\rho,\sigma) \leq D(\rho,\sigma) \leq \sqrt{1 - \mathcal{F}(\rho,\sigma)^2} \ . \tag{1.44}$$

This relation implies that both measures similarly capture the proximity between states, and in many cases they can be used interchangeably.

1.6 Quantum Error Mitigation

The fist type of approach to address errors in quantum circuits is the implementation of Quantum Error Mitigation (QEM) [43]. These techniques have been developed to minimize the impact of noise on the outcomes of quantum algorithms, thereby enhancing the performance of quantum devices. They are not an alternative for quantum error correction (see. Sec. 1.7) and have been ideated with the aim of making the achievement of a quantum advantage closer before the era of fault-tolerant computation. The fundamental distinction between these two approaches lies in their focus: quantum error correction aims to correct errors at the level of individual operations or qubits, thereby improving the quality of individual circuits, while QEM focuses on reducing the influence of noise

on the results of entire algorithms and is typically applied at the circuit level. Although QEM is less attractive for long-term applications, it has nonetheless demonstrated significant results and could play a key role in near-term applications.

Another conceptual difference between these two approaches is that quantum error correction requires errors to remain below a certain threshold level in order to be effective. In contrast, QEM can be applied independently to single error rates and remains effective as long as the final results are not overly corrupted. Consequently, there is no stringent requirement on error rates, and practical limitations primarily result in a maximum circuit complexity. As technology improves, error mitigation will become applicable to more demanding problems without requiring big steps in technological advances.

To be attractive, error mitigation techniques should meet certain criteria. Firstly, they should not introduce an excessive additional computational cost, both quantum and classical, that would limit their applicability. Moreover, these techniques should be general enough to apply to a wide range of problems. Lastly, it is advantageous if they can provide an error bound that quantifies the accuracy of the results they produce.

In the subsequent sections, two of the most common methods are briefly introduced.

Readout Error

In this paragraph, a mitigation technique, based on a classical post-processing procedure, for the correction of measurement or read-out errors is presented [48]. The technique was developed for measurements on multi-qubits and is also valid in the case of asymmetric errors. The method requires the construction of a so-called calibration matrix M_{cal} in which all probabilities of switching from one state to another, due to read-out errors, are estimated for all possible combinations of states. The construction of this matrix is done experimentally by creating and measuring all states repeatedly. In other words, the most rigorous approach requires implementing a complete tomography of the system readout [49]. The limitation of the method is that in general the cost of constructing the matrix grows exponentially with the size of the system and therefore is not scalable for large size systems. However, assuming the qubit errors independent of the problem is drastically simplified and the whole system matrix is obtained simply as the product of the single qubit matrices.

Assuming negligible construction errors, a more than plausible assumption given that a maximum of one rotation per qubit is needed to construct factorised states,

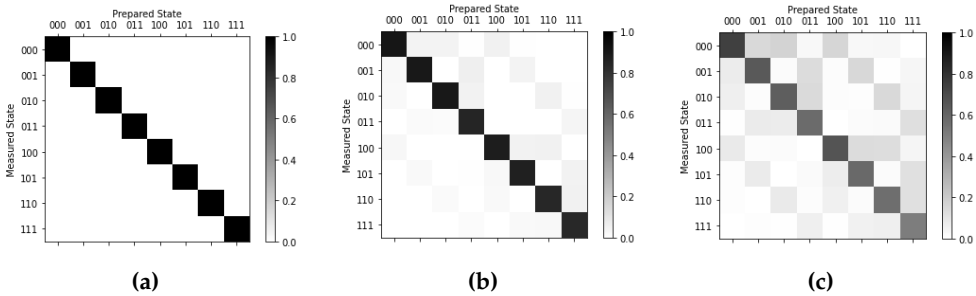

Figure 1.7: Visual representation of the calibration matrices for a three qubit circuit with different error rate probability. From left $p = 0$ (ideal case), $p = 0.1$, and $p = 0.2$. A small asymmetry $p_{p1m0} - p_{p0m1} = 0.05$ is also considered.

a faithful map of the effect of noise is obtained. Fig. 1.7 shows three different calibration matrices constructed for a three qubit circuit. On x axis are the prepared states, i.e. the theoretically constructed initial states, while on y axis are the output of the measure process. The grey scale gives a visual representation of the experimentally measured probabilities. The (A) matrices represent the ideal case where no error has occurred. It's shape is diagonal and this is visually highlighted by the strong contrast between white and black squares. Instead, (B) and (C) show two cases with a probability of $p = 0.1$ and $p = 0.2$ respectively for all qubits that an error occurs in the measurement process. Given the low error rates, the most common case, as indicated by the different shades of gray, is no error, then a single error, and then in order two or three. In fact, a small asymmetry $p_{p1m0} - p_{p0m1} = 0.05$ was also considered.
Defined the calibration matrix, the results are corrected by applying the inverse of this matrix to the vector of experimental probabilities $\vec{v}_{exp}$:

$$\vec{v}_{cal} = M_{cal}^{-1}\vec{v}_{exp} \tag{1.45}$$

where $\vec{v}_{cal}$ is the vector of the corrected probabilities. The higher the statistics of the experimental measurements and of the matrix itself, the more accurate is the technique.

Zero-Noise Extrapolation

Zero-noise extrapolation mitigation encompasses a wide range of methods with various applications. The core concept behind this approach is to study theoretically equivalent circuits that differ from each other for the noise level [49, 50]. A noise coefficient λ characterizes the various implementations of the theoretical

circuit. Any observable of interest obtained after measurement can be defined as a function of the λ rate. As the noise level increases, experimental results tend to deviate from the exact solution. By fitting the results, the zero-noise solution is obtained as the intercept extrapolation curve. This technique can be employed to target specific gates individually or several simultaneously and in general is very efficient when the errors are small and the solution can be calculated for a wide range level of noise.
Three main classes of implementation, which are distinguished by how the noise level of the circuit is calibrated, can be identified: gate redundancy, pulse stretching, and probabilistic insertion. In the first class, circuit noise is calibrated by inserting sequences of abundant gates that are equivalent to the identity. For instance, a single CNOT gate could be replaced by a sequence of three CNOT gates, resulting in equivalent logical operations but with a triple error rate. In the second case, pulse stretching introduces additional noise by modifying the gate implementation directly. For example, in a superconducting qubit architecture where gates are implemented using electromagnetic pulses, the strength and duration of the pulse can be controlled, altering the error contribution from decoherence and leakage. Lastly, in the probabilistic insertion the circuit noise is manipulated by inserting gates that actively simulate faults. In other words, the noise in the circuit is introduced artificially by additional gates. If an accurate modelling of the error source is known, this method could be very advantageous.

1.7 Quantum Error Correction

As introduced in the previous sections, error channels are a major problem for QIP. However, this kind of problem is not new for computer science as it also concerns classical computation. Computers are expected to perform tasks reliably and even a single bit flip can significantly impact calculations. Therefore, when designing an architecture, it is essential to strive to make them resilient to failures. A complete resilience is not always achievable by technological improvement, and therefore it is necessary to coexist with them. Classical computer science has developed a solution known as error-correction to address this issue. While a deep investigation of this topic is not the aim of this work, it is useful to introduce the general concept. In fact, from this, one can acquire a general idea of what QEC can be and also inherit the formalism [51, 52].
Storing the logical information of a bit (logical bit) in a single physical object (physical bit) is risky because if an error occurs, such as a bit flip, the information is lost. The solution founded by classical error correction is thus based on repetition codes. The simplest example is the three-repetition code, where a single

logical bit of information is mapped into three physical bits:

Logical		**Physical**
0	$\longrightarrow$	000
1	$\longrightarrow$	111

Let's assume that each bit is subject to independent symmetric bit flip errors, which occur with probability p. After an error, the bit can be in one of six states: 001, 010, 100, 110, 101 and 011. By employing majority voting, which means counting the number of zeros and ones, it is possible to recover the original information: the first three cases would correspond to logical 0, while the others would correspond to 1. This code is only secure against a single bit flip. If two

Initial state	Final state	Major Voting
000	000	0
	001	0
	010	0
	100	0
111	111	1
	110	1
	101	1
	011	1

Table 1.1: Detection table for the three-bit code.

or three errors occur, the information is lost. It can be demonstrated that this method is effective in improving computation reliability if $p < \frac{1}{2}$. Error correction methods are typically classified using three parameters, denoted as $[[n,k,d]]$, where n is the number of physical objects, k is the number of logical bits, and d is the distance between logical states. A three-bit code is denoted as $[[3,1,1]]$ since it uses three physical bits, stores one logical bit and protects against a single error. It's worth noting that the three-repetition code is the smallest code capable of error correction; a two-level code can only detect errors but cannot correct them. By increasing the number of physical objects n, the distance d between logical states increases, thereby providing protection against more errors.
With an established theory already in place, the aim is to seamlessly extend it to

quantum computers. However, prior to moving forward, it is crucial to outline several fundamental differences:

- **No Cloning**: Repetition codes require the reproduction of a state in multiple copies. However, as demonstrated in Sec. 1.7.1 the No-Cloning theorem forbids this for quantum states.

- **Continuous Errors**: Classical errors are discrete while Quantum states are subject to continuous errors. How can we distinguish between error and not error states? In addition, quantum states are subject to different types of errors, the effects of which can be combined.

- **Measurement Destroys Quantum States**: In classical computation, we can always access and manipulate data. If we tried to access quantum states, we would corrupt them, making correction impossible.

Fortunately, all these problems are surmountable. In the following sections, the two fundamental theorems at the basis of QEC theory, the no-cloning theorem and the Knill-Laflamme conditions, are presented. Then, basic 3-qubit and 9-qubit schemes are introduced.

1.7.1 No-Cloning Theorem

The No-Cloning Theorem is a fundamental principle in quantum computation with profound implications in various fields such as Quantum communication and Quantum Error Correction [53, 54]. It states that it is impossible to create an identical and independent copy of an arbitrary unknown quantum state of a system onto another system. A simple proof of the theorem valid in the case of pure states is given below. However, the theorem can also be proved in the case of generic states. This more general version is also known as No-Broadcast Theorem [55, 56].
Two quantum systems, denoted as A and B, exist within the same Hilbert space $H = H_A = H_B$. Initially, system A resides in an unknown pure state $|\chi_A\rangle$, while system B is in the state $|e_B\rangle$. Given the constraint that measuring the state of A would disrupt it, the sole viable approach for creating a copy is to introduce a unitary evolution operator U_{copy} designed to replicate any state.
The action of U_{copy} is as follows:

$$U_{copy} \left|\chi_A^1\right\rangle \otimes |e_B\rangle = \left|\chi_A^1\right\rangle \otimes \left|\chi_A^1\right\rangle$$
$$U_{copy} \left|\chi_A^2\right\rangle \otimes |e_B\rangle = \left|\chi_A^2\right\rangle \otimes \left|\chi_A^2\right\rangle$$

To assess the scalar product $a = \langle \chi_A^1 \otimes e_B | U_{copy}^\dagger U_{copy} | \chi_A^2 \otimes e_B \rangle$, two distinct methods exists:

$$a = \left\langle \chi_A^1 \otimes e_B \middle| U_{copy}^\dagger U_{copy} \middle| \chi_A^2 \otimes e_B \right\rangle = \left\langle \chi_A^1 \otimes e_B \middle| \chi_A^2 \otimes e_B \right\rangle = \left\langle \chi_A^1 \middle| \chi_A^2 \right\rangle$$
$$a = \left\langle \chi_A^1 \otimes e_B \middle| U_{copy}^\dagger U_{copy} \middle| \chi_A^2 \otimes e_B \right\rangle = \left\langle \chi_A^1 \otimes \chi_A^1 \middle| \chi_A^2 \otimes \chi_A^2 \right\rangle = \left(\left\langle \chi_A^1 \middle| \chi_A^2 \right\rangle \right)^2$$

Matching the two previous solutions, it is not difficult to conclude that either $|\chi^1\rangle = |\chi^2\rangle$ or $\langle \chi^1 | \chi^2 \rangle = 0$. This implies that a universally applicable cloning operator, capable of producing identical and independent copies of arbitrary quantum states, does not exist.
In conclusion, this theorem implies that the classical repetition code described above cannot be trivially extended to the quantum case.

1.7.2 Knill-Laflamme Conditions

For the classical three-repetition code, the fulfilment of two conditions was observed as necessary to correct errors: understanding the effects of errors and the capability to differentiate affected from unaffected states. This was relatively straightforward due to a unique, discrete error source. The computational basis encompassed states 000 and 111, with all other states recognized as corrupted. In this section, this concept is extended to account for continuous and diverse error sources influencing quantum states.
The basis of a single qubit is defined by two orthogonal logical states, $|0_L\rangle$ and $|1_L\rangle$ also known as code words, from which any generic state can be generated $|\Psi\rangle = \alpha |0_L\rangle + \beta |1_L\rangle$. At this stage, the specific form of the logical states is not fundamental, the important thing is that the two states are orthogonal.
As highlighted earlier, the knowledge of errors is essential for the correction. To achieve this, a set of interaction operators denoted as $\mathcal{E}_a$ is introduced, characterizing the action of the environment on the systems. The evolution of the systems follows:

$$\rho_{\text{fin}} = \sum_a \mathcal{E}_a \rho_{in} \mathcal{E}_a^\dagger \ . \tag{1.46}$$

Here, ρ represents the system density matrix, initially assumed to be non-entangled with the environment. The interaction operators can be constructed from an eigenstate basis $|\mu_a\rangle$ of the environment Hilbert space, the initial state $|e\rangle$ of the environment, and the time evolution operator U of the entire system as follows:

$$\mathcal{E}_a = \langle \mu_a | U | e \rangle \, . \tag{1.47}$$

A key property of these operators is that they satisfy the relation:

$$\sum_a \mathcal{E}_a^\dagger \mathcal{E}_a = I \ . \tag{1.48}$$

While these operators can be quite intricate in general, certain approximations are viable for many physical systems. First, the independent interaction with the environment for each qubit allows the representation of the interaction operator $\mathcal{E}_a$ as a tensor product of single-qubit operators. Second, when error rates are low, one of the operators can be approximated as an identity gate.
Given a set of error operators, a logical base is able to correct it if the following conditions are fulfilled:

$$\langle 0_L|\mathcal{E}_a^\dagger \mathcal{E}_b|1_L\rangle = 0 \tag{1.49}$$

$$\langle 0_L|\mathcal{E}_a^\dagger \mathcal{E}_b|0_L\rangle = \langle 1_L|\mathcal{E}_a^\dagger \mathcal{E}_b|1_L\rangle \ . \tag{1.50}$$

These conditions, known as the Knill-Laflamme conditions, are together necessary and sufficient [57, 58]. The first equation implicates that logical states $|0_L\rangle$ and $|1_L\rangle$ need to be transformed into orthogonal states when subjected to any error. In other words, the two subspaces formed by the two code words and their relative affected states must remain orthogonal. The second condition states that the size and the inner product of the states affected by the error must be the same. When constructing the code words, it is often convenient to impose $\langle 0_L|\mathcal{E}_a^\dagger \mathcal{E}_b|0_L\rangle = \langle 1_L|\mathcal{E}_a^\dagger \mathcal{E}_b|1_L\rangle = 0$. However, this requirement, which expresses a sufficient but not a necessary condition, could limit the code correction capability.

1.7.3 Three-Qubit Code

This section introduces the three-qubit code, which is the extension to the quantum case of the classical three-repetition code. Similar to its classical analogue, the three-qubit code is a [[3,1,1]] that means it exploits three physical qubits to encode a single logical qubit. According to its formulation, it is capable of correcting either a single bit or phase-flip errors. Both versions are presented in this section, starting with the one to protect against bit-flip error.
In the description of the classical procedure, the focus has been on outlining the procedure's logic without delving into the operation required for the implementation. Here, alongside explaining the procedure's logic, the quantum circuit required for implementation is also presented 1.53. For simplicity, this treatment assumes that errors occur only during a specific time lapse, known as memory time or error time, during which no operations are implemented. Therefore, all

gate implementations are considered as ideal, i.e. exact and instantaneous.
In the formulation for the bit flip error the logical states reads as:

$$|0\rangle_L = |000\rangle\,, \quad |1\rangle_L = |111\rangle\,, \tag{1.51}$$

from which a generic state $|\Psi\rangle = \alpha\,|0\rangle + \beta\,|1\rangle$ is defined as

$$\begin{aligned} \alpha\,|0\rangle + \beta\,|1\rangle &\rightarrow \alpha\,|0\rangle_L + \beta\,|1\rangle_L \\ &= \alpha\,|000\rangle + \beta\,|111\rangle \\ &= |\Psi\rangle_L \ . \end{aligned} \tag{1.52}$$

The logical information of a single qubit is rewritten on an entangled state formed by three physical qubits. Different from the classical approach, where information is copied over several bits, here the information is spread over several qubits by exploiting quantum entanglement. In this way, the no-cloning theorem is not violated.
The first step of the implementation of the QEC scheme consists indeed in the construction of the code words. This is easily done by means of two CNOT gates which entangles the first qubit with the other two as depicted in 1.53.

Three-Qubit Scheme for Bit-Flip Error (1.53)

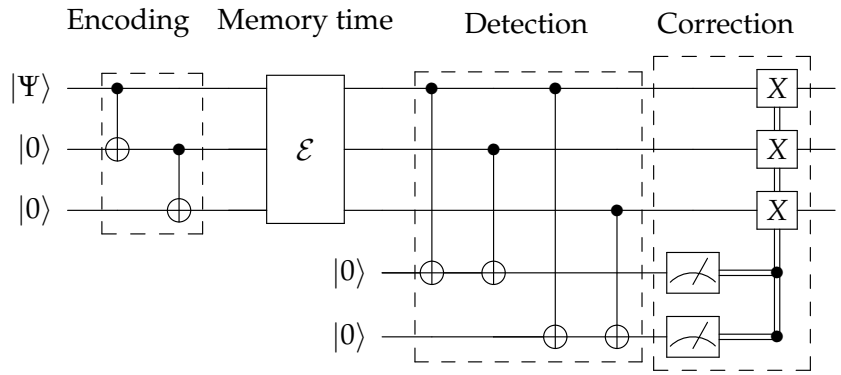

Subsequently, the state, which is now protected, is left under action of possible errors during the so-called memory time. Ended the memory time, the detection procedure begins. This latter serves to determine whether an error has occurred. Similarly at what is done for the three-bit code with the majority voting, errors are identified by means of parity checks. Unlike the classical case, where it is possible to directly access to the information on each bit, to not affect the quantum state it is required to exploit some ancillae. The parity checks are implemented by entangling a couple of code word qubits with an ancilla by means of CNOT gates. Supposing that a single error has occurred, measuring the state of the two

ancillae uniquely distinguish the different possible cases that are summarized in the detection table. Once the result of the measurement is known, classically

Bit-flip	Final state $\|qubits\rangle \|ancillae\rangle$
No Error	$\alpha \|000\rangle \|00\rangle + \beta \|111\rangle \|00\rangle$
Qubit 1 Error	$\alpha \|100\rangle \|11\rangle + \beta \|011\rangle \|11\rangle$
Qubit 2 Error	$\alpha \|010\rangle \|10\rangle + \beta \|101\rangle \|10\rangle$
Qubit 3 Error	$\alpha \|001\rangle \|01\rangle + \beta \|110\rangle \|01\rangle$

Table 1.2: Detection table for the three-qubit code. On the right are the four possible scenarios, and on the left are the states of the qubits and the ancillae. Each scenario is distinguished by a different state of the ancillae.

controlled X gates are implemented to restore the initial states.
Keeping the same circuit structure and logic, this algorithm can be adapted to correct phase-flip error with minor changes.

Three-Qubit Scheme for Phase-Flip Error (1.54)

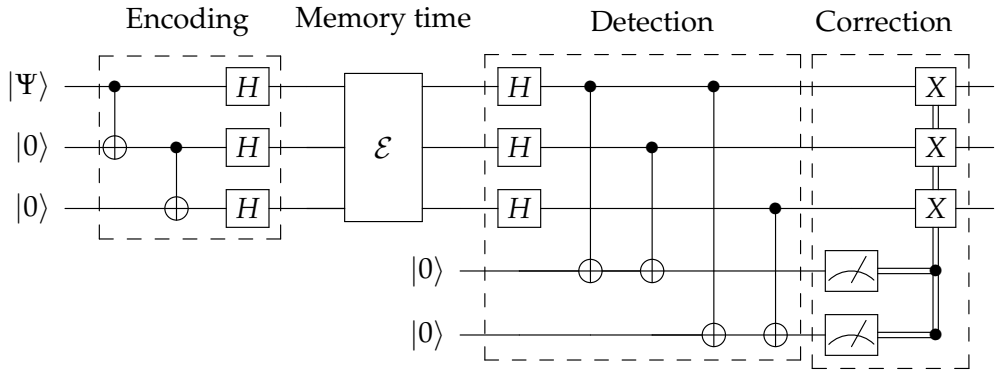

The code words are defined as

$$|0\rangle_L = |+++\rangle, \quad |1\rangle_L = |---\rangle, \tag{1.55}$$

where $|+\rangle = \frac{|0\rangle+|1\rangle}{\sqrt{2}}$ and $|-\rangle = \frac{|0\rangle-|1\rangle}{\sqrt{2}}$. These are constructed by entangling the first qubit with the other two, as before, and then applying a H gate to each qubit. Before the detection procedure, the states are remapped on the computational basis by means of H gates and here after the same procedure as before is applied. Although this simple scheme is helpful as an example for understanding the subject, it has severe limitations. Firstly, it is only secure against one type of error and is therefore not general. Secondly, it is not fault-tolerant, i.e. the way it is

designed, it is not capable of handling gate errors.
In the next section, the first of these limitations is overcome with the introduction of the nine-qubit code, which is capable of correcting both sources of error.

1.7.4 Nine-Qubit Code

The nine-qubit code, also known as Shor's code after its inventor, is the first complete QEC scheme [51, 59]. This code is capable of correcting both bit-flip and phase-flip errors, even when they occur simultaneously, making it suitable for general error correction. As the name suggests, it utilizes nine physical qubits to store a single logical qubit. The code words are created concatenating the three-qubit bit- and phase-flip codes. A hierarchical structure is defined among the nine qubits, and at each level, a three-qubit scheme is employed to encode the logical qubit [60]. The logical states are defined as follows:

$$|0\rangle_L = \frac{1}{2\sqrt{2}}(|000\rangle + |111\rangle)(|000\rangle + |111\rangle)(|000\rangle + |111\rangle) \tag{1.56}$$

$$|1\rangle_L = \frac{1}{2\sqrt{2}}(|000\rangle - |111\rangle)(|000\rangle - |111\rangle)(|000\rangle - |111\rangle) \ . \tag{1.57}$$

As shown in 1.58, the encoding procedure begins by applying a three-qubit phase flip encoding between qubits 1, 4, and 7. Next, a bit flip scheme is implemented within each triplet: $1-2-3$, $4-5-6$, and $7-8-9$. The encoding provides protection against up to three bit flip errors that occur in different triplets, as well as a single phase flip error. The scheme is classified as $[[9,1,3]]$.

Encoding Procedure for the Nine-Qubit Code (1.58)

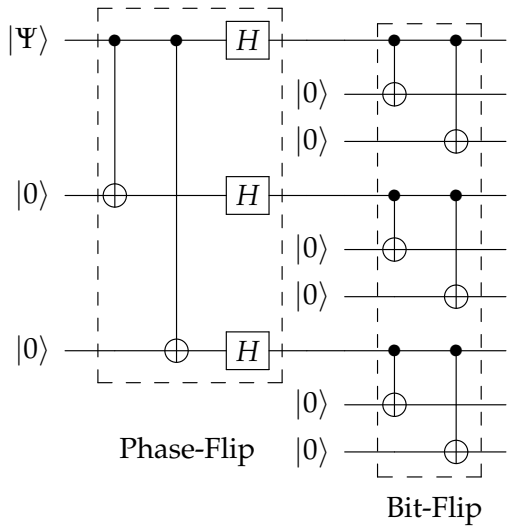

For the detection and correction procedures of bit-flip error, the same parity checks described earlier can be employed within the triplets $1-2-3$, $4-5-6$, and $7-8-9$. For phase flip errors, parity checks are performed among the triplets. For the detection procedure up to 8 ancillary qubits are needed [51].
Since this code is able to correct both sources of error, bit flips and phase flips, it can be the foundation for defining a fault-tolerant code. The next section introduces this concept and explains the requirements that a code has to meet.

1.8 Fault-Tolerant Computation

The previous sections have investigated protocols for detecting and correcting quantum errors. Nonetheless, these approaches rely on assumptions that errors exclusively manifest within designated time intervals and that the gates employed are ideal. Such assumptions do not align with real-world implementations. In addition, it has not yet been considered how to implement operations on the encoded logical states. To overcome these limitations, a method called fault-tolerant quantum error correction is introduced. This approach ensures the effectiveness of quantum error correction even in the presence of errors.
In the next section, the concept of error concatenation is introduced. First, the mechanisms by which errors propagate within a circuit are explored, and then it is shown how circuits can be designed to limit these phenomena. Subsequently, the stabilizer formalism is introduced, offering an efficient approach to defining operations on logical states.

1.8.1 Error concatenation

The key aspect that fault tolerance aims to address is the propagation of errors. In a fault-tolerant circuit, it is essential that an error occurring in one qubit does not cascade to affect others. It is easy to see that if every attempt to fix a failure leads to another failure, it would not be successful. Therefore, a fundamental requirement for a fault-tolerant circuit element is that (Simon J. Devitt et al., 2013, p. 076001) "a single error causes at most one error in the output for each logical qubit block". In cases where codes are capable of correcting multiple faults (denoted as t), this requirement can be relaxed to state that the circuit is fault-tolerant if (Simon J. Devitt et al., 2013, p. 076001) "a single error causes at most t errors in the output for each logical qubit block".
In quantum circuits, two main mediators of error propagation are two-qubit gates and the classical control correction procedure resulting from a faulty measurement. Both of these procedures connect different qubits and thus have the potential to propagate errors.Therefore, when a quantum circuit is designed, it is

crucial to consider the propagation of errors. Even though two circuits may be equivalent from a theoretical standpoint, they may not be equivalent in terms of error propagation. To illustrate this concept, let's consider a practical example. Imagine that there are two sets of three qubits each, representing two different logical states: $|1_L\rangle\,|0_L\rangle = |111\rangle\,|000\rangle$. The goal is to design a quantum circuit that transforms the initial state $|111\rangle\,|000\rangle$ into $|111\rangle\,|111\rangle$.

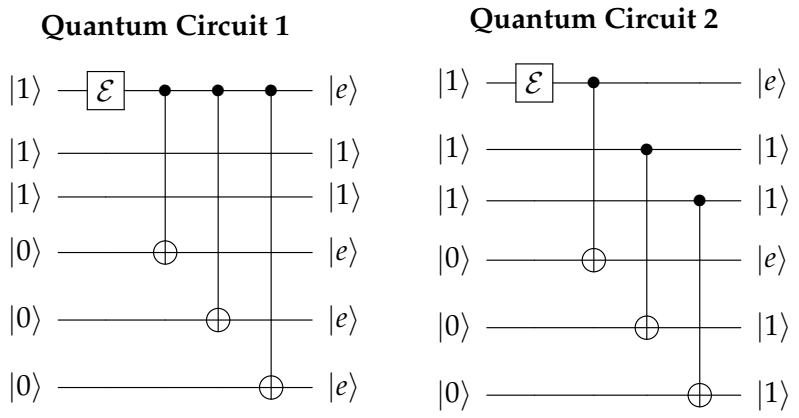

(1.59)

Quantum Circuit 1 and Quantum Circuit 2, shown in 1.59, depict two formulations that can produce the desired final state. In an ideal noiseless circuit, these two formulations would be equivalent. However, when errors are introduced, represented by $-\boxed{\mathcal{E}}-$, the propagation mechanism differs between the two circuits. In Quantum Circuit 1 (left), a single error on the first logical qubit affects three other qubits on the second logical qubit. On the other hand, in Quantum Circuit 2 (right), a single error on the first state only affects a single qubit on the second logical state. This example clearly demonstrates how the design of a circuit can significantly impact its fault tolerance. Therefore, when constructing quantum circuits, it is essential to consider the potential propagation of errors and devise strategies to minimize their impact. Circuit design plays a critical role in ensuring the robustness and reliability of quantum computations, especially in the presence of noise and errors inherent to quantum systems.

1.8.2 Stabilizer Formalism

In conclusion to this introduction to QEC, it is essential to show how operations on encoded states can be defined. However, before tackling into the problem, it proves beneficial to develop a suitable formalism.
Up to this point, code words and error-correcting codes have been described using the state vector representation of the encoded states. However, this description can be quite inefficient as it has to be adapted for each specific code.

It would be desirable to have a methodology for state representation and circuit design that is more general and independent of the specific code. This is where the *stabilizer formalism*, introduced by Gottesman [60], comes in. This formalism, based on the Heisenberg representation of quantum mechanics, describes states in terms of operators.
Let's start by introducing the concept of a stabilizer. An operator K is considered a stabilizer for a given state Ψ if it satisfies to the following condition:

$$K|\Psi\rangle = |\Psi\rangle \quad . \tag{1.60}$$

This means that K is a stabilizer for a state Ψ, if Ψ is an eigenstate of K with eigenvalue $+1$. In general, K can be any single qubit operator, but often the choices are made from the subgroup $\mathcal{P}$ defined by the Pauli operators:

$$\mathcal{P} = \{\pm\sigma_I, \pm i\sigma_I, \pm\sigma_x, \pm i\sigma_x, \pm\sigma_y, \pm i\sigma_y, \pm\sigma_z, \pm i\sigma_z\} \tag{1.61}$$

This set forms a group under matrix multiplication. The simplest example of a stabilizer is given by the Pauli matrix σ_z on the state $|0\rangle$ that gives $\sigma_z|0\rangle = |0\rangle$.
For an N-qubit system, the Pauli group $\mathcal{P}_N$ is defined as the tensor product of N groups $\mathcal{P}$. The Abelian subgroup $\mathcal{G}$ of stabilizer operators belonging to the group $\mathcal{P}_N$ satisfies the following properties:

$$\mathcal{G} = \left\{ K^i \;\middle|\; K^i|\Psi\rangle = |\Psi\rangle, [K^i, K^j] = 0, \forall(i,j) \right\} \subset \mathcal{P}_N \quad . \tag{1.62}$$

Here, the state $|\Psi\rangle$ can be represented either in terms of a state vector or by the generators of the stabilizer group $\mathcal{G}$. As an example, consider the Greenberger-Horne-Zeilinger (GHZ) state $|GHZ\rangle_3$ [61]:

$$|GHZ\rangle_3 = \frac{|000\rangle + |111\rangle}{\sqrt{2}} \qquad \leftrightarrow \qquad |GHZ\rangle_3 = \begin{pmatrix} K_1 = \sigma_x \otimes \sigma_x \otimes \sigma_x \\ K_2 = \sigma_z \otimes \sigma_z \otimes \sigma_I \\ K_3 = \sigma_I \otimes \sigma_z \otimes \sigma_z \end{pmatrix} \quad . \tag{1.63}$$

The $|GHZ\rangle_3$ state is ambiguously determined by the three stabilizers K_1, $K2$ and K_3. At this point, the aim is to utilize this formalism to define operations on encoded states. Given a logical state $|\Psi\rangle_L$, stabilized by K operator, if a general transformation U is applied on $|\Psi\rangle_L$, the evolved state $U|\Psi\rangle_L$ is stabilized by $UKU^\dagger$:

$$U|\Psi\rangle_L = UK|\Psi\rangle_L = UKU^\dagger U|\Psi\rangle_L \quad . \tag{1.64}$$

It is clear that once the set of stabilizers $\{K^i\} \in \mathcal{G}$ has been defined this cannot change during the computation or also the code words would change. So, it is

mandatory that the set of available operations transform stabilizers inside the subgroup $\mathcal{G}$, i.e.

$$UK^iU^\dagger = K^j \quad \text{for} \quad K^j \in \mathcal{G}, \ \forall\, i \ . \tag{1.65}$$

Now let's study the case of Shor's code, starting with the definition of the set of stabilizers. In this scheme, error detection involves performing parity checks among different subgroups of qubits. For instance, the detection of bit-flip errors is conducted on the parity of qubit pairs within the same triplets. The checks on first triplet correspond to measuring $\sigma_{z1}\sigma_{z2}$ and $\sigma_{z1}\sigma_{z3}$. Phase-flip errors are detected by observing the parity between triplets, which entails measuring $\sigma_{x1}\sigma_{x2}\sigma_{x3}\sigma_{x4}\sigma_{x5}\sigma_{x6}$ and $\sigma_{x1}\sigma_{x2}\sigma_{x3}\sigma_{x7}\sigma_{x8}\sigma_{x9}$. In total there are eight operators and for all of them the Shor's code words $|0\rangle_L$ and $|1\rangle_L$ are eigenstates with eigenvalue $+1$. This set of eight stabilizers uniquely defines a two-dimensional subspace and, consequently, a pair of logical states. Hence, it can be inferred that Shor's code words are stabilized through the mentioned set of operations (refer to Tab. 1.3).

The subsequent discussion revolves around the implementation of operations

K^1	σ_z	σ_z	I	I	I	I	I	I	I
K^2	σ_z	I	σ_z	I	I	I	I	I	I
K^3	I	I	I	σ_z	σ_z	I	I	I	I
K^4	I	I	I	σ_z	I	σ_z	I	I	I
K^5	I	I	I	I	I	I	σ_z	σ_z	I
K^6	I	I	I	I	I	I	σ_z	I	σ_z
K^7	σ_x	σ_x	σ_x	σ_x	σ_x	σ_x	I	I	I
K^8	σ_x	σ_x	σ_x	I	I	I	σ_x	σ_x	σ_x

Table 1.3: Stabilizer for Shor's code.

on encoded states, commencing with single-qubit operations. It is expected that a single-body operation A can be reformulated as a logical operation $\bar{A}$ that affects logical states through a sequence of single-qubit operations on the constituent qubits of the logical state [51]. In the case of the $[[9,1,3]]$ code, $\bar{X}$ and $\bar{Z}$ are defined as follows:

$$\bar{X} = XXXXXXXXX = X^{\otimes 9} \tag{1.66}$$

$$\bar{Z} = ZZZZZZZZZ = Z^{\otimes 9} \ . \tag{1.67}$$

It is easy to verify that the relations $\bar{X}K^i\bar{X} = K^i$ and $\bar{Z}K^i\bar{Z} = K^i$ hold for the set of Shor's stabilisers. Therefore, applying a sequence of X or Z gates are valid operations and their effect on the encoded state is equivalent to the expected X

or Z gates, respectively. Since there are no connections between different qubits (see 1.68), these operations are inherently implemented in a fault-tolerant manner.

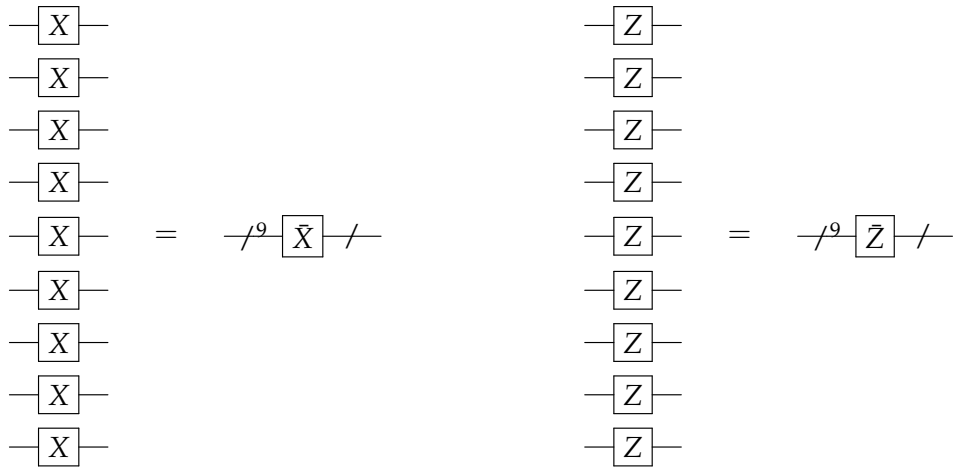

(1.68)

Proceeding in an analogous manner, other operations such as H or P gates can be generalized.

This last section focuses on the generalisation of two-qubit gates. The idea is to follow a similar approach as with single-qubit gates, rewriting two-qubit gates as transversal applications between pairs of qubits. For example, it has been demonstrated by Calderbank and Shor and independently by Steane that a transversal application of CNOT gates leave stabilizers invariant and its effect is a logical CNOT gate [62, 63]. A sketch of the proof can be given by looking at the effect of the CNOT on the stabilizers. As instance, let's consider K^1 and K^7 stabilizers:

$$\begin{aligned}
\text{CNOT} \circ \left(K^1 \otimes I\right) \circ \mathit{CNOT} &= K^1 \otimes I \\
\text{CNOT} \circ \left(I \otimes K^1\right) \circ \mathit{CNOT} &= K^1 \otimes K^1 \\
\text{CNOT} \circ \left(K^7 \otimes I\right) \circ \mathit{CNOT} &= K^7 \otimes K^7 \\
\text{CNOT} \circ \left(I \otimes K^7\right) \circ \mathit{CNOT} &= I \otimes K^7
\end{aligned}$$

where the first qubit acts as control while the second as target. The CNOT gates satisfy Eq. 1.65 and therefore is a valid operation for this set of stabilizers. The effect on the other stabilizers is found by proceeding in an analogous way. What remains to be comprehended is the effect of cross-application of CNOT gates on an encoded state or, in other words, which transformation is actually implemented.

Comparing the action of a single CNOT on the set of stabilizers of a two qubit systems (left) and the action of a transversal application of CNOT on the same

operators extended to the nine qubit space (right):

$$\begin{aligned} I \otimes I &\to I \otimes X & \overline{I} \otimes \overline{X} &\to \overline{I} \otimes \overline{X} \\ X \otimes I &\to X \otimes X & \overline{X} \otimes \overline{I} &\to \overline{X} \otimes \overline{X} \\ I \otimes Z &\to Z \otimes Z & \overline{I} \otimes \overline{Z} &\to \overline{Z} \otimes \overline{Z} \\ Z \otimes I &\to Z \otimes I & \overline{Z} \otimes \overline{I} &\to \overline{Z} \otimes \overline{I} \end{aligned} \tag{1.69}$$

The action of these transformations results in a corresponding transformation on the operators, hence it can be deduced that a transversal application of CNOT gives the equivalent of a CNOT on the encoded space. Furthermore, this approach is also intrinsically fault tolerant because it limits errors concatenation (see 1.8.1).

1.8.3 Threshold Theorem

The most important result of the fault-tolerant approach to quantum error correction (QEC) is the Threshold Theorem, which shows that it is possible to efficiently simulate any quantum algorithm while reducing the error rate to any desired level of precision [64–66]. Furthermore, the theorem makes it possible to estimate the threshold of error gates required for a procedure to be effective. Various formulations of the theorem exist in the literature, differing in their assumptions about error models and types of error correction codes. A generic version based on essential assumptions is presented in the following paragraph [10].
A fundamental concept in QEC is the scheme composability. As exemplified by Shor's code, which consists of a two-level concatenation of the three-qubit code, schemes can be concatenated to enhance their ability to correct errors and reduce error rates. By recursively applying multiple layers, the error on the final result can be significantly reduced. For instance, consider a target circuit, denoted as C, composed of R gates at the logical level, i.e. at the level of a not encoded circuit. Each of these gates can be replaced by a fault-tolerant procedure implementing the same operations. Assuming that all errors are independent, if p represents the fault probability for a single gate in the original circuit, at the first encoding level the probability of two faults occurring, rendering the correction procedure ineffective, is at least proportional to $c \times p^2$. If the condition $p > cp^2$ is satisfied, the scheme reduces the probability of faults and is therefore worthwhile. Instead of stopping here, it is possible to further improve the code by implementing a second level of encryption, where all the operations of the first level are themselves replaced by a fault-tolerant procedure. The code fault probability is further improved to $\propto c(cp^2)^2$. This concatenation process can be extended infinitely, and a

k-fold concatenation results in a worst-case error probability of $\propto \frac{(cp)^{2^k}}{c}$.
On the other hand, the total number of gates scales as RN^k, where N is a constant representing the number of operations used in a single step of the fault-tolerant procedures.
Intuitively, one can already discern the value of this mechanism. Despite the exponential growth in the number of gates with respect to k, the error introduced decreases double exponentially in k. In other words, error correction outpaces the introduction of errors. This relationship can be formally deduced as well.
Defining ϵ as the desired error level at the end of the computation for some concatenation of level k, ϵ must be greater than the number of logical operations implemented at the k-th stage multiplied by the error of those operations. In formulas:

$$Rp_k = R\frac{(cp)^{2^k}}{c} < \epsilon \tag{1.70}$$

Solving this inequality explicitly yields:

$$\begin{aligned} (cp)^{2^k} &< \frac{\epsilon c}{R} \\ \Rightarrow \quad 2^k &< \log_{cp}\left(\frac{\epsilon c}{R}\right) = \frac{\log\left(\frac{\epsilon c}{R}\right)}{\log(cp)} \\ \Rightarrow \quad k &< \log\left[\frac{\log\left(\frac{\epsilon c}{R}\right)}{\log(cp)}\right] , \end{aligned} \tag{1.71}$$

where the last equation provides a upper bound for the concatenation level k respect to ϵ. From this result, it is possible to obtain an upper bound on the number of physical gates allowed to achieve the ϵ level of precision:

$$N^k R < N^{\log\left[\frac{\log\left(\frac{\epsilon c}{R}\right)}{\log(cp)}\right]} R = \left(\frac{\log\left(\frac{\epsilon c}{R}\right)}{\log(cp)}\right)^{\log N} R \tag{1.72}$$

Notably, the number of operations scales only poly-logarithmically, making this approach highly favourable as expected from the considerations made earlier. All these results hold under the assumption that $p > cp^2$. The critical value at which the equality $p = cp^2$ holds is termed the threshold probability, and it is given by:

$$p_{th} = c^{-1} \ . \tag{1.73}$$

At this point, the logical error probability at concatenation level k can be expressed in terms of the threshold:

$$p_k = c^{-1+(cp)^{2^k}} = p_{th}\left(\frac{p}{p_{th}}\right)^{2^k} \ . \tag{1.74}$$

Looking at the response of this quantity with respect to p, it can be seen that p_{th} is a very sharp boundary and a small variation of p above or below the p_th threshold gives very distant results. Furthermore, as the degree of concatenation increases, the error committed decreases very rapidly.

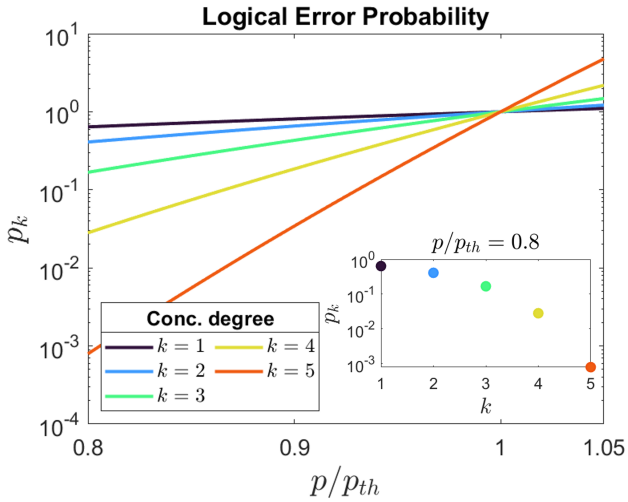

Figure 1.8: Logical error probability p_k as a function of the p/p_{th} ratio for different encoding degrees k. In the inset, p_k as function of the degree k of encoding for a fixed ratio of $p/p_{th} = 0.8$.

1.9 Multi-Level Quantum Computation

Similarly to classical information, which is based on the binary numeral system, quantum information presented so far has been based on two-level quantum systems. It is important to note that computation based on a "binary metric", where the reader would allow this term to be used also for quantum systems, is complete, i.e., it is capable of representing any information. Furthermore, this kind of computation is in a sense the most compact and efficient. In fact, binary logic minimizes the necessary resources of the underlying physical system. For example, a 64-dimensional computational space can be obtained by either six qubits, two 8-level qudits, or a single 64-level qudit. Although the computational space is the same, the underlying physical systems require a different number of physical states: 12 levels using 6 qubits, 16 considering two 8-level qudits, and 64 for single 64-level qudit. However, this does not exclude the possibility of computation based on a multi-valued logic and, therefore, relying on high-dimensional quantum digits (qudits) [67].
A qudit can be represented by a vector in the d-dimensional Hilbert space $\mathscr{H}_d$.

The basis is formed by d orthonormal vectors, and the most general state of a qudit, short of a global phase, can be represented as:

$$|\Psi\rangle_d = \alpha_0|0\rangle + \alpha_1|1\rangle + \alpha_2|2\rangle + \cdots + \alpha_{d-1}|d-1\rangle = \begin{pmatrix} \alpha_0 \\ \alpha_1 \\ \alpha_2 \\ \vdots \\ \alpha_{d-1} \end{pmatrix} \in \mathbb{C}^d \tag{1.75}$$

where the parameters α_i are complex numbers which must fulfil the condition $|\alpha_0|^2 + |\alpha_1|^2 + |\alpha_2|^2 + \cdots + |\alpha_{d-1}|^2 = 1$. Unfortunately, a visual representation such as the Block's sphere for qubits is not possible for qudits.

This alternative approach offers several advantages, stemming primarily from the possibility of processing more information per logical unit, but also from a more efficient experimental implementation.

Identifying a qubit in a physical system usually requires restricting a higher-dimensional Hilbert space to its lowest-energy levels, thus wasting potential resources. Indeed, many physical systems, already exploited to implement qubits, naturally allow the implementation of qudits. Among them, it is important to mention the proposals and experimental achievements obtained with photons [68, 69], ion traps [70, 71], superconducting systems [72–74], molecular nanomagnets [75–78], and trapped ions [71].

Qudits have the potential to store and process more information per unit, resulting in simpler experimental setups with fewer physical objects. To represent an N-dimensional space at least $n_1 = \log_2 N$ qubits are required. Moving to qudits, only $n_2 = log_d N$ qudits would be necessary, resulting in a reduction of a factor $k = \frac{n_1}{n_2} = \log_2 d$.

Computation based on qudits can lead to simpler and shallower circuits by reducing the number of two-body gates and increasing the number of operations that can be performed in parallel. Two-body gates are notoriously more difficult to implement and involve greater errors. In contrast, strategies to implement single-qudit gates are already well-developed for many architectures and can be performed with high precision. Particularly in noisy near-term architectures, these features could greatly facilitate the implementation of basic algorithms and move us closer to achieving quantum advantage [79].

Another crucial aspect to consider is that for certain types of problems, such as simulating bosonic particles, a qudit mapping can be more natural and thus simplify the gate decomposition process.

In the end, studies have shown that qudit-based computation could provide a significant advantage for the realization of effective quantum error-correction

schemes. One of the main drawbacks of standard block encoding QEC is the significant amount of resources required. Encoding a single logical qubit in a fault-tolerant manner can require up to thousands of physical qubits involved in storing and processing operations and therefore implying many single and two-body gates. Often, the implementation of quantum error correction schemes faces scalability challenges. Advanced schemes, which theoretically lead for a high precision computation, also require longer and thus noisier operation sequences. This leads to tighter tolerance thresholds requirements that practically limit the applicability of these techniques. In contrast, it has been shown that a qudit approach can relax error thresholds and hence result in a more easily realizable implementation [11].
Just as for qubits, to establish the foundation for qudit computation, it is necessary to identify a set of operations with which it is possible to decompose general algorithms. In the first part of this section, some examples of single- and two-qudit gates are introduced. Following that, the universality of gate sets is discussed. Finally, two decomposition strategies for breaking down single-qudit operations into simpler ones that can be directly implemented in hardware, are presented. These strategies provide an exact decomposition and are applicable to general unitary matrices.

1.9.1 Qudit Gates

As seen for qubits but in this case even more, a multitude of gates or classes of operations can be defined. Given d as the dimension of qudit space any $d \times d$ unitary matrix can represent a possible single qudit gate. However, it becomes useful to identify those operations that are most significant for their structure or logical meaning. In order to identify an elementary set of operations, it is useful that these are simple and can therefore be implemented directly on any hardware. Commonly, primitive gates on qudit are defined as local operation, i.e. operations which act only on a subspace of the total space $\mathscr{H}_d$. In this way, they can be defined with a small number of parameters and are potentially easier to implement. An example is the generalized X gate defined as [80]:

$$X_j(x,y) = \begin{pmatrix} I_{j-i} & & & \\ & \frac{x}{\sqrt{|x|^2+|y|^2}} & \frac{-y}{\sqrt{|x|^2+|y|^2}} & \\ & \frac{y^*}{\sqrt{|x|^2+|y|^2}} & \frac{x^*}{\sqrt{|x|^2+|y|^2}} & \\ & & & I_{d-j-i} \end{pmatrix}, \tag{1.76}$$

which acts only on a couple on subsequent levels while leaving untouched all other states.

Another significant operation is the generalized Z gate:

$$Z_d(\theta) = \begin{pmatrix} I_{d-i} & \\ & e^{i\theta} \end{pmatrix}, \tag{1.77}$$

which action is to add a phase θ only to the state $|d-1\rangle$ while other states are not affected .
Two-qudit gates can be defined starting from the above gates and tie them to a control command. A controlled operation $C[R_d]$ acting on a space $d^2 \times d^2$ is defined as:

$$C_2[R_d] = \begin{pmatrix} I_{d^2-d} & \\ & R_d \end{pmatrix}, \tag{1.78}$$

where R_d can be either X_d or Z_d. R_d operates on the lowest d subset of states, while all others are idle. The action of R_d is therefore subordinate to the state of the first quit.
Give this operation as demonstrated in [80], an available universal set can be formed by:

$$\Gamma = \{X_d, Z_d, C_2[R_d]\} . \tag{1.79}$$

As seen for qubits, the choice of the set is not unique and it can drastically affect the efficiency of algorithm implementation. To take the most from the hardware, it is therefore convenient to choose the set that most fits it.

1.9.2 Decomposition Strategies

In the above section, a universal gate set has been introduced with which it is theoretically possible to decompose any algorithm. The above set is characterized by the fact that single and two body gates act locally, i.e. in a qudit subspace of two levels. However, it is often convenient, at least from a logical point of view, to be able to define global operations that have an obvious action. For example, a very relevant single qudit-gate is the d-dimensional generalization of Hadamard. Its importance stems from the fact that, as seen for the qubit Hadamard gate, this operation corresponds to the Quantum Fourier Transform on a d-dimensional space. Its matrix representation is:

$$\mathrm{H}_d = \frac{1}{\sqrt{d}} \begin{pmatrix} 1 & 1 & 1 & 1 & \dots & 1 \\ 1 & w & w^2 & w^3 & \dots & w^{d-1} \\ 1 & w^2 & w^4 & w^6 & \dots & w^{2(d-1)} \\ 1 & w^3 & w^6 & w^9 & \dots & w^{3(d-1)} \\ \vdots & \vdots & \vdots & \vdots & & \vdots \\ 1 & w^{d-1} & w^{2(d-1)} & w^{3(d-1)} & \dots & w^{(d-1)(d-1)} \end{pmatrix}, \tag{1.80}$$

where $w = e^{\frac{2\pi i}{d}}$. Similarly to the qubit Hadamard, this gate is present in many qudit-based algorithms. Practically, its implementation requires the decomposition in simpler operations that act locally and can be directly implemented in the hardware. In the following sections, two different strategies, namely planar rotation and quantum householder reflection decomposition, are introduced to decompose arbitrary dimensional unitary gates into simpler operations.

Planar Rotation Decomposition

The Planar Rotation decomposition (PR) is a strategy that allows to break down any unitary matrix into a sequence of simpler local operations [81–83]. This method is based on the ononime planar rotation $U_{\mu\nu}(\theta,\beta)$, also known as Givens rotations in the context of quantum optimal control theory [84], which are rotations between pairs of levels. Given a d-dimensional space, these operations are usually defined as:

$$\begin{aligned} U_{\mu\nu}(\theta,\beta) &= \cos(\theta/2)\left(|\mu\rangle\langle\mu| + |\nu\rangle\langle\nu|\right) \\ &+ \sin(\theta/2)\left(|\nu\rangle\langle\mu| e^{i\beta} - |\mu\rangle\langle\nu| e^{-i\beta}\right) \\ &+ \sum_{\ell\neq\mu,\nu} |\ell\rangle\langle\ell| \,, \end{aligned} \tag{1.81}$$

where $|\mu\rangle$, $|\nu\rangle$, and $|\ell\rangle$ indicate the basis eigenstates and θ and β are two real parameters.
Any unitary matrix $W \in SU(d)$ is rewritten in terms of planar rotations as:

$$\begin{aligned} W = \Lambda(e^{i\alpha_1}, e^{i\alpha_2}, \ldots, e^{i\alpha_{d-1}}, e^{-i\sum_{k=1}^{d-1}\alpha_k}) \\ \times U_{1,2}(\theta_1,\beta_1)U_{1,3}(\theta_2,\beta_2)U_{2,3}(\theta_3,\beta_3)\ldots \\ \times U_{1,d}(\theta_{\frac{(d-1)(d-2)}{2}+1}, \beta_{\frac{(d-1)(d-2)}{2}+1}) \\ \times U_{2,d}(\theta_{\frac{(d-1)(d-2)}{2}+2}, \beta_{\frac{(d-1)(d-2)}{2}+2})\ldots \\ \times U_{d-1,d}(\theta_{\frac{d(d-1)}{2}}, \beta_{\frac{d(d-1)}{2}}) \,, \end{aligned} \tag{1.82}$$

where $\Lambda(e^{i\alpha_1}, e^{i\alpha_2}, \ldots, e^{i\alpha_{d-1}}, e^{-i\sum_{k=1}^{d-1}\alpha_k})$ is a diagonal matrix. This method requires a number of operations that scale quadratically with matrix size [82].
A stepwise approach to determine the various parameters can be outlined as follows. Initially, the target matrix W is right-multiplied by $U_{d-1,d}(\theta_{\frac{d(d-1)}{2}}, \beta_{\frac{d(d-1)}{2}})$ with rotation angles $\theta_{\frac{d(d-2)}{2}}$ and $\beta_{\frac{d(d-1)}{2}}$ taken so that the $(d, d-1)$ element of the resulting $W_1 = WU_{d-1,d}$ matrix is null. Then, one proceeds by computing $W_2 = W_1 U_{d-2,d}$ and fixing the rotation angles of $U_{d-2,d}$ so that, similarly as before, the $(d, d-2)$ element of W_2 is null. The algorithm continues until defining

the W_{d-1} matrix that has all-zero elements in the d-th column except for the (d,d)-th element, which must have a magnitude of 1 to conserve the unitarity of the matrix. At this point, one moves on to the upper line and restarts by nullifying the the element $(d-1,d-2)$. Proceeding in order from bottom to the top, all the rows can be nullified leaving only the diagonal elements. The overall decomposition can be expressed as a product of unitary matrices, as shown in the equation:

$$\begin{aligned} WU_{d-1,d}U_{d-2,d}\dots U_{1,d}U_{d-2,d-1}\dots\dots U_{1,3}U_{1,2} = \\ \Lambda(e^{i\alpha_1},e^{i\alpha_2},\dots,e^{i\alpha_{d-1}},e^{-i\sum_{k=1}^{d-1}\alpha_k}) \ , \end{aligned} \tag{1.83}$$

where Λ is a diagonal matrix with the various entries specified in brackets. In the end, the target matrix W can be reconstructed by multiplying Λ by $U_{1,2}^{-1}U_{1,3}^{-1}\dots U_{d-2,d-1}^{-1}U_{1,d}^{-1}\dots U_{d-1,d}^{-1}$. It's important to note that the relation $[U_{j,k}(\theta,\beta)]^{-1} = U_{j,k}^{\dagger}(\theta,\beta) = U_{j,k}(-\theta,\beta)]]$ applies for planar rotations. So the parameters to reconstruct W are the same β and θ changed in sign.

Quantum Householder Reflection Decomposition

Another viable approach for decomposing an arbitrary unitary matrix is the Quantum Householder Reflection decomposition (QHR). QHR is based on the Quantum Householder reflection, which, in the generalized form, is defined as follows:

$$M(v,\phi) = I + (e^{i\phi}-1)\,|v\rangle\langle v| \ . \tag{1.84}$$

Here, I represents the identity matrix, $|v\rangle$ is a normalized complex vector of dimension d, and ϕ is an arbitrary phase. Taking into account the normalization constraint, the transformation is defined by $2d-1$ real parameters. The geometric interpretation of this operation is not obvious for general parameters. In the case of $\phi = \pi$ and v is a real vector, it represents a reflection with respect to an d-dimensional plane perpendicular to the vector $|v\rangle$.
Any unitary matrix $W \in SU(d)$ can be expressed as a product of d such Quantum Householder reflections:

$$W = \prod_{i=1}^{d} M(v_i,\phi_i) \ . \tag{1.85}$$

Typically, the vectors v_i are not eigenstates of the base, and therefore $M(v_i,\phi_i)$ are global transformations on the d-dimensional space. Compared to the PR decomposition, QHR is in general more complex to implement but is more efficient as it requires only d elementary steps. The best choice between PR and QHR depends on the specific experimental implementation, which is not discussed at this stage.

By following an iterative procedure, all the parameters v_i and ϕ_i can be analytically calculated. The procedure begins by determinating the coefficient for the first transformation, i.e. $M_1 = M(v_1, \phi_1)$ that is defined as follows:

$$\begin{aligned} \phi_1 &= 2 \arg(1 - w_{11}) - \pi \\ v_1 &= \frac{1}{e^{-i\phi_1} - 1} \sqrt{\frac{2 \sin(\phi_1/2)}{|1 - w_{11}|}} (|w_1\rangle - |e_1\rangle) \ , \end{aligned} \tag{1.86}$$

where, w_1 represents the first column of W, w_{11} identifies the first element of the vector w_1, and $|e_1\rangle$ is a projector defined as $|e_1\rangle = [1,0,\ldots,0]^T$. Multiplying the original matrix W by the M_1 a new matrix $W_1 = M(w_1, -\phi_1)W$ is defined. W_1 has zeros on all the elements in the first row and column except for the $(1,1)$ entry which is one. At this point the procedure is repeated restating with the W_1 matrix instead of W. The parameters v_2, ϕ_2, and $|e_2\rangle$ are defined in a similar manner. By repeating this process d times, the entire matrix is diagonalised and all parameters v_i and ϕ_i are determined. The resulting W_{d-1} diagonal matrix has all ones except for the (d,d) element which in general can have a relative phase.

CHAPTER 2

Introduction to Molecular Nanomagnets:

Mn12O12(CH3COO)16(H2O)4, commonly known as Mn_{12}, is considered the ancestor of all Molecular Nanomagnets. Discovered in the early 90s, it immediately aroused interest for the magnetic hysteresis similar to classical magnets but with a quantum tunnelling mechanism in the relaxation it exhibits [85–87]. Since then, numerous other systems, such as Fe_8 [88], Cr_8 [89], Mn_6 [90], Fe_{30} [91], Dy-cene [92] or Cr_7Ni [93] have been synthesized and reported [94]. These systems possess unique features resulting from the combination of their magnetic properties and quantum effects arising from their small size. In addition to the aforementioned magnetic hysteresis and quantum tunnelling of magnetization, MNMs can exhibit a variety of other interesting phenomena such as Neel vector tunnelling [95], frustration [96–99], and well-understood decoherence effects [100–103].

Molecular Nanomagnets are characterised by a structure with a core of one or a few magnetic atoms, surrounded by organic ligands. These latter magnetically shield the cores from each other, so when molecules are arranged into crystals, the behaviour of a single molecule can be studied by bulk measurements greatly facilitating experimental studies. According to the elements that constitute their magnetic core, two main families of MNMs can be identified. The first family consists of transition metal ions ($3d$), such as iron or manganese, while the second family includes lanthanides ($4f$), such as gadolinium and ytterbium.

These systems are highly chemically tunable, as the size, shape and composition of molecular nanomagnets can be tailored to achieve specific properties. By modifying the ligands or ions, it is possible to tune the magnetic behaviour, including the strength of the magnetic moment, the magnetic anisotropy (the preferred direction of the magnetic moment) or enhancing system coherence.

Molecular nanomagnets have found potential applications in various areas including information storage, magnetic refrigeration, and, as deeply analysed in this work, quantum technologies. Indeed, thanks to the strong magnetic hysteresis, a single molecule can be used for storing a classical bit of information,

potentially enabling the realization of high-density data storage devices [92, 104, 105]. The magnetocaloric effect, which is the temperature change in a suitable material induced by a variable magnetic field, has been studied for refrigeration purposes [106–108]. It is worth noting that refrigeration accounts for a significant portion of the world's total electricity consumption. Magnetic caloric refrigerators have the potential to outperform conventional gas-cycle systems leading to a significant reduction in global electricity consumption [109].
Finally, perhaps the most interesting application, at least from the point of view of this work, is for quantum technologies. MNMs can be exploited to construct the elementary units of a quantum processor encoding the logical information of a quantum state into their magnetic states [103, 110–112]. The energy level spectrum, if properly engineered, can be well resolved and easily addressed by electromagnetic pulses. These systems can show very long decoherence times up to ~ 0.7 ms allowing coherent control and manipulation of the qubits [102]. All these features make MNMs promising candidates. Furthermore, the intrinsic quantum behaviour, together with the ability to form clusters of magnetically independent molecules, makes molecular nanomagnets excellent candidates also for quantum sensing applications [113].
Overall, molecular nanomagnets are highly relevant systems, both for the physical phenomena they exhibit and for their potential applications. In the following section 2.1, the Spin Hamiltonian formalism is introduced, allowing for the efficient description of MNMs. Subsequently, in Sec. 2.2, the physical properties relevant for Quantum Information Processing are discussed, and examples of molecules belonging to two classes are presented. In Sec. 2.3, the techniques with which MNMs can be controlled to manipulate their state are described. Section 2.4 explores the phenomenon of decoherence, investigating the mechanisms that generate it and the effects it induces on quantum states. Finally, section 2.5 discusses the implementation of embedded schemes of quantum error correction to protect the state of molecular spin qudits against decoherence.

2.1 The Spin Hamiltonian Approach

Molecular Nanomagnets (MNMs) are complex systems that involve many atoms, even for the smallest molecules. The magnetic properties of the core can be captured in principle by ab initio methods. These are usually computationally demanding and are not always reliable unless the strong correlations between magnetic electrons are properly accounted for [114]. In practice, the most convenient approach is to describe the core by an effective spin Hamiltonian (SH) whose parameters are fitted to experiments [115]. The SH formalism relies on the assumption, which is often reliable for these systems, that all magnetic ions composing the core can be described by an effective spin. Consequently, all energy contributions are expressed in terms of spin operators. When considering only the degrees of freedom of electronic spins, the spin Hamiltonian $\mathcal{H}_s$ for MNMs can be divided into three main terms:

$$\mathcal{H}_s = \mathcal{H}_{Ex} + \mathcal{H}_{ZFS} + \mathcal{H}_B \ . \tag{2.1}$$

The first one, $\mathcal{H}_{Ex}$, also known as the exchange term, represents a two-body interaction between core magnetic ions. In its most general form, the exchange interaction is as follows:

$$\mathcal{H}_{Ex} = \sum_{i>j} \mathbf{s}_i \cdot \mathbf{J}_{ij} \cdot \mathbf{s}_j \ . \tag{2.2}$$

Here, i and j are indices representing spin sites within the system, $\mathbf{s}$ denotes the spin operators, and $\mathbf{J}$ is the tensor that parametrizes the interaction. The specific form of this interaction, given by the structure of $\mathbf{J}$, determines the behaviour of the molecule and gives rise to many interesting phenomena. For example, giant-spin systems emerge when a leading isotropic interaction allows the whole molecule to be described by a single spin. This kind of systems has been proposed as the basis for memory devices due to their strong magnetic hysteresis.
To better understand the form of the interaction, it is often convenient to decompose it as:

$$\mathcal{H}_{Ex} = \mathcal{H}_{iso} + \mathcal{H}_{an} + \mathcal{H}_{DM} \ , \tag{2.3}$$

where

$$\mathcal{H}_{iso} = \sum_{i>j} \mathbf{J}_{ij} \cdot \mathbf{s}_i \cdot \mathbf{s}_j \tag{2.4}$$

$$\mathcal{H}_{an} = \sum_{i>j} \sum_{\alpha,\beta} \mathbf{J}_{ij}^{\alpha\beta} s_i^{\alpha} s_j^{\beta} \tag{2.5}$$

$$\mathcal{H}_{DM} = \sum_{i>j} \mathbf{G_{ij}} \cdot \mathbf{s_i} \times \mathbf{s_j} \ . \tag{2.6}$$

The first term, $\mathcal{H}_{iso}$, represents the isotropic interaction, characterized by $\mathbf{J}_{ij}$ being isotropic, i.e., equal in each spatial direction. The $\mathcal{H}_{iso}$ term is usually dominant in MNMs formed by transition metal ions. This term can be generated by direct coupling between magnetic ions or by indirect super-exchange interactions. When ions are too far apart to directly interact, a non-magnetic anion interposed between them can mediate an effective antiferromagnetic interaction.
The second term, $\mathcal{H}_{an}$, introduces possible anisotropies of the coupling tensor $\mathbf{J}_{ij}^{\alpha\beta}$ along different spatial orientation. In many cases, this term can be seen as a correction or perturbation of the dominating $\mathcal{H}_{iso}$ term. In the end, $\mathcal{H}_{DM}$ represents the anti-symmetric contribution, also known as the Dzyaloshinskii-Moriya Interaction (DMI), characterized by an anti-symmetric tensor $\mathbf{G_{ij}} = -\mathbf{G_{ji}}$.
Furthermore, $\mathcal{H}_{Ex}$ can also include a dipolar intra-molecular interaction. Indeed, the dipolar interaction has the same spin dependence as $\mathcal{H}_{Ex}$. This long-range interaction between magnetic ions acts at distances where all other couplings are suppressed. The interaction is often modelled using the point-dipole approximation [116]:

$$\left(J_{ij}^{\alpha\beta}\right)_{DIP} = \frac{\mu_B^2}{R_{ij}^3} \left[\sum_{\xi} g_i^{\alpha\xi} g_j^{\xi\beta} - 3 \frac{\left(\sum_{\xi} g_i^{\alpha\xi} R_{\xi}\right) \left(\sum_{\zeta} R_{\zeta} g_j^{\beta\zeta}\right)}{R_{ij}^2} \right] \ . \tag{2.7}$$

Here, ξ and ζ indicate the x, y, z components, μ_B is the Bohr magneton, R_{ij} is the distance between the i and j sites and $\mathbf{g}$ is the Landé factor. In the general case where $\mathbf{g}_i \neq \mathbf{g}_j$, the coupling constant $\left(J_{ij}^{\alpha\beta}\right)_{DIP}$ is not symmetric and comprises an isotropic, anisotropic, and anti-symmetric part.
Moving on, the second term in Eq. (2.1), $\mathcal{H}_{ZFS}$, called the zero-field splitting (ZFS), is a one-body term that describes how each ion perceives the global crystal field generated by all other ions:

$$\mathcal{H}_{ZFS} = \sum_i \mathbf{s}_i \cdot \mathbf{D}_i \cdot \mathbf{s}_i \tag{2.8}$$

This term can introduce strong asymmetries in the system. For example, it causes

the energy spectrum of an effective single-spin molecule with $S > 1/2$ to be non-equally spaced. The most frequently encountered form for this interaction is:

$$\begin{aligned} \mathcal{H}_{ZFS,i} &= D_i \left[(s_i^z)^2 - s_i(s_i+1)/3 \right] + \\ &+ E_i \left((s_i^x)^2 - (s_i^y)^2 \right) \end{aligned} \tag{2.9}$$

where, $D_i = D_i^{zz} - (D_i^{xx} - D_i^{yy})/2$ and $E_i = (D_i^{xx} - D_i^{yy})/2$.
Finally, the third term is the Zeeman interaction $\mathcal{H}_B$ that models the coupling of magnetic ions with an external static magnetic field:

$$\mathcal{H}_B = \mu_B \sum_i \mathbf{B} \cdot \mathbf{g_i} \cdot \mathbf{s_i} \tag{2.10}$$

Here, **B** is a vector that describes the orientation and magnitude of the external field. The Zeeman interaction resolves multiplet spin degeneracy and therefore it is crucial for quantum computing applications where a well-defined and resolved computational space is essential.

So far the discussion has focused solely on the electronic spin degrees of freedom, but this does not complete the picture. In fact, many ions also possess nuclear spins, and although these generally give a secondary contribution to the Hamiltonian, in some cases it is important to take them into account. As with the electronic spin Hamiltonian, a nuclear spin Hamiltonian $\mathcal{H}_{Nuc}$ is defined as composed of several terms that describe the interactions of nuclear spins with the electronic spins, among the nuclear spins themselves, and with the external magnetic field:

$$\mathcal{H}_{Nuc} = \mathcal{H}_{Hyp} + \mathcal{H}_{Qua} + \mathcal{H}_{Zee} \tag{2.11}$$

where

$$\begin{aligned} \mathcal{H}_{Hyp} &= \sum_i \mathbf{I}_i \cdot \mathbf{A}_{ij} \cdot \mathbf{s}_j \\ \mathcal{H}_{Qua} &= \sum_i \mathbf{I}_i \cdot \mathbf{U}_i \cdot \mathbf{I}_i \\ \mathcal{H}_{Zee} &= \mu_N \sum_i \mathbf{B} \cdot \mathbf{g_{I,i}} \cdot \mathbf{I}_i \end{aligned} \tag{2.12}$$

and **I** are the nuclear spin operators, μ_N is the nuclear magneton, and $\mathbf{g_I}$ denotes the nuclear g-factor. The first term $\mathcal{H}_{Hyp}$, historically known as the hyperfine interaction, describes the coupling between nuclear and electronic spins. The second term $\mathcal{H}_{Qua}$, characterized by the parameter **U**, is known as the quadrupole interaction. It accounts for the electrostatic interaction experienced by the nucleus within its local environment. While conceptually similar to the zero field

splitting seen in the electronic part, its magnitude is generally much smaller. The last term, the Zeeman interaction, operates in a similar manner as in the electronic case but due to the smaller value of the nuclear magneton μ_N compared to the Bohr magneton μ_B, its effect is significantly reduced.
In conclusion, the presented spin Hamiltonian approach provides a practical and effective formalism to model and describe the behaviour of MNMs. In the following section, several examples of molecular nanomagnets are presented exploring this formalism.

2.2 MNMs for Quantum Information Processing

Before introducing some examples of MNMs with potential applications for QIP, it is essential to define the key features and properties sought after.
As stated by the first DeVincenzo criterion 1.1.1, a candidate system must have some degree of freedom that can be harnessed for information storage and processing. In the case of MNMs, the magnetic states determined by the core spins are a suitable choice. These systems can exhibit several distinct and addressable energy states at low energy, providing an ideal platform. The energy gaps can be precisely addressed by electromagnetic pulses, allowing for precise data manipulation. Additionally, as anticipated in the introduction, the complex multi-level structure that many systems exhibit can also be exploited to encode qudits. As explained in 1.9, the qudit approach to quantum computation could bring several benefits especially for near-term applications. This feature distinguishes MNMs from most other more established technologies, for which a qudit approach may not be as natural or feasible.
Scalability is another crucial requirement stated by the first DeVincenzo criterion. To be truly scalable, an architecture must satisfy two fundamental prerequisites: the ability to create a large number of computational units, and the effective implementation of two-body quantum operations. The first condition is easily met. MNMs can be synthesized with good reproducibility, resulting in structures that are either completely equivalent or, in some cases, slightly inequivalent. Two promising strategies have emerged to implement two-body gates: supramolecular engineering and resonator integration [28, 117]. In the first case the different units are chemically linked forming supramolecular structures. In the second case, MNMs can be coupled within resonators, similar to the ones used with superconducting qubits. These possibilities are discussed in Sec. 2.3.2.
For effective quantum information manipulation and storage, an architecture must exhibit relatively long coherence times. The coherence time refers to the duration for which a quantum state remains intact before being severely cor-

rupted. Two critical parameters are considered: the relaxation time T_1, related to relaxation mechanisms, and the coherence time T_2, related partially to T_1, but mostly from pure dephasing (at least for MNMs). For MNMs at low temperatures (see 2.4 for more details), T_1 is generally much longer than T_2 and hence less relevant [118, 119]. T_2 values can span from a few to hundreds of micro seconds. Clearly, these values have to be considered in relation to the manipulation time, i.e. the time needed to implement an operation. For single-body operations, these values are generally quite short on the timescale of a few nanoseconds, operating with a driving field of the order of tens of Gauss. On the other hand, two-qudit gates could be more demanding, and depending on the method, they could take from tens to hundreds of nanoseconds (see 2.3).
Another interesting characteristic of MNMs is the possibility of chemical engineering molecules to control system properties [120]. This opportunity represents a key instrument to further develop this kind of architecture. An important part of this work actually focuses on designing a class of molecules that are intrinsically protected from decoherence(see Sec. 2.2.2).

In the following sections, specific examples of MNMs that align with these requirements are introduced. These systems will serve as models for the studies reported in the subsequent chapters, and they can be divided in two classes: single-ion molecules and multi-ion molecules. This categorization arises from both structural differences among these systems and the subsequent analyses of decoherence effects detailed in Sec. 2.4.

2.2.1 Single-Spin Molecules

The simplest class of systems that can be considered are the single-spin molecules (**S**), which include both mononuclear and polynuclear complexes that can be modelled by a single spin in the SH formalism (e.g., the giant spin molecules mentioned above). Considering only the electronic degrees of freedom and for simplicity assuming parallel axial anisotropy and magnetic field orientation, the spin Hamiltonian takes the form:

$$\mathcal{H}_S = DS_z^2 + g\mu_B B_0 S_z \ , \tag{2.13}$$

where D is the ZFS and B_0 the amplitude of magnetic field orientation along the z-axis. Examples of mononuclear systems include molecules composed of Cr^{3+}, Co^{2+}, Mn^{2+}, Fe^{3+}, Gd^{3+}, lanthanides, and actinides [77, 121–124].
Fig. 2.1 shows the energy level spectrum for a $S = 5/2$ like Mn^{2+} or Fe^{3+}. The computational space is potentially formed by all six levels. At $B = 0$, it's evident

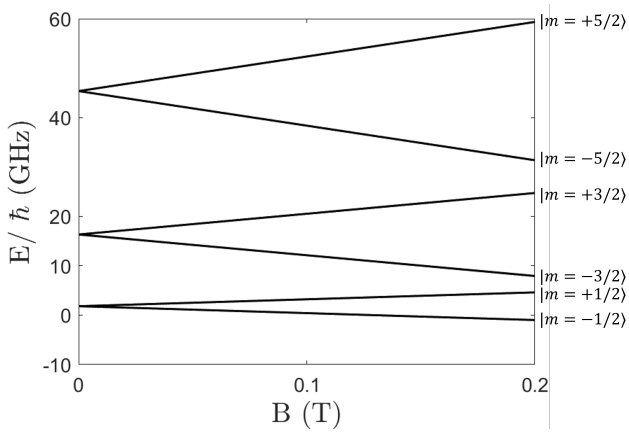

Figure 2.1: Energy spectrum as a function of the external magnetic field for a $S = 5/2$ as Mn^{2+} or Fe^{3+} parametrized by $D = 30$ μeV and $g = 2.0$.

the effect of the ZFS terms that shift levels into doublet with the same S_z^2. Applying an external magnetic field with a reasonable amplitude, for example $0.1 - 0.2$ T, all energy gaps between a couple of levels are well resolved. Typically, these gaps, which determine the control frequencies for single-body operations, are of the order of tens of GHz. Similar spectra can be obtained for the other mentioned systems.

2.2.2 Multi-Ion Molecules with Competing Interactions

The second class of molecules presented, multi-ion molecules with exchange interactions, is characterized by a magnetic core formed by multiple ions. Compared to the previous class, the spin Hamiltonian is more complex and thus generally of the form of Eq. (2.1). The low-energy spectrum cannot be mapped to that of an effective (giant) spin, like in 2.13.
The first molecule of this class introduced is a real system formed by three Cu^{2+} ions arranged in an almost isosceles triangle [125, 126] (**C**1). In the formalism of SH, the system is modelled as three interacting spin $s = 1/2$ as follows:

$$\mathcal{H} = \sum_{\substack{i,j=1 \\ j \neq i}}^{3} \left(\mathbf{J}_{i,j} \mathbf{s}_i \cdot \mathbf{s}_j + \mathbf{D}_{i,j} \cdot \mathbf{s}_i \times \mathbf{s}_i \right) + \mu_B \mathbf{B}_0 \sum_{i=1}^{3} \mathbf{g}_i \mathbf{s}_i \ . \tag{2.14}$$

A schematic representation of the molecule is reported in the inset of Fig. 2.2 panel a) where the three Cu ions ant their couplings are evidenced while in the background shows the complex ligands structure. The molecule is modelled considering an isotropic exchange interaction $J_{12} = 0.390$ meV, $J_{13} = J_{23} = 0.348$ meV

among ions, $g_1^{xx} = g_1^{yy} = 2.2$, $g_2^{xx} = g_2^{yy} = 2.1$, $g_3^{xx} = g_3^{yy} = 2.4$, $g_i^{zz} = 2.0$, and a DMI interaction parametrized by $D = 0.045$ meV oriented along bond directions (see [125] for details). The panel a) of Fig. 2.2 shows the energy spectrum as a function of the magnetic field. The field is directed in the xz plane forming an angle $\theta = 1$ rad with the z-axis. At low energy the system shows two doublets.

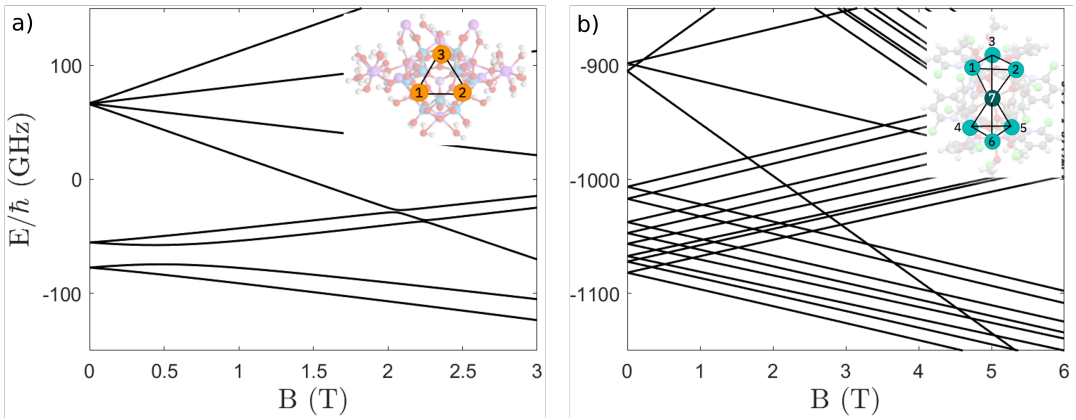

Figure 2.2: Energy level spectrum as a function of the external magnetic field for systems **C**1 (on the left) and **C**2 (right). The parameters of the systems are reported in the main text. Adapted from Ref. [127] under the terms of the Creative Commons Attribution 4.0 International license.

In first approximation, these doublets are made inequivalent and hence split by the difference between J_{12} and J_{13}. An anti-crossing emerges around 0.5 T, induced by the large Dzyaloshinskii-Moriya Interaction ($\sim J_{ij}/10$), which mixes the two multiplets. Across this region, m is no more a good quantum number. At higher energy, a $S = 3/2$ multiplet, which completes the system Hilbert space, is present.

The energy levels of the two doublets near the anti crossing region, for instance at $B \sim 0.8$ T, identify a potentially good subspace for the quantum computation. Indeed, this space offers two notable characteristics. Firstly, all levels within it have sizeable magnetic dipole matrix elements among each other. As investigated in chapter 5, this feature largely facilitates system external control for the implementation of single qudit operations. Secondly, this subspace is formed by two $S = 1/2$ doublets mixed and therefore S_z is $\leq 1/2$. This subspace, characterized by small local s_z values (even if not well defined), is more resilient to the effects of decoherence. This aspect will be explored in greater depth in section 2.4.

The peculiar features of this subspace derive from the almost degenerate ground state and the strong DMI interaction that mixes these levels. Furthermore, it is important to emphasise that the observations made are valid for a wide range

of parameters and that the gap values between the levels can be easily tuned by playing with the intensity and direction of the static field.
The second system presented is a hypothetical molecule specifically designed to extend the same properties of **C**1, i.e. a computational space highly connected and resilient against decoherence, but with a larger number of levels. The molecule, schematically represented in the inset of Fig. 2.2 panel b) has the same double-tetrahedron structure of the real Ni_7 system [128], and is described by the by the Hamiltonian:

$$H = \sum_{i>j} J_{i,j} \mathbf{s}_i \cdot \mathbf{s}_j + \sum_{i>j} D_{i,j}(s_i^x s_j^y - s_i^y s_j^x) + \mu_B B \sum_i g_i s_i^z, \tag{2.15}$$

where the six vertex are spin $s = 1/2$ while at the centre a spin $S = 3/2$ [127, 129] (now on referred as **C**2). Considering isosceles triangles at the base and on the top of the molecule with all vertices equally distant from the central ion and coupled by antiferromagnetic isotropic interactions, the energies are analytically computable. Indeed, the isotropic exchange is diagonal on the basis defined as $|S_{12}, S_{123}, S_{45}, S_{456}, S_{1-6}, S\rangle$ where $S_{12} = s_1 + s_2$, $S_{123} = S_{12} + s_3$, $S_{45} = s_4 + s_5$, $S_{456} = S_{45} + s_6$, $S_{1-6} = S_{123} + S_{456}$ and $S = S_{1-6} + s_7$. The energy levels are computed as

$$\begin{aligned} E(\{S_\alpha\}) &= (J_{12} - J_{13})\, S_{12}\, (S_{12}+1) \\ &+ J_{13}\, S_{123}\, (S_{123}+1) \\ &+ (J_{45} - J_{46})\, S_{45}\, (S_{45}+1) \\ &+ J_{46}\, S_{456}\, (S_{456}+1) \\ &+ J_{17}\, [S(S+1) - S_{1-6}(S_{1-6}+1)] \end{aligned} \tag{2.16}$$

where $J_{13} = J_{23}$, $J_{46} = J_{56}$ and $J_{17} = J_{27} = J_{37} = J_{47} = J_{57} = J_{67}$. It is easy to identify a parameter range where at low energy the system displays several energy doublets [129] (see Fig. 2.3).
A completely regular molecule would present degenerations. Small anisotropies in the parameters break the symmetries of the system and thus resolve the entire spectrum. This is the common scenario observed in real systems, which tend to be somehow irregular, and this is exactly what is aimed to obtain.
Assuming that the molecule is composed of six Cu^{2+} (s_{1-6}) and a Cr^{3+} (s_7) ions in a distorted octahedral crystal-field environment, a reasonable choice is set the exchange coupling $J_{i7} = 0.95$ meV, $J_{12} = 1.29$ meV, $J_{23} = J_{31} = 1.25$ meV, $J_{45} = 1.41$ meV, and $J_{56} = J_{64} = 1.36$ meV, isotropic g factors $g_1 = g_2 = g_4 = g_5 = 2.1$, $g_3 = g_6 = 2.15$, and $g_7 = 2$ and an axial component of DMI $G_{ij} = J_{ij}/10$ along z axis [127]. The molecule is designed taking into account small irregularities that would be more likely to occur in a real system. Figure 2.2 panel b) shows the

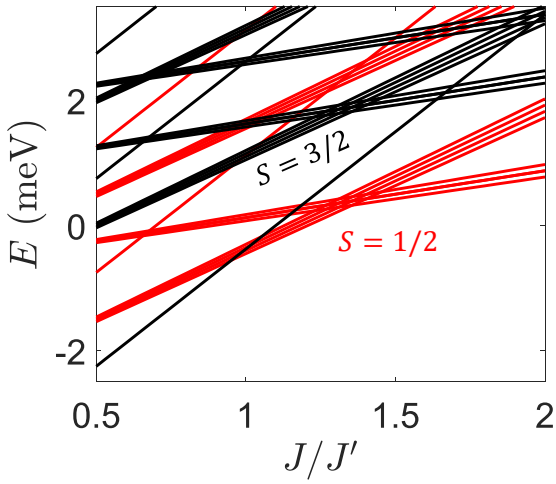

Figure 2.3: Energy level spectrum of a regular double tetrahedron with exchange interaction as a function of the ratio between the inner triangles J and the triangles to the central coupling constant J'. Adapted from Ref. [129] under the terms and conditions of the Creative Commons Attribution license (CC-BY 4.0)

energy level spectrum for the above system under the influence of an external magnetic field directed along the z axis. Fixing the external field at $B = 2.7$ T, a possible computational space is formed by the eight $m = -1/2$ levels together with the lowest $m = +1/2$ state. The computational space has a connectivity by pod schemes (see sections 1.9), which provides an advantageous way to decompose into pulses single qubit gates.
It is important to stress that the specific choice of parameters is not strictly determinant to obtain a similar spectrum. If the order of magnitude of the interactions is respected, a whole range of suitable choices is available.

2.3 Control and Manipulation of MNM Qudits

The control and manipulation of MNM computational units rely on the principles of magnetic resonance [130]. These techniques of spectroscopy exploit the interaction between the magnetic moments of spins (either electronic or nuclear) and an external magnetic field. Targeting the system with external electromagnetic radiation changes its state and, consequently, the information encoded in it. Commonly, the driving field $b_1(t)$ is oriented perpendicular to the direction of the static field B_0 (along the x or y axis) and the Hamiltonian that describes this

interaction takes the form

$$\mathcal{H}_1 = \mu_B \varepsilon_x(t)(g_x S_x \cos(\omega t + \phi_0) + g_y S_y \sin(\omega t + \phi_0)) \ , \tag{2.17}$$

where $\varepsilon(t)$ contains the time modulation of the pulse amplitude. For example, for a rectangular pulse, $\varepsilon(t) = \Theta(\tau - |t - t_0|)$, where Θ is the step function, while for a Gaussian-shaped pulse, $\varepsilon(t) = e^{-(t-t_o)^2/2\sigma^2}$. In single spin molecules, the S_x and S_y operators have matrix elements among states with $\Delta m = \pm 1$, and therefore induce transitions only between nearby levels. In multi-spin systems, where several interactions compete, these matrix elements have a much more general structure, and thus the connectivity between levels can be more complex, allowing operations among more levels.
In this section, different control techniques to implement single- (Sec. 2.3.1) and two-body gates (Sec. 2.3.2) are introduced.

2.3.1 Single Object Manipulation

While a general single-qudit gate is represented by a $SU(d)$ matrix [79], for practical implementations it is often more convenient to express them in terms of simpler operation in a 2×2 subspace. This approach simplifies basic operation definition and aligns with the practical implementation feasibility. In this context, here, it is illustrated how to implement rotations between pairs of states around the x or y axis, known as Planar rotations, and rotations around the z axis (direction of the applied field), known as Phase Gates.
Typically, these operations are performed using a driving field perpendicular to the direction of the static field, at a frequency that is resonant (or semi-resonant) with the target transition. Depending on the characteristic energies of the system and on the external magnetic field applied, these can vary from MHz for nuclear spins to GHZ for electronic spins.
To ensure an accurate control of the system, it is necessary that all involved transitions are well resolved. The transitions are primarily made inequivalent by zero-field splitting or quadrupole terms for electronic and nuclear spins, respectively. The required degree of separation to minimize leakage depends on the control techniques employed. Various techniques have been developed in this field, significantly enhancing control possibilities. This aspect is partially addressed in Chapter 3.

Planar Rotation

Consider a multi-level quantum system with two eigenstates, $|\mu\rangle$ and $|\nu\rangle$, having energies E_μ and E_ν, respectively. A single driving field, oriented along the x

direction with a frequency of $\frac{E_\mu - E_\nu}{h}$, induces a transition between these states, expressed as:

$$\begin{aligned} U_{\mu\nu}(\theta,\beta) = &\cos(\theta/2)\left(|\mu\rangle\langle\mu| + |\nu\rangle\langle\nu|\right) \\ &+ \sin(\theta/2)\left(|\nu\rangle\langle\mu|e^{i\beta} - |\mu\rangle\langle\nu|e^{-i\beta}\right) \\ &+ \sum_{\ell\neq\mu,\nu} |\ell\rangle\langle\ell| \quad . \end{aligned} \tag{2.18}$$

This operation represents a Givens rotation, also known as a planar rotation in the context of optimal pulse control, between qudit levels $|\mu\rangle$ and $|\nu\rangle$, while the rest of the subspace is unaffected [127]. If the driving field is oriented along the y-axis, the resulting operation is similar but with an additional phase $\beta = \pi/2$. The rotation angle θ and the phase β can be precisely adjusted by tuning the pulse amplitude, duration, and initial phase. For a rectangular-shaped pulse linearly polarized along x, such as $b_1 = B_1\cos(\omega\, t + \phi_0)\,\Theta(\tau - |t - t_0|)$, the pulse duration and phase are determined as follows:

$$\tau = \left|\frac{\theta\hbar}{\mu_B B_1 g_x S_x(\mu,\nu)}\right| \tag{2.19}$$

$$\beta = \phi_0 \ , \tag{2.20}$$

where θ is the rotation angle. For a Gaussian-shaped pulse, a renormalization factor of $\sqrt{\pi/2}$ needs to be considered for the duration. A rotation with $\theta = \pi$ is also known as a π pulse. Its effect is equivalent to the exchange of the two levels (up to a global phase). As explained in Sec. 1.9, this operation is a sort of a SWAP gate and is employed to connect levels that are not directly linked.

Phase Gate

Another type of elementary operation is a Phase gate, defined as:

$$\begin{aligned} P_{\mu\nu}(\alpha) = &|\mu\rangle\langle\mu|e^{i\alpha} + |\nu\rangle\langle\nu|e^{-i\alpha} \\ &+ \sum_{\ell\neq\mu,\nu} |\ell\rangle\langle\ell| \quad . \end{aligned} \tag{2.21}$$

This operation introduces a relative phase between levels $|\mu\rangle$ and $|\nu\rangle$ while leaving the rest of the space untouched. It can be implemented in two ways. The first strategy involves two consecutive π pulses among the target levels, with a different initial phase. The desired phase α should equal the difference between the phases of the two pulses.
An alternative strategy is to use a semi-resonant pulse:

$$G = \frac{\mu_B B_1 |M_x(\mu,\nu)|}{2\hbar} \qquad \tau = \frac{\pi}{\sqrt{G^2 + \Delta^2/4}}$$
$$\Delta = \frac{2G(\pi - \alpha)}{\alpha\sqrt{2\pi - \alpha}} \qquad \omega' = \omega_{\mu,\nu} \pm \Delta \tag{2.22}$$

Here, α is the expected phase ($-\pi < \alpha < \pi$), Δ is the frequency detuning, τ is the pulse duration, and ω' is the detuned frequency. The $\pm$ sign depends on the sign of α. The absolute value of Δ is minimum and equal to zero for $\alpha = \pi$, resulting in a relative phase of 2π. The duration of the detuned pulse approaches zero as α approaches zero. This implementation strategy is faster than the previous scheme, although it requires more advanced control techniques.

2.3.2 Scaling up the architecture

A crucial aspect for constructing a scalable architecture is the development of a method to design switchable two-body entangling gates. One potential strategy involves chemically linking two molecular units, denoted as Q_1 and Q_2, through an interposed spin-1/2 qubit (now switch Sw, see Fig. 2.4). This ancillary qubit effectively mediates an interaction between Q_1 and Q_2. The Hamiltonian for the composite system can be outlined as follows:

$$\mathcal{H}_{tot} = \sum_{\substack{i=Q_1,\\ Q_2,Sw}} \mathcal{H}_i + \mathcal{H}_{Q_1,Sw} + \mathcal{H}_{Q_2,Sw} \ . \tag{2.23}$$

Here, $\mathcal{H}_i$ are the Hamiltonians of the three separate objects, while the last two terms $\mathcal{H}_{Q_{1/2},Sw} = J_i \mathbf{S}_i \cdot \mathbf{S}_{Sw}$ are the spin-spin interaction between the qudits and the switch assumed to be isotropic. It is essential to highlight that utilizing a qubit to mediate couplings between qudits provides a crucial advantage compared to having two permanently interacting qudits. Indeed, in this way the coupling can be dynamically turned on and off. In other words, the linker acts as a switch of the effective interaction between the computational units. To ensure the proper functioning of the switch, qudit and switch states must be almost factorized; i.e. the eigenstates have to be close to $|\mu_1, m_{Sw}, \mu_2\rangle \cong |m_1\rangle\,|m_{Sw}\rangle\,|m_2\rangle$. This conditions implies that the coupling J_i cannot be too large and in particular it has to be significantly smaller than the difference between switch and qudit energy gaps. However, on the other hand, the duration of two-body gates depends on the coupling strength, and a stronger coupling would enable faster manipulations (see section below). Hence, a suitable compromise between these two conditions must be found.

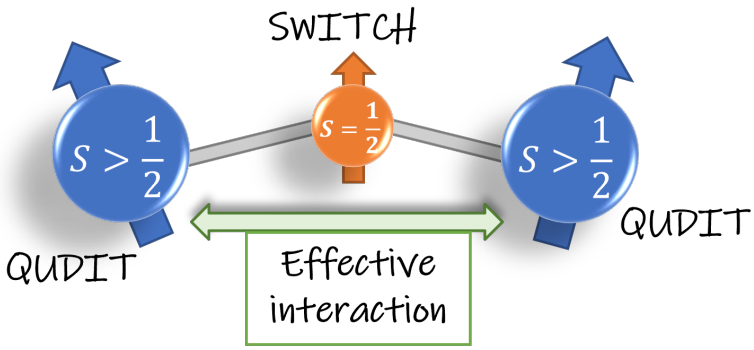

Figure 2.4: Simplified illustration of the fundamental hardware $Q_1 - Sw - Q_2$ configuration. The central qubits serves as a switch of the effective interaction between the qudits.

In a first approach this elementary unit could be extended as a mono dimensional chain of alternating inequivalent molecules [28, 131]. More complex connectivity schemes could be reached creating supramolecular structures.

However, this type of approach is more likely to offer a realistic perspective only for hardware of a limited size. A recent proposal suggests coupling Molecular Nanomagnets (MNM) computational units through resonators as an alternative strategy to scale up the architecture [103, 117]. This approach offers the advantage of leveraging technologies already developed for superconducting qubits. Since now, the limited coupling of single molecules with resonators has posed challenges to this approach, but advancements in technology are narrowing this gap, creating new possibilities. However, this approach is not investigated in this work and therefore will not be discussed in more details.

2.3.3 Two Qudit Gates

Starting from the Q-Sw-Q architecture presented above, the following sections show how to implement three two-body gates, namely a generalized Controlled-Phase (CPhase), a generalized XY and the M-gate (defined below).

Qudit controlled-phase gate

The generalized Controlled Phase gate is defined as follows:

$$\mathrm{CPhase}(\bar{\varphi}) \quad = \quad \sum_{\mu_1,\mu_2=1}^{d} e^{-i\varphi_{\mu_1,\mu_2}} \left|\mu_1,\mu_2\right\rangle\!\left\langle\mu_1,\mu_2\right|, \tag{2.24}$$

Its action is to introduce a distinct phase φ_{μ_1,μ_2} to each two-qudit state of the product space where μ_i identify the eigenstates of the two qudits. In practice this gate can be implemented by conditionally exciting the switch with 2π pulses depending on the state of both qudits. These pulses bring the switch in the excited state and thus turn on the effective interacting among qudits. This interaction is originated by the $\mathcal{H}_{Q_i,Sw}$. The different transitions are selectively addressable thanks to the interaction $\mathcal{H}_{Q_i,Sw}$ that makes excitation transition of the switch $\delta(\mu_1,\mu_2)$ dependent on the state of both qudits. In the case of **S** this can be easily computed to first order, finding:

$$\delta(\mu_1,\mu_2) = g_{Sw}\mu_B B_0 + J_1 m_1 + J_2 m_2 \tag{2.25}$$

where m_i are the eigenvalues of S_i^z. Hence, all the gaps are distinguishable, provided that J_i^z are significantly larger than the frequency broadening of the employed pulses. The implementation of each operations (one for each phase φ_{m_1,m_2}) involves the excitation and de-excitation the state of the switch addressing the transition $|m_1,\downarrow,m_2\rangle \longleftrightarrow |m_1,\uparrow,m_2\rangle$ (green arrows in Fig.2.5). A 2π pulse,

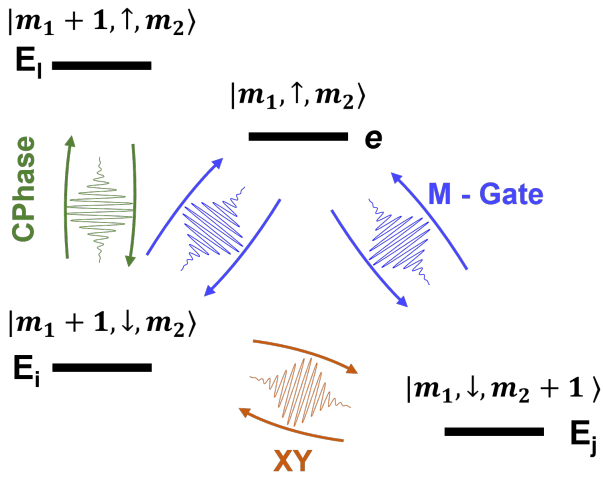

Figure 2.5: Two-qudit gates connectivity scheme. Green, blue and brown arrows identify the transition to target to implement Cphase, XY and M- gate respectively. Qudit eigenstates are assume to be diagonal in S_z basis.

i.e. a complete transfer and return, implemented by a resonant pulse perpendicular to the static magnetic field direction, introduces a phase π [132–135]. Arbitrary phases can be induced by a proper detuning (offset from resonance

frequency) and consequent adjustment of the pulse duration as follows:

$$\begin{aligned}\Delta &= \mathrm{sgn}(\varphi)\frac{2\Omega(\pi-|\varphi|)}{\sqrt{|\varphi|(2\pi-|\varphi|)}}\\ \tau &= \frac{\pi}{\sqrt{\Omega^2+\frac{\Delta_i^2}{4}}}\end{aligned}, \tag{2.26}$$

where Ω represents the Rabi frequency of the addressed transition, *sgn* is the sign function, and Δ is the frequency detuning. In principle, all the $\bar{\varphi}$ phases can be implemented in parallel, involving up to d^2 simultaneous frequencies (considering two d-dimensional qudits).
Fig. 2.6 left panel shows how the population evolves during the implementation of a single phase π on the level $|m_1,\downarrow,m_2\rangle$. The manipulation works on two levels, $|m_1,\downarrow,m_2\rangle$ (yellow), which belongs to the computational space, and $|m_1,\uparrow,m_2\rangle$ (blue), which is outside the computational space. All other levels remain idle (not shown in the figure). As can be seen from the curves, the population is first transferred to the auxiliary level and then brought back, thus acquiring the desired phase. For angles different from π, semi-resonant pulses are used, which induce a partial population transfer.
The CPhase gate is particularly useful also because it efficiently decomposes other gates like the qudit SWAP gate [136]. This letter is the extension of the qubit SWAP gate and can be decomposed into three generalized control phase gates and a few single qudit gates. The action of this gate is to exchange the states of two qudits and it is often crucial in algorithm implementation due to device connectivity constrictions.

Qudit XY gate

The qudit XY gate is defined as follows:

$$\begin{aligned}\mathrm{XY}_{\mu_1,\mu_2,\mu_1',\mu_2'}(\theta) &= \cos(\theta/2)\left(|\mu_1,\mu_2\rangle\langle\mu_1,\mu_2| + \left|\mu_1',\mu_2'\right\rangle\left\langle\mu_1',\mu_2'\right|\right)\\ &+ i\sin(\theta/2)\left(\left|\mu_1',\mu_2'\right\rangle\langle\mu_1,\mu_2| + |\mu_1,\mu_2\rangle\left\langle\mu_1',\mu_2'\right|\right)\\ &+ \sum_{(p,q)\neq(\mu_1,\mu_2),(\mu_1',\mu_2')} |p,q\rangle\langle p,q|,\end{aligned} \tag{2.27}$$

The definition of this qudit operation is an extension of the qubit YX gate defined in 1.14. Indeed, similarly to the XY qubit gate, the action of this transformation is to partially exchange the states involved ($|\mu_1,\mu_2\rangle$ and $|\mu_1',\mu_2'\rangle$), while introducing a phase i. All the rest of the space is left unchanged.

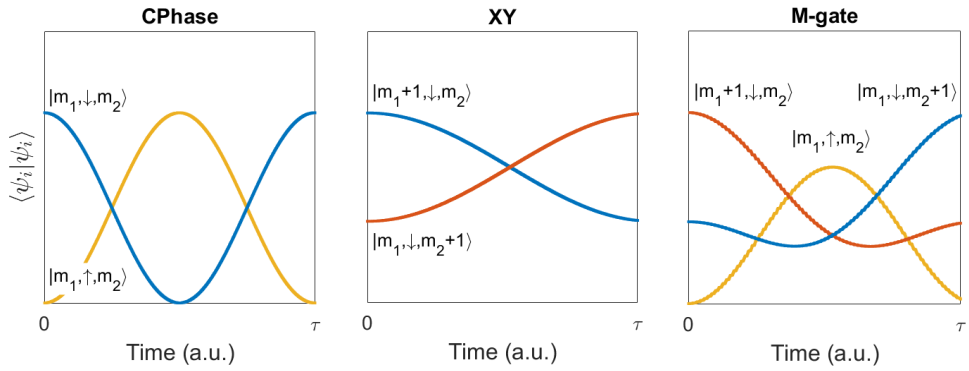

Figure 2.6: Simulated time evolution of the components of the two-qudit wave function during the implementation of the CPhase(π) (left), XY(π) (center), and M(π) (right) gates. Only the levels actively involved in the operations are shown. These are labelled by the local expectation values of S_z, assuming an underlying system diagonal on S_z basis.

On the considered architecture, the qudit XY gate can be induced by a driving field oriented along the direction of the static field (z-axis for convention) with a frequency resonant with the energy gap between the levels. This transition can only be induced between pairs of levels E_{m_1,m_2} and $E_{m_1',m_2'}$ that have the same $m_1 + m_2 = m_1' + m_2'$ and have differences between local spin operators ≤ 1 [133, 135]. In other terms, any pair satisfying the relation $E_i = |m_1 + 1, \downarrow, m_2\rangle \longleftrightarrow E_j = |m_1, \downarrow, m_2 + 1\rangle$ is suitable [133] (brown pulse in Fig. 2.5). The mechanism by which this operation is generated can be interpreted by describing the global Hamiltonian as consisting of a leading term $\mathcal{H}_0$, which includes all the single-body terms and only the J^z part of the qudits-switch couplings, and by a perturbation term $\mathcal{H}_1$, which includes the $J^{x,y}$ components of the couplings. On the basis of S_z, the eigenstates of $\mathcal{H}_0$ are perfectly factorized. Moving to the rotating frame, the affect of an external driving field along z-axis resonant with the energy gap $E_{m_1,m_2} - E_{m_1',m_2'}$, is to compensate this gap, making the two states energetically degenerate [132, 135, 137]. Finally, the transverse coupling, which mixes the eigenstates, induces the transition. Alternatively, this mechanism can be described in the total Hamiltonian basis $\mathcal{H}_0 + \mathcal{H}_1$ on which the eigenstates are almost but not perfectly factorized on the S_z basis. Hence, the eigenstate identified by $|m_1 + 1, \downarrow, m_2\rangle$ actually contains a small component of even $|m_1, \downarrow, m_2 + 1\rangle$ and vice versa. So these eigenstates are connected by S_z and applying the driving field induces the transition. It is important to note that this type of mechanism is allowed only if there is a transverse coupling in the Hamiltonian $J^{x,y} \neq 0$.

The gate duration τ is proportional to $\propto \frac{\theta}{(J^{x,y})^2 B_1}$. Since the coupling constant $J^{x,y}$ must be small for the states to be nearly factorized, these gates are generally slow. The rotation angle is linearly proportional to the pulse duration. Therefore, by calibrating the duration τ, any angle θ can be realized. This operation can be implemented in parallel on several couple of levels that fulfil the before mentioned condition. For example, considering two single spin $S = 3/2$ qudits, three possible couple are $|-3/2,-1/2\rangle \leftrightarrow |-1/2,-3/2\rangle$, $|-1/2,1/2\rangle \leftrightarrow |1/2,-1/2\rangle$ and $|3/2,1/2\rangle \leftrightarrow |1/2,3/2\rangle$,
In the central panel of Fig. 2.6, an example of the population evolution during the implementation of XY(π) between the levels $|m_1+1,\downarrow,m_2\rangle \longleftrightarrow |m_1,\downarrow,m_2+1\rangle$ is illustrated. It's worth noting that only the relevant levels participate in this operation, and there are no auxiliary levels involved. In the case shown, an XY(π) gate is demonstrated. However, by adjusting the pulse duration, one can achieve a general rotation angle.

Qudit M-Gate

The M-gate is defined as follows:

$$\begin{aligned} \mathrm{M}_{\mu_1,\mu_2,\mu_1',\mu_2'}(\theta) &= \cos(\theta/2)\left(|\mu_1,\mu_2\rangle\langle\mu_1,\mu_2| - \left|\mu_1',\mu_2'\right\rangle\left\langle\mu_1',\mu_2'\right|\right) \\ &+ i\sin(\theta/2)\left(-\left|\mu_1',\mu_2'\right\rangle\langle\mu_1,\mu_2| + |\mu_1,\mu_2\rangle\left\langle\mu_1',\mu_2'\right|\right) \\ &+ \sum_{(p,q)\neq(\mu_1,\mu_2),(\mu_1',\mu_2')} |p,q\rangle\langle p,q|, \end{aligned} \tag{2.28}$$

which is very similar to the XY gate apart from a phase. Indeed, combining this procedure with a CPhase gate of π angle a standard XY is obtained $\mathrm{XY}_{\mu_1,\mu_2,\mu_1',\mu_2'}(\theta) = \mathrm{CPhase}_{\mu_1',\mu_2'}(\pi)\mathrm{M}_{\mu_1,\mu_2,\mu_1',\mu_2'}(\theta)$. This transformation can be implemented by exploiting the Quantum Householder Reflection (see 1.9.2). This procedures requires the pod-system connectivity, i.e. a computational space where all levels are connected with an ancillary level (see Fig. 5.1). In presence of a transverse coupling $J^{x,y}$, this connectivity can be achieved among terns of levels of the form $|m_1+1,\downarrow,m_2\rangle \longleftrightarrow |m_1,\uparrow,m_2\rangle \longleftrightarrow |m_1,\downarrow,m_2+1\rangle$, where the $|m_1,\uparrow,m_2\rangle$ state serves as the auxiliary level. Like the XY gate, this transformation can be applied to several pairs of levels in parallel. The mechanism by which the transformation is generated is substantially the same described for XY gate. The transformation employs pulses along the static field axis (z-axis for convention) that induce a transition between pairs of levels with $m_1 + m_2 = m_1' + m_2'$. However, unlike before, in this case two simultaneous pulses are used and an auxiliary level outside the computational space is involved in the operation. As depicted

in Fig. 2.5, this triplet of levels form a pod system. Utilizing the quantum householder reflection to calibrate the pulse amplitudes, phases and detuning, similarly as done in 5.1.2 for single qudit gates, the M-gate is implemented [127, 138]. More in general, this procedure can be exploited to decompose any unitary transformation (in this case only among a couple of levels). Often, this procedure requires a controlled-phase gate to corrected a phase. In other words, this procedure together with a final CPhase gate implement any two-qudit gate among a couple of levels.

In the right panel of Fig. 2.6, an example of the population evolution during the implementation of M(π) between the levels $|m_1+1,\downarrow,m_2\rangle \longleftrightarrow |m_1,\downarrow,m_2+1\rangle$ is illustrated. The operation requires an auxiliary level $|m_1,\uparrow,m_2\rangle$, actually active during the gate implementation. In the case in figure, a M(π) gate is represented, but by adjusting the control parameters of the pulses different operations can be realized.

2.3.4 Initialization and Readout

The initial step in implementing any algorithm involves initializing the architecture in a fiducial state [19]. The fiducial state must be created with high fidelity and, ideally, quickly to enable "runtime" applications. The term "runtime" refers to a procedure implemented during the execution of an algorithm. Many algorithms, such as quantum error correction ones, require ancillary qubits (or qudits) for measurements on the system, necessitating frequent re-initialization.

The most straightforward method to initialize Molecular Nanomagnets (MNMs) is by cooling to low temperatures, typically $\lesssim 10$ mK [103, 117]. While this experimental approach yields good approximations, it often takes a considerable amount of time (longer than the system coherence time) and is unsuitable for "runtime" initialization. An alternative approach is optical initialization, as demonstrated experimentally on a chromium ion Cr^{4+} [139]. This method exploits optical transitions present in certain molecular systems, precisely addressable by laser pulses. However, it is worth noting that this approach has been recently proposed and requires additional time for development. A third perspective involves utilizing the Chiral Induced Spin Selectivity effect (see Chapter 7) for initialization [140–142]. Further details on this possibility can be found in Chapter 7.

During or at the end of the execution of a quantum algorithm, a "readout" procedure is conducted to provide access to the state of the quantum processor. Various types of measurements exist in quantum mechanics, but for most applications and algorithms, the measurement has to be projective [10]. Additionally,

each logical unit must be individually addressable. As extensively discussed in previous sections, a key feature that distinguishes molecular nanomagnets from most of the other technologies is the fact that these systems can be exploited to encode qudits. In this context, a measurement no longer has to distinguish between just two states but rather among d states in general. Like any other manipulation procedure, to maximize effectiveness it is essential to do it quickly, so as to limit decoherence, and accurately.
In this context, two potential strategies for measuring the state of a molecular nanomagnet-based quantum processor are introduced, both leveraging spin strongly coupled to cavity photons. These strategies operate in either a dispersive or resonant regime [103, 143].
Each regime has distinct advantages and disadvantages and depending on the experimental set-up any of these may or may not suit better. Here's a concise overview of them.

- **Dispersive regime**: In the dispersive regime, the condition is that the two quantum systems are energetically detuned from each other. The resonator-spin coupling causes the resonance frequency of the cavity to conditionally shift depending on the spin's state. The frequency shift goes proportional to the square power of the dispersive qudit-resonator coupling. By detecting the transmission frequency, it is possible to discern among the various spin states. The dispersive procedure gives a non-demolition measurement [144, 145]. The readout fidelity, i.e. the precision with which the procedure is implemented, depends on the degree to which shifted frequencies can be distinguished. Factors such as resonator losses and spin dephasing lead to the broadening of the resonance peaks, and thus limit the accuracy of the procedure. In particular, in order to be able to discern them, the broadening must be smaller than the gaps among them.

  Due to the limited spin-resonator coupling, the operational time for this approach, in the case of single molecules, can be relatively slow (on the order of μs). Considering the long T_1 times exhibited by these systems at low temperatures, this is not a significant limitation unless measurement-dependent operations are present in algorithms. The protocol can be extended to qudits [145].

- **Resonant Regime**: The fundamental difference with respect to the dispersive regime is that the frequency shift is proportional to the qudit-resonator coupling. This allows to target one particular transition at a time and thus implementing a projective measurement. Considering the case of a qubit

for simplicity, this is done by exploiting a field resonant with the transition $|0\rangle \leftrightarrow |1\rangle$. In this way, the cavity is brought into resonance with the qubit transition. If the system is in the excited state $|1\rangle$, it is induced to decay to the lower energy state $|0\rangle$ and a photon is emitted. By detecting the emitted photon with a single-photon counter, the state of the qubit can be determined. In case of a positive measurement, the original state $|1\rangle$ can be restored by applying a classical drive that rotates the qubit state. The same procedure can be extended to the qubit case by addressing multiple energy gaps simultaneously.

Compared to the dispersive regime, this approach provides a significant speedup and consequently a significant enhancement of readout fidelity. Indeed, even considering large size qudits, the operational time can be estimated to be a few hundreds of nano-seconds [103, 146].

In conclusion, resonant and dispersive readouts are two possible methods to access to qudits states. Dependently form the experimental set-up and the specific application one or the other could be more advantageous.

2.4 Modelling of Decoherence in MNMs

The quantum nature of the wave-function makes it inherently sensitive and fragile to interaction with the environment. Thus, one of the greatest challenges for quantum architectures is to be resilient to decoherence. As mentioned in the introduction of section 2.2, this term encompasses two different phenomena generated from two different mechanisms. The first one is thermal relaxation, which leads to the decay of both diagonal and off-diagonal elements of the density matrix. The second mechanism is pure-dephasing, which at low temperature is due the interaction of the qudit spins with the surrounding nuclear spin of the molecule's organic ligands and leads to the decay of the off-diagonal elements of the density matrix and hence to the loss of coherence between quantum states. In the working conditions of a hypothetical molecular hardware, relaxation mechanism is negligible with respect to pure dephasing. Indeed, as demonstrated by several experimental studies [147–149], at low temperatures $\sim 1 - 5$ K and considering a computational subspace composed by a group of states close in energy, i.e. with energy gaps much smaller than the Debye energy (~ 50 K), both phonon absorption and emission are suppressed. Thus the relaxation time T_1 is several orders of magnitude longer than the dephasing time T_2. Therefore in this work the focus is on pure-dephasing mechanisms.
The most complete treatment of this phenomenon would require the simulation

of the spin bath dynamics by many-body methods [118]. However, this approach is very expensive and it is often not necessary to capture the heart of the problem. In the section below, a simplified description is introduced capable of capturing the origins and effects of the mechanism, but greatly simplifying numerical studies. Subsequently, the cases of the two classes of molecules presented above are analysed and compared.

2.4.1 Derivation of the Master Equation

As mentioned before, pure-dephasing is generated by the interaction of the magnetic core ions with the nuclear spin of surrounding ligands. This kind of process can be modelled considering the main system S, composed of the magnetic ions immersed in a bath B of nuclear spins [101, 118, 150, 151]. The whole system Hamiltonian can be divided into three terms $\mathcal{H} = \mathcal{H}_S + \mathcal{H}_B + \mathcal{H}_{SB}$ where $\mathcal{H}_S$ and $\mathcal{H}_B$ are respectively the free Hamiltonians of the system and the bath and $\mathcal{H}_{SB}$ depicts the system-bath interaction [129]. The latter is formulated as:

$$\mathcal{H}_{SB} = \sum_{j=1}^{N_i} \sum_{n=1}^{N_s} \sum_{\alpha,\beta=x,y,z} d_{jn}^{\alpha\beta} s_j^{\alpha} \otimes I_n^{\beta}, \tag{2.29}$$

where $j = 1,\dots,N_i$ and $n = 1,\dots,N_s$ are respectively the indices of the magnetic ions and of the nuclear spins in the bath, s_j^{α} are the ion spin operators, and I_n^{β} are the bath nuclear spin operators. Ultimately, $d_{jn}^{\alpha\beta}$ are the dipolar coupling parameters which in the point-dipole approximation are defined as:

$$d_{jn}^{\alpha\beta} = \frac{\mu_B \mu_N g_N}{R_{jn}^3} \left[g_j^{\alpha\beta} - 3 \frac{R_{jn}^{\beta} (\sum_{\gamma} g_j^{\alpha\gamma} R_{jn}^{\gamma})}{R_{jn}^2} \right], \tag{2.30}$$

where g_N and μ_N are the nuclear $g-$factor and magneton constant, $g_j^{\alpha\beta}$ is the ion g-factor and R_{jn}^{α} is the distance between the j-th electronic spin and the n-th nuclear spin along the α-axis.
Moving into the interaction picture of the free Hamiltonians $\mathcal{H}_S + \mathcal{H}_B$, $\mathcal{H}_{SB}$ is rewritten as:

$$\begin{aligned} \mathcal{H}_{SB}(t) &= e^{i(\mathcal{H}_S+\mathcal{H}_B)t} \mathcal{H}_{SB} e^{-i(\mathcal{H}_S+\mathcal{H}_B)t} \\ &= \sum_{n=1}^{N_s} \sum_{\mu\nu} \sum_{\beta} L_{n,\mu\nu}^{\beta} e^{i(E_\mu - E_\nu)t} |\mu\rangle \langle\nu| \otimes I_n^{\beta}(t) \quad . \end{aligned} \tag{2.31}$$

Here, $|\mu\rangle$ and $|\nu\rangle$ are eigenstates of $\mathcal{H}_S$ and E_μ, E_ν their respective energies, and $L^{\beta}_{n,\mu\nu}$, which incorporates the dependence from the eigenstate structure $\langle\mu|\, s^{\alpha}_{j}\, |\nu\rangle$, is defined as follows:

$$L^{\beta}_{n,\mu\nu} = \sum_{j=1}^{N_i} \sum_{\alpha=x,y,z} d^{\alpha\beta}_{jn} \langle\mu|\, s^{\alpha}_{j}\, |\nu\rangle \quad . \tag{2.32}$$

Defining the system partial density matrix as $\rho(t) = \mathrm{tr}_B[\rho_{SB}(t)]$, its time evolution under Born and Markovian approximations can be calculated as :

$$\dot{\rho}(t) = -\int_0^{\infty} dt' \mathrm{tr}_B[\mathcal{H}_{SB}(t), [\mathcal{H}_{SB}(t-t'), \rho(t)\otimes\rho_B]] \quad . \tag{2.33}$$

At this point, replacing the expression (2.31) into Eq. (2.33) and considering the secular approximation, it follows:

$$\begin{aligned} \dot{\rho}(t) \quad = -\sum_{n,n'=1}^{N_s} \sum_{\mu,\nu} \sum_{\beta\beta'} \Big\{ & L^{\beta}_{n,\mu\mu} L^{\beta',*}_{n',\nu\nu} \\ & \chi^{\beta\beta'}_{nn'}(\omega) \Big[|\mu\rangle\langle\mu|\nu|\mu|\nu\rangle\langle\nu|\rho(t) - |\mu\rangle\langle\mu|\rho(t)|\nu|\mu|\rho(t)|\nu\rangle\langle\nu| \Big] + \text{h.c.} \Big\} \quad . \end{aligned} \tag{2.34}$$

Here $\chi^{\beta\beta'}_{nn'}(\omega)$ are the bath noise spectra, which carry information about the bath structure, and read as:

$$\chi^{\beta\beta'}_{nn'}(\omega) = \int_0^{\infty} dt\ \mathrm{tr}_B\left[I^{\beta}_{n}(t) I^{\beta'}_{n'}(0)\rho_B\right] e^{i\omega t} \quad . \tag{2.35}$$

These functions are computationally complex to compute and require cluster correlation methods [118, 152, 153]. Later in section 2.4.2 it will be shown how to drop the dependence of Eq. 2.34 from these coefficients and tie it to the experimentally measurable T_2 values.

In Eq. (2.34), the secular approximation suppresses all fast oscillating terms. So in this case, since the difference between system $E_\mu - E_\nu$ and bath energy gaps is significantly larger than the system-bath interaction, the jump operators as $|\mu\rangle\langle\nu|$ for $\mu \neq \nu$ can be neglected. Under this approximation, the effect of the environment on the system induces only pure-dephasing. Indeed, no off-diagonal operators are retained. The master equation (2.34) can be rewritten as:

$$\begin{aligned} \dot{\rho}(t) = & -i[\mathcal{H}_{LS}, \rho(t)] \\ & + \sum_{\mu\nu} \Gamma_{\mu\nu} \Big[2|\mu\rangle\langle\mu|\rho(t)|\nu\rangle\langle\nu| - |\mu\rangle\langle\mu|\delta_{\mu\nu}\rho(t) - \rho(t)|\nu\rangle\langle\nu|\delta_{\mu\nu} \Big], \end{aligned} \tag{2.36}$$

where $\mathcal{H}_{LS} = \sum_\mu S_\mu |\mu\rangle\langle\mu|$ represents the Lamb shift Hamiltonian and we have introduced $\Gamma_{\mu\nu}$. These latter are defined as:

$$\begin{aligned}\Gamma_{\mu\nu} &= \sum_{n,n'=1}^{N_s} \sum_{\beta,\beta'} L^{\beta}_{n,\mu\mu} L^{\beta',*}_{n',\nu\nu} \chi^{\alpha\alpha'}_{nn'}(0) \\ &= \sum_{jj'=1}^{N} \sum_{\substack{\alpha\alpha'= \\ x,y,z}} C^{\alpha\alpha'}_{jj'} \langle\mu|s^{\alpha}_{j}|\mu\rangle\langle\nu|s^{\alpha'}_{j'}|\nu\rangle,\end{aligned} \tag{2.37}$$

where

$$\chi^{\alpha\alpha'}_{nn'}(0) = \frac{1}{2}\int_{-\infty}^{\infty} dt\ \mathrm{tr}_B[I^{\alpha}_{n}(t) I^{\alpha'}_{n'}(0)\rho_B] \tag{2.38}$$

$$C^{\alpha\alpha'}_{jj'} = \sum_{nn'}\sum_{\beta\beta'} \chi^{\beta\beta'}_{nn'}(0) d^{\alpha\beta}_{jn} d^{\alpha'\beta'}_{j'n'} \quad . \tag{2.39}$$

The master equation 2.36 thus consists of two main parts. The first one, represented by the commutator between H_{LS} and the density matrix, introduces a renormalisation of the system energy due to the coupling with the spin bath. This term is generally small and can, therefore, be omitted from the calculations. Instead, the second part describes a pure-dephasing mechanism, and by solving the differential equation, one obtains:

$$\rho_{\mu\nu}(t) = exp(-\gamma_{\mu\nu}t)\rho_{\mu\nu}(0) \tag{2.40}$$

where the decay rates $\gamma_{\mu\nu}$ are determined by coefficients $\Gamma_{\mu\nu}$ as

$$\gamma_{\mu\nu} = \Gamma_{\mu\mu} + \Gamma_{\nu\nu} - 2\Gamma_{\mu\nu} \quad . \tag{2.41}$$

All the information regarding the mechanisms that generate decoherence is contained in $\Gamma_{\mu\nu}$. Equation 2.37 illustrates that $\Gamma_{\mu\nu}$ coefficients are basically formed by two components: the coefficients $C^{\alpha\alpha'}_{jj'}$ and the expectation values determined by the local spin operators on the system eigenstates $\langle\mu|s^{\alpha}_{j}|\mu\rangle\langle\nu|s^{\alpha'}_{j'}|\nu\rangle$. The $C^{\alpha\alpha'}_{jj'}$ coefficients carry the information about the specific molecular structure such as the positions of the nucleus and ions. On the other hand, the second term reflects a dependence on the structure of the eigenstates. Consequently, it follows that to minimize the $\gamma_{\mu\nu}$ terms and, consequently, reduce the effects of decoherence, small differences between the local expectation values of the spin operators are necessary. In simpler terms, the impact of decoherence is diminished on energy states that are magnetically similar. Multi-spin systems with competing interactions are, therefore, optimal candidates for resilience against decoherence. Indeed, these types of systems may exhibit magnetically similar states at low energy.

In conclusion, this analysis determines a general property, independent from the specific molecule structure, that identifies systems intrinsically protected by pure-dephasing.

2.4.2 Decoherence in an S multiplet

In this section, the analysis focuses on the case of systems with an S multiplet as ground state. To simplify, let's start by rewrite the expression 2.37 for the particular case of molecules with a single ion (**S**). As previously shown, several of these systems can be described by Eq. 2.13. Due to their axial symmetry, the eigenstates of the system are diagonal in the z-basis. Consequently, $\langle\mu|s^\alpha|\mu\rangle = \langle m|s^z|m\rangle\delta_{\alpha z}$ where eigenstates are labelled by s^z expectation values m, and so Eq. 2.37 can be simplified as follows:

$$\Gamma^{\mathbf{S}}_{mm'} = C^{zz}mm' = \frac{mm'}{T_2^{eff}} \quad . \tag{2.42}$$

Here, $C^{\alpha\alpha'}_{jj'} = (T_2^{eff})^{-1}$ is the experimental measured dephasing rate between two eigenstates with $\Delta m = 1$. This value contains all the information about the spin bath and the spectral functions $\chi^{\alpha\alpha'}_{nn'}$. Starting from this formulation, it is easy to obtain decay rates:

$$\gamma_{mm'} = \frac{(m-m')^2}{T_2^{eff}} \quad . \tag{2.43}$$

The impact of decoherence is expected to increase quadratically with the difference between m values of the eigenstates. This is a challenge for single-spin molecular qubits, because eigenstates with a large Δm would hardly be affected by decoherence.

Now, let's move to the case of a multi-spin system that exhibits an S multiplet at low energy. For instance, consider the double tetrahedron mentioned earlier and reverse the sign of all exchange interactions making them ferromagnetic **F**. Regardless of the specific values of J_{ij}, it would lead to an $S = \sum_i s_i = 9/2$ ground state. In the case of an almost axial system, the Wigner-Eckart theorem allows to approximate the expectation values $\langle\mu|s^\alpha_j|\mu\rangle = \zeta_j\langle m|S^z|m\rangle\delta_{\alpha z}$ [154]. Hence start-

ing from from Eq. 2.37 one obtains:

$$\begin{aligned}\Gamma^{\mathbf{F}}_{mm'} &= \chi_0 \sum_{jj'}\sum_{\alpha\alpha'} c^{\alpha\alpha'}_{jj'} \langle m|s^{\alpha}_{j}|m\rangle\langle m'|s^{\alpha'}_{j'}|m'\rangle \\ &= \chi_0 \sum_{jj'}\sum_{\alpha\alpha'} c^{\alpha\alpha'}_{jj'} \zeta_j\zeta_{j'}\langle m|S^{\alpha}|m\rangle\langle m'|S^{\alpha'}|m'\rangle \\ &= \chi_0 \left(\sum_{jj'} c^{zz}_{jj'}\zeta_j\zeta_{j\prime}\right) mm' = \frac{mm'}{T_2^{eff}}, \end{aligned} \tag{2.44}$$

where $c^{\alpha\alpha'}_{jj'} = \sum_{nn'}\sum_{\beta\beta'} d^{\alpha\beta}_{jn} d^{\alpha'\beta'}_{j'n'}$ and for simplicity $\chi^{\alpha\alpha'}_{nn'}(0)$ is approximated as a constant χ_0 [129]. The result obtained is entirely analogous to that of Eq. 2.42. In conclusion to this analysis, it is important to emphasize how the structure of the eigenstates determines the decay rates and thus the effect of the eigenstate. Eigenstates characterised by a multiplet S are expected to have rates that grow quadratically with the difference of Δm between levels.

2.4.3 Decoherence in multi-spin systems with competing interactions

Eq. 2.43, which is valid for systems characterized by an S multiplet ground state, expresses a clear and direct relation between the effect of decoherence and the form of the eigenstates. Now, the aim is to obtain a similar result for the class of systems with competing interactions. To illustrate this, the example of the double tetrahedron with antiferromagnetic interactions **C**2, discussed earlier, serves as a reference case. Starting from Eq. 2.37 and, as previously done for **F**, assuming an axial system and $\chi^{\alpha\alpha'}_{nn'}(0)$ to be constant, the expression is rewritten as follows:

$$\begin{aligned}\Gamma^{\mathbf{C}}_{\mu\nu} &= \chi_0 \sum_{jj'=1}^{N} \sum_{\substack{\alpha\alpha'= \\ x,y,z}} c^{\alpha\alpha'}_{jj'} \langle\mu|s^{\alpha}_{j}|\mu\rangle\langle\nu|s^{\alpha'}_{j'}|\nu\rangle \\ &= \chi_0 \sum_{jj'=1}^{N} c^{zz}_{jj'}\langle\mu|s^{z}_{j}|\mu\rangle\langle\nu|s^{z}_{j'}|\nu\rangle \end{aligned} \tag{2.45}$$

In this approximation, χ_0 depends only on the structure of the molecule and therefore is the same as for **F** and **C**2 [129]. Eq. 2.45 can be rewritten by substituting the expression found for **F**:

$$\Gamma^{\mathbf{C}}_{\mu\nu} = \frac{1}{T_2^{eff}\left(\sum_{jj'} c^{zz}_{jj'}\zeta_j\zeta_{j\prime}\right)} \sum_{jj'=1}^{N} c^{zz}_{jj'}\langle\mu|s^{z}_{j}|\mu\rangle\langle\nu|s^{z}_{j'}|\nu\rangle \quad . \tag{2.46}$$

As seen before, $\Gamma_{\mu\nu}$ depends on the expectation value of the local spin operators with the system eigenstates $\langle\mu|s^{z}_{j}|\mu\rangle\langle\nu|s^{z}_{j'}|\nu\rangle$. Although in this case it is not

possible to solve them explicitly, because the structure of the eigenstates is not trivial, it is not difficult to see that to minimize $\gamma_{\mu,\nu}$ it is important to have small differences of these expectation values.
Eq. 2.46 allows a direct and fair comparison of the effect of decoherence between **F** and **C**2 systems. In the Chapters 4 this analogy will be used to compare these molecules as elementary units for QEC.

2.5 Quantum Error Correction on MNM Qudits

In the previous sections, the discussion focused around how chemical engineering can enhance the resilience of MNMs to pure dephasing by designing inherently protected molecules. Nonetheless, despite the potential technological progress, decoherence is and will remain a significant limitation for QIP. The only way to overcome this issue in the long term is through the implementation of quantum error correction schemes (QEC).
In Chap. 1, a brief introduction to standard QEC methods is provided. The general idea can be summarized by saying that a quantum state can be protected against errors by spreading the information across a larger Hilbert space in the proper manner. This is commonly done by exploiting a block encoding, i.e. a single logical qubit is encoded into many physical qubits [155, 156]. The number of units required to achieve a high-precision computation scales rapidly, and for example, estimates suggest that for common algorithms such as the Shor factorisation about $10^3 - 10^4$ units are needed to reach a reasonable success rate in factoring a 2000-bit number [157].
An alternative strategy is offered by the qudit-encoding. Rather than increasing the number of physical objects, the enlarged Hilbert space can be obtained by exploiting a qudit. In this way, the encoded quantum state is within a single object. This approach offers several advantages: primarily by reducing the number of units to be controlled and secondly by eliminating the need for two-body gates during most of the manipulation procedures. Hereafter, an embedded QEC scheme specifically tailored to correct pure-dephasing in MNMs is presented.

2.5.1 Binomial Code Words for Pure Dephasing

The initial step in designing any Quantum Error Correction scheme consists of identifying and modelling the main sources of errors. In fact, codes are only able to correct a subset of all possible errors, so to maximize their utility it is advisable to correct the most important ones. As analysed in the previous sections, for MNMs at low temperatures the primary source of errors is pure dephasing.

This produces the decay of the off-diagonal elements of the density matrix, a phenomenon that can be represented by the action of the S_z operator:

$$\frac{d\rho(t)}{dt} = \frac{2}{T_2}\left(S_z\rho(t)S_z - \frac{1}{2}\{S_z^2,\rho(t)\}\right) \quad . \tag{2.47}$$

In order to construct the QEC scheme, it is convenient to express the above equation in terms of Kraus operators resulting in an expression of the form of $\rho(t) = \sum_{a=0}^{\infty}\mathcal{E}_a\rho(0)\mathcal{E}_a^\dagger$ [158]. By moving to the interaction frame with respect to the anti-commutator $\{S_z^2,\rho(t)\}$, the density matrix is redefined as:

$$\rho(t) = e^{-tS_z^2/T_2}\rho_I(t)e^{-tS_z^2/T_2} \quad . \tag{2.48}$$

Eq. 2.47 can be reformulated as:

$$\frac{d\rho_I(t)}{dt} = \frac{2}{T_2}S_z\ \rho_I(t)\ S_z \quad . \tag{2.49}$$

Upon integrating this equation over time, form zero to an arbitrary time t, as a Dyson series, the result is:

$$\rho_I(t) = \rho_I(0) + \frac{2}{T_2}\int_0^t dt_1 S_z\rho_I(0)S_z + \frac{(2/T_2)^2}{2!}\int_0^t dt_1\int_0^t dt_2\ S_z^2\rho_I(0)S_z^2 + \dots \quad . \tag{2.50}$$

Then, solving the integrals and going back to Schrödinger picture, the expression is rewritten as:

$$\rho(t) = \sum_{a=0}^{\infty}\frac{(2t/T_2)^a}{a!}e^{-tS_z^2/T_2}\ S_z^a\ \rho(0)\ S_z^a\ e^{-tS_z^2/T_2} \tag{2.51}$$

from where it is easy to see that Kraus operators are of the form of

$$\mathcal{E}_a = \sqrt{\frac{(2t/T_2)^2}{a!}}\ e^{-S_z^2t/T_2}\ S_z^a \quad . \tag{2.52}$$

The Knill-Laflamme conditions 1.49 impose that the code words for the logical state $|0_L\rangle$ and $|1_L\rangle$ satisfy the constraint:

$$\langle a_L|S_z^a|b_L\rangle = \beta_a\delta_{a,b} \qquad 0 \le a \le 2n \quad , \tag{2.53}$$

where β is a parameter. Satisfying this constraint ensures that the logical states are not deformed by errors, making correction possible through a unitary transformation depending on the detected error. In general, the number of different error operators that can be corrected simultaneously is limited and depends on

the size of the computational space. At short times, the dominant terms are the lowest powers of S_z. Therefore it is advisable to correct these errors first.
Having obtained an expression for error operators in terms of Kraus operators and the constraints that code words must respect, it is now time to introduce an explicit expression for the code words themselves. For now, it is assumed that the underlying physical system has eigenstates diagonal in the basis of S_z such as happens for single ion magnets in a large magnetic field. Inspired by binomial codes on bosonic systems [159, 160], this class is defined as:

$$\begin{aligned} |0_L\rangle &= \frac{1}{\sqrt{2^{2S-1}}} \sum_{k=1,\ \text{for } k \text{ odd}}^{2S} \sqrt{\binom{2S}{k}}\, |-S+k\rangle \\ |1_L\rangle &= \frac{1}{\sqrt{2^{2S-1}}} \sum_{k=0,\ \text{for } k \text{ even}}^{2S} \sqrt{\binom{2S}{k}}\, |-S+k\rangle \ , \end{aligned} \tag{2.54}$$

where $|-S+l\rangle$ are the eigenstates of the computational subspace. The two logical states $|0_L\rangle$ and $|1_L\rangle$ are encoded on two different subspaces identified by odd and even values of k respectively. These two subspaces are disjoint and therefore orthogonal by construction.
To verify that the condition 2.53 holds, one first has to note that, given the assumption about the eigenstate structure, the Kraus operators defined above are diagonal and thus their action does not mix different eigenstates. Therefore the expression 2.53 only needs to be checked for $a = b$. By substituting the explicit expression of code words, one finds:

$$\begin{aligned} \langle 1_L|S_z^l|1_L\rangle - \langle 0_L|S_z^l|0_L\rangle &= \frac{1}{2^{2S-1}} \sum_{k=0}^{2S} (-1)^k \binom{2S}{k} \langle k-S|S_z^l|k-S\rangle \\ &= \frac{1}{2^{2S-1}} \sum_{k=0}^{2S} (-1)^k \binom{2S}{k} (k-S)^l \ . \end{aligned}$$

Noting that the last expression can be seen as a binomial expansion in k and assuming that $l \leq 2S$, it is easy to find:

$$\begin{aligned} \sum_{k=0}^{2S} \binom{2S}{k} (-1)^k (k-S)^l &= \left[\left(x\frac{d}{dx} \right)^l \sum_{k=0}^{2S} (-1)^k x^{k-S} \right]_{x=1} \\ &= \left[\left(x\frac{d}{dx} \right)^l \frac{1}{x^S} (1-x)^{2S} \right]_{x=1} = 0 \ . \end{aligned}$$

As desired, the code words satisfy the Knill-Laflamme conditions for all the powers of S_z below $2S$. To achieve correction up to the order $(2t/T_2)^n$, it is necessary

to meet the conditions for powers of S_z up to $2n$ included: this means that the perturbative order n requires a spin $S = n + 1/2$. In other terms, the computational space of a d-dimensional qudit (even) is large enough to correct at most $N_{err} = d/2$ different errors.

2.5.2 Ideal error detection and correction procedure

Up to this point, the code words that form the core of the QEC scheme have been defined. The structure of these ensures that if an $\mathcal{E}_a$ error affects them, the logical states are brought to distinguishable orthogonal states and the original state superposition coefficients (α and β) are preserved. This condition guarantees that an error affected state can be recovered (in the limits of QEC scheme correction capabilities). To complete the presentation of the scheme, the procedures for detection and recovery [28] are formalized here.
Let's start by introducing the error space $\mathcal{V}_\ell$ where $\ell = \{0,1\}$, which defines the space comprehending all possible states generated by the action of the $\mathcal{E}_a$ errors on the code words. In formulae:

$$\mathcal{V}_\ell = \text{span}\left\{ \frac{S_z |\ell_L\rangle}{\|S_z |\ell_L\rangle\|}, \ldots, \frac{S_z^{\lfloor S \rfloor} |\ell_L\rangle}{\left\|S_z^{\lfloor S \rfloor} |\ell_L\rangle\right\|} \right\} \quad , \tag{2.55}$$

where $\lfloor S \rfloor$ indicates the largest integer smaller than S. Now, it is necessary to understand how different errors can be detected and distinguished without destroying the superposition of the logical state. Since the error space $\mathcal{V}_\ell$ does not define an orthonormal basis, the initial step involves defining one. The Knill-Laflamme conditions, Eq. 2.53, ensure that the code words, even under the influence of errors, maintain logical superposition. This property relies on the existence of a unitary operator $\mathcal{U}$ satisfying the condition:

$$\mathcal{U} S_z^a |0_L\rangle = S_z^a |1_L\rangle \quad . \tag{2.56}$$

Defining the basis $\{|e_\ell^a\rangle_{a=0,\ldots,\lfloor S \rfloor}\}$ for one of the two sub-spaces, for instance $\mathcal{V}_0$, the other must be defined by verifying $\mathcal{U}|e_0^a\rangle = |e_1^a\rangle$. An available choice is to take as basis the vectors resulting from a Gram-Schmidt orthonormalization of the states $S_z^a |\ell_L\rangle$. The error correction procedure $\mathcal{O}_R$ is then specified by the set of operations $\{O_a P_a\}_{a=0,\ldots,\lfloor S \rfloor}$, where O_a and P_a are defined as follows:

$$O_a |e_\ell^a\rangle = |\ell_L\rangle , \tag{2.57}$$

$$P_a = (|e_o^a\rangle\langle e_o^a| + |e_1^a\rangle\langle e_1^a|) \quad . \tag{2.58}$$

In essence, the correction procedure is divided into two steps: firstly, a measurement that projects the system state into one of the various two-dimensional subspaces, named detection; secondly, the corresponding correction of the logical state by O_a, denoted as recovery.

To complete this introduction, it would serve to show how these procedures are explicitly defined. However, for a complete definition of these it is necessary to take into account the underlying physical system. Therefore, the reader will forgive us if this is postponed to chapter 3, where it is shown in the specific case of a $S = 3/2$ qudit, and chapter 4 where it is discussed for general d-dimensional qudit belonging to **C** class.

In conclusion of the chapter, Fig. 2.7 reports the numerical results of an ideal implementation of the presented scheme. An ideal implementation means that you have perfect and instantaneous control over the system. Thus, the only forms of error introduced are those due to decoherence during memory time. The underlying physical architecture is assumed to be a single spin molecule. Thus, the qudit energy levels are diagonal in the S_z basis and the effect of decoherence goes as in Eq. 2.43. On the x-axis is reported the so called memory time t in terms of t/T_2 where T_2 is the system coherence time. The memory time is the time lapse between the encoding and the application of the correction procedure during which the system is left under the effect of errors (in this case pure-dephasing). For the sake of simplicity, the possibility of applying gates is not considered for the moment, so the system acts as a memory, hence the name memory time. The y-axis shows the infidelity, defined as $\mathcal{E} = 1 - \langle\psi_0|\rho_t|\psi_0\rangle$, calculated on the initial logical state $|\psi_L\rangle = \frac{|0_L\rangle+|1_L\rangle}{\sqrt{2}}$. The results are reported for an increasing qudit dimension from 4 ($S = 3/2$) to 16 ($S = 15/2$) (coloured continuous lines). The benchmark for the scheme performance is given by comparison with the behaviour free qubit (dashed black line) on which acts the same decoherence process but no QEC is applied. First, it is valuable to note that for all the cases the correction procedure is worthwhile, enabling to reduce the error. Both increasing the number of levels, that allows to correct more powers of S_z^k, and reducing the memory time, that would correspond to implement the scheme more often during the computation, the error $\mathcal{E}$ can be reduced in principle to any precision level. However, in absolute terms, the gain from increasing the qudit size is progressively smaller. This is mainly due to two factors. First, as the size of the qudit increases, more and more powers of S_z are corrected, but these have progressively a smaller effect. In addition, the correction capacity of the system under consideration decreases as the effect of decoherence increases with increasing Δm. As will be shown in Chapters 3 and 4, under the conditions of a real implementation, where the different procedures (encoding, detection and

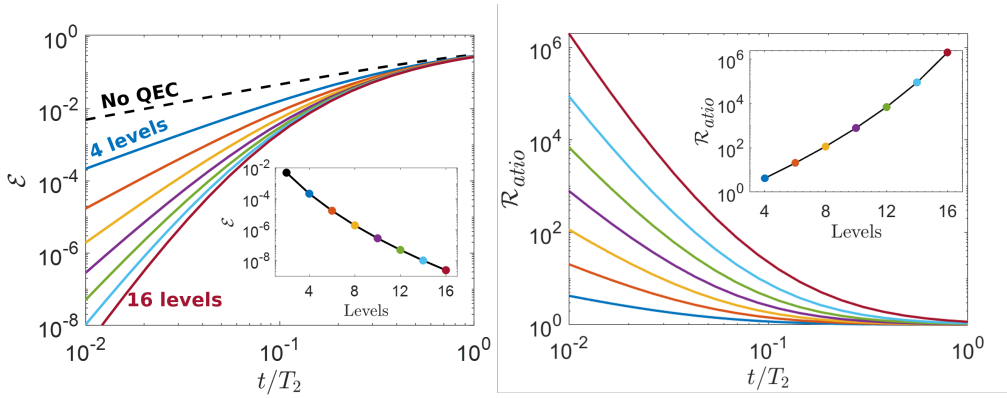

Figure 2.7: Left: Ideal performance of the presented QEC scheme to correct pure dephasing error on different size qudits (continuos coloured lines). On the x-axis is reported the memory-coherence time ratio while on the y-axis the infidelity $\mathcal{E} = 1 - \langle\psi_0|\rho_t|\psi_0\rangle$. The dashed black line is the comparison case given by a qubit without error correction. Inset: scheme performance at $t/T_2 = 10^{-2}$. Right: the gain calculated as the ratio between the error in the corrected (qudits) and uncorrected (qubit) cases. Inset: the gain at $t/T_2 = 10^{-2}$. Adapted from Ref. [161] with permission under the terms and conditions of the Creative Commons Attribution-NonCommercial 3.0 Unported Licence (CC BY-NC 3.0).

recovery) have a finite duration and are therefore also error-prone, these factors limit the correction possibilities of the system.

CHAPTER 3

Quantum Error Correction with Molecular Spin Qudits

QEC is a necessary way point on the path to the realization of reliable quantum computers. As explained in Sec. 1.7, in a similar way to how it is done on classical computers, QEC exploits a larger space to encode the information in a protected way. The conventional approach, known as block encoding, distributes the information of a single logical qubit across multiple entangled physical units. In contrast, qudit encoding leverages a single multi-level quantum system to store the information. This alternative strategy has the potential to significantly simplify QEC implementation by avoiding the need to control many objects and implement two-body gates, which are notoriously more challenging for state-of-the-art architectures. Molecular nanomagnets are promising systems for the practical realization of qudit encoded QEC. Indeed, these systems possess a coherent multi-level structure at low energy that can be easily manipulated by electromagnetic pulses.

This chapter investigates the feasibility of the scheme presented in Sec. 2.5 on three realistic molecules in which the qudit is provided by either an electronic or a nuclear spin. Both types of system have a spin-3/2 which provides the computational space for a four-level qudit, coupled with an electronic spin-1/2 ancilla which is used in the error detection to have access to the qudit state without affecting it. By means of numerical simulations the feasibility and effectiveness of this approach is demonstrated. Simulations take into account both decoherence and leakage effects, evidencing the need for a balance between these two influences. Large driving fields reduce pulse duration and therefore have a positive impact in decoherence. However, on the other hand, the pulses thus generated have a wider frequency spectrum and favour leakage.

To enhance the scheme's performance, the Derivative Removal by Adiabatic Gate (DRAG) pulse control technique is introduced. This method exploits a secondary driving field to reduce leakage to a single disturbing transition close to the driving one. More specifically, it creates a hole in the frequency spectrum cut-

ting out contributions to the unwanted frequency. The simulation results demonstrate significant improvement through the application of DRAG with respect to a standard Gaussian shaped pulse.

The chapter is organized as follows: in the first section 3.1, the three physical systems taken into consideration are introduced. The working parameter ranges are discussed, highlighting the advantages and disadvantages of the different choices. The explicit formulation of the binomial code words introduced in 2.5 for a four-level qubit is then reported, together with a scheme for their implementation. Sec. 3.3 gives an in-depth introduction to the DRAG technique, providing an explicit formulation and explaining how to implement it on a standard Gaussian shaped pulse. To demonstrate the feasibility of the presented QEC scheme, the results of extensive numerical simulations are reported and discussed in Sec. 3.4. Section 3.6 summarizes the results and concludes the chapter.

3.1 Physical Systems and Methods

As anticipated in the introduction, this study considers three distinct systems, each characterized by either an electronic (**e**) or a nuclear (**n**) spin-3/2 coupled with an electronic ancillary qubit. The comparison between these two classes is of particular interest due to differences in their coherence and manipulation time scales. Specifically, electronic systems (**e**) exhibit shorter coherence times but faster manipulation with respect to (**n**).
Using the spin Hamiltonian formalism developed in 2.1, the electronic systems under consideration can be modelled as follows:

$$H_e = \mu_B B_0 \left(g_z S_z + g_z^A s_z^A \right) + D S_z^2 + \mathbf{S} \cdot \mathbf{J} \cdot \mathbf{s}^A, \tag{3.1}$$

where S and s^A are respectively the qudit and the qubit electronic spins. The first two terms represent the Zeeman interactions of these spins with the external static field B_0 along the z-axis. The third term, parametrized by D, introduces the zero-field splitting for the qudit spin, which has the effect of splitting the energy levels and making the transitions between them inequivalent. The final term, parametrized by the tensor $\mathbf{J}$, accounts for the spin-spin exchange interaction. In the various simulations, the two dimers considered are CrCu (**e1**) and CrYb (**e2**). The former is a hypothetical system discussed in Ref. [25], while the latter is an existing molecule that has already been synthesized [162]. In both cases, the qudit is encoded in the $S = 3/2$ spin of the Cr^{3+} ion. Typical parameters of a single ion in an octahedral cage are assumed (see table 3.1).

The two systems differ for the qubit ancilla, namely Cu^{2+} and Yb^{3+} ions. As documented in Ref. [163], reasonable parameters for Cu^{2+} are g_z^A = 2.3 and $g_{x,y}^A$ = 2.1, and g_z^A = 4.2 and $g_{x,y}^A$ = 2.9 for Yb^{3+} trensal, as reported in [164].
An axially anisotropic exchange interaction with $J_x = J_y = 1.710^{-2}$ cm^{-1} and $J_z = -3.310^{-2}$ cm^{-1} has been considered. This type of interaction can be produced by a dipole-dipole coupling with the ions approximately 5-6 Å apart. Fig. 3.1-a) shows the energy level spectrum as a function of the external static magnetic field B_0 for (**e2**). Each line is labelled with the expectation values of S_z and s_z^A on the right side. For a sufficiently large magnetic field, all transitions are well resolved with frequencies in the order of GHz at most.
Similarly, for the nuclear spin system (**n**), the spin Hamiltonian is defined as:

$$H_n = B_0 \left(g_N \mu_N I_z + g_z^A \mu_B s_z^A \right) + Q I_z^2 + \mathbf{I} \cdot \mathbf{A} \cdot \mathbf{s}^A, \tag{3.2}$$

where I represents the nuclear spin, μ_N is the nuclear magneton and Q parametrizes the nuclear quadrupole coupling, which has a similar effect to the electronic zero-field splitting. The last term accounts for the hyperfine tensor **A**. The parameters considered in the simulations are taken from the $(PPh_4)_2[Cu(mnt)_2]$ complex presented in Ref. [119]. The qudit and the ancillary qubit are respectively provided by the nuclear $I = 3/2$ and electronic spin $S = 1/2$ of the Cu^{2+}. These spins are coupled by hyperfine interaction $A = (0.4, 0.4, 1.7) \times 10^{-2}$ cm^{-1}. Unfortunately, in Ref. [119] the nuclear quadrupole has not been measured. Thus, in the simulations a typical value $Q = 1.7 \times 10^{-3}$ cm^{-1} has been considered [165, 166]. Fig. 3.1-b) reports the energy spectrum of (**n**) as a function of the external magnetic field. The subspaces corresponding to the two states of the ancilla ($|\downarrow\rangle$ and $|\uparrow\rangle$) are clearly separated due to the large difference of electronic and nuclear excitation energies. All transitions are distinct with frequencies on the order of hundreds of MHz.
In the working conditions of a hypothetical logical qubit, the spin dimers must be in the weak coupling regime. This implies that the eigenstates of the system are nearly factorized, so that the expectation values of S_z (I_z) and s_z^A are good quantum numbers $|m_Q, m_A\rangle$. As far as (**n**) is concerned, this condition is satisfied if $g_z^A \mu_B B_0 \gg A_{x,y}$, which is readily met at external magnetic fields $B_0 \geq 0.1$ T. Considering (**e**), this condition is verified if the qudit-qubit exchange coupling is significantly smaller than the single body excitation energies $|J_{x,y}| << |(g_z - g_z^A)\mu_B B_0 + D(2M+1)|$. By appropriately selecting the amplitude of the external magnetic field and considering loosely coupled systems, it is also possible to find an appropriate regime of parameters for (**e**), with $B_0 \sim 1$ T.
Transitions between eigenstates of H_e or H_n are addressable through electromagnetic pulses. The time-dependent driving field $b_1(t)$, oriented along the x-axis,

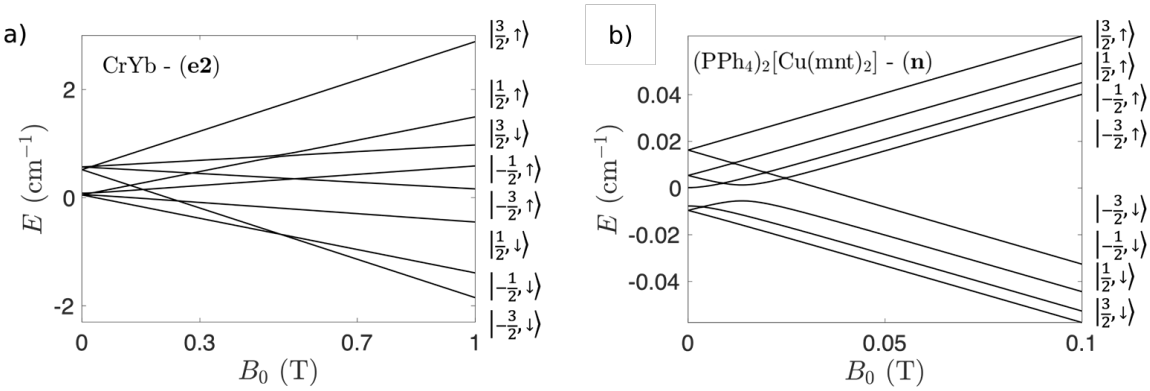

Figure 3.1: Energy levels as a function of the external magnetic field for (**e2**) (left) and (**n**) (right). Adapted from Ref. [161] with permission under the terms and conditions of the Creative Commons Attribution-NonCommercial 3.0 Unported license (CC BY-NC 3.0) .

	g	D/Q (cm^{-1})	$(J_x, J_y, J_z)/(A_x, A_y, A_z)$ (cm^{-1})	(g_x^A, g_y^A, g_z^A)	T_2 (μs)	T_2^A (μs)
CrCu (**e1**)	1.98	-0.24	$(1.7, 1.7, -3.3) \times 10^{-2}$	(2.1,2.1,2.3)	50	5
CrYb (**e2**)				(2.9,2.9,4.2)	50	$1-3$
$(PPh_4)_2[Cu(mnt)_2]$ (**n**)	1.48	1.7×10^{-3}	$(0.4, 0.4, 1.7) \times 10^{-2}$	(2.0,2.0,2.1)	$10^2 - 10^3$	68

Table 3.1: Table of parameters considered in the simulations for the hypothetical Cr-Cu/CrYb dimers and ion ^{63}Cu [25, 119, 162]. $\mathbf{J}$, $\mathbf{A}$, and $\mathbf{g}^A$ are assumed as diagonal tensors while the qudit's g is isotropic.

enters the Hamiltonian as follows:

$$H_{1e} = \mu_B b_1(t) \left(g_x^A s_x^A + g_x S_x \right) \tag{3.3}$$

$$H_{1n} = b_1(t) \left(\mu_B \, g_x^A s_x^A + \mu_N \, g_N I_x \right) \ . \tag{3.4}$$

Unless otherwise specified, the pulses are assumed to be Gaussian shaped $b_1(t) = B_1 \, e^{-(t-t_0)^2/2\tau^2} \cos(\omega t)$.

In the numerical simulations, the effect of pure dephasing is modelled by considering the simplified description given the master equation formalism introduced in Sec. 2.4. Overall, the time evolution of the (**e**) (left) and (**n**) (right) can be summarized as follows:

$$\frac{d\rho(t)}{dt} = -\frac{i}{\hbar}[H_e + H_{1e}(t), \rho(t)] + \frac{1}{T_2}[2S_z\rho(t)S_z - S_z^2\rho(t) - \rho(t)S_z^2] + \frac{1}{T_2^A}[2s_z^A\rho(t)s_z^A - (s_z^A)^2\rho(t) - \rho(t)(s_z^A)^2] \qquad \frac{d\rho(t)}{dt} = -\frac{i}{\hbar}[H_n + H_{1n}(t), \rho(t)] + \frac{1}{T_2}[2I_z\rho(t)I_z - I_z^2\rho(t) - \rho(t)I_z^2] + \frac{1}{T_2^A}[2s_z^A\rho(t)s_z^A - (s_z^A)^2\rho(t) - \rho(t)(s_z^A)^2] \quad .$$

3.2 Code Words and Scheme Implementation

The general theory and the mathematical derivation of the class of binomial code words to correct pure-dephasing has already been introduced in 2.5.1. The present section reports the specific formulation to correct the S_z error on a four-level qudit, together with a strategy to implement it on a MNM qudit.
Eq. 2.54 defines the code words which in the specific case of $S = 3/2$ qudit take the following form:

$$\begin{aligned} |0_L\rangle &= \frac{|3/2\rangle + \sqrt{3}|-1/2\rangle}{2} \\ |1_L\rangle &= \frac{\sqrt{3}|1/2\rangle + |-3/2\rangle}{2} \end{aligned} \quad , \tag{3.5}$$

where the qudit levels are labelled by the expectation values on S_z. Within a four-dimensional space ($d = 4$), the procedure permits to correct only the first power of S_z. Therefore, the possible error words $|e_0\rangle$ and $|e_1\rangle$, are obtained by considering the effect of the S_z error as follows:

$$\begin{aligned} |e_0\rangle &= \frac{S_z|0_L\rangle}{\|S_z|0_L\rangle\|} = \frac{\sqrt{3}|3/2\rangle - |-1/2\rangle}{2} \\ |e_1\rangle &= \frac{S_z|1_L\rangle}{\|S_z|1_L\rangle\|} = \frac{|1/2\rangle - \sqrt{3}|-3/2\rangle}{2} \end{aligned} \quad . \tag{3.6}$$

As analysed in Sec. 2.5.1, since S_z is diagonal on the basis of eigenstates, it does not mix the $|0_L\rangle$ and $|1_L\rangle$ subspaces but exclusively influences the relative phase of the code words. In this specific case, the error states are orthogonal to both $|0_L\rangle$ and $|1_L\rangle$ and with them an orthonormal basis set of the $S = 3/2$ space. Figure 3.2 illustrates a schematic representation of the strategy to implement the QEC scheme on a $S = 3/2$ MNM qudit. The scheme is supposed to have an ancillary qubit coupled to the qudit. As explained below, this is used in the procedure to have access to the state of the qudit without modifying it with a direct measurement. The horizontal lines represent the qudit levels labelled by $|m\rangle$, while the Gaussian symbols depict the sequence of electromagnetic pulses used

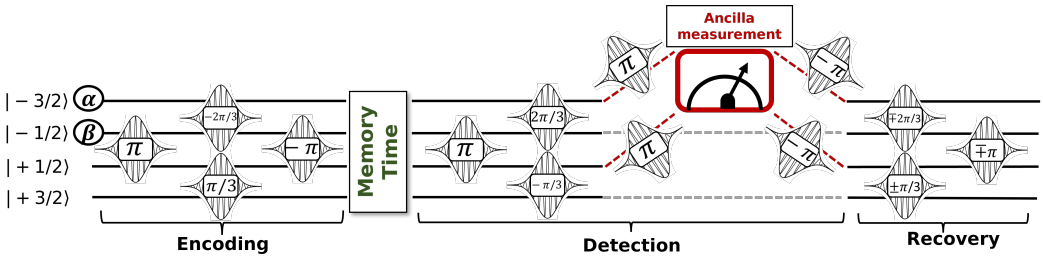

Figure 3.2: Schematic representation of the QEC scheme to correct S_z error on a four level qudit coupled with an ancillary qubit. The qudit computational space is represented by the black horizontal lines. The Gaussian symbols represent the electromagnetic pulses used to manipulate it. The whole procedure is divided into three steps: encoding, detection, and recovery. During the memory time, the system is left idle under the action of pure-dephasing acts. Reproduced from Ref. [161] with permission under the terms and conditions of the Creative Commons Attribution-NonCommercial 3.0 Unported license (CC BY-NC 3.0).

to control and manipulate the system. The entire procedure is divided into three distinct steps: encoding, detection, and recovery.

In the first step, encoding, the goal is to rewrite the quantum state $|\Psi\rangle = \alpha|0\rangle + \beta|1\rangle$, initially stored in the qudit levels $|-3/2\rangle$ and $|-1/2\rangle$, in terms of the code words $|0_L\rangle$ and $|1_L\rangle$. This transformation is achieved through the sequence of pulses illustrated in the Fig. 3.2.

The pulses that effectively construct the desired protected states are the two in the middle, and their angles are strictly related to the coefficients of the code words. Conversely, the two π pulses at the beginning and end of the sequence are accessory and serve to move the information across the qudit. If direct connections between $|-3/2\rangle \leftrightarrow |1/2\rangle$ and $|-1/2\rangle \leftrightarrow |3/2\rangle$ were possible, they would be unnecessary. At the end of this procedure, the state of the logical qubit is encoded, making possible the detection and correction of possible S_z errors.

Subsequently, during the so-called memory time, the system is left idle, under the only effect of decoherence. This interval represents the simulation time, and for simplicity, it is assumed that no gates are applied.

After the memory time, the qudit will be in a superposition of $\{|0_L\rangle, |1_L\rangle, |e_0\rangle, |e_1\rangle\}$ states. The detection procedure decodes the information, bringing the four possible states to different levels of the qudit. Specifically, the superposition of the logical states $|0_L\rangle$ and $|1_L\rangle$ goes to $\alpha|-3/2\rangle + \beta|1/2\rangle$, while the superposition of error-affected states goes to $\alpha|-1/2\rangle + \beta|3/2\rangle$. At this stage, by conditionally exciting the ancilla state, which is initially prepared in $|\downarrow\rangle$, with respect to the states $|-3/2\rangle$ and $|1/2\rangle$ (red dashed lines in the

figure), the ancilla becomes entangled with the states of the qudit. Measuring the ancilla state enables one to determine if the state is in the correct or affected state. Depending on the measurement outcome, a correction procedure can be used to correct (at first order) the state of the qudit and almost recreate the initial superposition. In the figure, the sequence of rotations to consider is the one with an upper (lower) sign if the qudit is in the corrected (erred) state.

In practice, the qubit state is not only affected by the first power of S_z, but also by higher powers. These additional errors can be corrected by using more than four levels for the encoding. The scheme can be easily extended to larger qudits by simply redesigning the sequence of pulses [118]. In the detection procedure, the ancilla would require $d/2$ levels when dealing with a d-dimensional qudit. This flexibility makes the approach scalable and suitable for a wide range of qudit sizes.

3.3 Derivative Removal by Adiabatic Gate (DRAG)

Pulse control techniques are exploited to enhance control capabilities on quantum systems, thus improving gate implementation. Generally, the primary objective is to carry out operations as quickly and accurately as possible. Technical limitations aside, the common problem in practical implementation is leakage. Large driving fields, which allow faster manipulation, also imply a larger spectral width of the pulse. This makes precise control of target systems particularly challenging where transitions are close in frequency. To address leakage, several pulse control techniques have been developed, including Sideband Modulation [167, 168], Speeding up Waveforms by Inducing Phases to Harmful Transitions [169, 170], and Derivative Removal by Adiabatic Gate (DRAG) [171–173], each tailored to work under specific conditions.

In this study, the DRAG method is investigated. As anticipated in the introduction of the chapter, this procedure allows one to mitigate the contribution in frequency to a single disturbing transition close to the target one. The elementary idea is to leverage a secondary driving field, oriented perpendicularly to the primary one and shaped as its derivative, in order to create a spectral hole in correspondence to the disturbing frequency. In essence, the secondary driving field reshapes the pulse spectrum by increasing the contribution near the target frequency while decreasing it near the unwanted frequency. This method effectively addresses single disruptive transitions. For its implementation, no exact derivation exists, and the control parameters of the secondary pulse are determined through numerical optimization.

In the mathematical formulation, the driving field takes the form of:

$$b_1(t) = \begin{cases} \varepsilon_x(t)\cos(\omega_0 t) + \varepsilon_y(t)\sin(\omega_0 t) & 0 < t < t_g \\ 0 & \text{otherwise} \end{cases}, \tag{3.7}$$

where the two independent quadrature controls $\varepsilon_x(t)$ and $\varepsilon_y(t)$ are driven by a single frequency $w_0/2\pi$. Considering a Gaussian-shaped pulse for the main field, the two controls are defined as:

$$\begin{aligned} \varepsilon_x(t) &= B_1\, e^{-(t-t_0)^2/2\tau^2}, \\ \varepsilon_y(t) &= \beta\lambda \frac{d\varepsilon_x(t)}{dt}\ , \end{aligned} \tag{3.8}$$

where λ serves as an auxiliary parameter to renormalize the relative strength among the unwanted and the desired transition, while β is the parameter actually used in the optimization process, typically taking values within the range of -1 and $+1$.
Panel a) and b) in Fig. 3.3 display the amplitude in the time domain of the primary driving field and its derivative, respectively. As indicated by the dotted curve, the primary pulse takes the form of a Gaussian but is truncated within $\pm\ 2\sigma$. In panel c), the Fourier transform of the standard Gaussian-shaped and the DRAG pulses, which encompass both driving fields, are depicted. The two vertical grey lines mark the target $\frac{\omega_0}{2\pi}$ (solid) and the disturbing $\frac{\omega}{2\pi}$ (dashed) frequencies. The secondary driving field produces two major effects on the frequency spectrum of the original pulse. Firstly, the main peak is shifted away from the disturbing frequency, and its amplitude is modulated. Additionally, the curve is no longer symmetric, leading to a significant reduction in frequency contribution around the unwanted transition. In the illustrated example, the effect of DRAG has been exaggerated to emphasize its impact, but typically, for optimized values, the distortion of the curve is not as pronounced.

3.4 Results

The strategy presented above to implement the QEC scheme relies on two assumptions. The first one is that the pulses are ideal, meaning they are instantaneous and perfectly monochromatic. Additionally, as previously discussed, the qudit and the ancilla are assumed to be perfectly factorized. However, in practical implementations, these hypotheses do not hold, and relaxing them leads to the introduction of three different sources of error:

1) **Qudit-Ancilla Coupling Effects**: A non-zero qudit-ancilla coupling (necessary for system control) comports the states of the qudit and ancilla to be

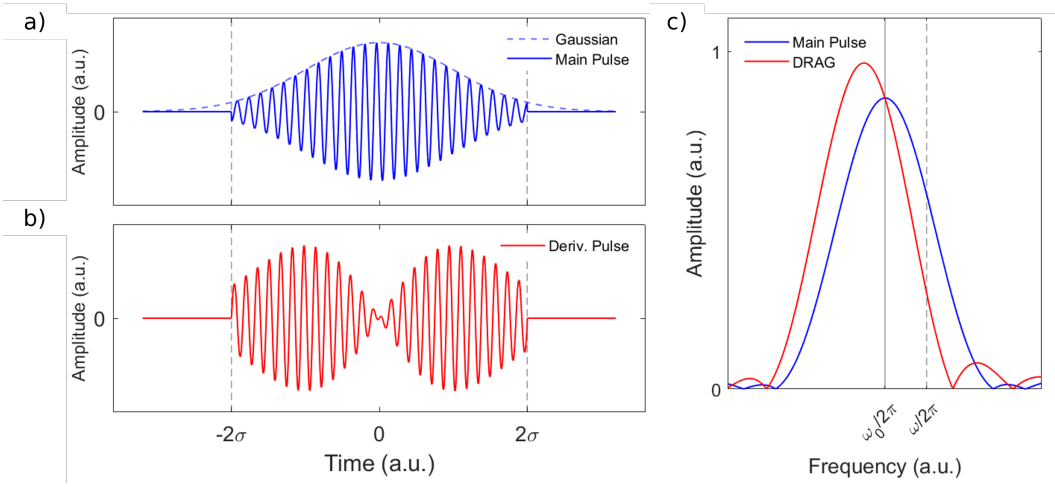

Figure 3.3: a) Standard Gaussian shaped pulse. b) Pulse shaped as the derivative of a Gaussian pulse. c) Comparison between the Fourier transform of a standard shaped pulse and the DRAG pulse control technique. Here, $\omega_0/2\pi$ is the target frequency while $\omega/2\pi$ is the frequency of a disturbing transition. The drag effect has been accentuated to make it visually more evident.

slightly mixed. Consequently, during the projection procedure, there is a finite probability that an error occurs and the ancilla is in $|\downarrow\rangle$ or vice versa. This incorrect implementation of the correction procedure fails to recover the state and introduce an additional error.

2) **Decoherence during control sequences**: A finite pulse duration causes decoherence effects even during control sequences. The logical state is not encoded in this time interval, so these errors cannot be corrected and inevitably corrupt the information.

3) **Leakage**: Finite-length pulses are not perfectly monochromatic. As a result, there may be contributions to other open transitions, potentially leading to leakage.

The following analysis investigates how these different sources affect the scheme performance. The results of the various simulations are reported in the following subsections, subdivided into electronic and nuclear spins.

3.4.1 QEC on Electronic Spin

Figure 3.4 illustrates the scheme's performance in terms of the infidelity $\mathcal{E}$, calculated as $\mathcal{E} = 1 - \mathcal{F}$, for the two electronic systems (**e1**) (orange) and (**e2**) (blue)

as a function of memory time t/T_2. The dashed grey line corresponds to the case of an uncorrected spin-1/2 subject to decoherence, while the solid black line represents the ideal performance of the presented quantum error correction scheme. In first place, considering an ideal implementation of the pulses but

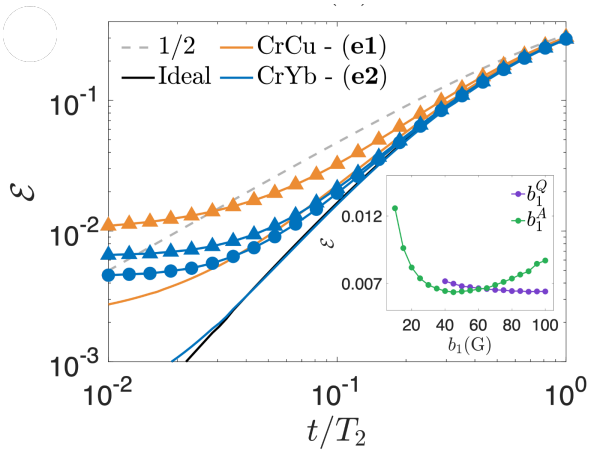

Figure 3.4: Main Panel: performance of the QEC scheme to correct pure-dephasing on an electronic $S = 3/2$ qudit, considering two realistic molecules (**e1**) and (**e2**). The results are plotted as a function of the t/T_2 ratio where t is the memory time and T_2 is the system coherence time. The benchmark for code effectiveness is shown by the grey dotted line, representing the case of an uncorrected qubit. The black line represents the ideal performance of the scheme, taking into account only errors due to decoherence during memory time. The orange and blue lines depict the scheme's performance when ideal pulses are applied, but the qudit-ancilla system is not perfectly factorized for (**e1**) and (**e2**), respectively. Relaxing the assumption of ideal pulses further reduces the scheme's performance, as indicated by triangles and dots (refer to the main text for specific parameters). Inset: scheme performance dependence on the amplitude of driving fields. Adapted from Ref. [161] with permission under the terms and conditions of the Creative Commons Attribution-NonCommercial 3.0 Unported license (CC BY-NC 3.0).

states not perfectly factorized, the contribution of only the first source of errors can be isolated (solid orange and blue lines). These simulations are performed by implementing the various operations through matrix multiplication. While the impact of this source is almost negligible for (**e2**), it significantly limits the performance of the scheme for (**e1**). This difference can be attributed to the larger gap between g_z^A and g_z in the case of (**e2**) compared to (**e1**). For both systems, an external magnetic field of $B_0 = 1$ T is assumed. It is evident that a more effective factorization could be achieved in the case of (**e1**) by utilizing a stronger magnetic field. However, it's essential to note that this would also result in higher

frequencies that are less easily accessible with large driving fields.
Now, relaxing the assumption of instantaneous and monochromatic pulses, leakage and decoherence are also introduced. As previously mentioned, in all the simulations, Gaussian-shaped pulses resonant with the target gaps are exploited. When studying the scheme implementation as a function of the external driving field amplitude b_1^Q, it is evident that leakage is irrelevant for all the transitions inside the qudit subspace. Indeed, as shown in the inset of Fig. 3.4, the error committed monotonically decreases with b_1^Q up to 100 G. The zero-field splitting D together with a sufficiently large magnetic field ensures well-separated and resolved transitions.
The same cannot be said for the transition to excite the ancilla state. These are split by J_z exchange coupling which, for the reasons seen earlier, cannot be too large. In this case the error does not monotonically decrease, and a minimum is found at $B_1^A = 45$ G. This value represents the optimal working point that mediates between leakage and decoherence.
The main panel reports the results for the optimal working point $B_1^Q = 100$ G and $B_1^A = 45$ G considering $T_2^Q = 50$ μs. The latter value, although very optimistic, is achievable for transition metal complexes with properly engineered ligand cage. Regarding the coherence time of the ancilla, $T_2^A = 5$ μs is considered for (**e1**) and two values $T_2^A = 1 - 3$ μs (respectively blue triangles and dots) for (**e2**). In first place, it is important to emphasise that for all the implementations, there is a region where the method is effective and reduces the error compared to the case of an uncorrected qubit. Moving on the left towards shorter t/T_2, all the implementations encounter a plateau, which results from the various forms of uncorrectable errors. In the case of (**e1**), the results are primarily limited by the qudit-ancilla not factorization. From the analysis of the results on (**e2**), it is evident the criticality of the measure procedure. Even if the ancilla stays in the excited state for a very short time, the impact of the error on the state is quite significant. Passing from $T_2^A = 1 - 3$ μs the infidelity is halved, moving from 0.01 to 0.005.

3.4.2 QEC on nuclear spin

This section investigates the QEC scheme implementation on the system (**n**) characterized by a nuclear spin $S = 3/2$ coupled with an electronic spin $S = 1/2$ exploited as an ancillary qubit. Compared to an electronic spin, nuclear spins are characterized by longer coherence times but, at the same, a slower manipulation. Indeed, in the case of nuclear spins in a relatively weak field, pure dephasing is induced by the coupling with the surrounding nuclear spins, which is mediated by the electronic spin. Due to this mechanism, the nuclear T_2 is usually related to the electronic one and generally with values ten times longer [163, 174]. Unfortunately there are no experimental data available for T_2 values of (**n**). However, a reasonable assumption can be made by looking at similar compounds. In particular, its has been recently measured on a vanadyl tetraphenylporphyrinate, which consist of an electronic spin 1/2 coupled with a nuclear spin 7/2, an electronic $T_2 = 68$ μs at 5 K. So, as a first approximation, is reasonable to assume a $T_2 = 68$ μs for the electronic spin and $T_2^A = 0.5$ ms for the nuclear one.

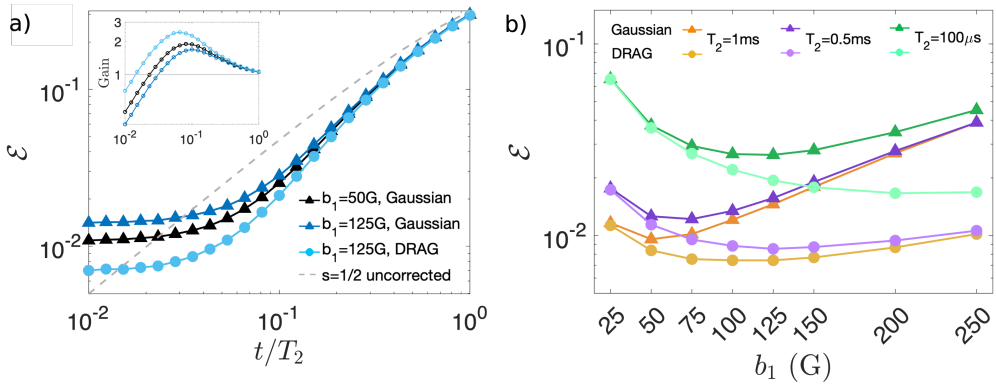

Figure 3.5: a) Performance of the presented QEC scheme to correct pure dephasing on the nuclear $S = 3/2$ qudit (**n**), taking into account various amplitudes and shapes of the driving field. The results are plotted as a function of the t/T_2 ratio where t is the memory time and T_2 is the system coherence time. Inset: The gain, calculated as the ratio between the error committed by the scheme and the benchmark case of the uncorrected qubit. b) Scheme performance as a function of the amplitude of the driving field, considering standard Gaussian-shaped pulses and DRAG, for different coherence times. Adapted from Ref. [161] with permission under the terms and conditions of the Creative Commons Attribution-NonCommercial 3.0 Unported license (CC BY-NC 3.0).

Similarly, as before, the first point to discuss in the implementation is factorization. Thanks to the large separation between nuclear and electric spins in energy,

factorization is not an issue and a nearly perfect factorization is easy to achieve even with relatively small static fields. However, it is important to note that a small residual mixing between nuclear and electronic spins is beneficial to the computation since it is able to enhance nuclear transition matrix elements of ~ 50 times [174, 175]. In the various simulations the external magnetic field has been fixed at $B_0 = 0.1$ T. This value represents an optimal working point that balances factorization error and computation speed.

Setting the $B_1^Q = 50$ G and $B_1^A = 30$ G, the scheme performance is reported in Fig. 3.5 a) (black triangle), while the inset reports the gain calculated as the ratio between the simulation results and the benchmark case of the uncorrected qubit. In a wide region of t/T_2, from 0.8 to 1, the scheme provides an effective gain. However, as observed for (**e**) systems, moving towards smaller t/T_2 values, there is a plateau that limits the efficacy of the code. In this case, the main source of error is leakage. As a first attempt to improve results, one could try to speed up the computation using a larger driving field $B_1^Q = 125$ G for the qudit transition. However, as shown in figure (blue triangles), this strategy is not successful as leakage errors predominate and the code overall performance is reduced. The nuclear qudit transitions, made inequivalent by Q, are not sufficiently spaced to be accurately addressed by such large driving field.

This issue can be mitigated by introducing the DRAG pulse control technique. In the specific, this scheme can be used and is really beneficial to distinguish transitions between $|3/2\rangle \leftrightarrow |1/2\rangle$ and $|-1/2\rangle \leftrightarrow |-3/2\rangle$ from $|1/2\rangle \leftrightarrow |-1/2\rangle$. As shown by the light-blue dots in Fig. 3.5 a), the scheme performance is significantly improved. Unfortunately, this method is not effective in addressing the ancilla excitation transition because more than a single disturbing frequency is present.

Moving on, the same implementation is investigated in Fig. 3.5 b) as a function of the external magnetic field and for different values of T_2. As expected, for all the intensity the DRAG leads to a reduction of error and therefore, an improvement in the scheme correction capability. Focusing on the $T_2 = 0.5$ ms data (violet) the optimal working point with and without drag moves from 50 to 125 G. By reducing the T_2 the effect of decoherence is dominant and the minimum moves to the right side. Conversely, by increasing T_2 leakage becomes dominant, and optimal working points shift on the left side.

3.5 Phase Gate on Encoded States

To achieve a fault-tolerant computation, it is necessary to be able to implement gates on the encoded states. In this section, a strategy for implementing the single

logical qubit phase gate $R_z(\vartheta)$ with an arbitrary angle ϑ on encoded states is presented [161]. By combining this operation with another rotation around a different axis, such as the $R_x(\theta)$ gate introduced in Sec. 4.4.2, any general single-qubit operation can be composed.
In terms of logical states, the action of an $R_z(\vartheta)$ gate is to introduce a relative phase θ between $|0_L\rangle$ and $|1_L\rangle$. Starting from this, it is easy to deduce the necessary transformation for the eigenstates of the system:

$$\begin{aligned} R_Z(\vartheta)\,|\psi\rangle &= \alpha\,|0_L\rangle + \beta e^{i\vartheta}\,|1_L\rangle = \\ &= \frac{\alpha}{2}\left(|3/2\rangle + \sqrt{3}|-1/2\rangle\right) + \frac{\beta}{2}e^{i\vartheta}\left(|-3/2\rangle + \sqrt{3}|1/2\rangle\right) . \end{aligned} \tag{3.9}$$

Therefore, as shown by Eq. 3.9, to implement this operation, it is necessary to introduce a phase θ to the $|-3/2\rangle$ and $|1/2\rangle$ eigenstates. One possible approach, based on the same principles seen for the CPhase gate presented in Sec. 2.3.3, involves the conditionally excitation of the ancilla state based on the qudit state using semi-resonant pulses. In essence, as depicted in Fig. 3.6, the relative phase can be introduced exciting the eigenstates $|-3/2,\downarrow\rangle$ and $|1/2,\downarrow\rangle$ to $|-3/2,\uparrow\rangle$ and $|1/2,\uparrow\rangle$, respectively, with appropriately tuned pulses (blue arrows). Any potential S_z error that occurs on the qudit state during gate implementation can be corrected later using the standard QEC procedure. This approach can easily be extended to larger qudits. However, it is important to note that errors occurring on the ancilla are outside the protected state. Therefore, they inevitably corrupt the encoded state. In order to maximise the effectiveness of the scheme, it is necessary to minimise the ancilla excitation time.

3.6 Conclusions

The study demonstrates the effectiveness of applying a quantum error correction scheme on molecular spin qudits. The proposed scheme exploits a four-level qudit to encode the state of a single qubit and protect it against the first power of S_z error induced by pure dephasing. Specifically, the study examines two distinct types of systems, one based on electronic and the other on nuclear spins. In both cases, an auxiliary qubit, encoded in an electronic spin 1/2, is coupled through exchange or hyperfine interaction and used in the error detection procedure.
Through extensive numerical simulations, the study demonstrates the effectiveness of the scheme in reducing the error rate by up to a 50% compared to the case of an uncorrected qubit.
The study takes into account the various complications of a real implementation, including non-ideal pulses and qudit-ancilla mixing, which influence the

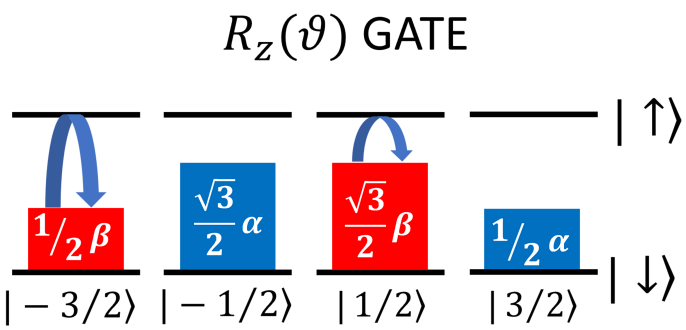

Figure 3.6: Schematic representation of the $R_z(\theta)$ gate implementation on the encoded state of a $S = 3/2$ spin qudit. By semi-resonant pulses (blue arrows) the states $|-3/2,\downarrow\rangle$ and $|1/2,\downarrow\rangle$ are excited to $|-3/2,\uparrow\rangle$ and $|1/2,\uparrow\rangle$. Properly tuning pulse duration a detuning an arbitrary phase can be implemented. Reproduced from Ref. [161] with permission under the terms and conditions of the Creative Commons Attribution-NonCommercial 3.0 Unported license (CC BY-NC 3.0).

scheme's performance. A deep analysis is dedicated to determining the appropriate range of couplings and coherence times necessary for effective error protection. An important aspect of the discussion revolves around the analysis of leakage and the strategies employed to mitigate it. Notably, the implementation of DRAG technique proves highly effective in reducing pulse duration while effectively managing leakage.

Finally, a strategy for implementing a R_z rotation on the encoded state is presented. The implementation of operations on logical states is a crucial step towards the realization of a fault-tolerant scheme. However, due to the limited connectivity between levels in **S** systems, which is restricted to those with $\Delta m = 1$, it is not possible to define other more general rotations, as they require moving outside the protected space. Consequently, fault-tolerant computation is not allowed since errors occurring outside the computational space cannot be corrected. To address this crucial issue, a promising solution may be to use multi-spin molecules, which, under certain conditions, exhibit more extensive connectivity between energy levels. This possibility is discussed in chapter 4.

CHAPTER 4

Theoretical Design of Optimal Molecular Qudits for Quantum Error Correction

In the previous chapter, it was shown how the presented QEC scheme is able to correct pure-dephasing errors. However, the above implementation presents several limitations. In particular, the linear connectivity of single-spin molecules does not allow the implementation of a universal set of gates on encoded states and thus does not allow fault tolerance. This chapter wants to go a step further by exploiting for QEC applications the class of multi-spin molecules, which are theorized to be resilient to decoherence and have a highly connected computational space. As will be shown, these two characteristics significantly improve the performance of the approach.

The study is carried out by comparing the two isostructural molecules **C**2 and **F** introduced in chapter 2. By analysing these molecules with identical structures, it is possible to directly compare the influence of the eigenstate structure on decoherence. The various numerical simulations reported validate the theoretical predictions regarding the resilience against pure-dephasing of the **C** class. This advantage, which grows with the system size, is particularly relevant in the implementation of QEC schemes. **C**2 and **F** are tested as units for QEC both considering an ideal implementation, i.e. with instantaneous and monochromatic control pulses, and when this hypothesis is relaxed. As expected, the **C**2 molecule shows a clear advantage over **F** in both cases. Finally, it is shown how it is possible to implement on **C**2 a $R_x(\theta)$ on encoded states. Together with the R_z gate shown in the previous chapter, this pair of single-body gates provides the basis for a universal set.

The chapter is organized as follows: in the first section 4.1, the two isostructural molecules, **C**2 and **F**, are reintroduced specifying additional details on the structure of the eigenstates. In Section 4.2, the binomial code words to correct pure dephasing, that were introduced in 2.5.1 for the particular case of diagonal eigenstates in the S_z basis, are explicitly calculated in the case of non-diagonal

eigenstates. Section 4.3 looks at detection and recovery processes, generalizing them to d-dimensional cases. In Section 4.4, various results of the numerical simulation in the implementation of the QEC scheme and gates on encoded states are reported. Section 4.5 closes the chapter by summarizing the results.

4.1 Theoretical Design

The analysis focuses on the comparison of the two molecules, denoted as **C**2 and **F**, introduced in Sec. 2.2.2 and 2.4.2 respectively. While the actual parameters considered in the following simulations (see below) are slightly different from those presented in Sec. 2.2.2, it's important to note that the specific choice of parameters doesn't significantly impact the general properties of the molecules. For simplicity and consistency, the same nomenclature is employed.
The molecules are described by the Hamiltonian:

$$H = \sum_{i>j} J_{i,j} \mathbf{s}_i \cdot \mathbf{s}_j + \sum_{i>j} D_{i,j} (s_i^x s_j^y - s_i^y s_j^x) + \mu_B B \sum_i g_i s_i^z, \tag{4.1}$$

comprising six $s_{1-6} = 1/2$ spins, such as Cu^{2+}, and a $S_7 = 3/2$ ion in the centre, such as Cr^{3+}, disposed in a double-tetrahedron structure similar to Ni_7 [128] (see Fig. 4.1 a)). Typical values for $g_i \sim 2.1 - 2.3$ has been considered see Ref. [125]. The exchange couplings are $J_{1,2} = 1.14$ meV, $J_{1,3} = J_{2,3} = 1.15$ meV, $J_{4,5} = 1.13$ meV, $J_{4,6} = J_{5,6} = 1.10$ meV, $J_{1,7} = 0.82$ meV, $J_{2,7} = 0.85$ meV, $J_{3,7} = 0.87$ meV, $J_{4,7} = 0.83$ meV, $J_{5,7} = 0.81$ meV, $J_{6,7} = 0.90$ meV. For the DMI interaction, a reasonable choice is $D_{i,j} = J_{i,j}/10$. In the case of **F** the signs are reversed giving raise to a ferromagnetic coupling. As detailed in Sec. 2.2.2, **C**2 exhibits eight low-energy doublets, constituting a potential 16-level computational subspace. In contrast, regardless of the specific values of J, **F** exhibits a $S = 9/2$ ground multiplet, resulting in a subspace of up to 10 levels. In the former case, the eigenstates are magnetically similar and thus characterized by small differences between the expectation values of the local spin operators. This is quantified in Fig. 4.1 b) where the blue dots represent the expectation value of $\langle s_z \rangle$ calculated on different eigenstates (taking one from each Kramers doublet). This is also reported in more detail in panel c), where the detailed distribution of $\langle s_i^z \rangle / s_i$ over different sites is shown. Conversely, in **F** the mean value $\langle m | s_j^z | m \rangle = m/9$ is strongly dependent on the eigenstate, as indicated by the red asterisk in Fig. 4.1 b).
As illustrated in Fig. 4.1 d), this difference in eigenstate structure results in a significant difference in coherence decay for these two systems. In these simulations, the systems, once initialized in a specific initial state ψ_0, are left under the influence of decoherence to then measure the fidelity as $\mathcal{F} = \langle \psi_0 | \rho | \psi_0 \rangle$ where

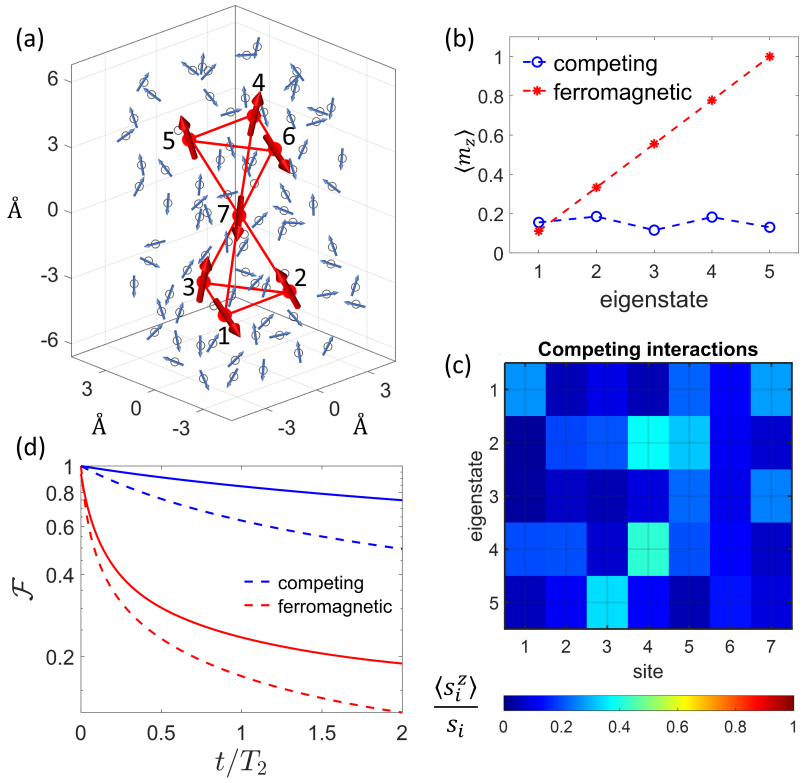

Figure 4.1: a) Hypothetical **C**2 and **F** systems composed by six $s = 1/2$ and a central $S = 3/2$ ion (red arrows). The clusters are surrounded by a random distribution of nuclear $s = 1/2$ ions (blue arrows) maintaining a minimum distance of 2 Å around each ion. b) Average expectation values of local spin operators $\langle m_z \rangle$ on different eigenstates (one for each of the lowest 5 Kramers doublets) for **C**2 (blue) and **F** (red). c) Distribution of expectation values of local spin operators $\langle s_i^z \rangle / s_i$ on various sites and eigenstates of **C**2. d) Fidelity as a function of memory time in terms of t/T_2 calculated on a state under the effect of decoherence. The initial state is a uniform superposition, i.e. a state equally populated on all qudit levels, (dashed lines) or the encoded state $(|0_L\rangle + |1_L\rangle)/\sqrt{2}$ (solid). Reproduced from Ref. [129] under the terms and conditions of the Creative Commons Attribution license (CC-BY 4.0).

ρ is the evolved density matrix. In particular, dashed lines refer to a generic uniform superposition, i.e. a state where all computational levels are equally populated with non-zero phases, while solid lines refer to the encoded state $(|0_L\rangle + |1_L\rangle)/\sqrt{2}$. For both the initial states, the measured fidelity is remarkably higher for **C**2 compared to **F**.

4.2 Codewords Derivation

The overall approach and methodology to define Kraus operators and thus code words to correct pure-dephasing are derived in Sec. 2.5. Here, that approach is extended to the case of systems with eigenstates not diagonal on the basis of S_z. The error operators $\mathcal{E}_a$, that previously were naturally derived from S_z operators as $\mathcal{E}_a = \sqrt{\frac{(2t/T_2)^2}{a!}}\, e^{-S_z^2 t/T_2}\, S_z^a$, now exhibit a more complex form.
The starting point is the solution of the Lindblad equation for the pure dephasing mechanism obtained in the Sec. 2.4, which is given here in the form

$$\rho(t) = \sum_{\mu,\nu} \rho_{\mu\nu}(0) e^{-\gamma_{\mu\nu} t} \left|\mu\right\rangle \left\langle\nu\right| \quad , \tag{4.2}$$

and the goal is to define a set of error operators $\mathcal{E}_a$ such that

$$\rho(t) = \sum_a \mathcal{E}_a \rho(0) \mathcal{E}_a^\dagger \quad . \tag{4.3}$$

From Eq. 4.2 it is easy to see that $\mathcal{E}_a$ must be diagonal and therefore there exist only d linearly independent operators where d is the system size [118]. In practice, these can be obtained by Quantum Process Tomography as explained in Ref. [10]. The $\mathcal{E}_a$ operators can always be reformulated in terms of projectors $\tilde{\mathcal{E}}_\mu = |\mu\rangle\langle\mu|$ onto the eigenstate basis:

$$\mathcal{E}_a = \sum_{i=1}^{d} \epsilon_{ia} \tilde{\mathcal{E}}_i \quad . \tag{4.4}$$

The evolution of the density matrix under the action of error operators takes the form:

$$\begin{aligned} \rho(t) &= \sum_{a=1}^{d} \tilde{\mathcal{E}}_a \rho(0) \tilde{\mathcal{E}}_a^\dagger \\ &= \sum_{i,j=1}^{d} \chi_{ij} \tilde{\mathcal{E}}_i \rho(0) \tilde{\mathcal{E}}_j^\dagger \, , \end{aligned} \tag{4.5}$$

where $\chi ij = \sum_a \epsilon_{ia} \epsilon_{ja}^*$. The elements of χ_{ij} matrix correspond to the experimental decay rates $e^{-\gamma_{ij} t}$. Given $V^\dagger$ and ξ as the matrix and the corresponding vector, respectively, that diagonalise χ:

$$\chi_{ij} = \sum_m V_{im} \xi_m V_{jm}^* \, , \tag{4.6}$$

the Kraus operators are expressed in terms of system eigenstates as:

$$\mathcal{E}_a = \sqrt{\xi_a} \sum_\mu V_{\mu a} \tilde{\mathcal{E}}_\mu = \sqrt{\xi_a} \sum_\mu V_{\mu a} \left|\mu\right\rangle \left\langle\mu\right| \, . \tag{4.7}$$

The errors with the larger eigenvalues $\sqrt{\xi_a}$ are the leading ones, and therefore have priority for correction.
Having established the error operators, the remaining task is to explicitly determine the codewords. Similarly as done in Sec. 2.5, these are as orthogonal superpositions of the system eigenstates:

$$\begin{aligned} |0_L\rangle &= \sum_{\mu\in A} a_\mu |\mu\rangle \\ |1_L\rangle &= \sum_{\mu\in B} b_\mu |\mu\rangle , \end{aligned} \tag{4.8}$$

where A and B define two separated subspaces of $d/2$ eigenstates $|\mu\rangle$. The second Knill-Laflamme condition 1.49 is automatically fulfilled since $\mathcal{E}_a$ operators do not mix $|0_L\rangle$ and $|1_L\rangle$ by construction, as can be seen from Eq. 4.7.
Regarding the first condition, it is met if the set of conditions:

$$\sqrt{\xi_a\xi_j}\sum_{\mu\in A} V_{\mu a}V^*_{\mu j}|a_\mu|^2 = \sqrt{\xi_a\xi_j}\sum_{\mu'\in B} V_{\mu' a}V^*_{\mu' j}|b_{\mu'}|^2 \ , \tag{4.9}$$

valid for $j,k = 0,...,d/2-1$, combined with the two normalization conditions $\sum_\mu |a_\mu|^2 = \sum_\mu |b_\mu|^2 = 1$, are respected. This system is generally overdetermined, and hence at least one solution can be found, either by matrix pseudo-inversion or by numerical optimization. It is important to note that since the specific coefficients depend on the ratio t/T_2 at which χ is calculated, the defined codewords are optimised for a particular time.

4.3 Detection and Recovery Procedures

Besides the encoding, QEC scheme comprises other two essential steps: the detection and recovery procedures. These steps are crucial for identifying and correcting errors that occur. In Section 3.2, these procedures have been specified for the case of a four-level qudit. In essence, an ancillary qubit's state is entangled with that of the qudit, allowing the detection of errors by measuring the qubit's state. Subsequently, an error-dependent recovery procedure is employed to restore the original state. Here, these procedures are generalized for a d-dimensional qudit. Given the codewords $|0_L\rangle, |1_L\rangle$ and the set of error operators $\mathcal{E}_{a=1,...,d/2}$ that the codewords correct, the orthonormal basis of the so-called error words $\{|e^0_a\rangle, |e^1_a\rangle\}$, $a = 0,...d/2-1$ can be defined as span$\{\mathcal{E}_a|0_L\rangle\}_{a=1,...,d/2}$ and span$\{\mathcal{E}_a|1_L\rangle\}_{a=1,...,d/2}$. These error-affected states represent all the possible corrupted states that the code is capable to correct. Error detection aims to identify these states in order to apply the appropriate correction. The identification

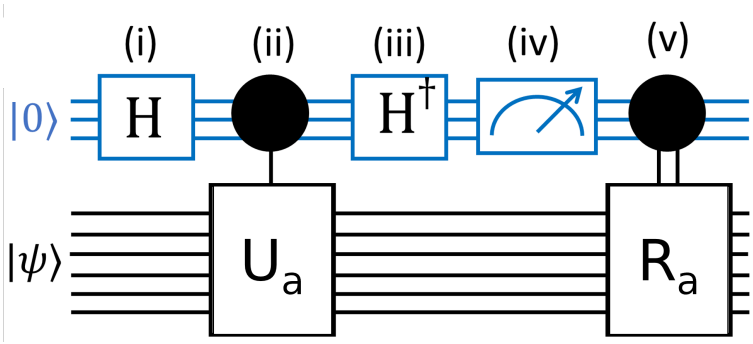

Figure 4.2: Quantum circuit to detect (i,ii,iii) and recover (iv,v) errors $\mathcal{E}_a$ induced by pure dephasing mechanism on a d dimensional qudit (black lines). The system is initialized in the state $|\psi\rangle = \alpha|0_L\rangle + \beta|1_L\rangle$ and the $d/2$ dimensional ancilla (blue lines) is exploited to access the qudit state without affecting it. The latter is initialised in state $|0\rangle$ and then a generalised H-gate is applied. Then, depending on the ancilla state, a different controlled unitary evolution U_a is applied for each $\mathcal{E}_a$ error in the qudit. Next, a $H^\dagger$ gate is applied to the ancilla and it is measured. Depending on the result of the measurement, a different recovery operation R_a is applied. Adapted from Ref. [129] under the terms and conditions of the Creative Commons Attribution license (CC-BY 4.0).

procedure involves to measure the projectors $P_a = |e_a^0\rangle\langle e_a^0| + |e_a^1\rangle\langle e_a^1|$. Directly applying these projectors onto superposition states of the system eigenstates can be operationally complex. An alternative strategy involves utilizing a $d/2$-level ancillary qudit entangled with a different error word (see Fig. 4.2). In this way, measuring the ancilla on its eigenstates automatically projects the qudit into one of the error states. At the beginning of the process, the ancilla is in its ground state $|0\rangle$ while the qudit originally initialized in the protected state $\alpha|0_L\rangle + \beta|1_L\rangle$, is now in the state ψ on which decoherence has acted. The combined ancilla-qudit state is given by the tensor product $|\Phi\rangle = |0\rangle \otimes |\psi\rangle$. Applying a generalized qudit Hadamard gate (i), $\mathrm{H} = \sqrt{\frac{2}{d}}\sum_{j,a=0}^{d/2-1} e^{i\frac{4\pi}{d}ja}|j\rangle\langle a|$, brings the ancilla state to a uniform superposition $|+\rangle = \sqrt{\frac{2}{d}}\sum_a |a\rangle$. The combined qudit-ancilla state is then $|\Phi\rangle = |+\rangle \otimes |\psi\rangle$. At this stage, a conditional evolution of the system $U_a = \sum_{j=0}^{d/2-1}\sum_{\ell=0,1} e^{i\frac{4\pi}{d}ja}\left|e_j^\ell\right\rangle\left\langle e_j^\ell\right|$ (ii), dependent on the ancilla's state, is implemented. The combined state becomes $|\Phi\rangle = \sqrt{\frac{2}{d}}\sum_{aj}\sum_\ell e^{i\frac{4\pi}{d}ja}\eta_j^\ell|a\rangle\left|e_j^\ell\right\rangle$.

Finally, applying $H^\dagger$ to the ancilla (iii), the combined state $|\Phi\rangle = \sum_j\sum_\ell \eta_j^\ell|j\rangle\left|e_j^\ell\right\rangle$ is an entangled state where each ancilla eigenstate corresponds to a different error state. Measuring the ancilla makes the qudit collapse into one of the error states (iv). With knowledge of the measurement result, correction becomes possible

by implementing an appropriate $R_a = \sum_\ell |e_0^\ell\rangle\langle e_a^\ell| + \text{h.c.}$ and then rotating back $\alpha|e_0^0\rangle + \beta|e_0^1\rangle \to \alpha|0_L\rangle + \beta|1_L\rangle$ (v).

4.3.1 Implementation of U_a

A crucial point for the effectiveness of the scheme is the implementation of U_a rotations. For a given U_a it is necessary to identify the effective Hamiltonian $\tilde{\mathcal{H}}_a = -\sum_{j,l} \frac{4\pi}{d} ja\, |e_a^l\rangle\langle e_a^l|$ from which it is generated $U_a = e^{-i\tilde{\mathcal{H}}_a}$. Thus, the implementation of U_a consists in the quantum simulation of the $\tilde{\mathcal{H}}_a$ operator. Since the diagonal and off-diagonal terms of the Hamiltonian do not commute, the implementation requires a Suzuki-Trotter decomposition. Given the full connectivity between computational levels in **C**2, this procedure can be efficiently implemented in two sequences of pulses: one for the off-diagonal terms $\langle\mu|\tilde{\mathcal{H}}_a|\nu\rangle$ and one for the diagonal terms $\langle\mu|\tilde{\mathcal{H}}_a|\mu\rangle$. Specifically, for off-diagonal terms, the transitions $|\mu\rangle \to |\nu\rangle$ are addressed with resonant pulses, while for diagonal terms, conditional excitations of the ancilla state with semi-resonant pulses are used.
The precision of the implementation depends directly on the number of trotter steps implemented. However, it is important to note that since all the required operations have an implementation time proportional to the implemented angle, increasing the number of trotters does not lengthen the pulse sequence duration.

4.4 Results

This section compares the performance of the two isostructural molecules **C**2 and **F** in implementing the QEC scheme presented above 4.4.1. The main difference between them is the type of interactions that take place between the different magnetic ions, either anti-ferromagnetic (competing) or ferromagnetic, which results in a different structure of the low-energy eigenstates. First, ideal control techniques are assumed, then this assumption is relaxed and finite pulse lengths are considered. Finally, it is shown how to implement the gate on the encoded states 4.4.2.

4.4.1 Quantum Error Correction

As a starting point, it is opportune to evaluate the code's performance through an ideal implementation, i.e. considering instantaneous and monochromatic pulses. This implies that the errors in the simulations stem solely from the effects of decoherence. As illustrated in Fig. 3.2, pure dephasing is introduced into the system during the memory time, which represents the simulation time. For simplicity,

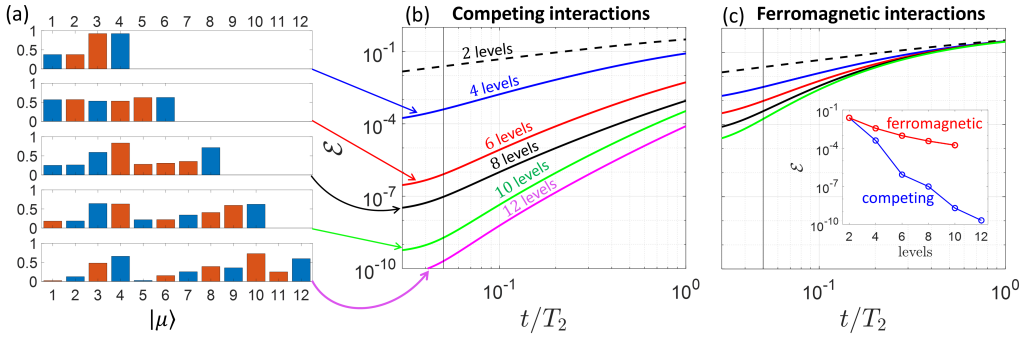

Figure 4.3: a) Absolute value of the code word component for different size quits. The blue and red components refer to $|0_L\rangle$ and $|1_L\rangle$ respectively. Panels b) and c) show the performance in terms of the error $\mathcal{E} = 1 - \mathcal{F}$ as a function of t/T_2 for the ideal implementation of the QEC scheme on **C**2 and **F** systems. Inset: comparison between **C**2 and **F** errors at $t/T_2 = 0.05$. Reproduced from Ref. [129] under the terms and conditions of the Creative Commons Attribution license (CC-BY 4.0).

no gates are applied during this period. Fig. 4.3 shows the error, calculated as $\mathcal{E} = 1 - \mathcal{F}$, for **C**2 and **F** as a function of the ratio t/T_2 considering different qudit size $d = \{4,6,8,10,12\}$. In panel a), the absolute values of the different codewords, blue and red for $|0_L\rangle$ and $|1_L\rangle$ respectively, are depicted. This has been obtained by numerically solving the system 4.9. In the encoding, the qudit is initialized in the "error prone" state $\psi_0 = (|0_L\rangle + |1_L\rangle)/\sqrt{2}$.

The scheme applied to both systems is effective in reducing the error with respect to the uncorrected case of a qubit (dashed black line). Similar to what was observed in the ideal case, by increasing the number of levels and thus the correction capability of the scheme, the more $\mathcal{E}_a$ errors can be corrected, the more the final error is reduced. Reducing the memory time also reduces the error, but unlike the ideal case shown in Fig. 2.7, there is a plateau at the smallest values. This is due to the fact that the code words are optimised (see Sec. 4.2) for a certain value of $t/T2 = 0.05$ (vertical black line in panels b) c)).

If panels b) and c) are now compared with each other, it is evident how **C**2 characterized by competing interactions, performs much better with respect to **F** characterized by ferromagnetic interactions. In the inset of Fig. 4.3 c), the errors at optimized value $t/T_2 = 0.05$, are directly compared. For a ten level qudit, the remaining error of **C**2 is five orders of magnitude smaller. This striking gain proves that the resilience of systems characterised by magnetically similar levels is fundamental and gives great advantages for QEC.

An actual realization of such a scheme must address other challenges. Firstly, control sequences cannot be approximated as instantaneous. Hence, hereafter

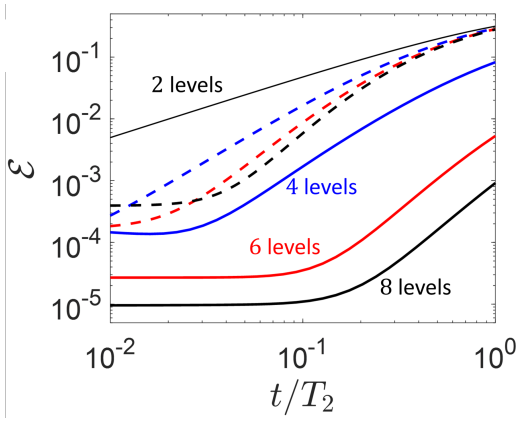

Figure 4.4: QEC scheme performance on **C**2 (solid lines) and **F** (dashed lines) for different qudit sizes taking into account errors due to the finite pulse sequence length. Adapted from Ref. [129] under the terms and conditions of the Creative Commons Attribution license (CC-BY 4.0).

the condition of instantaneous pulses is relaxed while still considering monochromatic pulses. Leakage, induced by the non-monochromaticity of pulses, is a technical difficulty strictly system-specific that can be addressed using sophisticated pulse control techniques [172, 176, 177]. The main difference in these simulations lies in the added impact of pure dephasing during pulse implementation, which introduces additional errors. During these stages, namely encoding detection and recovery, the state is not protected and hence the errors inevitably corrupt it. As shown in Fig. 4.4, this leads to a decrease in the performance of the scheme for both implementations compared to the previous case. However, if **F** (dashed lines) shows a reduction of the correction capacity increasing the number of levels, **C**2 (solid lines) is still able to reduce errors when increasing the qudit size. The key difference among the two systems, is the connectivity between qudit levels: **C**2 has a full connectivity, while **F** only has linear connectivity (see 2.3.1). Due to the limited connectivity among levels in **F**, pulse sequences require additional π pulses, the number of which increases with qudit size. As the size grows, these sequences become longer, introducing more errors. In contrast, the correction capability of the code diminishes, correcting fewer significant errors. Consequently, scaling up the qudit size is no longer advantageous due to these effects.

4.4.2 Computation on encoded qubits

A necessary condition in the realization of fault-tolerant computation is the ability to implement gates on encoded states. Here, the strategy for implementing a generic planar rotation $R_x(\theta)$ is introduced for the case of a four-level qudit. The same approach can be extended to larger qudits.
As seen above 4.8, the logical states are defined as a superposition of eigenstates and in this specific case take the form:

$$\begin{aligned} |0_L\rangle &= \cos(\phi)\,|1\rangle + \sin(\phi)\,|4\rangle \\ |1_L\rangle &= \cos(\chi)\,|2\rangle + \sin(\chi)\,|3\rangle \ , \end{aligned} \tag{4.10}$$

where $1,2,\ldots,4$ identify system eigenstates, and the angles ϕ and χ depend on the time at which the code words are optimized. In terms of these states, a planar rotation $R_x(\theta)$ is defined as follows:

$$\begin{aligned} R_x(\vartheta) = \quad & \cos\frac{\vartheta}{2}\left(|0_L\rangle\langle 0_L| + |1_L\rangle\langle 1_L| + |\varepsilon_0\rangle\langle\varepsilon_0| + |\varepsilon_1\rangle\langle\varepsilon_1|\right) \\ - \quad & i\sin\frac{\vartheta}{2}\left(|0_L\rangle\langle 1_L| + |1_L\rangle\langle 0_L| + |\varepsilon_0\rangle\langle\varepsilon_1| + |\varepsilon_1\rangle\langle\varepsilon_0|\right) \ , \end{aligned} \tag{4.11}$$

where the corrupted states $|\varepsilon_0\rangle$ and $|\varepsilon_1\rangle$ are defined as:

$$\begin{aligned} |\varepsilon_0\rangle &= \sin\phi\,|1\rangle - \cos\phi\,|4\rangle \\ |\varepsilon_1\rangle &= \sin\chi\,|2\rangle - \cos\chi\,|3\rangle \ . \end{aligned} \tag{4.12}$$

The Hamiltonian that generates this transformation, $R_x(\theta) = e^{-i\mathcal{H}_{R_x}\theta/2}$, is defined as follows:

$$\mathcal{H}_{R_x} = |0_L\rangle\langle 1_L| + |1_L\rangle\langle 0_L| + |\varepsilon_0\rangle\langle\varepsilon_1| + |\varepsilon_1\rangle\langle\varepsilon_0| \ , \tag{4.13}$$

which, when rewritten in terms of system eigenstates, takes the form:

$$\mathcal{H}_{R_x} = \cos(\phi-\chi)\left(|1\rangle\langle 2| + |3\rangle\langle 4|\right) + \sin(\phi-\chi)\left(-|1\rangle\langle 3| + |2\rangle\langle 4|\right) + \text{h.c.} \ . \tag{4.14}$$

From the latter equation, one deduces that an $R_x(\theta)$ can be implemented with two resonant pulses between $|1\rangle \to |2\rangle$ and $|4\rangle \to |3\rangle$ transitions of angle $2\arcsin\left[\cos(\phi-\chi)\sin\frac{\vartheta}{2}\right]$ and two pulses between $|1\rangle \to |3\rangle$ and $|2\rangle \to |4\rangle$ transitions of angle $2\arcsin\left[\pm\sin(\phi-\chi)\sin\frac{\vartheta}{2}\right]$. As often happens, $\phi \approx \chi$ and therefore the last operations do not need to be implemented.
Thanks to full connectivity between computational levels, **C**2 is able to directly implement the global transformation in a single step, while remaining within

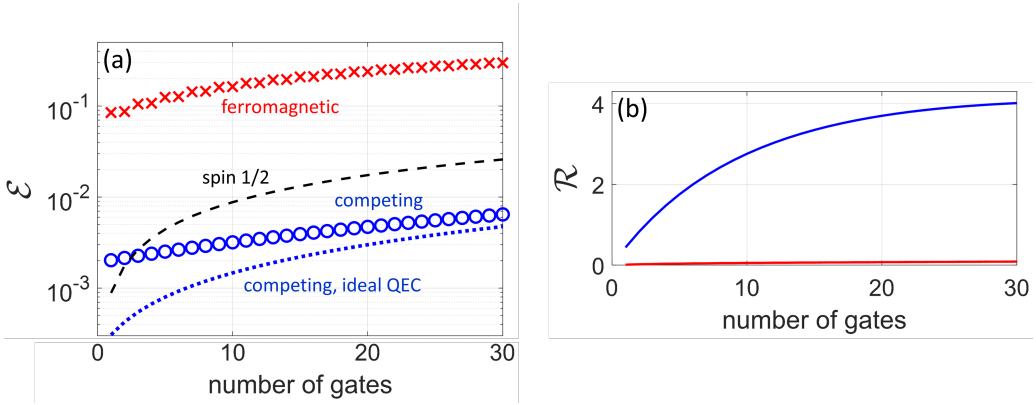

Figure 4.5: a) Infidelity as a function of the number of subsequent implementations of $R_x(\theta)$ gates on C2 (blue circles) and F (red crosses). b) Gain calculated as the ratio between the errors for corrected and uncorrected cases. Adapted from Ref. [129] under the terms and conditions of the Creative Commons Attribution license (CC-BY 4.0).

the protected space. This observation is valid independently of qudit size. Conversely, the linear connectivity between the qudit levels of **F** imposes the introduction of additional π pulses in the sequence, which, apart from introducing additional operations whose number grows with the qudit size, temporarily take the logical state out of the protected space. The errors generated by decoherence, which occur during the implementation of the gates, cannot be corrected. In conclusion, this procedure applied to systems with linear connectivity does not allow fault-tolerant computation.

Figure 4.5 presents the results of a numerical simulation testing the provided procedure for $R_x(\pi)$ on both **C**2 and **F** systems. The simulation assumes a gate time τ, and after each application, a 2τ memory time is observed, with a coherence time of $T_2 = 10^3\tau$. Similar to previous scenarios, the impact of leakage is neglected.

In this particular application, the QEC scheme applied to **F** (red crosses) is not convenient, introducing a higher error compared to the uncorrected case (black dashed line). Conversely, the greater resilience of **C**2 (blue circle) against decoherence, coupled with the capability to implement gates within the protected space, results in a significant gain, reducing the error by up to four times (see blue line in the right panel).

4.5 Conclusions

The analysis revolves around the comparison of the two hypothetical molecules **C**2 and **F** as units for the realization of embedded schemes of QEC. These systems are characterized by the same physical structure but a different type of interactions (anti-ferromagnetic and ferromagnetic, respectively), leading to a different low energy spectrum. In particular, **C**2 has several magnetically similar doublets, while **F** has an S ground multiplet. In practice, the effect of decoherence results to be suppressed in **C**2 compared to **F**. This feature along with the large connectivity of between levels turn out to be an advantage for QEC realization. On **C**2 it is also possible to realize R_x gates on the encoded states. This is a fundamental step towards fault tolerance.

CHAPTER 5

Molecular Nanomagnets for Qudit-Based Quantum Computation

In this chapter, single spin (**S**) and multi spin with competing interactions (**C**) systems, introduced in Chapter 2, are compared as elementary units for a qudit computation. The aim is to show how pure-dephasing affects these two classes differently, and thus their performance as computational units. As theorized in Chapter 2, thanks to the particular structure of its eigenstates, **C** is expected to be more resistant to decoherence compared to **S** and thus more effective as a unit. These systems are tested in the implementation of single and two-qudits gates.

With regard to single qudit gates, the two decomposition techniques introduced in Sec. 1.9.2, namely Planar Rotation (PR) and Quantum Householder Reflection (QHR), are exploited to efficiently break down general single qudit gates into simpler operations directly implementable in the hardware [81, 138]. In essence, PR is generally simpler and applicable across all systems, while QHR, although potentially more efficient, demands more stringent conditions. The study explores these methods, comparing their respective advantages and disadvantages. As a test case, the decomposition of the d-dimensional Hadamard gate is investigated. The implementation of this operation is of particular interest both because it is challenging, requiring several elementary operations, and because this gate is used in several algorithms.

For two qudit gates, the generalised control-phase gate is implemented on the two classes using the qudit-switch-qudit scheme introduced in Sec. 2.3.2. In the analysis, the parameter range within which the scheme operates effectively is discussed.

Summarizing, the chapter is organized as follows: Sec. 5.1 shows in an illustrative manner how to use and implement PR and QHR decomposition techniques. Then, in Sec. 5.2, the hypothetical systems taken under investigation

are introduced. Sec. 5.3 reports the results of the different numerical simulations, while Sec. 5.4 summarises some considerations and closes the chapter. The appendix 5.5 reports the parameters for the decomposition of the different Hadamard gates for both techniques.

5.1 Single Qudit Gate Decomposition Strategies

In the first chapter 1.9, two techniques, namely Planar Rotation and Quantum Householder decomposition, were introduced for breaking down arbitrary single qudit gates into simpler operations that can be implemented directly in hardware [81–83]. Here, these are resumed with a focus on implementation.

5.1.1 Planar Rotation Decomposition

The Planar Rotation Decomposition is based on the homonym planar rotation that has already been discussed in 2.3.1). The main feature of this method is that it can be implemented given any connectivity of the computational subspace. The standard pulse sequence derivation supposes a full connectivity (Fig. 5.1 a)), i.e. all levels connected with all others. In fact, there are planar rotations between all pairs of levels. However, if a such connectivity is not present, this limitation can be easily overcome by introducing additional planar rotations of angle π. These operations, commonly referred to as π pulses, are used to move information around the computational space, thus enabling those operations that cannot be implemented directly. In general, therefore, this decomposition can be implemented on any connected subspace at the price of reduced decomposition efficiency. Considering a single-spin qudit, electromagnetic pulses oriented perpendicularly to the direction of the static magnetic field can induce transitions between eigenstates with $\Delta m = \pm 1$. In other words, the matrix elements of $M_{x/y} = gS_{x/y}$ give a linear connectivity (Fig. 5.1 b)). If the minimum number of operations to decompose a generic unitary is $\frac{d(d-1)}{2}$, the linear connectivity requires $(d-1)(d-2)$ additional π pulses.

The second method, Quantum Householder Reflection decomposition (QHR) 1.9.2, is significantly more efficient, requiring only d non-parallel operations, but it demands a more complex connectivity, specifically a pod-connectivity (Fig. 5.1 c)). The elementary operation on which the decomposition is based is the Quantum Householder reflection. The following section explains how to calibrate pulses to implement this transformation on hardware.

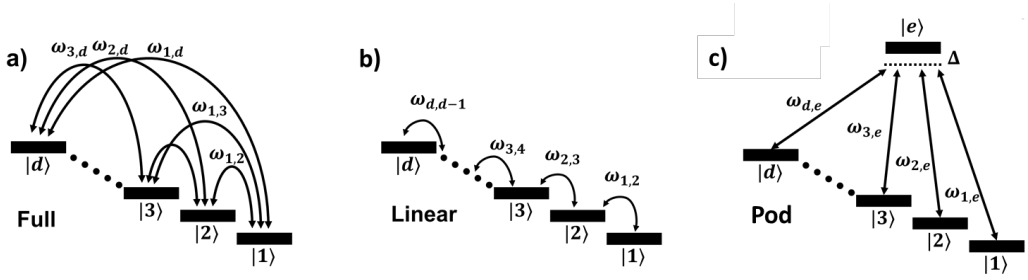

Figure 5.1: Schematic representation of "Full", "Linear", and "Pod" connectivity. $\omega_{i,j}$ indicates the frequency of the open transition for each connectivity scheme. Adapted from Ref. [127] under the terms of the Creative Commons Attribution 4.0 International license.

5.1.2 Quantum Householder Reflection Decomposition

Also the second method under consideration, generalized quantum householder reflection decomposition, takes its name from the elementary operation on which it is based, namely, the generalized quantum householder reflection defined in Eq. 1.84. Sec. 1.9.2 shows how to decompose an arbitrary matrix and thus derive the parameters for the various operations. However, it is necessary to explain how these mathematical transformations can be implemented by electromagnetic pulses.

To implement a d dimensional transformation, a $d+1$-level system is required, consisting of d levels belonging to the computational space and an auxiliary level $|e\rangle$. In principle, each operation requires d simultaneous semi-resonant pulses, i.e. that start and finish together, that target all the d transitions between the computational subspace and the auxiliary level. As anticipated, a pod-connectivity is therefore necessary (see Fig. 5.1). The vector $|v\rangle$ and phase ϕ that define the operation (see Eq. 1.84) determine the relative amplitudes, phases and detuning of the pulses [127]. Specifically, the amplitude of the pulses is proportional to the norm of the corresponding entry in the $|v\rangle$ vector. Similarly, the relative phases of the pulses are determined by the relative phases among the $|v\rangle$ entries. On the other hand, the phase ϕ determines the detuning of the pulses. Considering rectangular shaped pulses, the duration τ and detuning Δ are determined as follows:

$$\begin{aligned} \tau &= \sqrt{\frac{\phi(2\pi - \phi_i)}{\Omega_{1e}^2 + \cdots + \Omega_{de}^2}} \\ \Delta &= \pm\frac{\pi - \phi}{\tau} \quad , \end{aligned} \tag{5.1}$$

where $\Omega_{i,e}$ are the Rabi frequencies of the transitions among the computational

subspace and auxiliary level $|e\rangle$.

5.2 Physical Systems

The analysis considers three systems within the class of single-spin and two within the class of multi-spin systems with competing interactions (see 2.2 f). Among the latter, the systems under consideration are the copper triangle denoted as **C**1 and the double-tetrahedron denoted as **C**2, previously introduced in Sec. 2.2.2. These systems have been extensively discussed and thus require no further elaboration. For class S, three mononuclear systems among those presented in 2.2.1 are considered. A Cr^{3+} ion can be modelled as an $S = 3/2$ spin, thus providing a computational space of up to 4 levels. When placed within an octahedral crystal field, typical parameters include $D = 30$ μeV and $g = 1.98$ (**S**1). A spin of $S = 5/2$, offering up to 6 computational levels, can be provided by a Mn^{2+} or Fe^{3+} ion. Within the same ligand cage, reasonable parameters are $D = 30$ μeV and $g = 2.0$ (**S**2). Lastly, a spin of $S = 7/2$, allowing for up to 8 computational levels, can be generated by the Gd^{3+} ion. Typical parameters are $D = 20$ μeV and $g = 2.0$ (**S**3) [121].

5.3 Results

This section presents the various results obtained from numerical simulations. These are presented separately for one and two qubit gates.

5.3.1 Single Qudit Gates

Regarding single qudit gates, the systems under investigation have been tested in the implementation of the qudit Hadamard gate (H_d) using both PR and QHR decomposition methods. The H_d gate is defined as follows:

$$H_d = \frac{1}{\sqrt{d}} \sum_{\mu,\nu=1}^{d} e^{i\frac{2\pi}{d}(\mu-1)(\nu-1)} |\mu\rangle \langle\nu| , \tag{5.2}$$

where $|\mu\rangle$ and $\langle\nu|$ represent qudit levels. This operation represents a d-dimensional discrete quantum Fourier transform, and it is of interest as it is used in many applications such as Shor's factorization algorithm. The implementation of this gate serves as a benchmark to test the decomposition schemes and the performance of the systems.
In the following analysis, qudits of different sizes are examined. The accuracy of the different implementations is evaluated using the error $\mathcal{E}$ (or infidelity),

calculated as $1 - \langle\psi|\rho|\psi\rangle$, where ψ is the exact solution and ρ the evolved system density matrix.
The results reported in the main panels are averaged on thirty different initial states $|\psi_0\rangle$ characterized by a equally distributed population and random phases $|\psi_0\rangle = \sum_\mu e^{i\varphi_\mu} |\mu\rangle / \sqrt{d}$. These states are very error prone because all the components are populated and thus subject to decoherence. Instead, to verify the general validity of the study, the results reported in the insets are averaged over thirty completely randomly generated states.

Low Dimensional Qudits

In the first place, the systems (**C**1) and (**S**1), both of which provide a four-level computational space, are compared in the implementation of the H_4 gate using PR decomposition. Given the full connectivity, on (**C**1) the implementation can be done straightforwardly, and it requires six not parallelisable planar rotations and a phase gate. On the other hand, due to the linear connectivity for (**S**1), in addition to those operations, six extra π pulses must be introduced. The exact sequences of operations are reported in the Appendix (see Eq. 5.4 and Tab. 5.4).

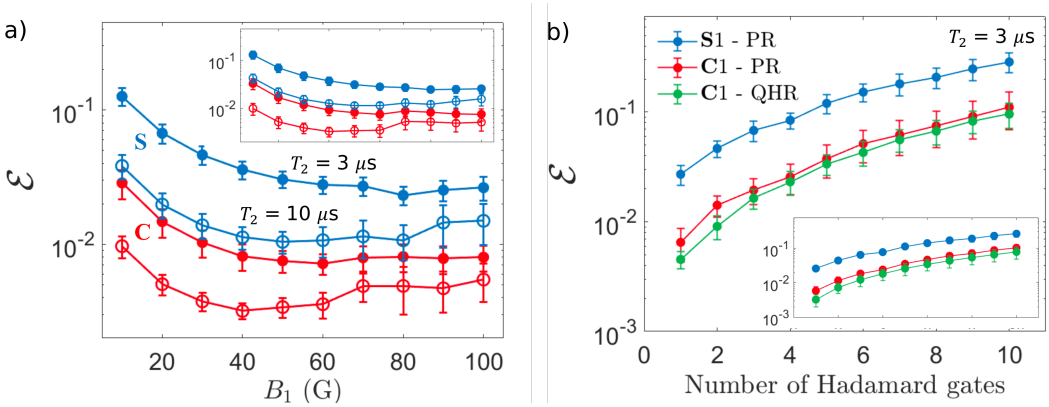

Figure 5.2: a) Implementation errors in the H_4 gate decomposed by PR on **S**1 (blue) and **C**1 (red) systems plotted against the external driving field amplitude B_1. Results are shown for two distinct coherence times, $T_2 = 3$ μs (full dots) and $T_2 = 10$ μs (empty dots). b) Error in the subsequent application of H_4 and H_3 gates, decomposed by PR or QHR, for **S**1 (blue) and **C**1 (red and green) systems. Simulations are based on a coherence time $T_2 = 3$ μs. In the main panels, results are averaged over thirty equally distributed superpositions $|\psi_0\rangle = \sum_\mu e^{i\varphi_\mu} |\mu\rangle / \sqrt{d}$, while in the inset, results are based on thirty random states. Adapted from Ref. [127] under the terms of the Creative Commons Attribution 4.0 International license.

Panel a) of Fig. 5.2 shows the infidelity for the various implementations as a

function of the amplitude of the external driving field B_1. Two values of T_2 are considered, indicated by solid and open circles, with T_2 values of 3 and 10 μs respectively. For the same driving field amplitude, the time required to implement the pulse sequence on the two systems is similar, ranging from $210 > \tau > 20$ ns in the range of values considered $10 - 100$G. (**S**1) compensates the longer sequence with larger matrix elements between energy levels. The curves for $T_2 = 3$ μs are almost monotonically decreasing within the error bars, indicating that pure dephasing is the main source of error, while leakage is found to be less important. This is slightly different when considering $T_2 = 10$ ns, in which infidelity seems to rise for larger values of B_1. The intrinsic resilience of **C**1 against decoherence leads to much better performance compared to **S**1, with errors on average 3-4 times smaller. This ratio appears to be practically independent of T_2 and B_1.
In panel b), with $T_2 = 3$ μs and $B_1 = 100$ G fixed, the error is reported as a function of the subsequent applications of the same gate. The advantage of (**C**1) shown before still remains after ten applications.
Additionally, green points show the results of implementing an H_3 gate using QHR on (**C**1), with the highest of the four levels used as an auxiliary level and the remaining three as the computational space. Thanks to the further improvement of the decomposition that only requires two pulses (parameters reported in Tab. 5.4), the final error is further reduced.

Larger Qudits

This section compares the results of the implementation of the H_4, H_6, and H_8 transformations on (**C**2) with (**S**1), (**S**2), and (**S**3) respectively. In this comparison, QHR is used for decomposition on (**C**2), while PR is used on the (**S**) systems. With the QHR decomposition, only 2, 4, and 5 non-parallelizable pulse sequences are needed to decompose the H_4, H_6, and H_8, respectively (parameters in Tab. 5.4). On the other hand, with the PR decomposition, a significantly larger number of pulses is required, specifically 13, 37, and 73 for the same operations (see Appendix 5.5 for pulse parameters). As noted before, the longer pulse sequence required by PR is partially compensated by the faster single operation time in (**C**) than (**S**). Moreover, a single QHR operation is generally slower than a PR. This can be intuitively understood as in QHR the population has to be first transferred to the auxiliary level $|e\rangle$ and then brought back to the computational space. The effective time required by the two methods is therefore very similar: $t_{gate} \sim 200, 400,$ *and* 600 ns for the three gates using a small driving field of 10 G.
The simulations reported in Fig. 5.3 are performed using a weak driving field with an amplitude of $B_1 = 10$ G, and the results are reported as a function of the

ratio T_2/t_{gate}. At such a small field, the impact of leakage is practically negligible, so the primary focus is on the effects of decoherence. In all the series, a range of T_2 values is considered, specifically $[1,3,10,25,50,100]$ μs. As expected, (**C**2)

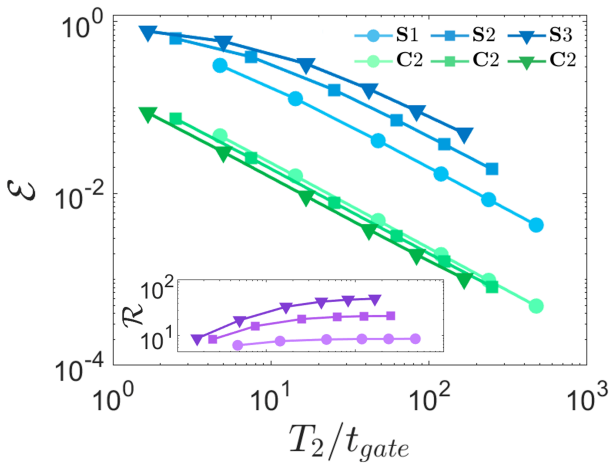

Figure 5.3: Implementation errors for H_4, H_6, and H_8 gates decomposed by PR on **S**1 (blue), **S**2 (squares), **S**3 (triangles), and by QHR on **C**2 (green) systems plotted against the $T2/t_{gate}$ ratio. To suppress leakage, simulations are performed using a small driving field of 10 G. Reproduced from Ref. [127] under the terms of the Creative Commons Attribution 4.0 International license.

outperforms the (**S**) systems, resulting in consistently smaller errors. The inset shows the gain, calculated as the ratio between errors, and it can be as high as 50 for the 8-level qudit implemented on (**C**2). This demonstrates the substantial performance improvement that (**C**2) offers in terms of error reduction and system scalability compared to the (**S**) systems. One significant advantage of (**C**2) is that the error does not increase as the system size grows. The curves for (**C**2) are almost superimposed, indicating that the error remains stable with larger computational spaces.

5.3.2 Two-Qudit Control-Phase Gate

The following simulations show the numerical results of the implementation of the generalized Control-Phase gate defined in Eq. 2.3.3. This operation is implemented using the modular and scalable scheme (qudit-switch-qudit) based on chemical engineering presented in Sec. 2.3.2. This scheme essentially consists of chemically linking two qudits by means of an auxiliary qubit. As the qudits are not directly connected, there is no permanent interaction among them. However, an effective coupling can be turned on by bringing the ancilla in the

excited state $|\uparrow\rangle$. Therefore, the ancilla works as a switch (σ) of the effective interaction. A necessary condition for the scheme to work is that the coupling between the switch and the qudits is small compared to single-body excitation energy, so that the entire system is almost factorized. As a result, the eigenstates can be expressed as a product of individual object eigenstates, denoted as $|\mu_1, m_\sigma, \mu_2\rangle = |\mu_1\rangle \otimes |m_\sigma\rangle \otimes |\mu_2\rangle$.
The elementary architecture unit, composed of a qudit-switch-qudit setup, can be modelled as follows:

$$\mathcal{H}_{TOT} = \mathcal{H}_1 + \mathcal{H}_2 + \mathcal{H}_\sigma + \mathcal{H}_{1-\sigma} + \mathcal{H}_{2-\sigma}, \tag{5.3}$$

where $\mathcal{H}_{1/2}$ stands for single qudit Hamiltonians, $\mathcal{H}_\sigma$ represents the switch's Hamiltonian, while $\mathcal{H}_{1/2-\sigma}$ denotes the coupling terms between the qudits and the switch.
In this analysis, (**S**1) and (**C**1) are considered for single qudits along with a Ni^{2+} ion acting as an auxiliary qubit. This ion is characterized by a large zero-field splitting of $d_\sigma = -0.3$ meV, a $g_\sigma = 2.2$, and an electronic spin $S = 1$. Due to the large splitting, the $|m_\sigma = 1\rangle$ eigenstate is well separated from the other two $|m_\sigma = -1\rangle$ and $|m_\sigma = 0\rangle$. Consequently, by restricting the computational space to the two lowest levels ($|m_\sigma = -1\rangle$ and $|m_\sigma = 0\rangle$), it can be treated as an effective spin $S = 1/2$.
In the case of (**S**1), the switch-qudit interaction is modelled as $\mathcal{H}_{1/2-\sigma} = J_i \mathbf{S}_i \cdot \boldsymbol{\sigma}$ considering a coupling constant $J_{1/2} = 5/7 \times 10^{-3}$ meV. Similarly, for (**C**1), an exchange interaction is established with only one of the molecule ions considering $J_{1/2} = 1/1.4 \times 10^{-2}$ meV, as illustrated in 5.5. The two coupling constants J_1 and J_2 are chosen to be slightly different to make two-body transitions distinct and so addressable. Similarly, to distinguish single-body transitions, the two qudits are made inequivalent: in the case of **C**1 by tilting them with respect to the direction of the static magnetic field, while for **S**1 two different $g = 1.95$ (2.05) values are considered. In conclusion, it's essential to emphasize that precise parameter values are not critical to building a functional system. Many configurations are possible as long as the hierarchies between interactions are respected.
Panel a) of Fig. 5.4 shows the energy level spectrum. As insets of the panel, there are two sketches of the qudit-switch-qudit scheme in the active and inactive states. The black lines represent the computational subspace while the purple one represents the subspace, where the auxiliary qubit is in the excited state. The three couples of levels highlighted by the thicker lines are the transitions involved in the implementation in panel b). This latter reports population evolution during the implementation of three parallel CPhase gates of angle π, $\pi/2$ and $\pi/4$ respectively for red, blue and green lines. Similarly as done be-

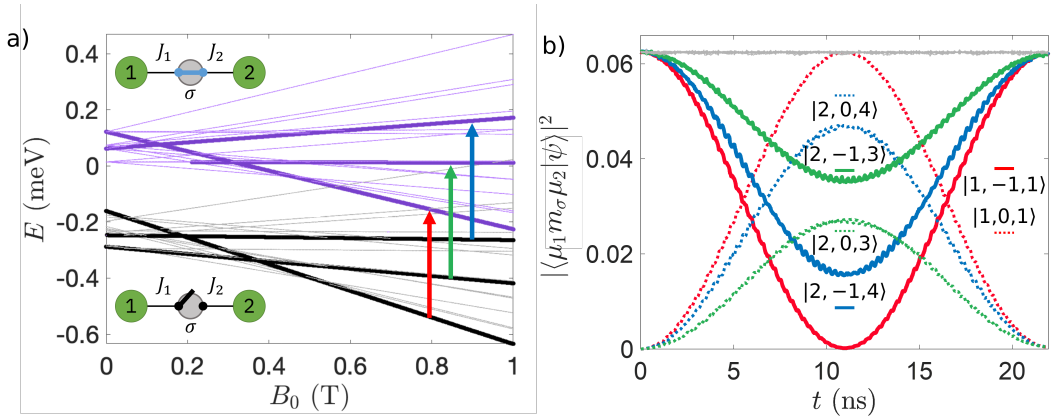

Figure 5.4: a) Energy level spectrum for the qudit-switch-qudit system involving the **S**1 system and a Ni^{2+} $S = 1$ switch. The computational subspace characterized by $m_\sigma = -1$ is shown in black, and the excited state with $m_\sigma = 0$ is in purple. The up-arrows highlight the three pairs of levels involved in the implementation of the CPhase gate simulated in panel b).b) Time evolution simulation of generalized CPhase-gates, applying phases π, $\pi/2$, and $\pi/4$ to red, blue, and green levels, respectively. Gray lines represent uninvolved energy levels, which remain untouched. The initial state is uniformly populated, $|\psi_0\rangle = \sum_{\mu_1\mu_2} |\mu_1, m_\sigma = -1, \mu_2\rangle / d$ (where $d = 4$ is the qudit dimension). Simulations use $B_1 = 20$ G as the maximum driving field amplitude. Adapted from Ref. [127] under the terms of the Creative Commons Attribution 4.0 International license.

fore for single-qudit gates, the initial state is equally populated among the whole computational space. In the simulation a driving field of 20 G is considered and a coherence time $T_2 = 3$ μs for the qudits and $T_2 = 1$ μs for the switch. The whole sequence is basically very fast and only lasts around 25 ns. As can be noticed by the not perfectly smooth population evolution, leakage is a limiting factor. The ancilla excitation transitions are solved by J and therefore for construction are quite close. In the optimal condition of leakage and decoherence balancing, the whole sequence is completed with a fidelity of around 96%.

In comparison, Fig. 5.5 reports the implementation of the same three transitions on (**C**1). The coherence and driving field parameters are the same as before. The first thing one notices is how the curves are segmented denoting a really strong effect of leakage. The implementation time is similar as before and around 25 ns. Panel c) reports the in-fidelity as a function of the external driving field. The optimal working point is around 20 G. Although the system is more susceptible to leakage, thanks to the intrinsic resilience to decoherence of the multi-spin system with competing interactions, the performance at the optimal operating point is ultimately greater than 98% and thus better than the previous case.

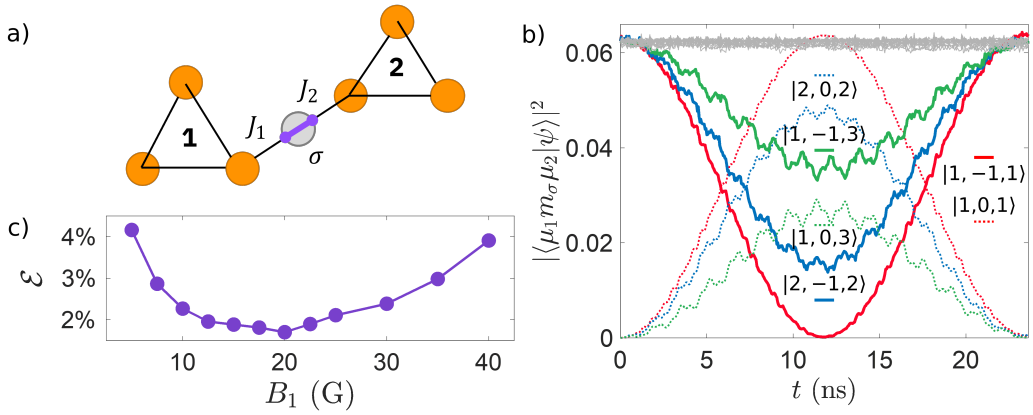

Figure 5.5: a) Schematic representation of the qudit-switch-qudit system involving the **C**1 system and a Ni^{2+} $S = 1$ switch. b) Time evolution simulation of generalized CPhase-gates, applying phases π, $\pi/2$, and $\pi/4$ to red, blue, and green levels, respectively. Gray lines represent uninvolved energy levels, which remain untouched. The initial state is uniformly populated, $|\psi_0\rangle = \sum_{\mu_1\mu_2} |\mu_1, m_\sigma = -1, \mu_2\rangle / d$ (where $d = 4$ is the qudit dimension). Error co Simulations use $B_1 = 20$ G as the maximum driving field amplitude. c) The committed error as a function of the external driving field amplitude. Adapted from Ref. [127] under the terms of the Creative Commons Attribution 4.0 International license.

5.4 Conclusions

The chapter explores the potential of molecular nanomagnets as units to encode qudits for quantum computation. By exploiting molecular chemical engineering, it is possible to synthesise complex multi-spin molecules with tailored properties, allowing a coherent and efficient manipulation of the encoded information. Systems with a nearly frustrated ground state, such as the **C** class, can exhibit multiple magnetically similar multiplets at low energy that form a subspace intrinsically protected from decoherence. Furthermore, dipole matrix elements between these multiplets can be introduced by anisotropic and/or low-symmetry terms. The resulting wide connectivity, in principle up to all-to-all (full), allows for more efficient data manipulation, drastically reducing the number of control pulses required to implement arbitrary operations. Through realistic numerical simulations that take into account decoherence and leakage effects in addition to coherent system dynamics, this class of systems has been compared to single spin molecules **S** in the implementation of the generalized Hadamard gate. The numerical results clearly show a significant advantage of multi-spin over single-spin systems.

In the second part of the analysis, two-qubit gates are considered. By exploiting

the bridge scheme presented in 2.3.2, where an auxiliary qubit is used to mediate an effective interaction between qudits, it is shown how a generalised control phase gate can be implemented. These gates, which produce entanglement, complete the gate set, allowing universality.
Overall, a qudit computation has inherent advantages over the corresponding qubit approach. First, for a generic unitary decomposition, it gives asymptotically logarithmic improvements in terms of gates [178]. Second, the quit approach generally reduces the number of two-body operations required. An illustrative case is the implementation of the QFT algorithm over H_d studied here. This is particularly advantageous for near-term applications where hardware connectivity is typically limited and two-body operations are particularly demanding.

5.5 Appendix

Eq. 5.4 reports the complete pulse sequence required to decompose H_4 into planar rotations, showing also the additional π gates needed with a linear connectivity. The relative gate angles are reported in Tab. 5.1.

$$\begin{aligned} H_4 = & P_{1,2}P_{3,4}\times \\ & \times U_{1,2}\times \\ & \times \pi^{+}_{1,2}U_{1,3}\pi^{-}_{1,2}U_{2,3}\times \\ & \times \pi^{+}_{3,4}\pi^{+}_{2,3}U_{1,4}\pi^{-}_{2,3}U_{2,4}\pi^{-}_{3,4}U_{3,4} \ . \end{aligned} \tag{5.4}$$

H_4 Planar Rotations decomposition

μ,ν	$\theta/2$	β	α
3,4	$-\pi/4$	$\pi/2$	
2,4	$\arctan\left(1/\sqrt{2}\right)$	0	
1,4	$\arctan\left(1/\sqrt{3}\right)$	$\pi/2$	
2,3	0.912	-0.464	
1,3	$\arctan\left(-1/\sqrt{2}\right)$	$-\pi/4$	
1,2	$\pi/4$	$\pi/4$	
3,4			$\pi/8$
1,2			$3\pi/8$

Table 5.1: Table of parameters to decompose H_4 into PR (keeping three significant digits).

Eq. 5.5 reports the complete pulse sequence required to decompose H_6 into planar rotations, showing also the additional π gates needed with a linear connectivity. The relative gate angles are reported in Tab. 5.2.

$$
\begin{aligned}
H_6 = {} & P_{5,6}P_{3,4}P_{2,3}\times \\
& \times U_{1,2}\times \\
& \times \pi^{+}_{2,3}U_{1,3}\pi^{-}_{2,3}U_{2,3}\times \\
& \times \pi^{+}_{3,4}\pi^{+}_{2,3}U_{1,4}\pi^{-}_{2,3}U_{2,4}\pi^{-}_{3,4}U_{3,4}\times \\
& \times \pi^{+}_{4,5}\pi^{+}_{3,4}\pi^{+}_{2,3}U_{1,5}\pi^{-}_{2,3}U_{2,5}\pi^{-}_{3,4}U_{3,5}\pi^{-}_{4,5}U_{4,5}\times \\
& \times \pi^{+}_{5,6}\pi^{+}_{4,5}\pi^{+}_{3,4}\pi^{+}_{2,3}U_{1,6}\pi^{-}_{2,3}U_{2,6}\pi^{-}_{3,4}U_{3,6}\pi^{-}_{4,5}U_{4,6}\pi^{-}_{5,6}U_{5,6} \ .
\end{aligned}
\tag{5.5}
$$

H_6 Planar Rotations decomposition

μ,ν	$\theta/2$	β	α
5,6	$\pi/4$	$-2\pi/3$	
4,6	$\arctan\left(1/\sqrt{2}\right)$	$-\pi/3$	
3,6	$\pi/6$	2π	
2,6	$\arctan(1/2)$	$\pi/3$	
1,6	$\arctan\left(1/\sqrt{5}\right)$	$2\pi/3$	
4,5	$\operatorname{arccot}(\sqrt{3/7})$	$-\arctan\left(3\sqrt{3}\right)$	
3,5	$\operatorname{arccot}(2\sqrt{5/19})$	$\operatorname{arccot}\left(4/\sqrt{3}\right)$	
2,5	$\arctan(\sqrt{31/65})$	$\pi-\arctan\left(5\sqrt{3}/7\right)$	
1,5	$\arctan(1/2)$	$-2\pi/3$	
3,4	$\arctan(\sqrt{37/13})$	$-\arctan\left(2\sqrt{3}/5\right)$	
2,4	$\operatorname{arccot}(2\sqrt{5/19})$	$1/2(\pi+\arctan\left(8\sqrt{3}/13\right))$	
1,4	$\pi/6$	$-\pi/2$	
2,3	$\arctan(\sqrt{7/3})$	$\arctan\left(1/3\sqrt{3}\right)$	
1,3	$\arctan\left(1/\sqrt{2}\right)$	$-5\pi/6$	
1,2	$\pi/4$	1.047	
5,6			$-\pi/3$
3,4			$\pi/2$
2,3			$2\pi/3$

Table 5.2: Table parameters to decompose H_6 into PR (keeping three significant digits).

Eq. 5.6 reports the complete pulse sequence required to decompose H_8 into planar rotations, showing also the additional π gates needed with a linear connectivity. The relative gate angles are reported in Tab. 5.3.

$$
\begin{aligned}
H_8 = {} & P_{7,8}P_{6,7}P_{5,6}P_{3,4}P_{1,2}\times \\
& \times U_{1,2}\times \\
& \times \pi^{+}_{2,3}U_{1,3}\pi^{-}_{2,3}U_{2,3}\times \\
& \times \pi^{+}_{3,4}\pi^{+}_{2,3}U_{1,4}\pi^{-}_{2,3}U_{2,4}\pi^{-}_{3,4}U_{3,4}\times \\
& \times \pi^{+}_{4,5}\pi^{+}_{3,4}\pi^{+}_{2,3}U_{1,5}\pi^{-}_{2,3}U_{2,5}\pi^{-}_{3,4}U_{3,5}\pi^{-}_{4,5}U_{4,5}\times \\
& \times \pi^{+}_{5,6}\pi^{+}_{4,5}\pi^{+}_{3,4}\pi^{+}_{2,3}U_{1,6}\pi^{-}_{2,3}U_{2,6}\pi^{-}_{3,4}U_{3,6}\pi^{-}_{4,5}U_{4,6}\pi^{-}_{5,6}U_{5,6} \\
& \times \pi^{+}_{6,7}\pi^{+}_{5,6}\pi^{+}_{4,5}\pi^{+}_{3,4}\pi^{+}_{2,3}U_{1,7}\pi^{-}_{2,3}U_{2,7}\pi^{-}_{3,4}U_{3,7}\pi^{-}_{4,5}U_{4,7}\times \\
& \times \pi^{-}_{5,6}U_{5,7}\pi^{-}_{6,7}U_{6,7}\times \\
& \times \pi^{+}_{7,8}\pi^{+}_{6,7}\pi^{+}_{5,6}\pi^{+}_{4,5}\pi^{+}_{3,4}\pi^{+}_{2,3}U_{1,8}\pi^{-}_{2,3}U_{2,8}\pi^{-}_{3,4}U_{3,8}\times \\
& \times \pi^{-}_{4,5}U_{4,8}\pi^{-}_{5,6}U_{5,8}\pi^{-}_{6,7}U_{6,8}\pi^{-}_{7,8}U_{7,8} \ .
\end{aligned}
\tag{5.6}
$$

Tab. 5.4 reports all pulse parameter required to decompose H_3, H_4, H_6, and H_8 into Householder reflections.

H_8 Planar Rotations decomposition

μ,ν	$\theta/2$	β	α
7,8	$\pi/4$	$-3\pi/4$	
6,8	$\arctan\left(1/\sqrt{2}\right)$	$-\pi/2$	
5,8	$\pi/6$	$-\pi/4$	
4,8	$2\arctan(1/2)$	0	
3,8	$\arctan\left(1/\sqrt{5}\right)$	$\pi/4$	
2,8	$\operatorname{arccot}\left(\sqrt{6}\right)$	$\pi/2$	
1,8	$\arctan\left(1/\sqrt{7}\right)$	$3\pi/4$	
6,7	1.016	4.457	
5,7	0.824	-0.5	
4,7	0.687	0.843	
3,7	0.573	2.213	
2,7	0.474	-2.657	
1,7	0.388	-1.178	
5,6	1.093	-1.249	
4,6	0.895	0.655	
3,6	0.731	2.585	
2,6	0.573	-1.714	
1,6	0.421	0.393	
4,5	1.113	-0.663	
3,5	0.895	1.834	
2,5	0.687	-1.906	
1,5	0.464	0.785	
3,4	1.093	-0.071	
2,4	0.824	3.034	
1,4	0.524	0	
2,3	1.016	0.530	
1,3	0.615	-1.963	
1,2	0.785	1.178	
7,8			$\pi/16$
6,7			π
5,6			$7\pi/16$
3,4			$11\pi/16$
1,2			$5\pi/16$

Table 5.3: Table of parameters to decompose H_8 into PR (keeping three significant digits).

Quantum Householder Parameters Table

H_d	v_i	ϕ_i
H_3		
1	$\frac{1}{2}\sqrt{1+\frac{1}{\sqrt{3}}}[1-\sqrt{3},1,1]^T$	π
2	$\frac{1}{\sqrt{2}}[0,1,-1]^T$	$\pi/2$
H_4		
1	$\frac{1}{2}[-1,1,1,1]^T$	π
2	$\frac{1}{\sqrt{2}}[0,1,0,-1]^T$	$\pi/2$
H_6		
1	$[0.544i,-0.375i,-0.375i,-0.375i,-0.375i,-0.375i]^T$	$-\pi$
2	$[0,0.575+0.220i,0.244-0.261i,0.071+0.103i,-0.331+0.135i,-0.559-0.197i]^T$	1.937
3	$[0,0,-0.490+0.626i,0.113-0.466i,0.352-0.055i,0.025-0.105i]^T$	-2.478
4	$[0,0,0,-0.322+0.537i,0.395-0.657i,-0.073+0.121i]^T$	-2.601
H_8		
1	$[0.569i,-0.311i,-0.311i,-0.311i,-0.311i,-0.311i,-0.311i,-0.311i]^T$	$-\pi$
2	$[0,0.432+0.384i,0.230-0.305i,0.238-0.048i,0.062+0.139i,-0.194+0.146i,-0.381-0.030i,-0.388-0.286i]^T$	2.297
3	$[0,0,0.174+0.819i,-0.228+0.008i,-0.097-0.316i,0.159-0.231i,0.060-0.056i,-0.067-0.22i]^T$	2.932
4	$[0,0,0,0.233+0.568i,-0.146+0.133i,-0.336-0.475i,0.352-0.320i,-0.103+0.094i]^T$	2.752
5	$[0,0,0,0,0.046+0.355i,0.032+0.251i,-0.110-0.856i,0.032+0.251i]^T$	3.014

Table 5.4: Table of Quantum Householder Reflection parameters to decompose H_d (keeping three significant digits).

CHAPTER 6

Qudit-Based Quantum Simulation of Fermionic Systems

Chapter 5 has shown how a universal gate set for qudit computation on MNM-based architecture can be formed and practically implemented. This chapter aims at taking a further step by exploring a practical application, i.e. the quantum simulation of fermionic systems. This problem is of relevance in various scientific domains, including high-energy and condensed matter physics, as well as quantum chemistry [35]. Simple models like the Hubbard model could contribute significantly to understanding phenomena such as high-temperature superconductivity or discovering new molecules and materials.

As highlighted throughout this work, the simulation of quantum systems is an area where quantum computers are expected to have a substantial impact. However, simulating certain systems, such as fermionic models discussed here, can be complicated and expensive even on quantum computers, particularly in the context of NISQ devices with limited resources.

The initial step in any application involves mapping the target problem onto the hardware. The challenge of simulating fermionic systems arises right at this stage. Conventional mappings, for now having in mind a qubit-based architecture, like Jordan-Wigner (JW) or Braviy-Kitaev (BK) transform local fermionic operators, acting on a limited number of sites, onto non-local qubit operators whose size depends on size of the problem [179, 180]. The practical issue with implementing these operators is that they require long sequences of entangling gates, making the approach inefficient. For example, applying the JW mapping to a standard Hubbard model, makes hopping terms to grow proportionally to the size of the problem, $\sim N$ (where N is the lattice size).

To overcome this limitation, a promising alternative to standard mappings is the Auxiliary Fermion Method [181–183]. Indeed, at the price of introducing a larger Hilbert space, this method is able to map local fermionic operators onto qubit operators of limited-size. Starting form the original qubit approach, this chapter demonstrates how it can be implemented efficiently on qudits. This qudit

extension brings additional benefits such as a further reduction of operator size, circuit parallelisability and the number of objects that have to be controlled. The effectiveness of this approach is demonstrated by numerical simulations where it is tested on a hypothetical MNM architecture [103, 117].
The chapter is organised as follows: Sec. 6.1 first introduces the most well-known fermion-qubit mappings, namely Jordan-Wigner and Braviy-Kitaev, and then describes the Auxiliary Fermion Method. The latter, since it is less common, is introduced more in detail, and an explicit example of its implementation is reported in 6.1.3. Then Sec. 6.2 introduces the qudit extension and explains how to map qubits to qudits. The different methods are compared in terms of the number of hardware physical objects, the largest operator weight, and the circuit depth of a single Trotter step in terms of two body gates. Sec. 6.3 presents the results of various numerical simulations where the proposed scheme is tested on a hypothetical MNM-based architecture. Sec. 6.4 concludes the chapter by summarizing the results and presenting some prospectives for future studies.

6.1 Fermion to Qubit Mapping

As mentioned in the introduction, the quantum simulation of Hubbard and Hubbard-like Hamiltonians is of strong interest because they are able to capture and describe various phenomena of interest. A standard Hubbard Hamiltonian takes the form:

$$\begin{aligned}\mathcal{H} &= \mathcal{H}_t + \mathcal{H}_U \\ &= -\sum_{p,q}\sum_{\sigma} t_{pq} a^\dagger_{p,\sigma} a_{q,\sigma} + U \sum_p a^\dagger_{p,\uparrow} a_{p,\uparrow} a^\dagger_{p,\downarrow} a_{p,\downarrow} \quad ,\end{aligned} \tag{6.1}$$

where p and q are site indices, $\sigma = \uparrow, \downarrow$ is the spin index, a is the fermionic annihilation operator and $\mathcal{H}_t$ and $\mathcal{H}_U$ indicate the hopping and Coulomb interactions, respectively. The former parametrized by t_{pq} describes the inclination of electrons to tunnel to neighbouring sites while the latter parametrized by U describes a repulsion among them localised on the same orbital. Due to its simplicity and the reasons mentioned earlier, this model is likely to be among the first problems where quantum computers will demonstrate valuable results. Consequently, it will serve as a benchmark for assessing the performance of quantum computers compared to classical devices.
As emphasized in the introduction, the mapping of the physical model onto the hardware is a crucial step. A well-designed mapping can significantly reduce the simulation cost. In the case of fermionic systems, the complicating factor arises from the fermionic statistic $[a_p, a_q]_+ = [a^\dagger_p, a^\dagger_q]_+ = 0$, $[a_p, a^\dagger_q]_+ = \delta_{pq}$ which does not correspond to the qubit one, and so it requires a careful consideration

and treatment. In order to provide the reader with a comprehensive overview of the standard methods, the two most common mappings, Jordan-Wigner and Bravyi-Kitaev will be first introduced [10, 179, 184–188]. Then, in Sec. 6.1.3 the Auxiliary Fermion Method, which is at the basis of the proposed qudit mapping, is explained.

6.1.1 Jordan-Wigner mapping

The Jordan-Wigner mapping is the first method proposed to map fermionic systems onto qubits [179, 184]. The underlying logic and operation of this method are easily comprehensible. Essentially, Jordan-Wigner directly translates the occupation information of each fermionic orbital into a specific qubit. The mapping explicitly transforms fermionic operators as follows:

$$\begin{aligned} &\textbf{Jordan-Wigner Mapping} && a^\dagger_{p,\uparrow}a_{p,\uparrow}a^\dagger_{p,\downarrow}a_{p,\downarrow} = A^\dagger_{p,\uparrow}A_{p,\uparrow}A^\dagger_{p,\downarrow}A_{p,\downarrow} \\ &a_{p,\sigma} = \bigotimes_{k=0}^{p-1} Z_{k,\sigma} \otimes A_{p,\sigma} && a^\dagger_{p,\sigma}a_{q,\sigma} = A^\dagger_{p,\sigma} \otimes \left(\bigotimes_{k=p+1}^{q-1} Z_{k,\sigma} \right) \otimes A_{q,\sigma}\,, \end{aligned} \tag{6.2}$$

where $A = (X + iY)/2$ is the qubit lowering operator and X, Y and Z are the Pauli operators. The strings $\bigotimes_{k=0}^{j-1} Z_{k,\sigma}$ ensure the correct implementation of fermionic commutation rules. As illustrated on the right side, there is no complication for interaction terms $A^\dagger_{p,\uparrow}A_{p,\uparrow}A^\dagger_{p,\downarrow}A_{p,\downarrow}$ where the chains of creation and annihilation operators cancel each other. The interaction operators remain local once mapped onto qubits, acting solely on the original sites p and q. Conversely, for any hopping terms involving two non-consecutive sites ($q \neq i + 1$), the qubit operator would entail a chain of $\bigotimes_{k=p+1}^{q-1} Z_{k,\sigma}$ acting on all the sites between p and q. For example, given N as the size of a square lattice, the length of these chains, also known as Pauli weight, scales as $O(N)$ for a 2D lattice and as $O(N^2)$ in a 3D cubic lattice [189].

The complementary approach is to employ the parity basis [190]. In this case, qubits store the parity of all the sites with a higher index while the occupation information is delocalized. However, this approach does not solve the problem but shifts it from counting parity to updating occupation. Each time a site changes occupation, all the sites before it must update parity, resulting in the same computational cost as the Jordan-Wigner method.

6.1.2 Braviy-Kitaev mapping

The Bravyi-Kitaev mapping can be seen as an evolution from the JW method, reducing the scaling to $O(\log_2(N))$ in 2D and as $O(\log_2(N^2))$ in 3D [184, 185,

188]. A comprehensive understanding of the BK method is facilitated by having mentioned the JW and parity basis earlier, as BK is a hybrid of these two approaches.
The information held by each qubit varies depending on the site index. Similar to JW, all even qubits store the occupation information relative to the respective fermionic site. Conversely, odd qubits hold the parity information of a specific subset of sites. Specifically, if $\log_2(p+1)$ is an integer, the parity is relative to all sites with indices $\lesssim p$, while in the other cases, the parity is a subset of sites. This mapping may be less intuitive compared to the earlier methods, but it can be easily understood by examining the transformation matrix that defines how the occupation of qubits q_p is determined based on the occupation of fermionic sites o_p. For example, considering an eight-site scenario, the transformation matrix takes the form:

$$\begin{bmatrix} 1 & 0 & 0 & 0 & 0 & 0 & 0 & 0 \\ 1 & 1 & 0 & 0 & 0 & 0 & 0 & 0 \\ 0 & 0 & 1 & 0 & 0 & 0 & 0 & 0 \\ 1 & 1 & 1 & 1 & 0 & 0 & 0 & 0 \\ 0 & 0 & 0 & 0 & 1 & 0 & 0 & 0 \\ 0 & 0 & 0 & 0 & 1 & 1 & 0 & 0 \\ 0 & 0 & 0 & 0 & 0 & 0 & 1 & 0 \\ 1 & 1 & 1 & 1 & 1 & 1 & 1 & 1 \end{bmatrix} \begin{bmatrix} o_0 \\ o_1 \\ o_2 \\ o_3 \\ o_4 \\ o_5 \\ o_6 \\ o_7 \end{bmatrix} = \begin{bmatrix} o_0 \\ o_0 + o_1 \\ o_2 \\ o_0 + o_1 + o_2 + o_3 \\ o_4 \\ o_4 + o_5 \\ o_6 \\ o_0 + o_1 + o_2 + o_3 + o_4 + o_5 + o_6 + o_7 \end{bmatrix} = \begin{bmatrix} q_0 \\ q_1 \\ q_2 \\ q_3 \\ q_4 \\ q_5 \\ q_6 \\ q_7 \end{bmatrix} \tag{6.3}$$

Explicitly, the transformation is defined as follows:

Braviy-Kitaev mapping

$$\begin{aligned} a_p &= \frac{1}{2}\left(X_{U(p)} \otimes X_p \otimes Z_{P(p)} + iX_{U(p)} \otimes X_p \otimes Z_{\rho(p)}\right) \\ a_p^\dagger &= \frac{1}{2}\left(X_{U(p)} \otimes X_p \otimes Z_{P(p)} - iX_{U(p)} \otimes X_p \otimes Z_{\rho(p)}\right), \end{aligned} \tag{6.4}$$

where $U(i)$, $P(i)$ and $\rho(i)$ are subset of qubits that are derived from the rules defined above. For brevity, these are not further detailed, and reference is made to [191].

6.1.3 The Auxiliary Fermion Method

Although the above methods have been extensively studied and a number of optimised variants have been proposed [186, 192], the underlying problem, i.e. the growth of operator size, still remains. A promising solution is given by the

Auxiliary Fermion Method (AFM). This method, originally proposed by two independent works in 2005 [181, 182], has been later revisited and clarified in some aspects in 2016 in [183]. The method is essentially based on the JW transformation, but applied to a modified Hamiltonian. In particular, auxiliary fermionic sites are introduced into the original model to store the parity information relative to those hopping terms that are not local when rewritten in terms of qubit operators, so that it has not to be counted, thus eliminating the Z chains. In this way, the AFM is able to map fermionic operators onto qubit operators of limited size. The length of these operators no longer depends on the lattice dimension, but only on the degree of the system, i.e. the number of bonds each site has. This significantly reduces the complexity of the Pauli strings to be simulated, resulting in circuits with lower depth. In addition, by reducing the number of sites involved in each term, more operators can be implemented simultaneously, further compressing the circuit. The price for all these benefits is the increased number of qubits that need to be used. However, this cost is nevertheless advantageous, particularly for NISQ applications, where circuit complexity is often the limiting factor.
The algorithm can be divided into three main steps:

1) **Indexing** : given a fermionic Hamiltonian and the relative graph representing sites and couplings, index sites along a snake-like path. For each site p, compute the number of non-local couplings D_p, i.e. couplings not along the snake-like path, and introduce ceil$(D_p/2)$ additional auxiliary fermionic sites indexed adjacent to p.

2) **Hamiltonian modification**: introduce auxiliary stabilizer operators M_{aux}, which act only on auxiliary sites, to the original Hamiltonian and construct an initial fermion state corresponding to a physical state.

3) **Transformation**: apply the Jordan-Wigner transformation to convert the fermionic Hamiltonian to qubit representation. Local fermionic operators are mapped to limited size qubit ones.

The three steps are explained in more detail in the following.

Indexing

In the initial step, the target Hamiltonian is graphically represented, wherein each fermionic site corresponds to a vertex, and interactions are depicted as links between vertices. A snake-like pattern is traced over the graph, numbering the

vertices in ascending order, as is commonly done with the Jordan-Wigner mapping. When applying the JW mapping, one expects that hopping operators between two consecutively indexed sites (if numbered from left to right, horizontal hopping terms) are mapped to local qubit operators, while hopping operators between two non-consecutive sites (vertical hopping) result in non-local qubit operators. In other words, for the letter a Z chain would be introduced. For any graph site p with at least one hopping deviating from the pattern, the Auxiliary Fermion Method requires the introduction of auxiliary sites adjacent to it (graphically displayed with $'$). Each such auxiliary site will be used to store the parity of at most two operators (not along the path), requiring ceil$(D_p/2)$ additional auxiliary fermionic sites, where D_p represents the number of sites coupled to site p not lying along the linear indexing.
For instance, consider a Hubbard Hamiltonian on a 2D lattice with nearest neighbour hopping terms. A general site not along the edges would have four connections, two along the pattern and two not along it. Therefore, a single auxiliary site is required. Introducing hopping terms with the next-nearest neighbour, eight terms for each site of which six not along the path, the number of auxiliary sites would be three.

Hamiltonian modification

The strategy to obtain qubit locality is to modify the original Hamiltonian by introducing stabilizer operators M_{aux} to the terms that would suffer from Z chains (the same for which auxiliary sites have been introduced). For example, given a standard hopping term $a_p^\dagger a_q + a_q^\dagger a_p$ among sites p and q not adjacent on the indexing, this is replaced by $a_p^\dagger M_{aux}(pq) a_q + a_q^\dagger M_{aux}^\dagger(pq) a_p$. The same approach can be applied to two-body four-point or higher coupling terms. These operators take the general form $M_{aux}(p,q) = i b_{p'} c_{q'}$ where:

$$\begin{aligned} b_{p'} &= (e^{-i\theta} a_{p'} + e^{i\theta} a_{p'}^\dagger) \\ c_{q'} &= (e^{-i\phi} a_{q'} + e^{i\phi} a_{q'}^\dagger) \ , \end{aligned} \tag{6.5}$$

θ and ϕ are parameters. M_{aux} operators act only on auxiliary sites, and their effect is to cancel the JW Z chains without changing the physics of the original fermionic model. For this to be true, M_{aux} must respect certain properties. By introducing auxiliary fermionic sites and thus increasing the dimension of the Hilbert space, not every qubit state corresponds to a physical state in the fermionic system. To address this issue, it is imposed that the physical fermionic states on qubits correspond to $+1$ eigenstates of all $M_{aux}(ij)$. In this sense, M_{aux} operators stabilize the physical subspace. Therefore, for construc-

tion, any pairs of stabilizers commute on this subspace. This implies that for all p that $[M_{aux}, a_p] = 0$, $a_p^\dagger M_{aux} a_q |\Omega\rangle = a_p^\dagger a_q M_{aux} |\Omega\rangle = a_p^\dagger a_q |\Omega\rangle$ where $|\Omega\rangle$ is the vacuum state. The θ and ϕ angles have to be set to respect the commutation rules described above.

Also the vacuum state $|\Omega\rangle$ has to be modified in order to respect the fermionic statistics. Indeed, the additional degrees of freedom introduced by the auxiliary sites lead to the presence of states that do not correspond to physical states. Starting from the state $|0,0,\ldots,0\rangle$, each auxiliary coupling has to be projectively measured.

$$|\Omega\rangle = \prod_{(p,q)} \frac{1 + M_{aux}(p,q)}{\sqrt{2}} |0,0,\ldots,0\rangle \ . \tag{6.6}$$

In practice, this procedure involves measuring the parity of these operators, and if the outcome is -1, apply a Z gate to the corresponding p' or q' sites. Special consideration is required when sites participate in two non-local couplings, as the -1 sign propagates to the other coupling. To rectify this, one must trace the linked chain of non-local sites and apply Z gates until reaching the end. In cases where closed loops are present, additional sites must be introduced to break these loops.

It is crucial to highlight that this procedure represents a weak point in this approach. The initialization of the vacuum state introduces a cost that, for general models, is proportional to that of a single Jordan-Wigner Trotter step. Nevertheless, the initialization procedure needs to be applied only once at the beginning of the computation and in the context of high-precision simulations, which typically involve many Trotter steps, the overall approach proves to be advantageous.

Finally, the desired initial Fock state can be prepared by populating the various sites. Therefore, starting from the vacuum state, an X gate is applied to each qubit corresponding to a site of the original model with occupation, while a Z gate is applied to qubits related to auxiliary sites if the parity of sites on their right is one.

Transformation

Finally, in the last step a standard Jordan-Wigner transformation is applied to the modified Hamiltonian. The introduced M_{aux} operators are transformed as

follows:

$$
\begin{aligned}
b_{p'} &= \left(\bigotimes_{i=0}^{p'-1} Z_i \right) \otimes B_{p'} \\
c_{q'} &= \left(\bigotimes_{i=0}^{q'-1} Z_i \right) \otimes C_{q'} \ ,
\end{aligned}
\tag{6.7}
$$

where $B_{p'} = [\cos(\theta)X + \sin(\theta)Y]_{p'}$ and $C_{q'} = [\cos(\phi)X + \sin(\phi)Y]_{q'}$. The Z chains introduced by the M_{aux} will cancel with the ones generated by the original Hamiltonian therefore resulting in local operators.

Example: Four site model

Hereafter, the above method is explicitly solved for a simple toy model consisting of four interacting spinless particles with hopping with nearest (N.N.) and next-nearest neighbours (N.N.N.) (see Fig. 6.1). On the left side, the model is

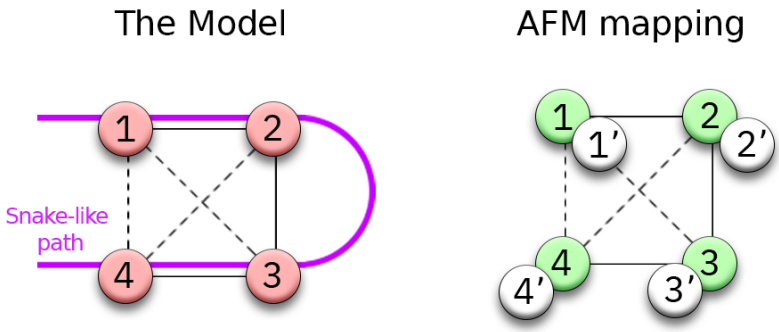

Figure 6.1: Schematic representation of a fully connected four-site spinless lattice. Left: the model where the black lines (dotted and continuous) represent hopping interactions between sites. The continuous purple one highlights the index snake-like pattern. Right: AFM mapping where ancillary sites are introduced.

graphically depicted as a graph where vertices are the fermionic sites and links represent hopping interactions. The site indexing is done following the snake-like path (purple line). Three of the hopping terms (continuous black lines) are along it while the other three outside (dashed). Since the model does not assume spin, an interaction between particles on different sites is considered. The system

is described by the following Hamiltonian:

$$\begin{aligned}\mathcal{H} = \mathcal{H}_t \;+\; \mathcal{H}_U = \\ = -t\big(a_1^\dagger a_2 + a_1 a_2^\dagger + a_2^\dagger a_3 + a_2 a_3^\dagger + \\ a_3^\dagger a_4 + a_3 a_4^\dagger + a_1^\dagger a_4 + a_1 a_4^\dagger + \\ a_2^\dagger a_4 + a_2 a_4^\dagger + a_1^\dagger a_3 + a_1 a_3^\dagger\big) + \\ U\big(a_1^\dagger a_1 a_2^\dagger a_2 + a_2^\dagger a_2 a_3^\dagger a_3 + \\ a_3^\dagger a_3 a_4^\dagger a_4 + a_4^\dagger a_4 a_1^\dagger a_1\big)\;.\end{aligned} \tag{6.8}$$

With regard to the mapping, the interaction term considered has the same peculiarities as the standard one. To implement the transformation one starts indexing sites in ascending order. Directly applying the JW transformation, the Hamiltonian would take the form:

$$\begin{aligned}\mathcal{H}_{JW} = \mathcal{H}_t + \mathcal{H}_U \\ = -\,t\big(A_1^\dagger A_2 + A_1 A_2^\dagger + A_2^\dagger A_3 + A_2 A_3^\dagger + \\ A_3^\dagger A_4 + A_3 A_4^\dagger + A_1^\dagger Z_2 Z_3 A_4 + A_1 Z_2 Z_3 A_4^\dagger + \\ A_2^\dagger Z_3 A_4 + A_2 Z_3 A_4^\dagger + A_1^\dagger Z_2 A_3 + A_1 Z_2 A_3^\dagger\big) + \\ + U\big(A_1^\dagger A_1 A_2 A_2^\dagger + A_2^\dagger A_2 A_3 A_3^\dagger + \\ A_3^\dagger A_3 A_4 A_4^\dagger + A_4^\dagger A_4 A_1 A_1^\dagger\big)\;.\end{aligned} \tag{6.9}$$

As expected, all hopping terms among sites not consecutive in the indexing ($1-3, 2-4, 1-4$) suffer from Z chains. Although they do not have a dramatic effect on this small model, for larger size problems they are very limiting.
The AFM requires auxiliary sites for any site with non-covered links. In this case all sites have one or two non-local coupling and hence they all require an auxiliary site as depicted on the right side on Fig. 6.1. The new indexing is $11'22'33'44'$. Following, the system Hamiltonian is modified by inserting M_{aux} operators into the three hopping terms for which the auxiliary sites were included:

$$\begin{aligned}\mathcal{H}_t = -t\big(a_1^\dagger a_2 + a_1 a_2^\dagger + a_2^\dagger a_3 + a_2 a_3^\dagger + a_3^\dagger a_4 + a_3 a_4^\dagger + \\ a_1^\dagger M_{aux}(14) a_4 + a_1 M_{aux}(14)^\dagger a_4^\dagger + \\ a_2^\dagger M_{aux}(24) a_4 + a_2 M_{aux}(24)^\dagger a_4^\dagger + \\ a_1^\dagger M_{aux}(13) a_3 + a_1 M_{aux}(13)^\dagger a_3^\dagger\big)\;.\end{aligned} \tag{6.10}$$

A convenient choice is to define M_{aux} with easy angles $\theta, \phi = \{0, \pm\pi/2\}$. The specific choice has to be done in accordance with commutation rules. To define these operators, however, it is more convenient to work in the qubit basis. A possible choice is:

$$
\begin{aligned}
M_{aux}(1,4) &= Y_{1'} Z_2 Z_{2'} Z_3 Z_{3'} Z_4 Y_{4'} \\
M_{aux}(2,4) &= X_{2'} Z_3 Z_{3'} Z_4 X_{4'} \\
M_{aux}(1,3) &= X_{1'} Z_2 Z_{2'} Z_3 X_{3'} \ ,
\end{aligned} \tag{6.11}
$$

where it is easy to verify the previously defined commutation rules. Finally, applying the Jordan-Wigner transformation to the entire Hamiltonian, one obtains:

$$
\begin{aligned}
\mathcal{H}_{AFM} = -t\big(& A_1^\dagger Z_{1'} A_2 + A_2^\dagger Z_{1'} A_1 + \\
& A_2^\dagger Z_{2'} A_3 + A_3^\dagger Z_{2'} A_2 + \\
& A_3^\dagger Z_{3'} A_4 + A_4^\dagger Z_{3'} A_3 + \\
& + i A_1^\dagger X_{1'} A_4 Y_{4'} - i A_1 X_{1'} A_4^\dagger Y_{4'} + \\
& - i A_2^\dagger Y_{2'} A_4 X_{4'} + i A_2 Y_{2'} A_4^\dagger X_{4'} + \\
& - i A_1^\dagger Y_{1'} A_3 X_{3'} + i A_1 Y_{1'} A_3^\dagger X_{3'} \big) + \\
+ U\big(& A_1^\dagger A_1 A_2^\dagger A_2 + A_2^\dagger A_2 A_3^\dagger A_3 + \\
& A_3^\dagger A_3 A_4^\dagger A_4 + A_4^\dagger A_4 A_1^\dagger A_1 \big) \ .
\end{aligned}
$$

In first place, it is important to note that all terms act only on qubits relative to the original fermionic sites involved in the interaction and on the auxiliary qubits relative to those sites. In this sense, the new Hamiltonian $\mathcal{H}_{AFM}$ is local in terms of qubit operators. It is important to remark that the size of the operators is independent of the system's size but depends only on the number of auxiliary sites and, hence, on the system's connectivity.

6.2 Qudit mapping for Auxiliary Fermion Method

The Auxiliary Fermion Method is based on the idea of storing parity information relative to couplings in auxiliary qubits and so eliminating the need for Z chains introduced by the Jordan-Wigner method. As discussed in Section 6.1.3, this alternative approach offers several advantages over conventional methods, such as eliminating the dependence of operator size on lattice size. However, by exploiting a qudit-based computation, these advantages can be further enhanced. Instead of introducing auxiliary qubits, the additional Hilbert space can be obtained by expanding the computational space of individual units, i.e. by using qudits. Starting from the original AFM qubit mapping, a profitable strategy is to map the product space of each qubit along with its relative auxiliary ones inside a single qudit. In first place, exploiting qudits naturally reduces the number of objects to control and, consequently, the count of two-body gates (see Tab. 6.1). Moreover, employing qudits enhances the parallelizability of the circuit, thereby

further reducing its depth. The qudit's dimension is determined by the number of auxiliary sites and, therefore, is related to the system's connectivity and not to the system's dimension. The most common and interesting models involve interactions between nearest (N.N.) or next-nearest (N.N.N) neighbours. Therefore, small- to medium- size qudits would allow for efficient simulations of arbitrary dimension lattices (see Tab. 6.1). For instance, a 2D rectangular lattice with nearest neighbour interactions could be adequately simulated using four-level qudits. Expanding it to next-nearest interactions would require 16-level qudits.

In Tab. 6.1, the JW, BK and qubit/qudit AFM methods are compared in terms the requirements to simulate of a square lattice of size N of spin $S = 1/2$ particles with hopping interactions among nearest (N.N.) and next-to-nearest neighbours (N.N.N). In particular, the table compares three aspects: the number of hardware physical objects, i.e. the counts of qubits/qudits, the largest operator weight, i.e. the Pauli weight of the larger operator to be implemented, and the circuit depth of a single Trotter step in terms of two body gates.

From the first box, one observes that qubit AFM suffers from the proliferation of units with respect to JW and BK. The qudit AFM compensates the larger required computational space with the larger Hilbert space given by qudits (4 and 16 levels for N.N and N.N.N., respectively) by using the same number of computational units. In the second box, the largest operators to be implemented are compared. This table shows the main difference between AFM and JW and BK. AFM eliminates the operator size dependence on the lattice dimension e hence resulting in limited size operators. The larger the size of the system to be simulated, the greater the advantage. Using qudits, and assuming that the model involves only two-body interactions, the operators can always be mapped as two qudit gates. Finally, in the third box, are reported the counts of the depth of a single Trotter step in terms of two qudit gates. These values reflect the final gain that AFM gives i.e. the reduction of the whole circuit depth. Given a specific model using the AFM it is possible to calculate circuit depth, independently by model size, just by summing the depth of non-commuting terms.

Let's start by looking at the qudit case. Considering the model with N.N. (N.N.N.) hopping, each site is involved in 4 (8) hopping terms and a single interaction (only on site interaction). All of these terms can be potentially implemented as a single qudit gate and hence resulting in a depth of 5 (9) gates considering full hardware connectivity. In a more realistic scenario, where the hardware has a grid connectivity, the two sub-reticles containing the up and down spins can be horizontally nested. In this way, 4 (8) SWAP gates, here counted as 3 two-qudit gates, are required.

Moving to qubits, the reasoning is a little more complex because the number

Number of Hardware Physical Units

	JW	BK	Qubit AFM	Qudit AFM
N.N.	$2N^2$	$2N^2$	$4N^2$	$2N^2$
N.N.N.	$2N^2$	$2N^2$	$8N^2$	$2N^2$

Largest Operator Weight

	JW	BK	Qubit AFM	Qudit AFM
N.N.	$N+1$	$\propto \log(N)$	4	2
N.N.N.	$N+2$	$\propto \log(N)$	8	2

Depth of a Trotter Step

	JW	BK	Qubit AFM		Qudit AFM	
	All	All	All	Grid	All	Grid
N.N.	$\propto N$	$\propto \log(N)$	30	42	5	17
N.N.N	$\propto N$	$\propto \log(N)$	94	118	9	33

Table 6.1: Requirements and costs to simulate the Hubbard model wit spin on a square lattice with nearest (N.N.) or next-to-nearest neighbours (N.N.N) hopping interactions exploiting Jordan-Wigner, qubit and qudit Auxiliary Fermion Method mappings. Two types of hardware connectivity are considered: all-to-all (All) and square grid (Grid). The top panel shows the number of physical units, i.e. the number of qubits or qudits, required. The middle panel reports the largest operator weight, i.e. the maximum number of operators involved in the hopping terms. The bottom panel shows the depth of a Trotter step in terms of two-body gates.

of gates depends on the decomposition strategy used. An efficient strategy to decompose Pauli string operators of small-medium size uses $2n$ entanglement gates, where n is the Pauli weight of the operator [180]. In the case of hopping between N.N., each site would be involved in 2 horizontal hoppings, which have a Pauli weight of 3, and so each of these can be decomposed into 6 two-body gates, and into two vertical ones with weight 4 (8 gates) and one site interaction term with Pauli weight 2 (2 gates), giving a total of 30 gates. Now, considering a hardware with a lattice connection, the two sub-reticles containing up and down spin can be horizontally nested with the auxiliary qubits mapped under their relative ones. In this case, 4 SWAP gates have to be introduced. In the case of

N.N.N, the number of hopping terms for the site would be 8 with different Pauli weights ranging from 4 to 8, while a single interaction term with Pauli weight 2 is present. The count gives a sum of 94 gates with one having to add 4 SWAP gates in the case of lattice (note that the parallelizability of the circuit is reduced thus increasing the circuit depth).

6.3 Results

The proposed qudit mapping is tested on a simple toy model consisting of four interacting spinless particles, the same studied in Sec. 6.1.3, described by the following Hamiltonian:

$$H = -t \sum_{p,q=1,p\neq q}^{4} a_p^\dagger a_q + U \sum_{i=1}^{4} a_p^\dagger a_p a_{p+1}^\dagger a_{p+1}. \tag{6.12}$$

where periodic boundary conditions ($p = 5 \to 1$) are considered. The model is studied without spin to lower the computational complexity of the simulations. The interaction-like term considered defines a repulsion between particles on different sites. From the mapping prospective, this term implies the same challenges as a regular interaction term.

Starting from the standard AFM mapping on qubits, the qudit method is obtained by mapping the product space of each site and relative auxiliary ones within a single qudit as highlighted by the green hexagons in Fig. 6.2. Since each site has a single auxiliary qubit, the model is mapped into four 4-level qudits.

Now, let's analyse how to decompose the various operators in terms of qudit gates. The simplest ones are the interaction terms, as they can be directly expressed in terms of generalized control phase gates. To understand this, it is simpler to begin by reasoning on the qubit basis. Considering a two-qubit interaction $e^{i\mathcal{H}_t^{pq}\tau} = e^{iU(A_p^\dagger A_p A_q^\dagger A_q)\tau}$ where p and q are the site indices, the action of the operator is to add a phase $\theta = U\tau$ to the state $|\downarrow,\downarrow\rangle$ of the system. For the qubit AFM method and considering the presence of auxiliary qubits, the interaction terms can be expressed in the form $A_p^\dagger A_p \, \mathrm{I}_{p'} \, A_q^\dagger A_q \, \mathrm{I}_{q'}$ where the identity operators I acting on auxiliary sites are explicitly stated. The action of the transformation on this enlarged space has to be the same. Hence, independently of the state of the two auxiliary qubits, a phase θ has to be added to all the four states where p and q are simultaneously in the $\downarrow$. Now, it is not difficult to see that this operation, in terms of the proposed qudit mapping, results in four (parallelizable) generalized control phase gates (defined in Sec. 2.3.3).

For hopping terms, one can proceed in a similar manner. A standard hopping term $a_p^\dagger a_q + a_p a_q^\dagger$ is naturally expressed as a XY gate by definition (see 1.14). In

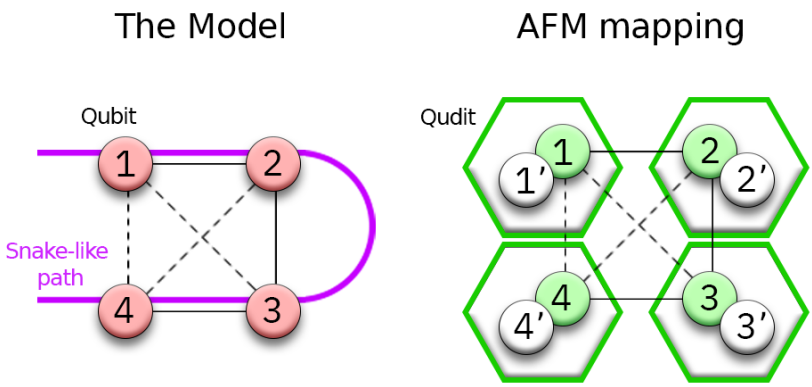

Figure 6.2: Fully connected four-site spinless lattice.. Left: the model where the black lines (dotted and continuous) represent hopping interactions between sites. The continuous purple one highlights the index snake-like pattern. Right: qubit and qudit AFM mapping where ancillary sites are introduced. The green hexagons highlight the qubits that are brought together for qudit AFM.

the simplest case, the hopping operators required by the mapping are of the form $t\left(A_p^\dagger Z_{p'} A_q \mathrm{I}_{q'} + A_p Z_{p'} A_q^\dagger \mathrm{I}_{q'}\right)$. These, in the qudit space, are translated into four parallelizable generalized XY gates, two of them with an angle $\theta = t\tau$ and the others with an angle $-\theta$ (introduced by the - sign of the Z operator). The form of other operators such as $t\left(A_p^\dagger X_{p'} A_q \mathrm{Y}_{q'} + A_p X_{p'} A_q^\dagger \mathrm{Y}_{q'}\right)$ can be similarly deduced. In turn, the XY gate can be rewritten in terms of CPhase and M-Gate gates. Similarly as done with qubits (see Sec. 1.15), a generalized XY gate can be rewritten as two generalized CPhase gates and a few single qudit gates. The qudit decomposition can be easily obtained by extending this one. Alternatively, a XY gate can be obtained by combining the M-Gate plus a CPhase to correct the phases (see Sec. 2.3.3).

The feasibility of this approach and the validity of MNMs as a basis for quantum computation are demonstrated in the following sections by numerical simulations.

6.3.1 Underling physical system

The core of the hypothetical underlying architecture is the Qudit-Switch-Qudit scheme introduced in 2.3.2. Relying on this, a thorough characterization of all required operations is achieved through Quantum Process Tomography (outlined in Section 1.3.3). Then, by combining these linear maps representing individual gates, any quantum circuit can be simulated. In the case under consideration,

this is formed by four four-level qudits. In this way, the entire system dynamics are simulated without having to solve large size differential equations.

For the qudits two $S = 3/2$ ions with isotropic g values of 1.95 and 2.05 and zero-field splitting of $D = -2.4\ (3.0) \times 10^{-2}$ meV are considered. The static magnetic field is set along the z axis with an amplitude of $B_0 = 1.3$ T. Choosing slightly different parameters makes the qudits non-equivalent, ensuring that all transitions are distinct. Alternatively, one could consider anisotropic g and orient the qudits differently with respect to the magnetic field.

The switch (Sw), a spin $S = 1/2$ with a g value of 4, is coupled to the qudits through an isotropic Heisenberg interaction with $J = 0.8\ (1.0) \times 10^{-2}$ meV. The relatively large value of g serves for two purposes: first, it ensures a good factorization between excited and non-excited switch states, and second, it helps to speed up the execution of XY and M gates, although, as shown later, they are remarkably slow.

Considering alternative strategies, one might explore utilizing a spin $S = 1$ with a significant zero-field splitting $D > 0$. By leveraging well-separated energy levels, a two-level subspace such as $|m = 0\rangle$ and $|m = 1\rangle$ can be considered. An example is the Ni^{2+} considered for simulations in chapter5.

6.3.2 Four site model with qudit AFM

Fig. 6.3 a) presents the gate implementation time as a function of the rotation angle θ for XY (green), M-gate (brown), and CPhase (blue) (legend in panel b)). Initially, it is evident that both CPhase and XY gate durations exhibit a strong dependence on the rotation angle. These gates have durations that approach zero for $\theta \to 0$ or 2π, with the maximum duration occurring at $\theta = \pi$. In contrast, the M-gate has a nearly constant duration for any angle. The fact that the minimum duration does not occur at $\theta = \pi$ is an accident stemming from the specific characteristics of the underlying system.

For the considered system parameters, the CPhase gate proves to be the fastest operation. The XY gate is quicker than the M-gate for small angles $\lesssim \pi/10$ or very large angles $\gtrsim 2\pi - \pi/10$, while in the intermediate region, the M-gate becomes more convenient.

A similar behaviour is observed in the decomposition of each hopping term (see Fig. 6.3 b)). In these decompositions, besides the two-qudit gates, single-qudit gates are also taken into account. Each decomposition strategy introduces some. While for the CPhase gate these were already mentioned earlier by describing the decomposition, actually also the other two methods require some. The reason stems from the fact that XY and M-gate are not directly implementable be-

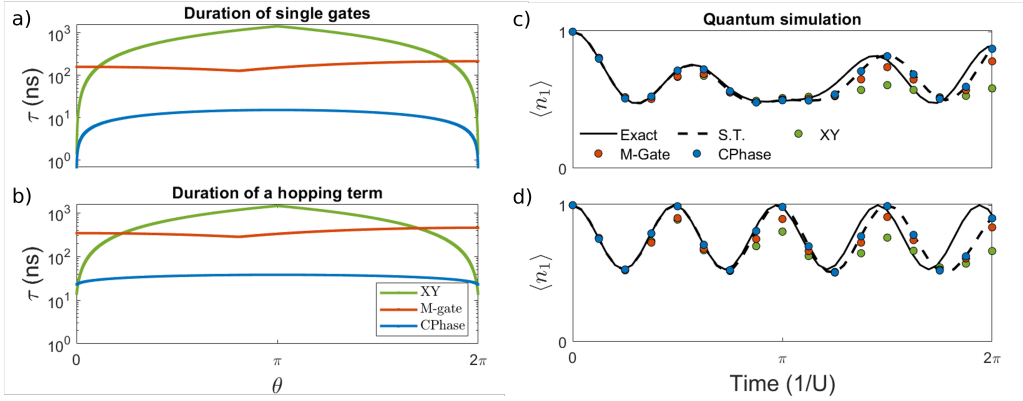

Figure 6.3: a) Comparison of gate duration as a function of rotation angle (θ) for CPhase (blue), XY (green), and M gate (brown). A driving field of 50 G is assumed. While the exact duration is strictly dependent on the physical system, the observed behavior and order of magnitude are generally applicable. b) Comparison of the duration for hopping terms as a function of rotation angle (θ) using CPhase (blue), XY (green), and M - Gate (brown) gates. A driving field of 50 G is assumed. This evaluation also takes into account single qubit gates. c, d) Simulations of the four-site spinless interacting particles shown in Fig 6.2. The top (bottom) panel illustrates the evolution of the population on site 1, where sites 1-2 (1-3) are initially populated. The solid black line represents the exact solution, the dashed line depicts the trotterized curve with $n_{TR} = 6$, and the green, blue, and red points correspond to simulations using CPhase, XY, and M gates, respectively, considering a $T_2 = 100$ μs.

tween all pairs of levels but only between some, and so in some cases several π pulses are required before and after two-body gates. Therefore, all the decompositions have a minimum duration of at least a few tens of nanoseconds due to single qudit gates. For a small range of angles around 0 and 2π the XY decomposition turns out to be faster than CPhase. The above considerations are clearly reflected in the full model simulation. Fig. 6.3 panel c,d) shows the population evolution for two different initial states where the black continuous line is the exact solution, the dashed black line is the trotterized solution $n_{TR} = 6$ and coloured points (green, blue , brown) are the simulation results for using Cphase (green dots), XY(blue dots) and M-gate (cyan dots). The top (bottom) panel reports the occupation probability on site one $\langle n_1 \rangle$ with the system initialized in a halved populated state where sites 1-2 (1-3) are populated. All simulations are performed considering a $T_2 = 100$ μs and a driving field of 50 G. It is important to remark that the name indicates the gate used to decompose the hopping parts while in all cases the interaction terms are decomposed by a single CPhase gate. The whole circuit depth in terms of two-qudit gates is 30 using XY and 48 for M

and CPhase decompositions. These counts are easily explained. Each hopping term is decomposed or into four parallelizable XY, resulting in a depth of 1, or two not parallelizable generalized CPhase gates plus some single qudit rotations, resulting in a depth of 2, or four parallelizable M-gates plus a generalized CPhase gate, giving a depth of 2. A single generalized CPhase gate is used for each interaction term, giving a depth of 1. Since couplings between opposite sites can be implemented simultaneously, 3 steps are required for hopping and another 2 for interaction terms. Considering the 6 Trotter steps, it is easy to obtain the given values. The qubit AFM decomposition of the same model would require a depth of minimum 72 CNOT even considering a fully connected coupling map.

In terms of physical implementation time, the circuits take approximately ~ 500 ns for each Trotter step using the M-gate. For CPhase and XY gates, the circuit time is more dependent on the simulation time and ranges from ~ 150 to 300 ns for the former, and from ~ 100 ns to ~ 6 μs for the latter. The maximum angle considered in the presented simulation is $\pi/3$. This choice was made because the CPhase and XY gates had already reached almost their maximum duration, and with the XY gate, the effect of decoherence was already significant.

All the decomposition strategies effectively approximate the trotterized curve up to $\sim \pi$. However, at longer times, a clear classification of the approaches emerges. Despite CPhase not being the most efficient in terms of gate count, as anticipated due to the differences in single gate duration, it results as the most effective strategy for implementing various operations. The second-best approach appears to be the M-gate, while the XY gate lags behind. The XY gate, in particular, struggles in the long-time region where large angles are required. However, the actual advantage of these different strategies can vary depending on the architecture and specific application. For instance, in the case of an architecture with very long coherence times and a problem that demands high-precision results with a strong trotterization, the XY gate approach may be advantageous. Therefore, the ability to implement different gate schemes is an interesting feature of the proposed architecture.

Given the good results achieved with CPhase decomposition, Fig. 6.4 illustrates the simulation using only CPhase and considers three shorter coherence times $T_2 = \{2, 10, 50\}$ μs. Even with $T_2 = 50$ μs, the simulation results are qualitatively robust, accurately reproducing the curve up to the simulation time $\tau = 2\pi U$ (the largest angle to implement). However, with progressively decreasing coherence times, depicted in the figure as green, blue, and brown lines for $T_2 = 50, 10$, and 2 μs, respectively, the impact of decoherence becomes more pronounced, leading to a decrease in the quality of the simulation results.

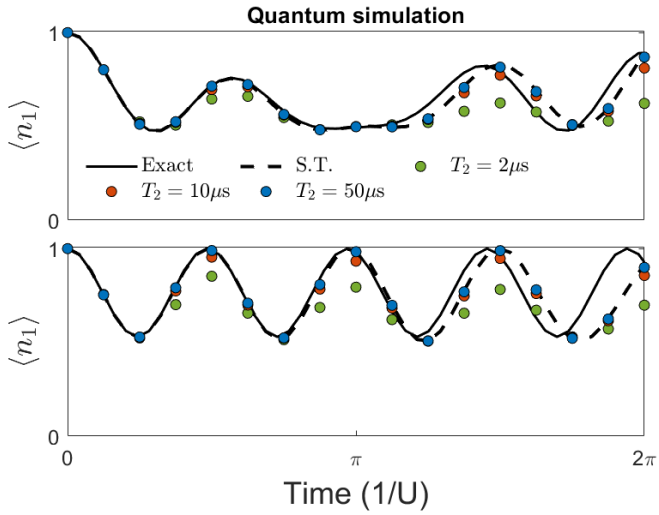

Figure 6.4: Simulations of the four site spinless interacting particles shown in Fig 6.2. The top (bottom) panel shows the evolution of the population at site 1, where sites 1-2 (1-3) are initially populated. The solid black line is the exact solution, the dashed line is the trotterized curve with $n_{TR} = 6$, and the green, blue and red points are simulated with CPhase, gates considering a coherence time of $T_2 = 2, 10, 50$ μs, respectively.

6.4 Conclusions

This chapter showcases the potential of a qudit extension of the auxiliary fermion method as an efficient strategy for simulating Hubbard-like Hamiltonians. A qudit-based logic minimizes the number of two-body operations to be executed in series, thereby reducing circuit depth. This feature is a crucial factor for near-term quantum computing platforms that are characterized by a finite coherence time. Molecular Nanomagnets emerge as promising candidates for such applications, leveraging their most prominent features, i.e. a coherent multi-level structure and a high chemical tunability. Through realistic numerical simulations, the feasibility of this approach has been demonstrated. The diverse range of two-body control techniques explored in this work, CPhase, XY, and M-gate, provides flexibility for adapting to various system architectures and target model Hamiltonians. In fact, any of them could work better depending on the actual architecture and application. In particular, although it seems the least promising at the moment, XY-gate could work very well for highly trotterized simulations.

A natural extension of this work would be to consider qudits of **C** class that are inherently more resilient against decoherence compared to single-spin qudits, as

recently demonstrated [127, 129].
Another interesting opportunity would be to consider architectures in which molecules are coupled through resonators, providing further opportunities for manipulation and control. These technologies, already well developed for superconducting qubits [193], would allow architectures to be scaled much more easily. Indeed, the limited coupling of the spins with the cavities that has limited this approach so far, has been overcome by recent studies [103, 194, 195].

CHAPTER 7

Assessing Chiral-Induced Spin Selectivity Effect by Magnetic Resonance Experiments

The Chiral-Induced Spin Selectivity effect (CISS) is a phenomenon that has recently generated a significant interest in the scientific community, as it is believed to underlie numerous biological reactions [196–198]. Several independently conducted experiments of electron transport have revealed that the flow of current through a helical molecule (χ) can induce spin polarization in electrons [199]. This polarization depends on the handedness of the molecule, and it has been observed even at room temperature [200]. These experiments encompass self-assembled monolayers of chiral molecules and single molecules addressed by an atomic force microscope [201–203].

Despite numerous attempts, a comprehensive theoretical explanation that unequivocally clarifies the origin of CISS is still lacking [204–218]. To uncover its origins and construct a reliable theoretical model, detailed information on the spin wave function's form after the electron has traversed the chiral bridge is necessary. The experiments conducted so far are generally complex, involving several elements such as interfaces, electrodes, etc., which obscure the nature of the phenomena and provide access only to indirect information [196]. To address this challenge, a new approach is required.

In this chapter, three different magnetic resonance experiments investigating the Electron Transfer (ET) process at the single-molecule level are presented [140]. By employing a highly coherent qubit ($\mathcal{Q}$) chemically attached to the Donor-χ-Acceptor (D-χ-A) system, as an external sensor, polarization can be directly detected. Through time-resolved electron paramagnetic resonance (TR-EPR) techniques [219–223], the qubit provides access to the electron state without influencing the ET process, allowing to get information on the spin state immediately after the process has occurred. Furthermore, it is demonstrated that it is possible to obtain information on the ET process even with a randomly oriented ensemble of $D - \chi - A$ molecules. In conclusion, the presented experiments lay the groundwork for building a comprehensive theoretical model.

The chapter is organized as follows: in the first section 7.1, it is first introduced the ET and the structure of the hypothetical D-χ-A-Q molecule considered in the simulations is presented and its feasibility is discussed. The following section 7.2 introduces the TR-EPR technique and explains how the calculations were performed. Then, Sec. 7.3, the different proposed experiments are presented. Finally, section 7.4 closes the chapter by summarizing the results.

7.1 Electron Transfer Through a Chiral Bridge

The presented magnetic resonance experiments study the ET process occurring at the single molecule level in systems characterized by D-χ-A structure. As schematically depicted in Fig. 7.1, the experimental scenario supposes the system is initially at equilibrium with the donor in a doubly occupied ground state. After a photon excitation (PE), one of the electrons gains energy and the system goes into the D^*-χ-A singlet state. The relaxation mechanisms induce the ET that yields the systems in a charge separated state D^+-χ-A^-. At this stage, what is commonly observed in the presence of a linear bridge are spin-correlated radical pairs (RP). If CISS phenomenon works as experimental results suggest, it is expected that by changing the linear bridge to a chiral one the final state should have a full or at least partial polarization in spin. In particular, in the following simulations three scenarios are considered:

- **Singlet**: $|S\rangle = (|\uparrow\downarrow\rangle - |\downarrow\uparrow\rangle)/\sqrt{2}$, entangled non polarized state characteristic of ET through a linear bridge.

- **Polarized**: $\rho_p = \frac{1+p}{2}|\uparrow\downarrow\rangle\langle\uparrow\downarrow| + \frac{1-p}{2}|\downarrow\uparrow\rangle\langle\downarrow\uparrow|$ (with $-1 \leq p \leq 1$ and $\neq 0$), a full or partial polarized state is expected due to spin selectivity after ET through a chiral bridge.

- **Non-polarized**: $|\psi_U\rangle = \cos\frac{\theta}{2}\frac{e^{i(\lambda+\phi)}|\uparrow\downarrow\rangle - |\downarrow\uparrow\rangle}{\sqrt{2}} - \sin\frac{\theta}{2}\frac{e^{i\lambda}|\uparrow\uparrow\rangle + e^{i\phi}|\downarrow\downarrow\rangle}{\sqrt{2}}$, entangled non polarized state generated by a coherent rotation of the transferred electron belonging to $|S\rangle$ as suggested in Ref. [224].

In summary, the proposed experiments have the aim to distinguish among the not polarized $|S\rangle$ and $|\phi_U\rangle$ states which represent a situation in which the supposed spin-filter mechanism does not happens with the polarized state $|\rho_p\rangle$ where the spin-filter works with a certain probability p.

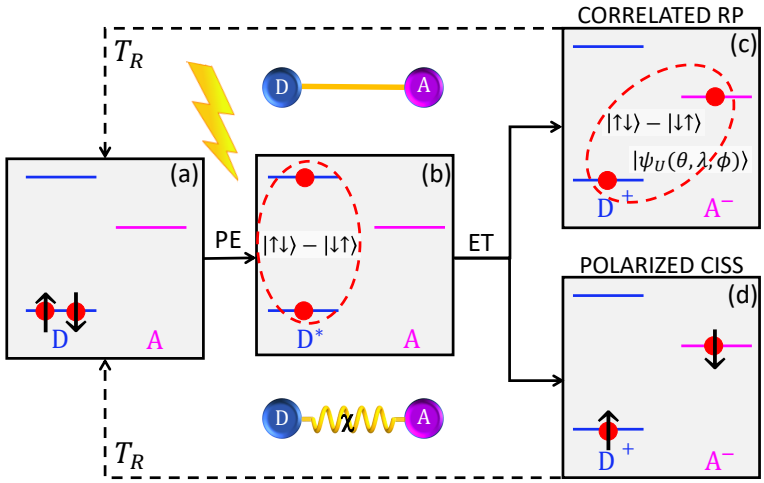

Figure 7.1: Schematic representation of the electron-transfer mechanism: (a) Two electrons on the ground orbital of the donor D are in a double occupation state. (b) Due to photo-excitation one of electron is excited and brings to the D*A entangled (red dashed line) singlet state. The relaxation mechanism induces the electron-transfer of the excited electron to the acceptor (A). Depending on the bridge form, linear or helical, the final state is expected to be not-polarized (c) or polarized (d). The recombination mechanism recreates the initial state on a time scale T_R (dashed arrows). Reproduced from Ref. [140] with permission under the terms and conditions of the Creative Commons Attribution license CC-BY 4.0.

7.1.1 D-χ-A molecule

A suitable molecule to observe the phenomenon must meet some requirements. First of all, it would be desirable for the electron transfer process to be highly efficient and to generate radical pairs with relatively long lifetimes. A suitable choice could be to exploit C_{60} or derivatives of naphthalenediimide as acceptor with good donors as pyrene, oligophenylene-vinylene, and tetrathiafulvalene [225, 226]. Particular considerations have to be made also on the structure of the chiral bridge. This helicoidal structure should be stable in solution, relatively rigid and if both enantiomers can be separately synthesized is a considerable advantage. Possible systems could be helicene characterized by rigid helicoidal scaffolds or helically folded oligoamide of 8-amino-2-quinolinecarboxylic acid which has a more long structure [227]. The spin state of the charge-separated can be described by the following spin Hamiltonian:

$$H_{D\text{-}\chi\text{-}A} = \mu_B \sum_{i=D,A} g_i \, \mathbf{S}_i \cdot \mathbf{B} + \mathbf{S}_A \cdot \mathbf{J}_{AD} \cdot \mathbf{S}_D, \tag{7.1}$$

where $\mathbf{B}$ is an external magnetic field and $\mathbf{J}_{AD}$ parametrized a dipole-dipole interaction among the spins of the un-paired electron on the acceptor S_A and on the donor S_D. Considering the point-dipole approximation the coupling constant can be calculated as $\mathbf{J}_{ij} = [\mathbf{g}_i \cdot \mathbf{g}_j - 3(\mathbf{g}_i \cdot \mathbf{r}_{ij})(\mathbf{g}_j \cdot \mathbf{r}_{ij})]\mu_B^2/r_{ij}^3$. In the numerical simulations reported below, the following parameters were considered: a distance of $r_{DA} = 25$ Å and $g_{1,2} = g_e \mp \Delta g/2$, with $\Delta g = 0.002$.

7.1.2 External Q sensor

A molecular spin qubit Q, chemically attached to the D-χ-A unit, could be exploited as an external sensor to detect the spin polarization on the radical pair. Indeed, thanks to their natural long time of coherence and the chemical engineering, MNMs are an optimal candidate for this task. The D-χ-A-Q system, under the effect of an external magnetic field $\mathbf{B}$, is described by the following spin Hamiltonian:

$$\begin{aligned} H_S =& H_{D\text{-}\chi\text{-}A} + \\ & \mu_B g_Q \, \mathbf{S}_Q \cdot \mathbf{B} + \mathbf{S}_A \cdot \mathbf{J}_{AQ} \cdot \mathbf{S}_Q \end{aligned} \tag{7.2}$$

where $\mathbf{J}_{AQ}$ parametrizes the dipole-dipole interaction between acceptor and qubit spins under the point-dipole approximation. In order for the sensor to not disturb the state of the radical pair, the former has to be almost factorized. Therefore the coupling $\mathbf{J}_{AQ}$ has to be sufficiently small then $\mu_B \, |g_A - g_Q^z| \, B$. On the other side, J_{AQ}^z has to be larger than Q gaps. Considering a fwhm $= 2.35$ mT (full width at half maximum) as estimation of the transitions of metal ion qubit, the above conditions can be met working in the Q-band and assuming a distance of $6 \, Å \lesssim r_{AQ} \lesssim 11 Å$. A suitable choice could be the well characterized VO^{2+} which typically has $\mathbf{g}_Q = (1.98, 1.98, 1.96)$.

7.2 Time-Resolved Electron Paramagnetic Resonance

Differently from standard continuous wave EPR, time-resolved EPR studies the $\langle S_y(B,t) \rangle$ response not only as a function of the external magnetic field but also as a function of time [219, 221, 223, 228]. This procedure permits access to out of equilibrium phenomena. The sample subject to a static field $\mathbf{B}$ is excited by a driving oscillating field of the form $\mathbf{B}_1(t) = B_1(\cos \omega t \, \hat{\mathbf{x}} + \sin \omega t \, \hat{\mathbf{y}})$ which induces transitions between states with energy gap ω. Commonly, it is convenient to move into the rotating frame of the driving field. In this manner the time dependence of the spin Hamiltonian can be eliminated. Considering the secular approximation, valid in the high-field limit, the whole system Hamiltonian is rewritten as follows:

$$\begin{aligned} H_{\text{rot}}(\Omega) &= \sum_i (\mu_B B g_i^{zz}(\Omega) - \hbar\omega) S_i^z \\ &+ \sum_{i,j} J_{ij}^{zz}(\Omega)(2S_i^z S_j^z - S_i^x S_j^x - S_i^y S_j^y) \\ &+ \bar{g}\mu_B B_1 \sum_i S_i^x. \end{aligned} \tag{7.3}$$

where i and j indicate D, A and χ and Ω is a set of three Euler angles that describe the orientation of the molecule with respect to the external fields [221].
The evolution of a real system is also subject also to incoherent processes such as relaxation, dephasing and recombination. Including them, the system evolution is computed by solving the following Liouville equation:

$$\frac{\partial \rho_r(\Omega,t)}{\partial t} = -i\left[\frac{1}{\hbar}\tilde{H}(\Omega) + i\tilde{R} + i\tilde{K}\right]\rho_r(\Omega,t), \tag{7.4}$$

Here, for convenience, the formalism of super-operators, denoted by ˜ symbol, is used. $\rho_r(\Omega,t)$ represents the system density matrix in the rotating frame, $\tilde{R}$ the relaxation/decoherence and $\tilde{K}$ the recombination mechanisms.
In accordance with Ref. [219], applying the slow-motional limit some terms of $\tilde{K}$ are negligible. In particular, the relaxation process is assumed to be parametrized by $1/T_1$ for all the diagonal elements of the density matrix, $1/T_2$ for the off-diagonal terms, and zero for all other entries. Expressing R in the singlet-triplet basis this can be summarized as $\tilde{R}_{iijj} = 1/T_1$, $\tilde{R}_{ijij} = -1/T_2$ and $\tilde{R}_{ijlk} = 0$. For the recombination mechanism, parametrized by $1/T_R$, the super operator $\tilde{K}$ takes the form $\tilde{K}_{ijkl} = -1/T_R(\delta_{ik}\delta_{jl} + \delta_{ij}\delta_{ik})$.
An alternative approach, as shown in Ref. [229], is to consider the relaxation and dephasing processes independently for the three spins. The diagonal elements of $\tilde{R}$ are determined by the stationary condition $\sum_j R_{jjii} = 0$. In the simulations on the D-χ-A-Q system in Q-band this second approach is considered (see Fig. 7.2 a)).
At this stage, the Liouville equation can be explicitly integrated, leading to

$$\rho_r(\Omega,t) = \exp\left\{\left[-\frac{i}{\hbar}\tilde{H}(\Omega) + \tilde{R} + \tilde{K}\right]t\right\}\rho_r(\Omega,0) \ . \tag{7.5}$$

Finally, the EPR response $\langle S_y(B,t)\rangle$ is computed by $\text{Tr}[\rho_r(\Omega,t)S_y]$. It is important to highlight that in case of a randomly oriented sample a spherical average has to be considered. Experimentally, this kind of measurement are affected by experimental difficulties such as inhomogeneous broadening of the system parameters and the coupling of the probed electronic spins with the surrounding nuclear.

To take into account also these experimental issues a convolution of the spectra with a Gaussian line shape function is inserted [223, 228].

7.3 Results

In this section the numerical results of the different simulations are reported. As anticipated in the introduction, the first experimental proposal considers a D-χ-A molecule chemically linked to an MNM qubit Q acting as a sensor. The results show how the three possible states reported in 7.1 can be clearly distinguished from the TR-EPR spectrum of the D-χ-A-Q molecule. In Sec. 7.3.2 it is shown how the polarization on the acceptor A can be transferred to the qubit by a sequence of electromagnetic pulses. With this technique, the EPR qubit response gives an even clearer signature to distinguish polarised from non-polarised states. Furthermore, this mechanism, if properly designed and optimised, could have interesting applications for quantum technologies. Finally, Sec. 7.3.3 reports the results of studies on the randomly oriented ensemble of D-χ-A, which show that even in this simple setup some information about the wave-function can be obtained after the ET process.

7.3.1 TR-EPR signal of a Qubit Sensor

The first experimental proposal exploits a qubit Q, chemically attached to the D-χ-A unit, as an external sensor to get information about the polarization of the electron spin on A after the ET process. The experimental set-up considers a solution that contains only one enantiomer (only one chirality verse) aligned with the external magnetic field direction, achievable through poling due to the large electric dipole moment of chiral molecules based on oligopeptides [214, 230–232]. The free qubit response field, set at $\hbar\omega / \left(g_Q^z \mu_B\right)$, is shifted due to the coupling J_{AQ} with the acceptor, by $\pm J_{AQ}^z / \left(2 g_Q^z \mu_B\right)$ depending on the acceptor electron state. To ensure well-separated peaks, J_{AQ}^z should exceed the line width of the excitation band (Q-band). For un-polarized states like $|S\rangle$ or $|\phi_U\rangle$, two peaks of equal height would be present. Conversely, a partially or fully polarized state like ρ_p introduces a disparity between peak amplitudes proportional to the polarization.
In Fig. 7.2, the results of numerical simulations for electronic (a) and nuclear (b) spin qubits are presented. In the electronic case, the response spectrum $\langle S_y \rangle$, shown as a function of the external driving field, illustrates the donor-acceptor signal (grey-dashed area) and the qubit signal (white area). The qubit is assumed to be initialized in the $|\downarrow\rangle$ state, while for the radical pairs three possible situa-

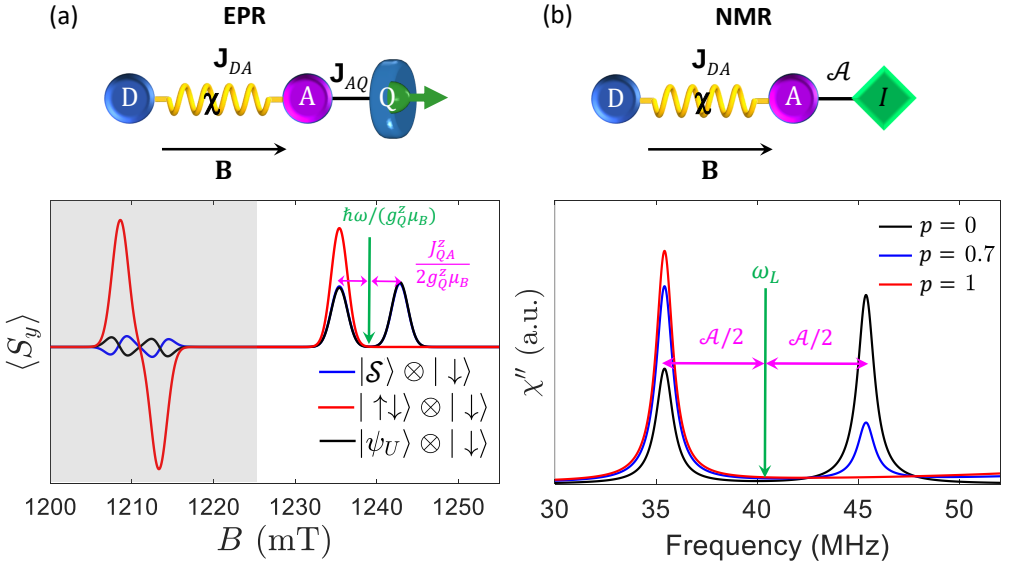

Figure 7.2: (a) TR-EPR spectrum of the D^+-χ-A^--Q system, showcasing states $|S\rangle$, $|\phi_U\rangle$, and ρ_p, with the qubit initialized in the $|\downarrow\rangle$ state. The left side (grey-shaded area) represents the donor-acceptor signal, while the right side displays Q-band absorption peaks relative to the qubit. The spectrums are integrated form 100 to 300 ns. Parameters include $h\nu = 34$ GHz, $J_z \approx 200$ MHz, $r_{DA} = 25$ Å, $r_{AQ} = 8$ Å, $\mathcal{A} = 10$ MHz, $g_{1,2} = g_e \mp \Delta g/2$ with $\Delta g = 0.002$, $\mathbf{g}_Q = (1.98, 1.98, 1.96)$ (typical for VO^{2+} or Ti^{3+}), $T_1 = 2$ μs, $T_2 = 0.5\mu$s, and $T_R = 10$ μs. (b) Broadband NMR spectrum illustrating nuclear excitations on a nuclear spin 1/2 coupled by isotropic hyperfine interaction $\mathcal{A}$ to the donor. The relative amplitude of the two picks give a direct probe of the system polarization. Parameters include $B_0 = 1$ T, $\nu_L \approx 40$, (typical for ^{19}F). Dephasing, relaxation, and inhomogeneous broadening effects are considered with a Gaussian broadening of peaks (FWHM 2.35 mT). Reproduced from Ref. [140] with permission under the terms and conditions of the Creative Commons Attribution license CC-BY 4.0).

tions are compared: a singlet $|S\rangle$, a non-polarized $|\phi_U\rangle$, and a polarized ρ_p state. In the white region, the spectrum provides a qualitative feature allowing differentiation between polarized states like ρ_p and non-polarized states like $|S\rangle$ or $|\phi_U\rangle$. As mentioned earlier, the relative amplitude of the peaks directly reflects the polarization. If the second enantiomer is available, further proof of the phenomenon can be obtained. Indeed, changing the enantiomer would invert the peak positions. Finally, it is important to note that the two considered non-polarized states can be distinguished from the signal of the donor-acceptor (grey region): their response is opposite in frequency.

A similar discrimination can be obtained exploiting a nuclear qubit $I = 1/2$, such as a ^{19}F that has a Larmor frequency $\nu L \simeq 40$ MHz at 1 T, coupled to the acceptor by a hyperfine interaction $\mathcal{A}\mathbf{S}_A \cdot \mathbf{I}$ ($\mathcal{A} = 10$ MHz) in a broad band NMR setup. In Fig. 7.2 (b) the NMR absorption signal (χ'') is plotted as a function of frequency in the region corresponding to the excitation of nucleus spin, split by hyperfine interaction with $\mathcal{A}$. Here, considering ρ_p as the initial state for radical pairs, three different polarization degrees ($p = [1, 0.7, 0]$ red, blue, and black, respectively) are compared. In this case as well, the ratio between peak amplitudes serves as a direct probe of the radical pair state polarization.

7.3.2 Transferring Polarization to a Qubit sensor

The second experiment proposed considers to use a properly designed sequence of electromagnetic pulses, to transfer the possible polarization form the acceptor to the qubit. The analysis of the qubit TR-EPR response unambiguously discerns polarized and not polarized states. As depicted in Fig. 7.3 the pulse sequence (panel (a,b)) consists of two subsequent π pulses that address respectively transitions $|\uparrow_A\downarrow_Q\rangle \rightarrow |\downarrow_A\downarrow_Q\rangle$ with frequency $h\nu_A$ (purple) and $|\uparrow_A\uparrow_Q\rangle \rightarrow |\uparrow_A\downarrow_Q\rangle$ with frequency $h\nu_Q$ (green). The difference between a polarized state (red and blue) and a not-polarized state (black) is well evident. Indeed, the response of the latter is practically negligible, while the former shows distinct picks.
This mechanism could have interesting applications for quantum technologies. Indeed, this procedure could be used to convert spin information, which is difficult to detect, into charge information, which is much easier to read, and vice versa. Thus, it could be used to initialize and read out spin qubits at high temperatures. Of course, for the procedure to be effective, the mechanism needs to be optimised and, in particular, the spin-filtering effect needs to work at a high rate. A further step could be to replace the photoexcitation by an electrically induced CISS-ET and an electrical readout.

7.3.3 TR-EPR on a Randomly Oriented Ensemble

To facilitate and encourage the first investigations, a third experiment involving an even simpler setup is presented. The study focuses on the TR-EPR response of an isotropic solution of D-χ-A molecules. This experiment allows us to determine if the initial state of the radical pairs is singlet or a ρ_p but not whether the latter is polarized. As illustrated by the colour maps in Fig. 7.4 and highlighted by the horizontal (c), integrated over the first maxima-minima picks, and vertical (d), around $B = 349.5$ mT, cuts, the $|S\rangle$ and ρ_p states have opposite absorption/emission picks. The reason behind this feature becomes clear when examining

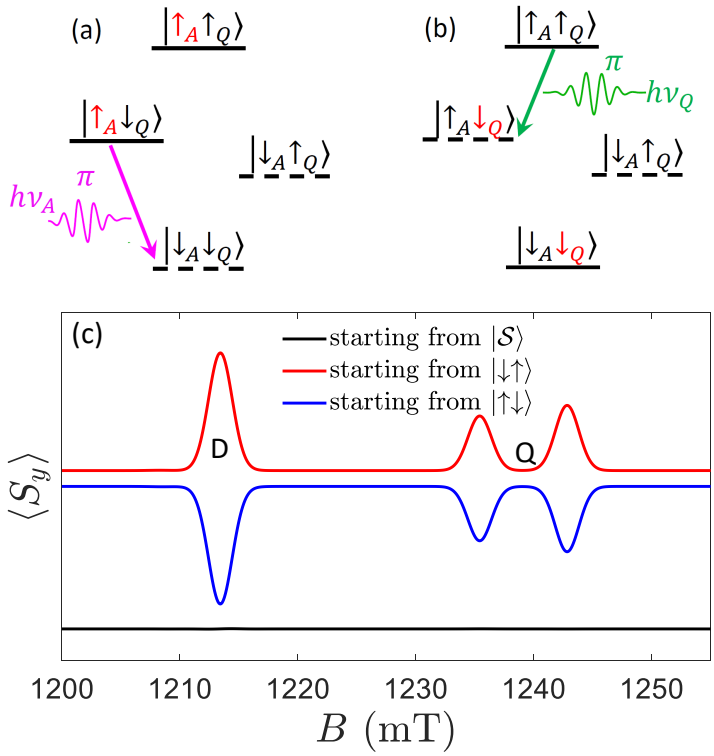

Figure 7.3: Transferring polarization to a qubit sensor. (a, b) Pulse sequence (pink and green arrows) scheme for transferring polarization (red states) from the acceptor A to the sensor qubit Q pair. The state of the donor D remains unaffected by the applied pulses. In the representation, full (dashed) lines denote occupied (non-occupied) states. (c) Time-resolved electron paramagnetic resonance response, integrated over the time lapse from 100 to 300 ns, following the implementation of the pulse sequence. Reproduced from Ref. [140] with permission under the terms and conditions of the Creative Commons Attribution license CC-BY 4.0.

the energy level scheme in the inset of panel (d). For single state $|S\rangle = \frac{|\uparrow\downarrow\rangle - |\downarrow\uparrow\rangle}{\sqrt{2}}$ the free Hamiltonian induces partial population transfer to the symmetric states $|T_0\rangle = \frac{|\uparrow\downarrow\rangle + |\downarrow\uparrow\rangle}{\sqrt{2}}$. Consequently, the system shows absorption lines for $2 \rightarrow 4$ and $3 \rightarrow 4$ transitions while emission for $2 \rightarrow 1$ and $3 \rightarrow 1$. This pattern holds for any orientation angle due to the spherical symmetry of the $|S\rangle$ state. In contrast, the ρ_p state, being strongly anisotropic, exhibits a different behaviour. Regardless of the molecule orientation, the initial population predominantly resides in $|\uparrow\uparrow\rangle$ and $|\downarrow\downarrow\rangle$ states. Assuming these components are larger than those on $|T_0\rangle$, the principal pattern at short times shows emission lines for $4 \rightarrow 2$ and $4 \rightarrow 3$ transi-

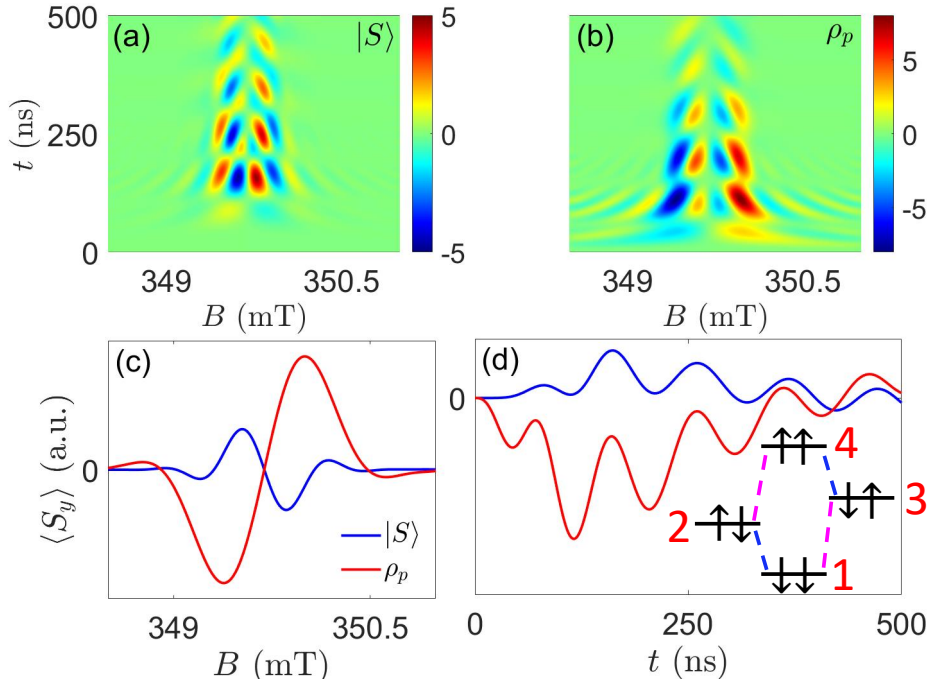

Figure 7.4: TR-EPR on a Randomly Oriented Ensemble of D-χ-A molecules. (a, b) Colour maps of the time-resolved electron paramagnetic resonance (TR-EPR) spectrum for radical pairs in states $|S\rangle$ or ρ_p, respectively. (c) TR-EPR spectrum integrated over the time-lapse corresponding to the first maxima-minima in the maps of panels (a, b). (d) Cut around $B \approx 349.5$ mT, illustrating the time dependence of the maps in panels (a, b). Parameters: $\Delta g = 0.001$, $r_{DA} = 25$ Å, $h\nu = 9.8$ GHz, $T_1 = 2$ μs, $T_2 = 0.5$ μs, $T_R = 10$ μs. Reproduced from Ref. [140] with permission under the terms and conditions of the Creative Commons Attribution license CC-BY 4.0.

tions and absorptions for $1 \to 2$ and $1 \to 3$. This second pattern is the opposite of the one described for the $|S\rangle$ state. Specifically, this can be demonstrated by calculating absorption/emission peaks for different orientations.

In the molecule's frame of reference, a fully polarized state along the chiral axis, such as $|\uparrow\downarrow\rangle$, transforms as follows along the principal axes in the laboratory frame:

$$|\psi_0^{\pm x}\rangle = e^{\mp i S_y \pi/2}|\uparrow\downarrow\rangle = \frac{|\mathcal{S}\rangle}{\sqrt{2}} \pm \frac{|\uparrow\uparrow\rangle - |\downarrow\downarrow\rangle}{2} \tag{7.6}$$

$$|\psi_0^{\pm y}\rangle = e^{\mp i S_x \pi/2}|\uparrow\downarrow\rangle = \frac{|\mathcal{S}\rangle}{\sqrt{2}} \pm i\frac{|\uparrow\uparrow\rangle + |\downarrow\downarrow\rangle}{2} \tag{7.7}$$

$$|\psi_0^{z}\rangle = |\uparrow\downarrow\rangle,\ |\psi_0^{-z}\rangle = |\downarrow\uparrow\rangle\ . \tag{7.8}$$

For all three orientations, it is possible to explicitly calculate the fields corresponding to absorptions (B_a) and emissions (B_e). Assuming $g_1 < g_2$ and $\Delta g \mu_B B < J$, the orientations are computed as follows:

$$\begin{aligned} & Z & & X,Y \\ B_a = & \frac{\hbar\omega}{g_{1,2}\mu_B B} - \frac{J_z}{2g_{1,2}\mu_B B} & B_a = & \frac{\hbar\omega}{g_{1,2}\mu_B B} + \frac{J_{x,y}}{2g_{1,2}\mu_B B} \\ B_e = & \frac{\hbar\omega}{g_{1,2}\mu_B B} + \frac{J_z}{2g_{1,2}\mu_B B}, & B_e = & \frac{\hbar\omega}{g_{1,2}\mu_B B} - \frac{J_{x,y}}{2g_{1,2}\mu_B B}, \end{aligned} \tag{7.9}$$

where for Z direction, absorption is for $2 \to 4$ and $3 \to 4$ and emission for $2 \to 1$ and $3 \to 1$ while for X,Y directions absorption $1 \to 2$ and $1 \to 3$ and emission for $4 \to 2$ and $4 \to 3$. However, due to $J_z < 0$ while $J_{x,y} > 0$, $B_z > B_e$ is both cases. Consequently, also in the spherical average $B_z > B_e$.

However, due to this mechanism working for any value of p, including zero, this experiment does not probe whether the state is polarized. It solely distinguishes ρ_p from $|S\rangle$. The situation becomes even more complex when considering the $|\phi_U\rangle$ state. The latter yields a pattern that, depending on the specific parameters, is intermediate between ρ_p and $|S\rangle$. Therefore, to distinguish also the state $|\phi_U\rangle$, a preliminary accurate characterisation of the samples is necessary.

7.4 Conclusions

This chapter presents three magnetic resonance experiments to investigate CISS effect in electron transfer process through a helical molecule. These experiments are a direct way to have access to the electron wave function after ET and hence measure the expected polarization.
In the first two experiments (Sec. 7.3.1 and Sec. 7.3.2), a MNMs qubit, chemically attached to the D-χ-A molecule, is exploited as an external local sensor. Without altering the ET process, the spectrum of this sensor ultimately allows to distinguish between a polarized and a non-polarized state. Additionally, throughout a sequence of electromagnetic waves, the polarization can be transferred from the acceptor to the qubit. This mechanism not only allows an even clearer picture of polarization in EPR experiments, but could also be used for initialization and readout of qubits, potentially even at high temperatures.
Finally, in the third proposed experiment 7.3.3, it is studied the EPR spectrum of a randomly oriented ensemble of D-χ-A molecules. This analysis, which from an experimental point of view would be simpler, allows to distinguish between a singlet and a ρ_p state but does not provide a direct measure of polarisation.

Therefore, although this experiment can be useful for initial studies, it can not give definitive proof of CISS.

CHAPTER 8

Study of Magnetic Molecules on Prototypes of Quantum Computers

As described in the introduction of chapter 2, molecular nanomagnets have emerged as highly promising candidates for a wide range of applications, including low-temperature refrigeration [108], high-density storage [104, 233], quantum sensing, and as a platform for quantum computation [234–236]. Underlying these applications are interesting quantum phenomena that these systems exhibit. As a result, the study of these systems holds significant relevance across various fields. However, simulating such systems on classical devices can be challenging, primarily due to the exponential growth of the Hilbert space as the size of the molecule increases. For instance, taking Mn_{12} as an example, its Hilbert space, even considering only the spin degrees of freedom of the molecule, has a dimension of the order of 10^8 [237]. Performing brute force calculations for the ground state wave function and its dynamical properties is an arduous task for classical devices. In contrast, quantum computers could offer an exponential advantage by making the scaling of resources polynomial. This means that a quantum computer can efficiently solve problems that would be computationally intractable for classical devices. However, current quantum technologies are still limited by resource constraints and noise effects, and it is not possible to run arbitrarily complex algorithms such as Quantum Phase Estimation. To reduce resource requirements and bring closer the achievement of quantum advantage, a new class of hybrid quantum-classical algorithms enters into play. In particular, the Variational Quantum Eigensolver (VQE), which is based on the variational principle, uses a variational quantum ansatz that, through a classical optimisation process, attempts to reproduce the ground state and thus provides an estimate of the ground state energy of a target system.

In this chapter, simple molecular models described by anti-ferromagnetically coupled chains of spins 1/2 are investigated [238]. In particular, in the first part of the chapter the focus is on static properties, including ground state energy,

magnetization, finite size and parity effects. Comparisons are made between the strengths and weaknesses of two classes of VQE ansatzs: the Hardware Heuristic Ansatz (HHA) and the Physically Motivated Ansatz (PMA). The analysis encompasses factors such as precision, convergence speed, and the ability to respect system symmetries, providing valuable insights into the performance of these ansatzs. It has been observed that physically motivated ansatzs, even if generally more expensive to implement, in general overcome in performance HHA. In fact, by being constrained to respect the symmetries of the system, PMAs are able to reconstruct the state more accurately and reach convergence faster. The two class of ansatzs are tested by extensive numerical simulations with and without noise.
In the second part of the study, real quantum processors are exploited to calculate dynamical spin-spin correlation functions. This observable is of interest because it is the key ingredient in the calculation of several quantities, including the magnetic inelastic neutron cross section [239]. To improve the reliability of results, a mitigation of readout error and a physically motivated mitigation technique called Phase and Scale (PaS) have been applied [43, 239–241].

8.1 Hybrid Quantum-Classical Methods

Despite increasing research in quantum computing, current technologies still fall short when it comes to implementing large-scale quantum algorithms. Algorithms such as Quantum Phase Estimation (QPEA) demand the execution of circuits with a number of qubits and depth that far exceed the capabilities of present and near-future devices. Additionally, achieving these applications requires a fault-tolerant quantum computation, which entails an integrated Quantum Error Correction. This scenario has prompted the pursuit of a new class of algorithms for short-term applications that can leverage limited quantum resources to yield a quantum advantage [242, 243]. NISQ devices can implement narrow and shallow circuits with precision constrained by noise. Therefore, it becomes crucial to minimize the quantum resource requirements and develop algorithms that are inherently error-proof or at least that can give valuable results even in the presence of noise. The class of Hybrid Quantum-Classical algorithms has emerged as a response to these needs.
Hybrid algorithms aim to harness the strengths of both classical and quantum computers, delegating quantum devices to handle only the tasks that are inefficiently done on the classical counterparts while utilizing classical computers for all other aspects. These algorithms can be included in the branch of the Quan-

tum Approximate Optimization Algorithms (QOAO) i.e. algorithms that have been designed to address optimization problems [244–246]. One of these is the Variational Quantum Eigensolver (VQE) which, based on the time-independent variational principle, is specifically designed to determine an upper bounded estimation of the ground state energy of a target system [247].

The following sections explore the specifics of the VQE, providing the necessary theoretical background and examining practical realizations in detail.

8.2 Variational Quantum Eigensolver Algorithms

The Variational Quantum Eigensolver (VQE) belongs to the family of variational methods. This class of algorithms, based on the variational principle, are hybrid quantum-classical methods that iteratively [26, 242, 247, 248]. As mentioned earlier, the VQE is a hybrid quantum-classical algorithm that iteratively searches for an optimal approximation of the ground state eigenvector by minimizing the energy of a parametric ansatz state $|A(\bar{\theta})\rangle$. The choice of the ansatz strongly influences the accuracy of the method.

The VQE algorithm is divided into three steps: state preparation, measurement, and optimization (see Fig.8.1). The first step, carried out on a quantum computer, involves the generation of a quantum state that represents the variational ansatz. Subsequently, the energy of the quantum state is measured. In the final stage, purely classical, an optimizer utilizes the energy estimation to determine how to adjust the ansatz parameters to minimize the energy.

The following sections delve into the method in greater detail, beginning with the theory support of the variational theorem. From there, the sections explore the three steps of the VQE algorithm, providing a thorough examination of each step.

8.2.1 Variational Theorem

The theoretical foundation of all variational methods, such as the Variational Quantum Eigensolver, relies on the variational theorem [26]. This guarantees that any ansatz state $|A\rangle$ has an average energy E_A greater or equal to the ground state energy E_0. This principle is particularly useful for estimating E_0. Indeed, by employing a trial-and-error approach, an optimal solution can be sought by identifying the ansatz that minimizes the energy E_A. A simple proof of the theorem is reported hereafter .

Let's start by express the ansatz state $|A\rangle$ as an expansion in terms of the N

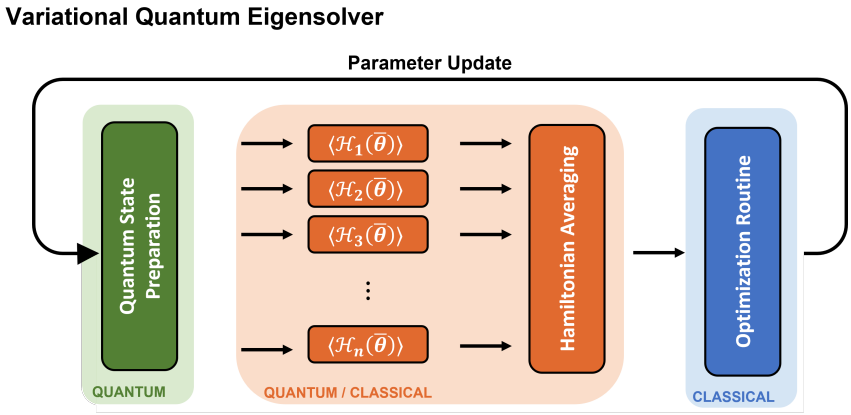

Figure 8.1: Schematic representation of the VQE algorithms.

eigenstates $|\mu\rangle$ of the system:

$$|A\rangle = \sum_{\mu=0}^{N} |\mu\rangle \langle\mu|A\rangle \quad . \tag{8.1}$$

Using the definition $\mathcal{H}|\mu\rangle = E_\mu |\mu\rangle$, the ansatz energy E_A of can be re-written as follows:

$$\begin{aligned} E_A &= \frac{\langle A|\mathcal{H}|A\rangle}{\langle A|A\rangle} \\ &= \frac{\sum_{\mu=0}^{N} |\langle\mu|A\rangle|^2 E_\mu}{\sum_{\mu=0}^{N} |\langle\mu|A\rangle|^2} \\ &= \frac{\sum_{\mu=1}^{N} |\langle\mu|A\rangle|^2 (E_\mu - E_0)}{\sum_{\mu=0}^{N} |\langle\mu|A\rangle|^2} + E_0 \geq E_0 \quad . \end{aligned} \tag{8.2}$$

This proves that any ansatz state has an energy $\geq E_0$. In practice, exploiting a parametrized ansatz $|A(\bar{\theta})\rangle$, an optimal approximation of the ground state can be obtained by tuning the set of parameters $\bar{\theta}$. Without having any prior information on the state $|0\rangle$, this method yields information about both the eigenstate $|E_0\rangle$ and the related eigenvalue E_0.

8.2.2 Ansatz State Preparation

In the previous sections, a comprehensive overview of the variational methods and a theoretical background of the method have been presented. Hereafter, the focus shifts to the practical implementation of the VQE algorithm.

The zero step of any quantum algorithm requires mapping the target systems onto the quantum hardware. This process entails rewriting the system Hamiltonian in terms of qubit operators. In the specific cases addressed in this chapter, i.e. the simulation of spin 1/2 chains, the mapping is straightforward. Taking into account a normalization factor, the spin operators can be directly expressed in terms of qubit operators. In other words, each spin is associated to a qubit. However, it's important to note that this mapping is not always obvious and, for certain problems, it plays a crucial role. A well-designed mapping strategy can significantly reduce the resource requirements for the computation.
Having identified a mapping it is possible to start with the actual algorithm. As described above, the variational methods are based on constructing a parametrized ansatz $\left|A(\bar{\theta})\right\rangle$ approximating the ground state of the target Hamiltonian. By operating iteratively, the parameters are updated to obtain an increasingly better approximation. It is intuitive to understand that the performance of the algorithm, in terms of computational cost and accuracy, strongly depends on the choice of the ansatz.
The dimension of the Hilbert space of the target system and thus the volume of information to be processed grows exponentially with its size. In order for the ansatz to be efficiently implemented and processed it needs to require (at most) polynomial resources. It is therefore beneficial if the ansatz is limited by construction to explore only relevant parts of the Hilbert space exploiting a limited number of parameters. While using a flexible and broad ansatz makes the algorithm more general and suitable for a wide class of problems, a specific ansatz is usually more performant. By leveraging on the physical knowledge of the system, such as symmetries or conserved quantities, it is possible to create a targeted ansatz that reduces the number of parameters and the dimension of the accessed sub-space without loss of validity.
Using a quantum computer, the construction of a variational ansatz corresponds to searching for the sequence of unitary operations that best approximates the evolution from the initialization state to the desired state. In addition to correctly approximating the target state, a good ansatz should be implementable with a low-depth circuit. This second characteristic is crucial in the case of NISQ devices, where errors are significant and limit the accuracy. In general, the parameters are the angles of rotations, i.e. single-qubit gates.
Based on this consideration, two classes of ansatz can be distinguished:

- **Hardware Heuristic Ansatz** (HHA): This class is designed to adapt to hardware capabilities and is not tied to the specific model being studied, making it generally applicable. Typically, these ansatzs have a modular block struc-

ture in which single-qubit and two-qubit gates alternate. The variational parameters are generally the single qubit rotation angles. These gates are usually chosen from the native hardware operation set. Furthermore, this class provides direct control over the circuit depth, allowing the hardware capabilities to be exploited at maximum [242, 247, 249].

- **Physically Motivated Ansatz** (PMA): Based on a prior knowledge of the target system, an initial state is designed to best approximate it. This class is based on methods or numerical techniques that systematically provide better approximations of the state and thus are expected to produce high quality results. Several forms have been derived from classical variational methods. An example is the Unitary Coupled Cluster (UCC), derived from Coupled Cluster (CC) [242, 250].

In summary, PMAs are problem-specific, require fewer parameters, and yield accurate results, while HAs are generally applicable, can be implemented with shallower circuits, and try to take the most from hardware capabilities. The choice between these two classes of ansatz depends on carefully weighing their advantages and disadvantages, which are further investigated in Section 8.3.

8.2.3 Measurements

Once the parametric state has been constructed, the second step consists of measuring its energy, which entails extracting the expectation values of the system Hamiltonian on the ansatz state: $E(\vec{\theta}) = \left\langle \Psi(\vec{\theta}) \middle| H \middle| \Psi(\vec{\theta}) \right\rangle$. Practically, the approach used is known as Hamiltonian Averaging [242]. The target Hamiltonian, already mapped onto qubit operators, is expressed as a sum of tensor products of Pauli matrices [25]:

$$\mathcal{H} = \sum_{i_1\alpha_1} h^{i_1}_{\alpha_1} \sigma^{i_1}_{\alpha_1} + \sum_{i_1\alpha_1 i_2\alpha_2} h^{i_1 i_2}_{\alpha_1\alpha_2} \sigma^{i_1 i_2}_{\alpha_1\alpha_2} + \dots ,$$

and, due to linearity, the expectation values are given by:

$$\langle \mathcal{H} \rangle = \sum_{i_1\alpha_1} h^{i_1}_{\alpha_1} \left\langle \sigma^{i_1}_{\alpha_1} \right\rangle + \sum_{i_1\alpha_1 i_2\alpha_2} h^{i_1 i_2}_{\alpha_1\alpha_2} \left\langle \sigma^{i_1 i_2}_{\alpha_1\alpha_2} \right\rangle + \dots ,$$

where i_j represents the qubit index, α indicates the x, y, and z components of the Pauli matrices σ_α, and h are the corresponding coefficients. Each term can be estimated by calculating the expectation value of the corresponding operator,

and the energy expectation value is reconstructed as the weighted sum of these different terms.

Some complications arise from the measurement procedure itself. This procedure is inherently subject to statistical errors, which not only affect the accuracy of the obtained results but can also impact optimization algorithms, potentially slowing down or even impeding convergence. Moreover, a more practical issue arises with Hamiltonian Averaging, as it in theory could violate the variational principle. Due to statistical errors, the sum of the expectation values of local operators may yield values for the global Hamiltonian that are below the ground state energy. This directly undermines the method. However, it's worth noting that with adequate statistical analysis, all these errors can be minimized. As precision requirements increase, larger samples are needed to mitigate the impact of statistical errors. In the numerical studies reported below the statistical measures are averaged on 8192 shots.

In general, the computational cost of Hamiltonian Averaging increases proportionally to $O(k)$, where k is the number of local Pauli operators. For large systems with many terms in the Hamiltonian, this approach can become computationally expensive. To address this, several strategies have been proposed. For example, it is possible to group and extract simultaneously commuting operators [242, 250, 251]. In this case, error estimation must take into account the correlations between measurements. Another technique to reduce computational cost is truncating the Hamiltonian with a certain precision [242]. By knowing the coefficients h_i of the various terms, one can choose not to measure those with magnitudes lower than the desired accuracy of the computation.

An alternative approach to Hamiltonian Averaging is Quantum Phase Estimation (QPE), which allows the extraction of $\langle \mathcal{H} \rangle$ in a single measurement. However, as said in the introduction, QPE requires the implementation of complex circuits that are currently beyond the capabilities of existing devices. Hamiltonian Averaging, on the other hand, reduces circuit complexity at the cost of multiple measurements.

In conclusion, the measurement procedure extracts the energy expectation value from the ansatz state. This classical information can now be transferred to a classical device and serves as the starting point for the optimization procedure.

8.2.4 Optimization Process

Optimization is a well-known problem extensively addressed in classical computation. Various algorithms, supported by strong mathematical derivations, have been widely studied and documented. However, optimization procedures

for quantum applications pose new challenges and require specific strategies. Multiple studies have addressed this problem with the aim of improving the performance of algorithms [242, 247, 250].
Two main reasons justify the significant effort given to these studies. Firstly, the efficiency of the algorithm is closely tied to the optimization process. In a context where quantum resources are limited, it is crucial to extract maximum benefit from the available resources. Secondly, the data obtained from quantum devices is affected by noise, arising from both intrinsic quantum computer errors and statistical noise. While statistical noise can be directly addressed by increasing statistics, the challenge is more complex for the former source.
The presence of noise introduces another variability in the outcomes of the measurement procedure. For instance, in VQE applications, two statistical measurements on the same ansatz state would not give the same energy values as output. These aspects pose new challenges for optimization procedures, thereby complicating the optimizer's task.
Several studies have shown that not all optimizers adapt well to such situations, in particular gradient-based methods struggle to achieve convergence. The following studies consider two algorithms, COBYLA and SPSA, which have been extensively analysed in the literature [247, 249]. A deep mathematical treatment of these algorithms is beyond the scope of this work, but the practical aspects necessary for their application are discussed below.

- **COBYLA** (Constrained Optimization By Linear Approximations) was developed in 1994 by S. Gomez and J.-P. Hennart [252]. Like most optimization algorithms, it is based on a gradient method. These methods are potentially very efficient but suffer in the presence of a large number of parameters or noise. Indeed, as the spatial dimension increases, gradients tend to zero, and algorithms struggle to navigate the space. Also noise can confound the routine as the noise can modify gradients.

- **SPSA** (Simultaneous Perturbation Stochastic Approximation), is an optimization algorithm created in the late 1990s by James C. Spall [253]. It distinguishes itself from most other methods by relying solely on measurements of the objective function to determine the next moves. By avoiding the need to compute gradients or other mathematical derivatives, SPSA often exhibits high efficiency for problems in high-dimensional spaces. Furthermore, SPSA is also less affected by noise.

Both methods are used in the reported studies: COBYLA in noiseless simulations

and SPSA in the presence of noise.

8.3 Investigation of Static Properties of Spin Chains

In this section, the Variational Quantum Eigensolver algorithm is employed to extract static properties, including ground state energy, magnetization, and local spin expectation values from simple spin models. Specifically, the considered models are closed chains (rings) composed of four and six spin-1/2 particles interacting through the Heisenberg antiferromagnetic interaction. The selection of these straightforward models is motivated by their ability to describe some Molecular nanomagnets.
Including the effect of an external magnetic field, these chains are described by the following Hamiltonian:

$$\mathcal{H} = 2J\sum_{i}^{N} \mathbf{s}_i \cdot \mathbf{s}_{i+1} + B\sum_{i=1}^{N} s_i^z \,, \tag{8.3}$$

where i represents the site index with periodic boundary conditions ($N+1=1$), s_i^α denotes the spin operators associated with the site i, and J and B are constants that respectively parametrize Heisenberg and Zeeman interactions. It is easy to see that the total spin $\mathbf{S}^2$ and local spin operators S_z are conserved quantities for $\mathcal{H}$:

$$[\mathcal{H}, \mathbf{S}^2] = 0 \quad \text{and} \quad [\mathcal{H}, S_z] = 0 \,. \tag{8.4}$$

As a result, the eigenstates of the systems can be characterized by the quantum numbers $\mathcal{S}$ and m, where $S = 0,1,2(,3)$ and $m = -S, -S+1, \ldots, S$. Fig. 8.2 a) and c) illustrate the energy diagram (grey lines) for the two models as a function of B/J. The ground state is highlighted by a black line. For low B/J both systems exhibit a ground state $|S=0, m=0\rangle$. Increasing the ratio, the Zeeman interaction becomes more influential and a first crossing is encountered around $B/J \sim 2$. Here, the ground state transforms into $|S=1, m=-1\rangle$. A further increment up to $B/J \sim 4$ produces another crossing. The focus of the study is primarily on these first two regions, denoted as the low- and intermediate-field regimes, as they present the most interesting behaviour. Specifically, for large values of B/J, all the spins in the ground state become aligned, resulting in a trivial factorized state $|\downarrow,\downarrow,\ldots,\downarrow\rangle$.

8.3.1 Ansatz derivation

As mentioned in Sec. 8.2.2, the analysis compares the performance of the HHA and PMA classes of ansatz. The former has a modular structure consisting of

parameterised single-qubit rotations and two-qubit entanglement gates. Each set of single- and two-qubit gates forms a block V. Each block identifies a layer of the ansatz, which together determines its depth. It is advantageous to adopt native hardware gates to avoid introducing additional operations during the implementation on real devices. Moreover, it is crucial to respect the hardware coupling map, which represents the physical connections between qubits. With IBM Quantum devices in mind, a suitable choice designed the modular block $V_j(\vec{\theta}_j)$ by employing rotations around the y-axis single-qubit gate $R_y(\theta) = U(\theta,0,0)$ 1.6 and CNOT gates.

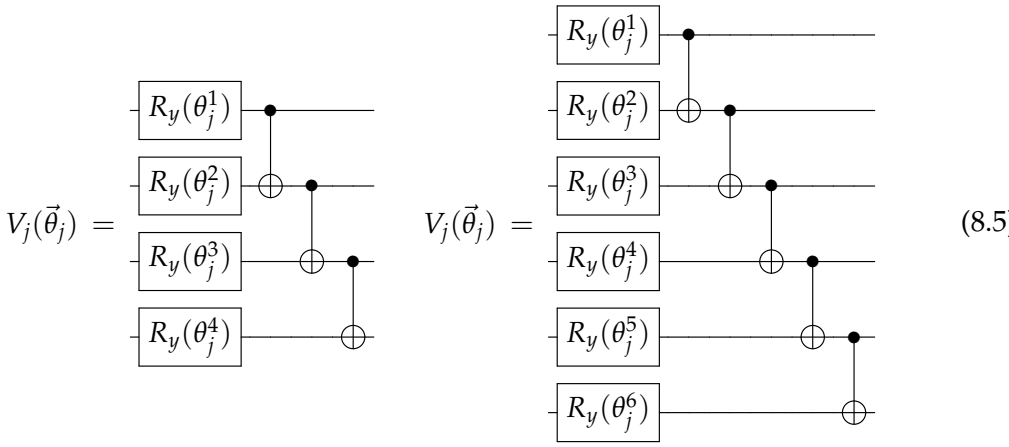

(8.5)

where the left (right) figure clearly corresponds to the case of the four (six) spin chain. It is worth noting that this ansatz only requires linear connectivity between hardware qubits, a condition that can be easily met on most devices. In general, a more global rotation such as $U(\theta,\phi,\lambda)$ should be considered. However, in these particular cases, since the Hamiltonian is real and hence its eigenstates are real, the rotations can be restricted around the y-axis. This choice leads to a significant reduction in the number of variational parameters, from 12 (18) per layer to 4 (6). The optimal number of layers j can be practically determined by gradually increasing it and observing the results. After the block of the last layer, a set of parametrized rotations, commonly referred to as post-rotations, is usually added.

For the class of PMA (Physical Model Ansatz), our aim is to design an ansatz that reflects and respects the properties of the underlying physical system. As observed earlier, the eigenstates of the rings under study are well-defined by the quantum numbers S and m. Therefore, a smart choice is to work with ansatz that holds the correct quantum numbers. This can be done by defining a variational circuit that conserves these values. The idea is to initialize the ansatz into a state that has the correct quantum numbers and then apply a parametrized cir-

cuit that, while conserving them, can reproduce the ground state. This approach ensures that the ansatz always resides in the "correct" subspace, thereby reducing the variational search. Additionally, it ensures that the optimizer does not become trapped in a local minimum corresponding to an excited state. This is particularly advantageous when dealing with regions of parameter space near crossings.

For chains with antiferromagnetic nearest-neighbor couplings, it has been shown that for sufficiently small values of the magnetic field B, low-field region, the ground state minimizes the total spin S [254]. Consequently, in the case of even-number spin 1/2 chains, the ground state has $S = 0$. However, as the magnetic field is increased, the Zeeman term becomes more significant and favours the $S = 1, m = -1$ state, which, after the first crossing, becomes the new ground state (intermediate field). Depending on the region studied, either the low- or intermediate-field regime, an appropriate initial state can be defined as follows:

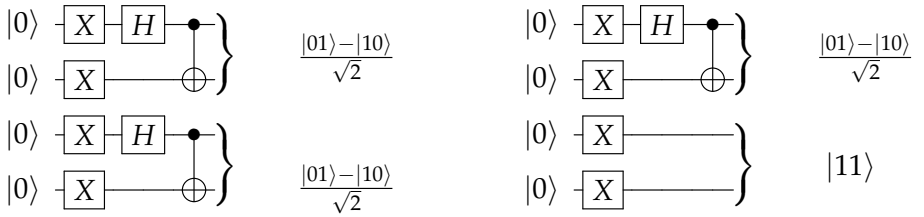

for the four qubits chain, and

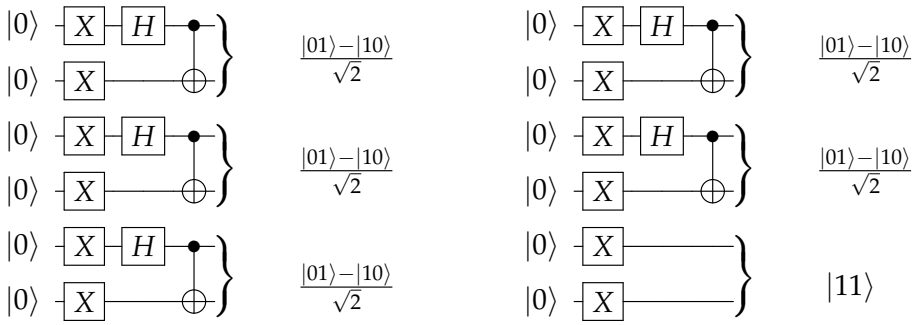

for the six qubit chain, where the circuits on the left (right) side have a total $S = 0$ ($S = 1$) and $m = 0$ ($m = -1$). Although these states have the correct quantum values, they break the symmetries of the system and therefore do not approximate the ground state well. Furthermore, it is important to note that it is not necessary to know the crossing point, since it can be determined practically by exploiting the variational theorem.

The natural choice to create a variational circuit that conserves the quantum values is to base the circuit on the physical interaction that generates it, i.e. a Heisenberg interaction [255]:

$$W_{ij}(\theta) = e^{-i\theta \mathbf{s}_i \cdot \mathbf{s}_j} \tag{8.6}$$

This interaction is efficiently decomposed into gates using only 3 CNOT and few single qubit gates [25]:

$$W_{ij}(\theta) \;=\; \begin{array}{l} \text{—}\bullet\text{—}\,\boxed{\mathrm{R}_x(\frac{\theta}{2}-\frac{\pi}{2})}\,\boxed{\mathrm{H}}\,\text{—}\bullet\text{—}\,\boxed{\mathrm{H}}\,\text{—}\bullet\text{—}\,\boxed{\mathrm{R}_x(\frac{\pi}{2})} \\ \text{—}\oplus\text{—}\,\boxed{\mathrm{R}_z(\frac{\theta}{2})}\,\text{—}\oplus\text{—}\,\boxed{\mathrm{R}_z(\frac{-\theta}{2})}\,\text{—}\oplus\text{—}\,\boxed{\mathrm{R}_x^{\dagger}(\frac{\pi}{2})} \end{array} \tag{8.7}$$

A PHA variational block can be formed by altering $W_{ij}(\theta)$ circuits on different qubits couples:

$$V_k(\vec{\theta}_k) = \begin{array}{l} \boxed{W_{12}(\theta_k^1)}\;\boxed{W_{23}(\theta_k^2)} \\ \boxed{W_{34}(\theta_k^3)}\;\boxed{W_{14}(\theta_k^4)} \end{array} \qquad V_k(\vec{\theta}_k) = \begin{array}{l} \boxed{W_{12}(\theta_k^1)}\;\boxed{W_{23}(\theta_k^2)} \\ \boxed{W_{34}(\theta_k^3)}\;\boxed{W_{45}(\theta_k^4)} \\ \boxed{W_{56}(\theta_k^5)}\;\boxed{W_{16}(\theta_k^6)} \end{array} \tag{8.8}$$

In conclusion, the ansatz is formed by combining an initialization layer, which fixes the quantum values of the initial state, together with a sequence of variational blocks (see 8.9). These blocks have the main purpose of reconstructing the ground state symmetry that is broken by the initial state. In practice, it has been observed that for the investigated systems, coupling the nearest sites using W_{ij} blocks is sufficient for reconstructing the ground state. Another observation made after conducting several tests is that it is advantageous to couple qubits between different triplets or singlets before coupling them within those groups. For instance, in the case of the four-spin ring at low field, the optimal configuration is as follows:

As with HHA, it may be necessary to apply the variational block several times

$$\begin{array}{l} |0\rangle\;\boxed{X}\;\boxed{H}\text{—}\bullet\text{—}\;\boxed{W_{23}(\theta^1)}\;\boxed{W_{12}(\theta^2)} \\ |0\rangle\;\boxed{X}\text{—}\oplus\text{—}\;\boxed{W_{14}(\theta^3)}\;\boxed{W_{34}(\theta^4)} \\ |0\rangle\;\boxed{X}\;\boxed{H}\text{—}\bullet\text{—} \\ |0\rangle\;\boxed{X}\text{—}\oplus\text{—} \\ \quad\textit{Initialization}\qquad\qquad\textit{Variational Block} \end{array} \tag{8.9}$$

Schematic representation of a PMA consisting of an initialization layer that set the ansatz state with $S = 0$, plus a single variational layer composed of four W circuits.

in order to have a faithful reconstruction of the ground state, and the optimal number of applications can be practically determined.
In the next sections, the results from noiseless and noisy simulations are reported.

8.3.2 Noiseless simulations

To validate the accuracy of our ansatz, let's start by examining the VQE results obtained from noiseless simulations. These calculations are performed using exact matrix multiplications and are therefore not susceptible to any errors, including statistical noise. As an optimizer,it is employed by COBYLA, which proves to be more efficient than SPSA under these conditions.
In panel a) of Fig. 8.2, the energy diagram (gray and black lines) of the four-spin rings is reported as a function of the ratio B/J. The dark green dots and light green stars represent the simulation results for the HHA and PMA ansatz, respectively. PMA requires only a single layer (consisting of 4 parameters) of variational blocks in both the low- and intermediate-field regions. On the other hand, HHA demands 3 layers (16 parameters) or 2 layers (12 parameters) in low-medium-field regions, respectively. While both methods achieve high fidelity, measured between the variational and exact solutions (see the insight), almost one for all points, the more compact circuits of PMA result in significantly faster convergence (as seen in panel b).
Panels c) and d) extend the same investigation to the six-spin ring. In this case, PMA necessitates 2 layers (12 parameters), while HHA requires 5 layers (36 parameters) or 4 layers (30 parameters) at low- and medium-field, respectively. Similarly to the previous scenario, although both ansatz achieve maximum fidelity, PMA requires about ten times fewer optimization steps.

8.3.3 Noisy VQE simulations

The last step is to verify the consistency of the above studies in a more realistic scenario where the effects of noise are included. These investigations are particularly interesting for near-term applications where devices have to deal with noise. A noise model has been built based on the most advanced hardware from IBM as a reference. The presented simulations take into account the most important sources of errors, including:

- **Relaxation and decoherence effects**: thermal relaxation T_1 and pure dephasing T_2, which respectively lead to amplitude and phase damping.

- **Manipulation**: single- and two-qubit gate errors due to imperfect manipulation of qubits or other sources of incoherence errors.

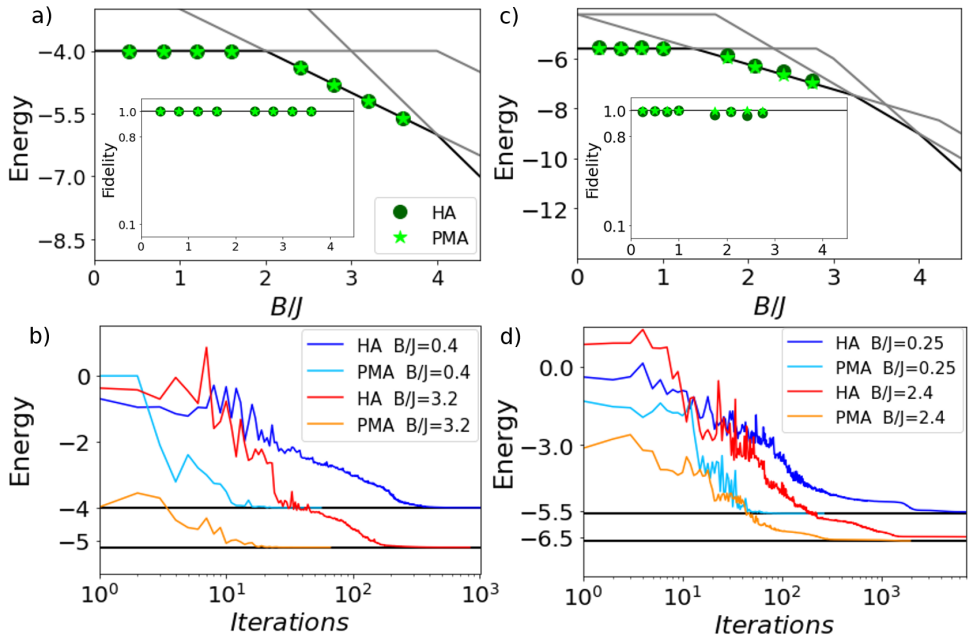

Figure 8.2: Panel a) reports the results of VQE noiseless simulation for a four spins 1/2 ring with anti-ferromagnetic couplings using the HHA (dark green dots) and PMA (light green stars) ansatz. Black and grey lines represent the exact ground and excited states, respectively. In the insight, the fidelity of VQE points. b) Comparison of the convergence process for the two ansatz classes at two values $B/J = 0.4$ and $B/J = 3.2$. Panels c) and d) extend the same studies to the six spin rings. Optimizing is done using COBYLA. Reproduced from Ref. [238] under the terms and conditions of the Creative Commons Attribution (CC BY) license (https://creativecommons.org/licenses/by/4.0/).

- **Readout**: measurement errors due to an incorrect readout of the measurement process.

The presence of noise affects the estimation of local Hamiltonian terms, thereby modifying the cost function. Additionally, these effects can be inconsistent, meaning that the outcome of two consecutive measurements is not the same. Taking inspiration from the error values provided by IBM for the `ibmq_kolkata` 27-qubit device, one of the best available at the time of this study (early 2021), the noise model was created by averaging the values on different qubits: relaxation and decoherence time $T_1 = 135\mu$s and $T_2 = 125\ \mu$s, single-qubit gate error of 2.5×10^{-4}, two-qubit gate errors of 8×10^{-3}, and symmetric readout error of 10^{-2}. Single and two-body errors group different sources and hence effects of errors such as depolarizing, phase and amplitude damping. Readout errors have

been mitigated by exploring the post-processing method described in Sec. 1.6. As mentioned in the previous sections, SPSA has been used as the optimizer in all noisy simulations.

In Fig. 8.3 are presented the results of the noisy simulations for the four-spin ring. Both ansatz qualitatively reconstruct the energy diagram, although the presence of noise reduces the quality of the results compared to the previous case. The fidelity with respect to the ground state is now around $0.8 - 0.9$. The system's magnetization $M = \sum_i s_i^z$ and total spin S^2, shown in panel b), are accurately reproduced by both ansatz. The local expectation values $\langle s_i^z \rangle$ and correlations $\langle s_i^z s_{i+1}^z \rangle$ are also well reproduced by both ansatz forms, as shown in the radar plot in panel d). Consistently with what was observed in the noiseless case, convergence is much faster for PMA compared to HHA. Moving on to the six-spin

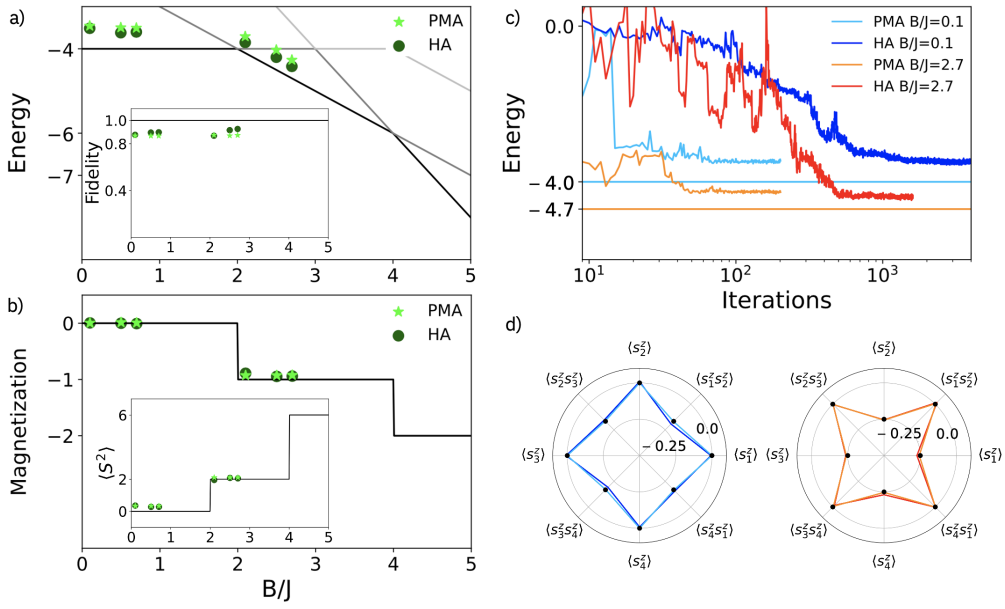

Figure 8.3: Panel a) reports the results of VQE noisy simulation for a four spin 1/2 ring with anti-ferromagnetic couplings using the HHA (dark green dots) and PMA (light green stars) ansatz. In the insight, the fidelity of VQE points. b) Magnetization and $\langle S^2 \rangle$ (in the insight) as a function of the ratio B/J. c) Comparison of the convergence process for the two ansatz class at two values $B/J = 0.1$ and $B/J = 2.7$. d) Radar plot of local spin observables, exact solutions are indicated by black dots. Optimizing is done using SPSA. Reproduced from Ref. [238] under the terms and conditions of the Creative Commons Attribution (CC BY) license (https://creativecommons.org/licenses/by/4.0/).

ring Fig. 8.4, which is a slightly more complex problem, there is a noticeable

difference in the performance of the ansatz. While the results for energy estimation and fidelity are comparable between the two ansatz, PMA excels in reconstructing local and global properties such as magnetization and spin correlations. Specifically, when examining the radar plot for the intermediate-field regime (orange), it is evident that PMA exhibits a significantly better correspondence with the exact solution.

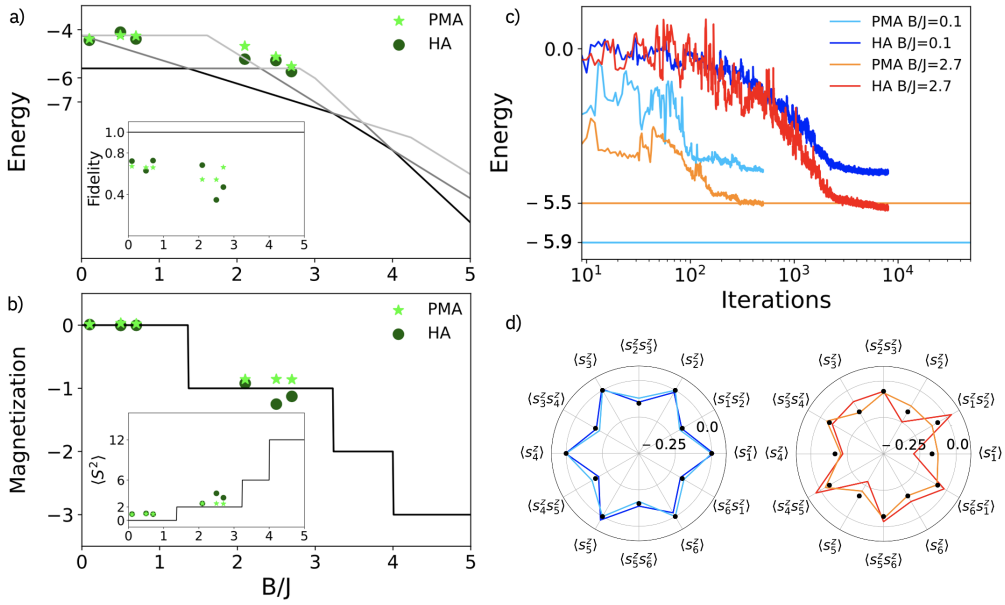

Figure 8.4: Panel a) reports the results of VQE noisy simulation for a six spin 1/2 ring with anti-ferromagnetic couplings using the HHA (dark green dots) and PMA (light green stars) ansatz. In the insight, the fidelity of VQE points. b) Magnetization and $\langle S^2 \rangle$ (in the insight) as a function of the ratio B/J. c) Comparison of the convergence process for the two ansatz class at two values $B/J = 0.1$ and $B/J = 2.7$. d) Radar plot of local spin observables, exact solutions are indicated by black dots. Optimizing is done using SPSA. Reproduced from Ref. [238] under the terms and conditions of the Creative Commons Attribution (CC BY) license (https://creativecommons.org/licenses/by/4.0/).

8.3.4 Finite-size and parity effects

This section investigates the finite-size and parity effects in some open and closed chains of anti-ferromagnetically coupled spin-1/2 systems described by Hamiltonians analogous to Eq. 8.8. The ground state of these systems is reconstructed by exploiting the VQE. In particular, having demonstrated the advantages of PMA over HHA, the former class of ansatz is used.

The systems under investigation are 4- and 6-spin rings and 4-, 5-, and 6-spin open chains. The 5-spin is not considered due to its degenerate ground state, which makes it unsuitable for VQE analysis.
Fig. 8.5 reports the local expectation values of the s_i^z operators, calculated from the solutions of the noisy VQE simulations using the PMA ansatz. As noise model is considered the same described in the previous section.
Open chains are symmetric with respect to the central spin or bond, depending on whether they are odd or even. At low-field even chains have vanishing total magnetization hence all the sites have as expectation value zero. Conversely, odd chains have a total spin $S = 1$ and hence exhibit alternating up and down magnetized sites. At intermediate fields, both the 4- and 6-spin have $S = 1$ and display an alternating magnetization pattern.
Regarding the rings, they show transnational invariance symmetry. At low temperatures the ground state has $S = 0$ thus all sites exhibit null magnetization, while at intermediate temperatures, the ground state has $S = 1$ hence they become partially magnetized $\langle s_i^z \rangle = 1/N$.
All the results obtained are in agreement with the theoretical solutions (dashed lines). In conclusion, the presented studies confirm that the PMA ansatzs are capable of reconstructing local properties and symmetries accurately.

8.4 Investigation of Dynamical Correlation on Spin Chains

In the previous sections, the focus has been on the static properties of small molecule models, utilizing VQE to reproduce the ground state. Here, the analysis focuses on dynamic correlations, particularly the spin-spin correlation function, which is the key ingredient for computing the magnetic inelastic neutron scattering cross-section [25, 239]. Calculating this quantity on classical computers is challenging, if not practically infeasible for many relevant systems. In contrast, quantum computers can handle these calculations more efficiently, providing a significant advantage. The results of real quantum experiments on the IBM Quantum processor (early 2021) are presented hereafter.
The spin-spin correlation function at temperature $T = 0$ is defined as follows:

$$\mathcal{C}_{ij}^{\alpha\beta}(t) = \left\langle s_i^\alpha(t) s_j^\beta \right\rangle_0 = \sum_p \langle 0|s_i^\alpha|p\rangle\langle p|s_j^\beta|0\rangle e^{-iE_p t} \tag{8.10}$$

where α and β indicate the x, y, and z components, while i and j represent the indexes of system sites.
This quantity has some interesting properties. At $t = 0$, regardless of the specific Hamiltonian, $\mathcal{C}_{ii}^{\alpha\alpha}(0) = \left\langle s_i^\alpha s_i^\alpha \right\rangle_0$ is a sum of squared values and thus must have

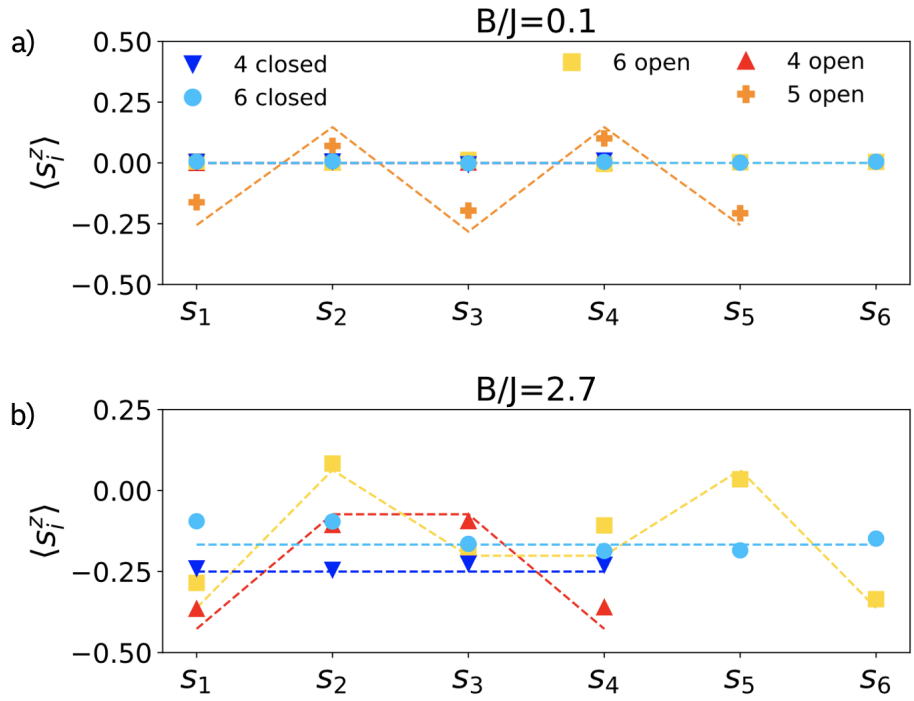

Figure 8.5: Local expectation values of s_i^z operators at low- and intermediate-field for different size open and closed chains. Reproduced from Ref. [238] under the terms and conditions of the Creative Commons Attribution (CC BY) license (https://creativecommons.org/licenses/by/4.0/).

a real phase. Furthermore, at time zero, $\mathcal{C}_{ii}^{xx} + \mathcal{C}_{ii}^{yy} + \mathcal{C}_{ii}^{zz} = s_i(s_i + 1) = 3/4$. As shown later, by exploiting these properties it is possible to implement error mitigation. Raw experimental data can be improved by applying a global phase and amplitude correction so as to fix the phase and amplitude to the expected values at time zero (PaS = Phase and Scale). Extending the same correction to any time, in practice one finds a significant improvement in results. The system under investigation is the four-spin ring analysed earlier, but in the high-field region. In this regime, the initial ground state is easy to reconstruct because all spins are aligned with the external magnetic field, simplifying the circuit complexity.

The quantum circuit for measuring $\mathcal{C}_{ij}^{\alpha\beta}(t)$ is as follows:

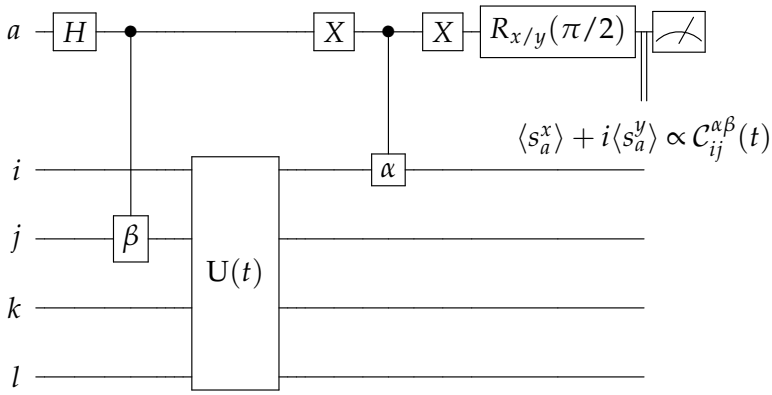

(8.11)

Here, $\mathrm{U}(t)$ represents the system's dynamics, a is an ancillary qubit used in the measurement procedure, and the remaining quantum register (i, j, k, l) is employed to simulate the dynamics of the target system. Due to the peculiarity of the target system, after the initialization of the qubits in $|0\rangle$ the system is already in the ground state $|\downarrow,\downarrow,\ldots,\downarrow\rangle = |0,0,\ldots,0\rangle$. By applying a Hadamard gate, the ancilla is put in a superposition state $\frac{|0\rangle+|1\rangle}{\sqrt{2}}$. Then, a controlled-$\beta$ gate is implemented from the ancilla to the j qubit where $\beta = x,y,z$. The system is allowed to evolve for a time t, and at the end, a controlled-α gate is applied when the ancilla is in the $|0\rangle$ state (the two X gates are used to exchange $0 \leftrightarrow 1$) $\alpha = x,y,z$. Finally, by measuring the ancilla in the x and y bases, which is done by applying $R_y(\pi/2)$ and $R_x(\pi/2)$ gates, respectively, the real and imaginary parts of the correlation function are extracted. The spin-spin correlation function is reconstructed as $\mathcal{C}_{ij}^{\alpha\beta}(t) = \langle \sigma^\beta(t)\sigma^\alpha \rangle = \langle 2\sigma_a^+ \rangle = \langle 2\sigma_a^x \rangle + i\langle 2\sigma_a^y \rangle$.
For the specific case of the four-spin ring investigated, the evolution operator is decomposed into gates as follows:

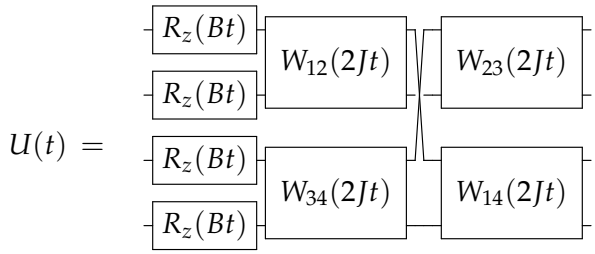

(8.12)

Here, W_{ij} represents the same block presented above for the PMA ansatz. In general, this type of evolution requires a Suzuki-Trotter decomposition. However, in this case, all terms commute, resulting in exact evolution.
Fig. 8.6 shows the results of real quantum experiments performed on the `ibmq_bogota` IBM quantum processor for $\mathcal{C}_{ij}^{xx}$ on sites 1 and 2. The black lines represent the

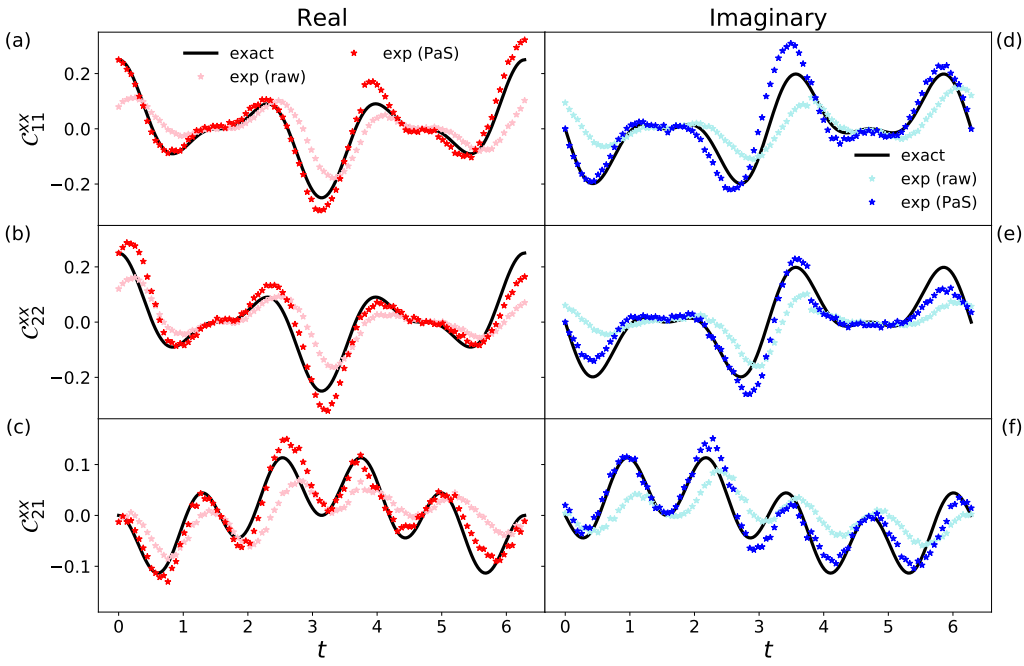

Figure 8.6: Spin-spin correlation functions C_{ij}^{xx} calculated on a four spin ring with antiferromagnetic couplings in the high-field region. The black lines represent the exact solutions, the light-colored stars denote the raw data obtained from real quantum experiments on the `ibmq_bogota` IBM Quantum processor, while the dark-colored stars depict the corrected data using the PaS technique. Reproduced from Ref. [238] under the terms and conditions of the Creative Commons Attribution (CC BY) license (https://creativecommons.org/licenses/by/4.0/).

exact solutions, while the light-colored stars indicate the raw experimental data. However, these results, although qualitatively reproducing the expected behaviour, lack precision. A significant improvement is achieved by applying the phase and scale correction (dark-coloured stars).

8.5 Conclusions

Quantum computers are expected to bring disruptive contributions to many fields including the simulation of quantum systems. The first significant results are expected from hybrid quantum-classical algorithms such as the variational quantum eigensolver.
Starting from the mathematical foundation, i.e. the variational theorem, to the

practical implementation, this chapter gives an overview over the VQE. The algorithm is tested on small spin chains with Heisenberg interactions. From these toy models, which potentially represent small MNMs, the ground state energy, magnetization and local spin expectation values are calculated. This analysis allows us to investigate the method and to evaluate the state of the art of current technologies.

The analysis of the algorithms is mainly focused on the comparison of two classes of ansatzs: hardware heuristic and physically motivated. The various numerical simulations performed, both in the presence and absence of noise, have shown that a properly designed PMA can outperform HHA. In particular, in addition to better reproducing the system properties and symmetries, the PMA achieves convergence much faster, drastically reducing the optimisation cost. To improve the results, a readout error mitigation is always implemented.

In the second part of the results section, the dynamical spin-spin correlation functions on a closed Heisenberg chain are calculated. This quantity, of considerable interest but difficult to calculate on classical devices, is extracted using the same methodology as in Ref. [239]. Of considerable interest is the phase and scale error mitigation strategy, which, together with the readout mitigation, is able to drastically improve the raw data.

The natural extension of this work would be to explore more complex cases, such as systems with anisotropic or antisymmetric exchange couplings. Such systems would exhibit a more complex energy spectrum, with eigenstates characterised by highly entangled states. Together with future advances in quantum devices, which are anticipated to allow the simulation of more complex circuits, PMAs are expected to play a fundamental role.

Conclusions

To summarize, this work investigates the potential application of Molecular Nanomagnets for the realization of a reliable and scalable quantum architecture. As extensively discussed throughout this work, these systems possess numerous features that make them well-suited for this scope.
Firstly, the ability to encode multi-level logical units, i.e qudits, could prove highly beneficial. In chapters 3 and 4, this potential is explored in the context of realizing embedded schemes of error correction. Although the presented scheme does not enable fault-tolerant computation and so requires further developments, it highlights the potential of this approach. By eliminating the need for two-body gates, this method significantly simplifies scheme implementation, a common bottleneck for effective QEC scheme realization. The effectiveness of this approach is maximized when a fully connected computational space is available. The theoretically designed molecule **C**2, investigated in chapter 4, serves as an example of a system that could be an optimal basis. It not only provides the desired fully connected subspace but also combines another fundamental property, resilience to pure-dephasing.
A relevant part of this thesis revolves around the analysis of decoherence. Through modelling, it has been possible to determine the factors influencing decoherence and consequently identify a class of molecules that are intrinsically protected against it. By examining the dependence of the decoherence mechanism on the system's eigenstate structure, we have highlighted how systems with magnetically similar eigenstates are intrinsically protected from this mechanism. The proposed class **C** of systems, composed of multiple magnetic ions with competing interactions, exhibits multiple doublets widely connected at low energy and addressable by electromagnetic pulses. This class of molecules provides an optimal ground for guiding research and synthesizing new systems with extended properties.

In parallel with the exploration of applications for the QEC, chapters 5 and 6 delve into the potential use of these systems for a qudit-based computation. Also in this framework, the qudit approach could be really beneficial in simplifying the mappings, reducing the number of two body gates and the circuit depth. Chapter 6 investigates how Fermionic models can be efficiently simulated using a qudit extension of the auxiliary fermion method. Through numerical simulations, the feasibility of this approach is demonstrated. As an elementary building block of the hypothetical architecture we have used the Qudit-Switch-Qudit unit introduced in chapter 2. This scheme enables a switchable interaction among qudits, thus permitting the implementation of various entangling gates. This approach relies on chemical engineering to synthesize suitable systems and represents a concrete opportunity for realizing small to medium-sized prototypes. However, it must be recognized that to achieve effective modular scalability, coupling these molecules with resonators, as recently proposed, appears to be a more promising approach.
Chapter 7 diverges slightly in focus from the rest of the work, centering around the Chiral-Induced Spin Selectivity effect. This phenomenon is an attractive topic for researchers due to its perceived implications in various biological processes. Despite being a relatively recent subject of study, the scientific community has shown significant interest, as evidenced by numerous publications in recent years. Once thoroughly understood and engineered, this mechanism could be leveraged for the initialization and read-out of Molecular Nanomagnet qubits. This prospect not only opens new strategies to realize these procedure but also suggest the possibility for realizing high-temperature working devices.
In the final chapter, chapter 8, we delved into the Variational Quantum Eigensolver algorithm, applying it to small spin systems. Firstly, this analysis revealed how a meticulously designed, physically motivated ansatz can significantly enhance and extend the performance of the method. Moreover, this study served as a benchmark for state-of-the-art quantum devices, providing valuable insights into their limitations and capabilities.

Bibliography

[1] R. P. Feynman, "Simulating physics with computers", Int. J. Theor. Phys. **21** (1982) (cit. on p. 1).

[2] Royal Swedish Academy of Sciences, ed., "Entangled states – from theory to technology", (2022) (cit. on p. 1).

[3] "40 years of quantum computing", Nat. Rev. Phys. **4**, 1 (2022) (cit. on p. 1).

[4] N. S, H. Singh, and A. U. N, "An extensive review on quantum computers", Adv. Eng. Softw. **174**, 103337 (2022) (cit. on p. 1).

[5] A. G. J. MacFarlane, J. P. Dowling, and G. J. Milburn, "Quantum technology: the second quantum revolution", Philos. Trans. Royal Soc. A **361**, 1655–1674 (2003) (cit. on p. 1).

[6] J. Preskill, "Quantum Computing in the NISQ era and beyond", Quantum **2**, 79 (2018) (cit. on pp. 1, 3, 13).

[7] J. Preskill, "Quantum computing and the entanglement frontier", (2012) (cit. on p. 1).

[8] T. D. Ladd, F. Jelezko, R. Laflamme, Y. Nakamura, C. Monroe, and J. L. O'Brien, "Quantum computers", Nature **464**, 45–53 (2010) (cit. on p. 2).

[9] B. Schumacher, "Quantum coding", Phys. Rev. A **51**, 2738–2747 (1995) (cit. on p. 2).

[10] M. A. Nielsen and I. Chuang, "Quantum computation and quantum information", edited by C. U. Press (2002) (cit. on pp. 2, 14, 16, 19, 42, 70, 104, 131).

[11] G. K. Brennen, D. P. O'Leary, and S. S. Bullock, "Criteria for exact qudit universality", Phys. Rev. A **71**, 052318 (2005) (cit. on pp. 2, 46).

[12] J. S. Bell, "On the einstein podolsky rosen paradox", Physics **1**, 195–200 (1964) (cit. on p. 3).

[13] S. J. Freedman and J. F. Clauser, "Experimental Test of Local Hidden-Variable Theories", Phys. Rev. Lett. **28**, 938–941 (1972) (cit. on p. 3).

[14] A. Aspect, P. Grangier, and G. Roger, "Experimental Tests of Realistic Local Theories via Bell's Theorem", Phys. Rev. Lett. **47**, 460–463 (1981) (cit. on p. 3).

[15] J. S. Bell and A. Aspect, "Speakable and unspeakable in quantum mechanics: collected papers on quantum philosophy", 2nd ed. (Cambridge University Press, 2004) (cit. on p. 3).

[16] H. J. Kimble, "The quantum internet", Nature **453**, 1023–1030 (2008) (cit. on p. 4).

[17] W. K. Wootters, "Entanglement of Formation of an Arbitrary State of Two Qubits", Phys. Rev. Lett. **80**, 2245–2248 (1998) (cit. on p. 4).

[18] D. C. Marinescu and G. M. Marinescu, "CHAPTER 6 - Physical Realization of Quantum Information Processing Systems", in *Classical and Quantum Information* (Academic Press, Boston, 2012), pp. 563–649 (cit. on p. 4).

[19] D. P. DiVincenzo, "The physical implementation of quantum computation", Fortschritte der Phys. **48**, 771–783 (2000) (cit. on pp. 4, 70).

[20] G. Wendin, Rep. Prog. Phys. **80**, 106001 (2017) (cit. on p. 5).

[21] "Quantum supremacy using a programmable superconducting processor", Nature **574**, 505–510 (2019) (cit. on p. 5).

[22] A. J. Daley, I. Bloch, C. Kokail, S. Flannigan, N. Pearson, M. Troyer, and P. Zoller, "Practical quantum advantage in quantum simulation", Nature **607**, 667–676 (2022) (cit. on p. 5).

[23] D. Bluvstein, S. J. Evered, A. A. Geim, et al., "Logical quantum processor based on reconfigurable atom arrays", Nature **626**, 58–65 (2024) (cit. on p. 5).

[24] A. Barenco, C. H. Bennett, R. Cleve, et al., "Elementary gates for quantum computation", Phys. Rev. A **52**, 3457–3467 (1995) (cit. on p. 6).

[25] F. Tacchino, A. Chiesa, S. Carretta, and D. Gerace, "Quantum Computers as Universal Quantum Simulators: State-of-the-Art and Perspectives", Adv. Quantum Technol. **3**, 1900052 (2020) (cit. on pp. 6, 8, 13, 86, 88, 166, 172, 177).

[26] J. J. Sakurai, "Modern quantum mechanics" (San Fu Tuan, 1994) (cit. on pp. 7, 163).

[27] G. E. Crooks, "Gates, States, and Circuits", (2019) (cit. on p. 8).

[28] P. Santini, S. Carretta, F. Troiani, and G. Amoretti, "Molecular nanomagnets as quantum simulators", Phys. Rev. Lett. **107**, 230502 (2011) (cit. on pp. 10, 56, 65, 81).

[29] Qiskit contributors, *Qiskit: An Open-source Framework for Quantum Computing*, 2023 (cit. on p. 11).

[30] D. Coppersmith, "An approximate Fourier transform useful in quantum factoring", (2002) (cit. on p. 11).

[31] P. Shor, "Algorithms for quantum computation: discrete logarithms and factoring", in Proceedings 35th annual symposium on foundations of computer science (1994), pp. 124–134 (cit. on p. 12).

[32] A. Y. Kitaev, "Quantum measurements and the Abelian Stabilizer Problem", (1995) (cit. on p. 12).

[33] Wikipedia contributors, ed., "Quantum fourier transform — Wikipedia, the free encyclopedia", (2024) (cit. on pp. 12, 209).

[34] J. Eisert and M. M. Wolf, "Quantum Computing", in *Handbook of Nature-Inspired and Innovative Computing: Integrating Classical Models with Emerging Technologies*, edited by A. Y. Zomaya (Springer US, Boston, MA, 2006), pp. 253–286 (cit. on p. 13).

[35] I. Georgescu, S. Ashhab, and F. Nori, "Quantum simulation", Rev. Mod. Phys. **86**, 153–185 (2014) (cit. on pp. 13, 129).

[36] D-Wave Quantum Inc., "https://www.dwavesys.com/", (2023) (cit. on p. 13).

[37] S. Lloyd, "Universal quantum simulators", Science **273**, 1073–1078 (1996) (cit. on p. 14).

[38] M. Suzuki, "General theory of fractal path integrals with applications to many-body theories and statistical physics", J. Math. Phys. **32**, 400–407 (1991) (cit. on p. 15).

[39] D. W. Berry, A. M. Childs, R. Cleve, R. Kothari, and R. D. Somma, "Simulating Hamiltonian Dynamics with a Truncated Taylor Series", Phys. Rev. Lett. **114**, 090502 (2015) (cit. on p. 15).

[40] G. H. Low and I. L. Chuang, "Hamiltonian Simulation by Qubitization", Quantum **3**, 163 (2019) (cit. on p. 15).

[41] A. M. Childs, Y. Su, M. C. Tran, N. Wiebe, and S. Zhu, "Theory of Trotter Error with Commutator Scaling", Phys. Rev. X **11**, 011020 (2021) (cit. on p. 15).

[42] M. Mohseni, A. T. Rezakhani, and D. A. Lidar, "Quantum-process tomography: Resource analysis of different strategies", Phys. Rev. A **77**, 032322 (2008) (cit. on p. 16).

[43] Z. Cai, R. Babbush, S. C. Benjamin, et al., "Quantum error mitigation", (2023) (cit. on pp. 22, 26, 162).

[44] A. W. Cross, L. S. Bishop, S. Sheldon, P. D. Nation, and J. M. Gambetta, Phys. Rev. A **100**, 032328 (2019) (cit. on p. 24).

[45] N. Moll, P. Barkoutsos, L. S. Bishop, et al., "Quantum optimization using variational algorithms on near-term quantum devices", Quantum Sci. Technol. **3**, 030503 (2018) (cit. on p. 25).

[46] Omdia Blog Posts, "https://tractica.omdia.com/advanced-computing/quantum-volume-a-new-quantum-metric/", (2019) (cit. on p. 25).

[47] Quantinuum, "https://www.quantinuum.com/news/quantinuum-h-series-quantum-computer-accelerates-through-3-more-performance-records-for-quantum-volume-217-218-and-219", (2023) (cit. on p. 25).

[48] S. Bravyi, S. Sheldon, A. Kandala, D. C. Mckay, and J. M. Gambetta, "Mitigating measurement errors in multiqubit experiments", Phys. Rev. A **103**, 042605 (2021) (cit. on p. 27).

[49] A. Kandala, A. Mezzacapo, K. Temme, M. Takita, M. Brink, J. M. Chow, and J. M. Gambetta, "Hardware-efficient variational quantum eigensolver for small molecules and quantum magnets", Nature **549**, 242–246 (2017) (cit. on pp. 27–28).

[50] Y. Li and S. C. Benjamin, "Efficient Variational Quantum Simulator Incorporating Active Error Minimization", Phys. Rev. X **7**, 021050 (2017) (cit. on p. 28).

[51] S. J. Devitt, W. J. Munro, and K. Nemoto, "Quantum error correction for beginners", Rep. Prog. Phys. **76**, 076001 (2013) (cit. on pp. 29, 36–37, 40).

[52] J. Roffe, "Quantum error correction: an introductory guide", Contemp. Phys. **60**, 226–245 (2019) (cit. on p. 29).

[53] W. K. Wootters and W. H. Zurek, "A single quantum cannot be cloned", Nature **299**, 802–803 (1982) (cit. on p. 31).

[54] D. Dieks, "Communication by EPR devices", Phys. Lett. A **92**, 271–272 (1982) (cit. on p. 31).

[55] H. Barnum, C. M. Caves, C. A. Fuchs, R. Jozsa, and B. Schumacher, "Noncommuting Mixed States Cannot Be Broadcast", Phys. Rev. Lett. **76**, 2818–2821 (1996) (cit. on p. 31).

[56] A. Kalev and I. Hen, "No-Broadcasting Theorem and Its Classical Counterpart", Phys. Rev. Lett. **100**, 210502 (2008) (cit. on p. 31).

[57] E. Knill and R. Laflamme, "Theory of quantum error-correcting codes", Phys. Rev. A **55**, 900–911 (1997) (cit. on p. 33).

[58] E. Knill, R. Laflamme, and L. Viola, "Theory of Quantum Error Correction for General Noise", Phys. Rev. Lett. **84**, 2525–2528 (2000) (cit. on p. 33).

[59] P. W. Shor, "Scheme for reducing decoherence in quantum computer memory", Phys. Rev. A **52**, R2493–R2496 (1995) (cit. on p. 36).

[60] D. Gottesman, "Stabilizer Codes and Quantum Error Correction", (1997) (cit. on pp. 36, 39).

[61] D. M. Greenberger, M. A. Horne, and A. Zeilinger, "Going Beyond Bell's Theorem", (2007) (cit. on p. 39).

[62] A. R. Calderbank and P. W. Shor, "Good Quantum Error-Correcting Codes Exist", Phys. Rev. A **54**, 1098–1105 (1996) (cit. on p. 41).

[63] A. Steane, "Multiple-particle interference and quantum error correction", Proc. R. Soc. A: Math. Phys. Eng. **452**, 2551–2577 (1997) (cit. on p. 41).

[64] P. W. Shor, "Fault-tolerant quantum computation", (1997) (cit. on p. 42).

[65] D. Aharonov and M. Ben-Or, "Fault-tolerant quantum computation with constant error rate", SIAM J. Comput. **38**, 1207–1282 (2008) (cit. on p. 42).

[66] A. Y. Kitaev, "Fault-tolerant quantum computation by anyons", Annals of Physics **303**, 2–30 (2003) (cit. on p. 42).

[67] K. Mato, M. Ringbauer, S. Hillmich, and R. Wille, "Compilation of Entangling Gates for High-Dimensional Quantum Systems", in Proceedings of the 28th Asia and South Pacific Design Automation Conference, ASPDAC '23 (2023), pp. 202–208 (cit. on p. 44).

[68] H.-H. Lu, Z. Hu, M. S. Alshaykh, et al., "Quantum Phase Estimation with Time-Frequency Qudits in a Single Photon", Adv. Quantum Technol. **3**, 1900074 (2020) (cit. on p. 45).

[69] A. Babazadeh, M. Erhard, F. Wang, M. Malik, R. Nouroozi, M. Krenn, and A. Zeilinger, "High-Dimensional Single-Photon Quantum Gates: Concepts and Experiments", Phys. Rev. Lett. **119**, 180510 (2017) (cit. on p. 45).

[70] A. B. Klimov, R. Guzmán, J. C. Retamal, and C. Saavedra, "Qutrit quantum computer with trapped ions", Phys. Rev. A **67**, 062313 (2003) (cit. on p. 45).

[71] M. Ringbauer, M. Meth, L. Postler, R. Stricker, R. Blatt, P. Schindler, and T. Monz, "A universal qudit quantum processor with trapped ions", Nat. Phys. **18**, 1053–1057 (2022) (cit. on p. 45).

[72] E. Kiktenko, A. Fedorov, A. Strakhov, and V. Man'ko, "Single qudit realization of the deutsch algorithm using superconducting many-level quantum circuits", Phys. Lett. A **379**, 1409–1413 (2015) (cit. on p. 45).

[73] M. Blok, V. Ramasesh, T. Schuster, et al., "Quantum Information Scrambling on a Superconducting Qutrit Processor", Phys. Rev. X **11**, 021010 (2021) (cit. on p. 45).

[74] A. Cervera-Lierta, M. Krenn, A. Aspuru-Guzik, and A. Galda, "Experimental High-Dimensional Greenberger-Horne-Zeilinger Entanglement with Superconducting Transmon Qutrits", Phys. Rev. Appl. **17**, 024062 (2022) (cit. on p. 45).

[75] C. Godfrin, A. Ferhat, R. Ballou, S. Klyatskaya, M. Ruben, W. Wernsdorfer, and F. Balestro, "Operating Quantum States in Single Magnetic Molecules: Implementation of Grover's Quantum Algorithm", Phys. Rev. Lett. **119**, 187702 (2017) (cit. on p. 45).

[76] E. Moreno-Pineda, C. Godfrin, F. Balestro, W. Wernsdorfer, and M. Ruben, "Molecular spin qudits for quantum algorithms", Chem. Soc. Rev. **47**, 501–513 (2018) (cit. on p. 45).

[77] A. Gaita-Ariño, F. Luis, S. Hill, and E. Coronado, "Molecular spins for quantum computation", Nat. Chem. **11**, 301–309 (2019) (cit. on pp. 45, 57).

[78] H. Biard, E. Moreno-Pineda, M. Ruben, E. Bonet, W. Wernsdorfer, and F. Balestro, "Increasing the Hilbert space dimension using a single coupled molecular spin", Nat. Commun. **12**, 4443 (2021) (cit. on p. 45).

[79] Y. Wang, Z. Hu, B. C. Sanders, and S. Kais, "Qudits and high-dimensional quantum computing", Front. Phys. **8**, 479 (2020) (cit. on pp. 45, 62).

[80] M. Luo and X. Wang, "Universal quantum computation with qudits", Sci. China Phys. Mech. Astron. **57**, 1712–1717 (2014) (cit. on pp. 46–47).

[81] S. G. Schirmer, A. D. Greentree, V. Ramakrishna, and H. Rabitz, "Constructive control of quantum systems using factorization of unitary operators", J. Phys. A: Math. Gen. **35**, 8315 (2002) (cit. on pp. 48, 113–114).

[82] P. J. Low, B. M. White, A. A. Cox, M. L. Day, and C. Senko, "Practical trapped-ion protocols for universal qudit-based quantum computing", Phys. Rev. Research **2**, 033128 (2020) (cit. on pp. 48, 114).

[83] L. E. Fischer, D. Miller, F. Tacchino, P. K. Barkoutsos, D. J. Egger, and I. Tavernelli, "Ancilla-free implementation of generalized measurements for qubits embedded in a qudit space", Phys. Rev. Res. **4**, 033027 (2022) (cit. on pp. 48, 114).

[84] D. D'Alessandro, "Introduction to quantum control and dynamics" (Chapman & Hall/CRC Applied Mathematics & Nonlinear Science, CRC Press, 2007) (cit. on p. 48).

[85] A. Caneschi, D. Gatteschi, R. Sessoli, A. L. Barra, L. C. Brunel, and M. Guillot, "Alternating current susceptibility, high field magnetization, and millimeter band EPR evidence for a ground S = 10 state in [Mn_{12} O_{12} (Ch_3COO) 16 (H_2O)4].2CH_3COOH.4H_2O", J. Am. Chem. Soc. **113**, 5873–5874 (1991) (cit. on p. 51).

[86] R. Sessoli, H. L. Tsai, A. R. Schake, et al., "High-spin molecules: [Mn_{12} O $_{12}$ (O_2 CR) 16 (H_2O)4]", J. Am. Chem. Soc. **115**, 1804–1816 (1993) (cit. on p. 51).

[87] R. Sessoli, D. Gatteschi, A. Caneschi, and M. A. Novak, "Magnetic bistability in a metal-ion cluster", Nature **365**, 141–143 (1993) (cit. on p. 51).

[88] R. Caciuffo, G. Amoretti, A. Murani, R. Sessoli, A. Caneschi, and D. Gatteschi, "Neutron Spectroscopy for the Magnetic Anisotropy of Molecular Clusters", Phys. Rev. Lett. **81**, 4744–4747 (1998) (cit. on p. 51).

[89] J. van Slageren, R. Sessoli, D. Gatteschi, et al., "Magnetic anisotropy the antoferromagnetic ring [$Cr_8F_8Piv_{16}$]", Chemistry - A European Journal **8**, 277–285 (2002) (cit. on p. 51).

[90] C. J. Milios, M. Manoli, G. Rajaraman, et al., "A Family of [Mn_6] Complexes Featuring Tripodal Ligands", Inorg. Chem. **45**, 6782–6793 (2006) (cit. on p. 51).

[91] A. Müller, S. Sarkar, S. Q. N. Shah, et al., "Archimedean Synthesis and Magic Numbers: "Sizing" Giant Molybdenum-Oxide-Based Molecular Spheres of the Keplerate Type", Angew. Chem. Int. Ed. **38**, 3238–3241 (1999) (cit. on p. 51).

[92] C. A. P. Goodwin, F. Ortu, D. Reta, N. F. Chilton, and D. P. Mills, "Molecular magnetic hysteresis at 60 kelvin in dysprosocenium", Nature **548**, 439–442 (2017) (cit. on pp. 51–52).

[93] G. F. S. Whitehead, J. Ferrando-Soria, L. Carthy, R. G. Pritchard, S. J. Teat, G. A. Timco, and R. E. P. Winpenny, "Synthesis and reactions of N-heterocycle functionalised variants of heterometallic {Cr_7Ni} rings", Dalton Trans. **45**, 1638–1647 (2016) (cit. on p. 51).

[94] Y. Duan, L. E. Rosaleny, J. T. Coutinho, et al., "Data-driven design of molecular nanomagnets", Nat. Commun. **13**, 7626 (2022) (cit. on p. 51).

[95] A. Chiolero and D. Loss, "Macroscopic Quantum Coherence in Molecular Magnets", Phys. Rev. Lett. **80**, 169–172 (1998) (cit. on p. 51).

[96] R. Schmidt, J. Richter, and J. Schnack, "Frustration effects in magnetic molecules", J. Magn. Magn. Mater. **295**, 164–167 (2005) (cit. on p. 51).

[97] Y. Furukawa, K. Kiuchi, K.-i. Kumagai, et al., "Evidence of spin singlet ground state in the frustrated antiferromagnetic ring Cr_8Ni", Phys. Rev. B **79**, 134416 (2009) (cit. on p. 51).

[98] J. Schnack, "Effects of frustration on magnetic molecules: a survey from Olivier Kahn until today", Dalton Trans. **39**, 4677–4686 (2010) (cit. on p. 51).

[99] W. Florek, M. Antkowiak, and G. Kamieniarz, "Sequences of ground states and classification of frustration in odd-numbered antiferromagnetic rings", Phys. Rev. B **94**, 224421 (2016) (cit. on p. 51).

[100] A. Ardavan, O. Rival, J. J. L. Morton, S. J. Blundell, A. M. Tyryshkin, G. A. Timco, and R. E. P. Winpenny, "Will Spin-Relaxation Times in Molecular Magnets Permit Quantum Information Processing?", Phys. Rev. Lett. **98**, 057201 (2007) (cit. on p. 51).

[101] F. Troiani, V. Bellini, and M. Affronte, "Decoherence induced by hyperfine interactions with nuclear spins in antiferromagnetic molecular rings", Phys. Rev. B **77**, 054428 (2008) (cit. on pp. 51, 73).

[102] J. M. Zadrozny, J. Niklas, O. G. Poluektov, and D. E. Freedman, "Millisecond Coherence Time in a Tunable Molecular Electronic Spin Qubit", ACS Cent. Sci. **1**, 488–492 (2015) (cit. on pp. 51–52).

[103] A. Chiesa, S. Roca, S. Chicco, et al., "Blueprint for a molecular-spin quantum processor", Phys. Rev. Appl. **19**, 064060 (2023) (cit. on pp. 51–52, 65, 70–72, 130, 147).

[104] D. N. Woodruff, R. Winpenny, and R. A. Layfield, "Lanthanide single-molecule magnets", Chem. Rev. **113**, 5110–5148 (2013) (cit. on pp. 52, 161).

[105] F.-S. Guo, B. M. Day, Y.-C. Chen, M.-L. Tong, A. Mansikkamäki, and R. A. Layfield, "Magnetic hysteresis up to 80 kelvin in a dysprosium metallocene single-molecule magnet", Science **362**, 1400–1403 (2018) (cit. on p. 52).

[106] J. Schnack, R. Schmidt, and J. Richter, "Enhanced magnetocaloric effect in frustrated magnetic molecules with icosahedral symmetry", Phys. Rev. B **76**, 054413 (2007) (cit. on p. 52).

[107] E. Garlatti, S. Carretta, J. Schnack, G. Amoretti, and P. Santini, "Theoretical design of molecular nanomagnets for magnetic refrigeration", Appl. Phys. Lett. **103**, 202410 (2013) (cit. on p. 52).

[108] J. W. Sharples, D. Collison, E. J. L. McInnes, J. Schnack, E. Palacios, and M. Evangelisti, "Quantum signatures of a molecular nanomagnet in direct magnetocaloric measurements", Nat. Commun. **5**, 5321 (2014) (cit. on pp. 52, 161).

[109] K. A. Gschneidner and V. K. Pecharsky, "Thirty years of near room temperature magnetic cooling: Where we are today and future prospects", Int. J. Refrig. **31**, 945–961 (2008) (cit. on p. 52).

[110] M. N. Leuenberger and D. Loss, "Quantum computing in molecular magnets", Nature **410**, 789–793 (2001) (cit. on p. 52).

[111] F. Meier, J. Levy, and D. Loss, "Quantum Computing with Spin Cluster Qubits", Phys. Rev. Lett. **90**, 047901 (2003) (cit. on p. 52).

[112] F. Troiani, A. Ghirri, M. Affronte, et al., "Molecular Engineering of Antiferromagnetic Rings for Quantum Computation", Phys. Rev. Lett. **94**, 207208 (2005) (cit. on p. 52).

[113] C.-J. Yu, S. von Kugelgen, D. W. Laorenza, and D. E. Freedman, "A Molecular Approach to Quantum Sensing", ACS Cent. Sci. **7**, 712–723 (2021) (cit. on p. 52).

[114] A. Chiesa, S. Carretta, P. Santini, G. Amoretti, and E. Pavarini, "Many-Body Models for Molecular Nanomagnets", Phys. Rev. Lett. **110**, 157204 (2013) (cit. on p. 53).

[115] D. Gatteschi, R. Sessoli, and J. Villain, "Molecular nanomagnets" (Oxford University Press, 2006) (cit. on p. 53).

[116] A. Bencini and D. Gatteschi, "Epr of exchange coupled systems" (Springer Verlag, Berlin, 1990) (cit. on p. 54).

[117] S. Carretta, D. Zueco, A. Chiesa, A. Gómez-León, and F. Luis, "A perspective on scaling up quantum computation with molecular spins", Appl. Phys. Lett. **118**, 240501 (2021) (cit. on pp. 56, 65, 70, 130).

[118] F. Petiziol, A. Chiesa, S. Wimberger, P. Santini, and S. Carretta, "Counteracting dephasing in molecular nanomagnets by optimized qudit encodings", npj Quantum Inf. **7**, 133 (2021) (cit. on pp. 57, 73–74, 91, 104).

[119] K. Bader, D. Dengler, S. Lenz, B. Endeward, S.-D. Jiang, P. Neugebauer, and J. van Slageren, "Room temperature quantum coherence in a potential molecular qubit", Nat. Commun **5**, 5304 (2014) (cit. on pp. 57, 87–88).

[120] M. R. Wasielewski, M. D. E. Forbes, N. L. Frank, et al., "Exploiting chemistry and molecular systems for quantum information science", Nat. Rev. Chem. **4**, 490–504 (2020) (cit. on p. 57).

[121] A. Caneschi, A. Dei, D Gatteschi, C. A. Massa, L. A. Pardi, S. S. Poussereau, and L. Sorace, "Evaluating the magnetic anisotropy in molecular rare earth compounds. gadolinium derivatives with semiquinone radical and diamagnetic analogues", Chem. Phys. Lett. **371**, 694 (2002) (cit. on pp. 57, 116).

[122] Y.-S. Ding, Y.-F. Deng, and Y.-Z. Zheng, "The Rise of Single-Ion Magnets as Spin Qubits", Magnetochemistry **2**, 40 (2016) (cit. on p. 57).

[123] S. G. McAdams, A.-M. Ariciu, A. K. Kostopoulos, J. P. S. Walsh, and F. Tuna, "Molecular single-ion magnets based on lanthanides and actinides: Design considerations and new advances in the context of quantum technologies", Coord. Chem. Rev. **346**, 216–239 (2017) (cit. on p. 57).

[124] M. Atzori and R. Sessoli, "The Second Quantum Revolution: Role and Challenges of Molecular Chemistry", J. Am. Chem. Soc. **141**, 11339–11352 (2019) (cit. on p. 57).

[125] K.-Y. Choi, Y. H. Matsuda, H. Nojiri, et al., "Observation of a half step magnetization in the cu_3-type triangular spin ring", Phys. Rev. Lett. **96**, 107202 (2006) (cit. on pp. 58–59, 102).

[126] U. Kortz, N. K. Al-Kassem, M. G. Savelieff, N. A. Al Kadi, and M. Sadakane, "Synthesis and characterization of copper-, zinc-, manganese-, and cobalt-substituted dimeric heteropolyanions, [(α-XW9O33)2M3(H2O)3]n- (n = 12, X = AsIII, SbIII, M = Cu2+, Zn2+; n = 10, X = SeIV, TeIV, M = Cu2+) and [(α-AsW9O33)2WO(H2O)M2(H2O)2]10- (M = Zn2+, Mn2+, Co2+)", Inorg. Chem. **40**, 4742 (2001) (cit. on p. 58).

[127] M. Chizzini, L. Crippa, A. Chiesa, et al., "Molecular nanomagnets with competing interactions as optimal units for qudit-based quantum computation", Phys. Rev. Res. **4**, 043135 (2022) (cit. on pp. 59–60, 63, 70, 115, 117, 119, 121–122, 147, 209).

[128] E. Garlatti, S. Carretta, M. Affronte, E. C. Sanudo, G. Amoretti, and P. Santini, "Magnetic properties and relaxation dynamics of a frustrated Ni7 molecular nanomagnet", J. Phys.: Condens. Matt. **24**, 104006 (2012) (cit. on pp. 60, 102).

[129] A. Chiesa, F. Petiziol, M. Chizzini, P. Santini, and S. Carretta, "Theoretical Design of Optimal Molecular Qudits for Quantum Error Correction", J. Phys. Chem. Lett. **13**, 6468–6474 (2022) (cit. on pp. 60–61, 73, 77, 103, 106, 108–109, 111, 147, 209).

[130] C. P. Slichter, "Principles of Magnetic Resonance", edited by M. Cardona, P. Fulde, K. Von Klitzing, H.-J. Queisser, and H. K. V. Lotsch, Vol. 1, Springer Series in Solid-State Sciences (Springer, Berlin, Heidelberg, 1990) (cit. on p. 61).

[131] A. Chiesa, P. Santini, and S. Carretta, "Supramolecular Complexes for Quantum Simulation", Magnetochemistry **2**, 37 (2016) (cit. on p. 65).

[132] A. Chiesa, G. F. S. Whitehead, S. Carretta, et al., "Molecular nanomagnets with switchable coupling for quantum simulation", Sci. Rep. **4**, 7423 (2014) (cit. on pp. 66, 68).

[133] J. Ferrando-Soria, E. Moreno-Pineda, A. Chiesa, et al., "A modular design of molecular qubits to implement universal quantum gates", Nat. Commun. **7**, 11377 (2016) (cit. on pp. 66, 68).

[134] M. Atzori, A. Chiesa, E. Morra, M. Chiesa, L. Sorace, S. Carretta, and R. Sessoli, "A two-qubit molecular architecture for electronmediated nuclear quantum simulation", Chem. Sci. **9**, 6183 (2018) (cit. on p. 66).

[135] J. Ferrando-Soria, S. A. Magee, A. Chiesa, et al., "Switchable Interaction in Molecular Double Qubits", Chem **1**, 727–752 (2016) (cit. on pp. 66, 68).

[136] J. C. Garcia-Escartin and P. Chamorro-Posada, "A swap gate for qudits", Quantum Inf. Process. **12**, 3625–3631 (2013) (cit. on p. 67).

[137] M. Kälin, I. Gromov, and A. Schweiger, "The continuous wave electron paramagnetic resonance experiment revisited", J. Magn. Reson. **160**, 166–182 (2003) (cit. on p. 68).

[138] P. A. Ivanov, E. S. Kyoseva, and N. V. Vitanov, "Engineering of arbitrary U(N) transformations by quantum householder reflections", Phys. Rev. **74**, 022323 (2006) (cit. on pp. 70, 113).

[139] S. L. Bayliss, D. W. Laorenza, P. J. Mintun, B. D. Kovos, D. E. Freedman, and D. D. Awschalom, "Optically addressable molecular spins for quantum information processing", Science **370**, 1309–1312 (2020) (cit. on p. 70).

[140] A. Chiesa, M. Chizzini, E. Garlatti, et al., "Assessing the Nature of Chiral-Induced Spin Selectivity by Magnetic Resonance", J. Phys. Chem. Lett. **12**, 6341–6347 (2021) (cit. on pp. 70, 149, 151, 155, 157–158, 209).

[141] H. J. Eckvahl, N. A. Tcyrulnikov, A. Chiesa, et al., "Direct observation of chirality-induced spin selectivity in electron donor–acceptor molecules", Science **382**, 197–201 (2023) (cit. on p. 70).

[142] E. Macaluso, A. Chiesa, P. Santini, R. Bittl, and S. Carretta, "Chiral-induced spin selectivity in photo-induced electron transfer: Investigating charge and spin dynamics in a master equation framework", J. Chem. Phys. **159**, 084301 (2023) (cit. on p. 70).

[143] A. Gómez-León, F. Luis, and D. Zueco, "Dispersive Readout of Molecular Spin Qudits", Phys. Rev. Appl. **17**, 064030 (2022) (cit. on p. 71).

[144] V. B. Braginsky, Y. I. Vorontsov, and K. S. Thorne, "Quantum nondemolition measurements", Science **209**, 547–557 (1980) (cit. on p. 71).

[145] D. Zueco, G. M. Reuther, S. Kohler, and P. Hänggi, "Qubit-oscillator dynamics in the dispersive regime: Analytical theory beyond the rotating-wave approximation", Phys. Rev. A **80**, 033846 (2009) (cit. on p. 71).

[146] J. Wang, F. Sciarrino, A. Laing, and M. G. Thompson, "Integrated photonic quantum technologies", Nat. Photonics **14**, 273–284 (2020) (cit. on p. 72).

[147] M. S. Fataftah, J. M. Zadrozny, S. C. Coste, M. J. Graham, D. M. Rogers, and D. E. Freedman, "Employing Forbidden Transitions as Qubits in a Nuclear Spin-Free Chromium Complex", J. Am. Chem. Soc. **138**, 1344–1348 (2016) (cit. on p. 72).

[148] Y.-S. Ding, Y.-F. Deng, and Y.-Z. Zheng, "The rise of single-ion magnets as spin qubits", Magnetochemistry **2**, 40 (2016) (cit. on p. 72).

[149] K. Bader, M. Winkler, and J. van Slageren, "Tuning of molecular qubits: very long coherence and spin-lattice relaxation times", Chem. Commun. **52**, 3623–3626 (2016) (cit. on p. 72).

[150] A. Ghirri, A. Chiesa, S. Carretta, et al., "Coherent Spin Dynamics in Molecular Cr8Zn Wheels", J. Phys. Chem. Lett. **6**, 5062–5066 (2015) (cit. on p. 73).

[151] J. Chen, C. Hu, J. F. Stanton, S. Hill, H.-P. Cheng, and X.-G. Zhang, "Decoherence in Molecular Electron Spin Qubits: Insights from Quantum Many-Body Simulations", J. Phys. Chem. Lett. **11**, 2074–2078 (2020) (cit. on p. 73).

[152] W. Yang and R.-B. Liu, "Quantum many-body theory of qubit decoherence in a finite-size spin bath", Phys. Rev. B **78**, 085315 (2008) (cit. on p. 74).

[153] W. Yang and R.-B. Liu, "Quantum many-body theory of qubit decoherence in a finite-size spin bath. ii. ensemble dynamics", Phys. Rev. B **79**, 115320 (2009) (cit. on p. 74).

[154] A. Bencini and D. Gatteschi, "Epr of exchange coupled systems" (Springer Verlag, 1990) (cit. on p. 76).

[155] S. J. Devitt, W. J. Munro, and K. Nemoto, "Quantum error correction for beginners", Rep. Progr. Phys. **76**, 076001 (2013) (cit. on p. 78).

[156] B. M. Terhal, "Quantum error correction for quantum memories", Rev. Mod. Phys. **87**, 307–346 (2015) (cit. on p. 78).

[157] A. G. Fowler, M. Mariantoni, J. M. Martinis, and A. N. Cleland, "Surface codes: Towards practical large-scale quantum computation", Phys. Rev. A **86**, 032324 (2012) (cit. on p. 78).

[158] A. Chiesa, E. Macaluso, F. Petiziol, S. Wimberger, P. Santini, and S. Carretta, "Molecular nanomagnets as qubits with embedded quantum-error correction", J. Phys. Chem. Lett. **11**, 8610–8615 (2020) (cit. on p. 79).

[159] M. H. Michael, M. Silveri, R. Brierley, V. V. Albert, J. Salmilehto, L. Jiang, and S. M. Girvin, "New class of quantum error-correcting codes for a bosonic mode", Phys. Rev. X **6**, 031006 (2016) (cit. on p. 80).

[160] V. V. Albert, K. Noh, K. Duivenvoorden, et al., "Performance and structure of single-mode bosonic codes", Phys. Rev. A **97**, 032346 (2018) (cit. on p. 80).

[161] M. Chizzini, L. Crippa, L. Zaccardi, E. Macaluso, S. Carretta, A. Chiesa, and P. Santini, "Quantum error correction with molecular spin qudits", Phys. Chem. Chem. Phys. **24**, 20030–20039 (2022) (cit. on pp. 83, 88, 90, 94, 96, 98–99, 209).

[162] T. Sanada, T. Suzuki, T. Yoshida, and S. Kaizaki, "Heterodinuclear complexes containing d- and f-block elements: synthesis, structural characterization, and metal-metal interactions of novel chromium(iii)-lanthanide(iii) compounds bridged by oxalate", Inorg. Chem. **37**, 4712 (1998) (cit. on pp. 86, 88).

[163] S. J. Lockyer, A. Chiesa, G. A. Timco, et al., "Targeting molecular quantum memory with embedded error correction", Chem. Sci. **12**, 9104 (2021) (cit. on pp. 87, 96).

[164] K. S. Pedersen, A.-M. Ariciu, S. McAdams, H. Weihe, J. Bendix, F. Tuna, and S. Piligkos, "Toward molecular 4f single-ion magnet qubits", J. Am. Chem. Soc. **138**, 5801–5804 (2016) (cit. on p. 87).

[165] M. Fujii, F. Wakai, H. Abe, and A. Hirai, "63cu and 65cu nmr in a single crystal of k2cuf4", J. Phys. Soc. Japan **50**, 1109 (1981) (cit. on p. 87).

[166] C Mazzoli, G Allodi, G Guidi, R De Renzi, and P Ghigna, "Nmr-nqr of orbitally ordered kcuf3", J. Magn. Magn. Mater. **272**, 106 (2004) (cit. on p. 87).

[167] R. Schutjens, F. A. Dagga, D. J. Egger, and F. K. Wilhelm, "Single-qubit gates in frequency-crowded transmon systems", Phys. Rev. A **88**, 052330 (2013) (cit. on p. 91).

[168] L. S. Theis, F. Motzoi, and F. K. Wilhelm, "Simultaneous gates in frequency-crowded multilevel systems using fast, robust, analytic control shapes", Phys. Rev. A **93**, 012324 (2016) (cit. on p. 91).

[169] S. P. Premaratne, J.-H. Yeh, F. C. Wellstood, and B. S. Palmer, "Implementation of a generalized controlled-not gate between fixed-frequency transmons", Phys. Rev. A **99**, 012317 (2019) (cit. on p. 91).

[170] S. E. Economou and E. Barnes, "Analytical approach to swift nonleaky entangling gates in superconducting qubits", Phys. Rev. B **91**, 161405 (2015) (cit. on p. 91).

[171] F. Motzoi, J. M. Gambetta, P. Rebentrost, and F. K. Wilhelm, "Simple pulses for elimination of leakage in weakly nonlinear qubits", Phys. Rev. Lett. **103**, 110501 (2009) (cit. on p. 91).

[172] J. M. Gambetta, F. Motzoi, S. T. Merkel, and F. K. Wilhelm, "Analytic control methods for high-fidelity unitary operations in a weakly nonlinear oscillator", Phys. Rev. A **83**, 012308 (2011) (cit. on pp. 91, 109).

[173] A. De, "Fast two-quadrature adiabatic quantum gates for weakly nonlinear qubits: a tight-binding approach", Quantum Inf. Process. **18**, 165 (2019) (cit. on p. 91).

[174] R. Hussain, G. Allodi, A. Chiesa, et al., "Coherent manipulation of a molecular ln-based nuclear qudit coupled to an electron qubit", J. Am. Chem. Soc. **140**, 9814–9818 (2018) (cit. on pp. 96–97).

[175] S. Chicco, A. Chiesa, G. Allodi, et al., "Controlled coherent dynamics of [VO(TPP)], a prototype molecular nuclear qudit with an electronic ancilla", Chem. Sci. **12**, 12046 (2021) (cit. on p. 97).

[176] A. Castro, A. García Carrizo, S. Roca, D. Zueco, and F. Luis, "Optimal control of molecular spin qudits", Phys. Rev. Applied **17**, 064028 (2022) (cit. on p. 109).

[177] C. P. Koch, U. Boscain, T. Calarco, et al., "Quantum optimal control in quantum technologies. Strategic report on current status, visions and goals for research in Europe", EPJ Quantum Technol. **9**, 1–60 (2022) (cit. on p. 109).

[178] A. Muthukrishnan and C. R. Stroud, "Multivalued logic gates for quantum computation", Phys. Rev. A **62**, 052309 (2000) (cit. on p. 123).

[179] R. Somma, G. Ortiz, J. E. Gubernatis, E. Knill, and R. Laflamme, "Simulating physical phenomena by quantum networks", Phys. Rev. A **65**, 042323 (2002) (cit. on pp. 129, 131).

[180] D. Wecker, M. B. Hastings, N. Wiebe, B. K. Clark, C. Nayak, and M. Troyer, "Solving strongly correlated electron models on a quantum computer", Phys. Rev. A **92**, 062318 (2015) (cit. on pp. 129, 140).

[181] F Verstraete and J. I. Cirac, "Mapping local hamiltonians of fermions to local hamiltonians of spins", Journal of Statistical Mechanics: Theory and Experiment **2005**, P09012 (2005) (cit. on pp. 129, 133).

[182] R. C. Ball, "Fermions without fermion fields", Phys. Rev. Lett. **95**, 176407 (2005) (cit. on pp. 129, 133).

[183] J. D. Whitfield, and M. Troyer, "Local spin operators for fermion simulations", Phys. Rev. A **94**, 030301 (2016) (cit. on pp. 129, 133).

[184] S. B. Bravyi and A. Y. Kitaev, "Fermionic Quantum Computation", Ann. Phys. **298**, 210–226 (2002) (cit. on p. 131).

[185] J. T. Seeley, M. J. Richard, and P. J. Love, "The Bravyi-Kitaev transformation for quantum computation of electronic structure", J. Chem. Phys. **137**, 224109 (2012) (cit. on p. 131).

[186] K. Setia and J. D. Whitfield, "Bravyi-Kitaev Superfast simulation of electronic structure on a quantum computer", J. Chem. Phys. **148**, 164104 (2018) (cit. on pp. 131–132).

[187] R. W. Chien, S. Xue, T. S. Hardikar, K. Setia, and J. D. Whitfield, "Analysis of superfast encoding performance for electronic structure simulations", Phys. Rev. A **100**, 032337 (2019) (cit. on p. 131).

[188] M. B. Hastings, D. Wecker, B. Bauer, and M. Troyer, "Improving quantum algorithms for quantum chemistry", Quantum Info. Comput. **15**, 1–21 (2015) (cit. on p. 131).

[189] J. D. Whitfield, J. Biamonte, and A. Aspuru-Guzik, "Simulation of electronic structure hamiltonians using quantum computers", Molecular Phys. **109**, 735–750 (2011) (cit. on p. 131).

[190] A. Tranter, P. J. Love, F. Mintert, and P. V. Coveney, "A Comparison of the Bravyi–Kitaev and Jordan–Wigner Transformations for the Quantum Simulation of Quantum Chemistry", J. Chem. Theory Comput. **14**, 5617–5630 (2018) (cit. on p. 131).

[191] A. Tranter, S. Sofia, J. Seeley, et al., "The Bravyi–Kitaev transformation: Properties and applications", Int. J. Quantum Chem. **115**, 1431–1441 (2015) (cit. on p. 132).

[192] V. Havlíček, M. Troyer, and J. D. Whitfield, "Operator locality in the quantum simulation of fermionic models", Phys. Rev. A **95**, 032332 (2017) (cit. on p. 132).

[193] M. D. Jenkins, D. Zueco, O. Roubeau, G. Aromí, J. Majer, and F. Luis, "A scalable architecture for quantum computation with molecular nanomagnets", Dalton Trans. **45**, 16682–16693 (2016) (cit. on p. 147).

[194] I. Gimeno, W. Kersten, M. C. Pallarés, et al., "Enhanced Molecular Spin-Photon Coupling at Superconducting Nanoconstrictions", ACS Nano **14**, 8707–8715 (2020) (cit. on p. 147).

[195] V. Rollano, M. C. de Ory, C. D. Buch, et al., "High cooperativity coupling to nuclear spins on a circuit quantum electrodynamics architecture", Commun. Phys. **5**, 1–9 (2022) (cit. on p. 147).

[196] R. Naaman, Y. Paltiel, and D. H. Waldeck, "Chiral molecules and the electron spin", Nat. Rev. Chem. **3**, 250–260 (2019) (cit. on p. 149).

[197] R. Naaman, Y. Paltiel, and D. H. Waldeck, "Chiral induced spin selectivity gives a new twist on spin-control in chemistry", Acc. Chem. Res. **53**, 2659–2667 (2020) (cit. on p. 149).

[198] T. S. Metzger, S. Mishra, B. P. Bloom, et al., "The electron spin as a chiral reagent", Angew. Chem. Int. Ed. **59**, 1653–1658 (2020) (cit. on p. 149).

[199] R. Naaman and D. H. Waldeck, "Spintronics and chirality: spin selectivity in electron transport through chiral molecules", Annu. Rev. Phys. Chem. **66**, 263–281 (2015) (cit. on p. 149).

[200] O. Ben Dor, S. Yochelis, A. Radko, et al., "Magnetization switching in ferromagnets by adsorbed chiral molecules without current or external magnetic field", Nat. Commun. **8**, 14567 (2017) (cit. on p. 149).

[201] C. Nogues, S. R. Cohen, S. S. Daube, and R. Naaman, "Electrical properties of short dna oligomers characterized by conducting atomic force microscopy", Phys. Chem. Chem. Phys. **6**, 4459–4466 (2004) (cit. on p. 149).

[202] Z. Xie, T. Z. Markus, S. R. Cohen, Z. Vager, R. Gutierrez, and R. Naaman, "Spin specific electron conduction through dna oligomers", Nano Lett. **11**, 4652–4655 (2011) (cit. on p. 149).

[203] A. C. Aragonès, E. Medina, M. Ferrer-Huerta, et al., "Measuring the spin-polarization power of a single chiral molecule", Small **13**, 1602519 (2017) (cit. on p. 149).

[204] A.-M. Guo and Q.-F. Sun, "Spin-dependent electron transport in protein-like single-helical molecules", Proc. Natl. Acad. Sci. **111**, 11658–11662 (2014) (cit. on p. 149).

[205] I. Carmeli, K. S. Kumar, O. Heifler, C. Carmeli, and R. Naaman, "Spin selectivity in electron transfer in photosystem i", Angew. Chem. Int. Ed. **53**, 8953–8958 (2014) (cit. on p. 149).

[206] S. Varela, V. Mujica, and E. Medina, "Effective spin-orbit couplings in an analytical tight-binding model of dna: spin filtering and chiral spin transport", Phys. Rev. B **93**, 155436 (2016) (cit. on p. 149).

[207] T.-R. Pan, A.-M. Guo, and Q.-F. Sun, "Spin-polarized electron transport through helicene molecular junctions", Phys. Rev. B **94**, 235448 (2016) (cit. on p. 149).

[208] S. Matityahu, Y. Utsumi, A. Aharony, O. Entin-Wohlman, and C. A. Balseiro, "Spin-dependent transport through a chiral molecule in the presence of spin-orbit interaction and nonunitary effects", Phys. Rev. B **93**, 075407 (2016) (cit. on p. 149).

[209] E. Díaz, F. Domínguez-Adame, R. Gutierrez, G. Cuniberti, and V. Mujica, "Thermal decoherence and disorder effects on chiral-induced spin selectivity", J. Phys. Chem. Lett. **9**, 5753–5758 (2018) (cit. on p. 149).

[210] M. Geyer, R. Gutierrez, V. Mujica, and G. Cuniberti, "Chirality-induced spin selectivity in a coarse-grained tight-binding model for helicene", J. Phys. Chem. C **123**, 27230–27241 (2019) (cit. on p. 149).

[211] M. S. Zöllner, S. Varela, E. Medina, V. Mujica, and C. Herrmann, "Insight into the origin of chiral-induced spin selectivity from a symmetry analysis of electronic transmission", J. Chem. Theory Comput. **16**, 2914–2929 (2020) (cit. on p. 149).

[212] S. Varela, I. Zambrano, B. Berche, V. Mujica, and E. Medina, "Spin-orbit interaction and spin selectivity for tunneling electron transfer in dna", Phys. Rev. B **101**, 241410 (2020) (cit. on p. 149).

[213] E. Medina, L. A. González-Arraga, D. Finkelstein-Shapiro, B. Berche, and V. Mujica, "Continuum model for chiral induced spin selectivity in helical molecules", J. Chem. Phys. **142**, 194308 (2015) (cit. on p. 149).

[214] K. Michaeli and R. Naaman, "Origin of spin-dependent tunneling through chiral molecules", J. Phys. Chem. C **123**, 17043–17048 (2019) (cit. on pp. 149, 154).

[215] M. Geyer, R. Gutierrez, and G. Cuniberti, "Effective hamiltonian model for helically constrained quantum systems within adiabatic perturbation theory: application to the chirality-induced spin selectivity (ciss) effect", J. Chem. Phys. **152**, 214105 (2020) (cit. on p. 149).

[216] J. Fransson, "Chirality-induced spin selectivity: the role of electron correlations", J. Phys. Chem. Lett. **10**, 7126–7132 (2019) (cit. on p. 149).

[217] L. Zhang, Y. Hao, W. Qin, S. Xie, and F. Qu, "Chiral-induced spin selectivity: a polaron transport model", Phys. Rev. B **102**, 214303 (2020) (cit. on p. 149).

[218] P.-J. Hu, S.-X. Wang, X.-H. Gao, Y.-Y. Zhang, T.-F. Fang, A.-M. Guo, and Q.-F. Sun, "Spin-dependent electron transport along hairpinlike dna molecules", Phys. Rev. B **102**, 195406 (2020) (cit. on p. 149).

[219] G. Kothe, S. Weber, R. Bittl, E. Ohmes, M. C. Thurnauer, and J. R. Norris, "Transient epr of light-induced radical pairs in plant photosystem i: observation of quantum beats", Chem. Phys. Lett. **186**, 474–480 (1991) (cit. on pp. 149, 152–153).

[220] G. Zwanenburg and P. Hore, "Epr of spin-correlated radical pairs. analytical treatment of selective excitation including zero-quantum coherence", Chem. Phys. Lett. **203**, 65–74 (1993) (cit. on p. 149).

[221] G. Kothe, S. Weber, E. Ohmes, M. C. Thurnauer, and J. R. Norris, "Transient epr of light-induced spin-correlated radical pairs: manifestation of zero quantum coherence", J. Phys. Chem. **98**, 2706–2712 (1994) (cit. on pp. 149, 152–153).

[222] S Weber, E Ohmes, M. C. Thurnauer, J. R. Norris, and G Kothe, "Light-generated nuclear quantum beats: a signature of photosynthesis", Proc. Nati. Acad. Sci. **92**, 7789–7793 (1995) (cit. on p. 149).

[223] S. Weber, T. Biskup, A. Okafuji, et al., "Origin of light-induced spin-correlated radical pairs in cryptochrome", J. Phys. Chem. B **114**, 14745–14754 (2010) (cit. on pp. 149, 152, 154).

[224] T. P. Fay, "Chirality-induced spin coherence in electron transfer reactions", J. Phys. Chem. Lett. **12**, 1407–1412 (2021) (cit. on p. 150).

[225] H. Levanon, "Time-resolved electron paramagnetic resonance spectroscopy — principles and applications", in *Biophysical techniques in photosynthesis*, Vol. 94, edited by A. J. Amesz Janand Hoff (Springer Netherlands, 1996), pp. 211–233 (cit. on p. 151).

[226] S. Weber, "Transient epr", in *Emagres*, Vol. 6 (John Wiley & Sons, Ltd, 2017), pp. 255–270 (cit. on p. 151).

[227] X. Li, N. Markandeya, G. Jonusauskas, N. D. McClenaghan, V. Maurizot, S. A. Denisov, and I. Huc, "Photoinduced electron transfer and hole migration in nanosized helical aromatic oligoamide foldamers", J. Am. Chem. Soc. **138**, 13568–13578 (2016) (cit. on p. 151).

[228] M. T. Colvin, R. Carmieli, T. Miura, et al., "Electron spin polarization transfer from photogenerated spin-correlated radical pairs to a stable radical observer spin", J. Phys. Chem. A **117**, 5314–5325 (2013) (cit. on pp. 152, 154).

[229] K. M. Salikhov, S. G. Zech, and D. Stehlik, "Light induced radical pair intermediates in photosynthetic reaction centres in contact with an observer spin label: spin dynamics and effects on transient epr spectra", Molecular Phys. **100**, 1311–1321 (2002) (cit. on p. 153).

[230] W. G. Hol, "The role of the α-helix dipole in protein function and structure", Prog. Biophys. Mol. Biol. **45**, 149–195 (1985) (cit. on p. 154).

[231] P. M. Wallace, D. R. B. Sluss, L. R. Dalton, B. H. Robinson, and P. J. Reid, "Single-molecule microscopy studies of electric-field poling in chromophore-polymer composite materials", J. Phys. Chem. B **110**, 75–82 (2006) (cit. on p. 154).

[232] S. Varela, B. Montañes, F. López, B. Berche, B. Guillot, V. Mujica, and E. Medina, "Intrinsic rashba coupling due to hydrogen bonding in dna", J. Chem. Phys. **151**, 125102 (2019) (cit. on p. 154).

[233] A. Chiesa, F. Cugini, R. Hussain, et al., "Understanding magnetic relaxation in single-ion magnets with high blocking temperature", Phys. Rev. B **101**, 174402 (2020) (cit. on p. 161).

[234] F. Troiani, M. Affronte, S. Carretta, P. Santini, and G. Amoretti, "Proposal for quantum gates in permanently coupled antiferromagnetic spin rings without need of local fields", Phys. Rev. Lett. **94**, 190501 (2005) (cit. on p. 161).

[235] P. Santini, S. Carretta, F. Troiani, and G. Amoretti, "Molecular nanomagnets as quantum simulators", Phys. Rev. Lett. **107**, 230502 (2011) (cit. on p. 161).

[236] C. Godfrin, A. Ferhat, R. Ballou, S. Klyatskaya, M. Ruben, W. Wernsdorfer, and F. Balestro, "Operating quantum states in single magnetic molecules: implementation of grover's quantum algorithm", Phys. Rev. Lett. **119**, 187702 (2017) (cit. on p. 161).

[237] A. Chiesa, T. Guidi, S. Carretta, et al., "Magnetic exchange interactions in the molecular nanomagnet Mn_{12}", Phys. Rev. Lett. **119**, 217202 (2017) (cit. on p. 161).

[238] L. Crippa, F. Tacchino, M. Chizzini, et al., "Simulating Static and Dynamic Properties of Magnetic Molecules with Prototype Quantum Computers", Magnetochemistry **7**, 117 (2021) (cit. on pp. 161, 174–176, 178, 180, 209).

[239] A. Chiesa, F. Tacchino, M. Grossi, P. Santini, I. Tavernelli, D. Gerace, and S. Carretta, "Quantum hardware simulating four-dimensional inelastic neutron scattering.", Nat. Phys. **15**, 455–459 (2019) (cit. on pp. 162, 177, 181).

[240] A. Kandala, K. Temme, A. D. Córcoles, A. Mezzacapo, J. M. Chow, and J. M. Gambetta, "Error mitigation extends the computational reach of a noisy quantum processor", Nature **567**, 491–495 (2019) (cit. on p. 162).

[241] S. Bravyi, S. Sheldon, A. Kandala, D. C. Mckay, and J. M. Gambetta, "Mitigating measurement errors in multiqubit experiments", Phys. Rev. A **103**, 042605 (2021) (cit. on p. 162).

[242] Y. Cao, J. Romero, J. P. Olson, et al., "Quantum Chemistry in the Age of Quantum Computing", Chem. Rev. **94**, 030301 (2019) (cit. on pp. 162–163, 166–168).

[243] M. Kjaergaard, M. E. Schwartz, J. Braumüller, P. Krantz, J. I.-J. Wang, S. Gustavsson, and W. D. Oliver, "Superconducting Qubits: Current State of Play", Annu. Rev. Condens. Matter Phys. **11**, 369–395 (2020) (cit. on p. 162).

[244] E. Farhi, J. Goldstone, and S. Gutmann, "A Quantum Approximate Optimization Algorithm", (2014) (cit. on p. 163).

[245] J. Choi and J. Kim, "A Tutorial on Quantum Approximate Optimization Algorithm (QAOA): Fundamentals and Applications", in 2019 International Conference on Information and Communication Technology Convergence (ICTC), Vol. 94 (2019), pp. 138–142 (cit. on p. 163).

[246] L. Zhou, S.-T. Wang, S. Choi, H. Pichler, and M. D. Lukin, "Quantum Approximate Optimization Algorithm: Performance, Mechanism, and Implementation on Near-Term Devices", Phys. Rev. X **10**, 021067 (2020) (cit. on p. 163).

[247] A. Peruzzo, J. McClean, P. Shadbolt, et al., "A variational eigenvalue solver on a photonic quantum processor", Nat. Commun. **5**, 4213 (2014) (cit. on pp. 163, 166, 168).

[248] J. Tilly, H. Chen, S. Cao, et al., "The Variational Quantum Eigensolver: A review of methods and best practices", Phys. Rep. **986**, 1–128 (2022) (cit. on p. 163).

[249] A. Kandala, K. Temme, A. D. Córcoles, A. Mezzacapo, J. M. Chow, and J. M. Gambetta, "Error mitigation extends the computational reach of a noisy quantum processor", Nature **567**, 491–495 (2019) (cit. on pp. 166, 168).

[250] J. R. McClean, J. Romero, R. Babbush, and A. Aspuru-Guzik, "The theory of variational hybrid quantum-classical algorithms", New J. Phys. **18**, 023023 (2016) (cit. on pp. 166–168).

[251] N. C. Rubin, R. Babbush, and J. McClean, "Application of fermionic marginal constraints to hybrid quantum algorithms", New J. Phys. **20**, 053020 (2018) (cit. on p. 167).

[252] D. R. Jones, C. D. Perttunen, and B. E. Stuckman, "Lipschitzian optimization without the Lipschitz constant", J. Optim. Theory Appl. **79**, 157–181 (1993) (cit. on p. 168).

[253] J. C. Spall, "An overwiev of the simultaneous perturbation method for efficient optimization", Johns Hopkins Apl Technical Digest **19**, 482–492 (1998) (cit. on p. 168).

[254] O. Waldmann, "Spin dynamics of finite antiferromagnetic heisenberg spin rings", Phys. Rev. B **65**, 024424 (2001) (cit. on p. 171).

[255] K. Seki, T. Shirakawa, and S. Yunoki, "Symmetry-adapted variational quantum eigensolver", Phys. Rev. A **101**, 052340 (2020) (cit. on p. 171).

Publications

Referred publications:

- M. Chizzini, L. Crippa, A. Chiesa, F. Tacchino, F. Petiziol, I. Tavernelli, P. Santini and S. Carret-ta, "Molecular Nanomagnets with Competing Interactions as Optimal Units for Qudit-Based Quan-tum Computation", Phys. Rev. Res., 4, 043135 (2022).

- M. Chizzini*, L. Crippa*, l. Zaccardi, E. Macaluso, S. Carretta, A. Chiesa and P. Santini, "Quantum error correction with molecular spin qudits", Phys. Chem. Chem. Phys., 24, 20030-20039 (2022).

- A. Chiesa, F. Petiziol, M. Chizzini, P. Santini and S. Carretta, "Theoretical Design of Optimal Mo-lecular Qudits for Quantum Error Correction",J. Phys. Chem. Lett., 13, 6468-6474 (2022).

- A. Chiesa, M. Chizzini, E. Garlatti, E. Salvadori, F. Tacchino, P. Santini, I. Tavernelli, R. Bittl, M. Chiesa, R. Sessoli and S. Carretta, "Assessing the Nature of Chiral-Induced Spin Selectivity by Magnetic Resonance", J. Phys. Chem. Lett., 12, 6341–6347 (2021).

- L. Crippa, F. Tacchino, M. Chizzini, A. Aita, Michele Grossi, A. Chiesa, P. Santini, I. Tavernelli, and S. Carretta, "Simulating Static and Dynamic Properties of Magnetic Molecules with Prototype Quantum Computers", Magnetochemistry, 7, 117 (2021).

Publications in preparation:

- M. Chizzini, et al., “Qudit-based Quantum Simulation of Fermionic Systems”.

Copyright Permissions

Images reproduced from published sources:

- Figures 1.3 has been reproduced from Ref. [33] under the license CC BY-SA 4.0.

- Figures 2.7, 3.1, 3.2, 3.3, 3.4, 3.5, 3.6 are reproduced or adapted from Ref. [161] with permission under the terms and conditions of the Creative Commons Attribution-NonCommercial 3.0 Unported license (CC BY-NC 3.0).

- Figures 2.3, 4.1, 4.2, 4.3, 4.4, 4.5 are reproduced or adapted from Ref. [129] under the terms and conditions of the Creative Commons Attribution license (CC-BY 4.0).

- Figures 2.2, 5.1, 5.2, 5.3, 5.4, 5.5 are reproduced or adapted from Ref. [127] under the terms of the Creative Commons Attribution 4.0 International license.

- Figures 7.1, 7.2, 7.3, 7.4 are reproduced or adapted from Ref. [140] with permission under the terms and conditions of the Creative Commons Attribution license CC-BY 4.0.

- Figures 8.1, 8.2 8.3, 8.4, 8.5, 8.6 are reproduced or adapted from Ref. [238] under the terms and conditions of the Creative Commons Attribution (CC BY) license (https://creativecommons.org/licenses/by/4.0/).

Acknowledgments

In conclusion of this work, I want to express my deepest gratitude to all the people that have guided and supported me during these intense and rewarding years. To all of them, my heartfelt gratitude for the availability and the assistance they have generously offered me on countless occasions, while I was navigating by sight through the depths of a subject that demands a lot, but gives back so much more.

I want to express my profound gratefulness to my esteemed supervisor, Prof. Paolo Santini, a brilliant scientist who guided me with insightful observations. Over the years, he has consistently displayed kindness and helpfulness, making my academic journey all the more enriching.

I extend my sincere gratitude to my co-supervisor, Prof. Alessandro Chiesa, whose unwavering support has been a beacon, guiding me through the challenges with patience and understanding. His commitment to research serves as a remarkable example of diligence and dedication.

I also want to convey my appreciation to Prof. Stefano Carretta for his invaluable and thoughtful advice, his dedicated teaching, and the stimulating discussions that have significantly contributed to my growth as a Physics student and as a person.

A special mention is reserved for Dr. Luca Crippa, with whom I shared most of the daily work. After numerous collaborative efforts, I believe that we both can derive great satisfaction from the remarkable results. His unwavering assistance, patience, and politeness have truly made him an exceptional collaborator and friend.

Dr. Ivano Tavernelli and Dr. Francesco Tacchino, both distinguished scientists and enjoyable individuals, I thank for their valuable scientific contributions to our publications and for the enjoyable period I spent with them at IBM research.

Last but not least, I would like to thank my office colleagues, Emilio and Marco, for the engaging scientific and non-scientific discussions that undoubtedly lightened many long working days.
In conclusion of my long academic journey, my thoughts naturally go to my big family who have always given me unyielding support and have been the driving force through the challenges and triumphs of all my studies. Their unwavering encouragement has been the fuel that has powered my research and my curiosity. As I embark on a new chapter with enthusiasm, I look back and I find myself immensely grateful for the collaborative spirit and the lessons learnt that have defined this stimulating chapter of my life.

Fundings

The various researches carried out and related activities have received funding from the European Union's Horizon 2020 research and innovation program (FET-OPEN FATMOLS project) under Grant Agreement No. 862893, the European project Scaling Up quantum computation with MOlecular spins (SUMO) under QuantERA, the Italian Ministry of Education and Research (MUR) through PRIN project 2017 QchiSS "Quantum detection of chiral-induced spin-selectivity at the molecular level", PNRR MUR project PE0000023-NQSTI, and the Fondazione Cariparma.